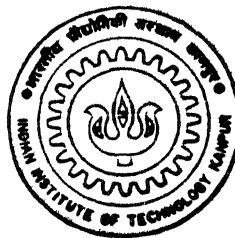


# HOT WORKING BEHAVIOUR OF Ti-6.4Al-2.6Mo-1.5Cr-0.4Fe-0.3Si ALLOY

by  
SUDIPTO GHOSH

TH  
MME/1998/P  
G1346-h.



DEPARTMENT OF MATERIALS AND METALLURGICAL ENGINEERING

**Indian Institute of Technology, Kanpur**

JUNE , 1998

# HOT WORKING BEHAVIOUR OF Ti-6.4Al-2.6Mo-1.5Cr-0.4Fe-0.3Si ALLOY

*A Thesis Submitted*

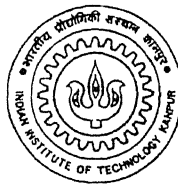
in Partial Fulfillment of the Requirements

for the Degree of

**Doctor of Philosophy**

*by*

**Sudipto Ghosh**



*to the*

**DEPARTMENT OF MATERIALS AND METALLURGICAL ENGINEERING**

**INDIAN INSTITUTE OF TECHNOLOGY KANPUR**

**June, 1998**

**Dedicated to**

**My Parents**

Dr. Ahindra Ghosh

*and*

Dr. (Mrs.) Radha Ghosh

*and*

**My Gurudev**

His Divine Grace

Bhaktisvarupa Damodara Swami

(Sri!a Sripada)

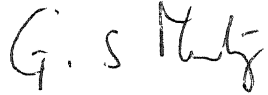


# Certificate

It is certified that the work contained in the thesis entitled **HOT WORKING BEHAVIOUR OF Ti-6.4Al-2.6Mo-1.5Cr-0.4Fe-0.3Si ALLOY** by Sudipto Ghosh has been carried out under our supervision and that this work has not been submitted elsewhere for a degree.

  
(Dr. S. Bhargava )

Professor  
Department of Materials  
and  
Metallurgical Engineering  
Indian Institute of Technology  
Kanpur-208016, India

  
(Dr. G. S. Murty )

Professor (Retd )  
Department of Materials  
and  
Metallurgical Engineering  
Indian Institute of Technology  
Kanpur-208016, India

JUNE, 1998



# Acknowledgements

I wish to express my sincere and profound gratitude to Professors Sanjeev Bhargava and G. S Murty for introducing me to the area of deformation processing and extending enthusiastic aid to bring this investigation to its present shape. Apart from guiding the thesis work, they have provided me with strong moral support at the moments of difficulties and a more mature outlook towards scientific and technological profession.

I wish to thank Professor Y.V.R.K. Prasad and Mr. Shashidhar of IISc Bangalore for the sincere help they have provided me in connection with the compression tests on DARTEC machine. I am also grateful to Dr. C. R. Chakraborty, Dr. Abhijit Dutta, Dr. Asim Mukhopadhyaya and Dr. Trilok Singh of DMRL for various critical helps they have provided.

I wish to also thank MIDHANI, Hyderabad for providing me with the material for my thesis work. Many valuable helps have come from the staff of MIDHANI. I take this opportunity to thank Mr. B. Saha of CRE, Hyderabad for his valuable helps at Hyderabad.

At IIT Kanpur many of my teachers have contributed towards my work. I am specially indebted to Professor A. K. Biswas for his strong and selfless support at the moment of serious crisis. Similarly I wish to thank Professors R. K. Ray, G. Biswas, N. K. Batra, S. Sangal, S. C. Koria, B. Deo, A. K. Sharma, and K.K.Saxena, for their

valuable help during the thesis work.

I wish to thank my colleagues: Dr. S. K. Choudhary, Dr.(Mrs) Uma Devi, Dr. N. K. Nath, Dr. S. K. Bhowmik, Dr. H. N. Azari, Dr. P. K. Bagdi, Dr. Nagarajan, Dr. T. K. Roy, Dr.(Mrs) M. Sujata, Dr. G. G. Roy, Mr. Devender Singh, Mr. Kamlesh Singh, Dr. B. Bhattacharya, Dr. S. Daniel, Mr. Ananda Katti, Mr. Ashish Roberts, Joy Mitra, Mr. Atanu Bhattacharya, Mr. Tonmoy Mitra and Mr. K. Mandal.

Mr. A. Sharma, Mr. Tripathi, Mr. V. P. Gupta, Mr. H. C. Srivastava, Mr. Ramavatar, Mr. Kumar, Mr. Awasthi, Mr. Srivastava, Mr. R. K. Singh, Mr. R. Sharma and Mr. Bartwal have provided to various types of help. I wish to sincerely thank Central Workshop IIT Kanpur for providing me necessary helps. My special thanks to Mr. B. K. Jain, Mr. P. K. Paul and Mr. K. P. Mukherjee for their sincere involvement in my work.

I would like to express my gratitude to Paravati aunty, Sarita didi, Suvrat and Akanksha for their affection, encouragement and valuable helps. Gautamda and Amaravati boudi had from time to time provided good support. Along with them I would also like to thank my old well wishers at IIT Campus.

Many of my friends have made my life happy during the stay at IIT Kanpur: Dr. S. C. Mishra and Sree Rani bhabhi, Kamlesh and Bharati bhabhi, Rupamanohar and Nutan bhabhi, Kailash and Vandana bhabhi, SvarupaKrishna, Japesh, Giri, GouriLila, Joy, Himanshu, Shibu, Nemade, Srinivas, Paritosh, Dr. S. Bhattacharya, Manoj Srivastava, Dr. U. S. Dixit, Mr. K.K.Dhawan, Sandip Raheja, P.K.Singh and Dolly bhabhi, Mr. and Mrs. S. Mishra, Mr. and Mrs. P.K.Paul, Dr. Jha, Rishiraj, Varun, Anubhav, Bhaskar, Vijay, Haria, Hare Krishna, Rajan, Kedar, Mahesh, Dr. Praveen Bhatia, Ramgopal, Vasudev, Gautam, Prabhakar, Prateep, Mukesh and many others.

My special thanks to Gautam Sinha, H. K. Reddy, Anubhav, Kamlesh, Varun,

Shibu, Bhaskar, Ramgopal and Vijay for their help in the thesis processing.

My family members have been constant source of encouragement. My sister Sudeshna and brother Avidipto always provided all sorts of help required. Mamima selflessly served me with choice food whenever I desired. Mamuji had a very serious concern for my work and didn't allow me to worry about household duties. I cannot express my indebtedness to my mother. She took all troubles for me and quietly tolerated many disturbances. My father has been source of my interest in scientific field of activities. With out getting the seed of interest from him I would have never taken up research profession. During my Ph.D he has provided me constant encouragement and valuable advice

Sudipto Ghosh

# Contents

|   |          |
|---|----------|
| List of Figures   | vii      |
| List of Tables  | xvii     |
| List of Symbols   | xviii    |
| Synopsis  | xxiii    |
| <b>1 INTRODUCTION</b>   | <b>1</b> |
| 1.1 Alloying of Titanium and Types of Titanium Alloys[1, 2] . . . . . | 3        |
| 1.2 Processing of ( $\alpha+\beta$ ) Titanium Alloys[1] . . . . .     | 6        |
| 1.2.1 Casting . . . . .   | 6        |
| 1.2.2 Powder Metallurgy Processing . . . . .                          | 6        |
| 1.2.3 Deformation Processing . . . . .                                | 7        |
| 1.3 Fundamentals of Hot Workability . . . . .                         | 9        |
| 1.3.1 Constitutive Equation . . . . .                                 | 9        |

|          |   |           |
|----------|---|-----------|
| 1.3.2    | Instability During Uniaxial Compression . . . . .   | 12        |
| 1.3.3    | Other Approaches to Workability . . . . .   | 18        |
| 1.3.4    | Dynamic Changes Occurring During the Hot Deformation and<br>Their Influence on the Flow Behavior and Flow Instability . . . . | 24        |
| <b>2</b> | <b>OBJECTIVE OF THE PRESENT STUDY AND PLAN OF THE<br/>WORK</b>  | <b>30</b> |
| <b>3</b> | <b>EXPERIMENTAL PROCEDURE</b>   | <b>34</b> |
| 3.1      | Processing of Ti-622Si Alloy and its Characterization . . . . .   | 34        |
| 3.1.1    | The As-Received Material . . . . .  | 34        |
| 3.1.2    | Modification of the As-Received Microstructure . . . . .  | 36        |
| 3.1.3    | Determination of the $\beta$ Transus Temperature . . . . .  | 36        |
| 3.2      | Preparation of Compression Specimens . . . . .  | 37        |
| 3.3      | Compression Testing of Ti-622Si Alloy with the $\beta$ Structure . . . . .  | 38        |
| 3.3.1    | Load-Displacement Curves . . . . .  | 38        |
| 3.3.2    | True Stress versus True Plastic Strain Curves . . . . .   | 39        |
| 3.3.3    | Strain Rate Sensitivity and Efficiency of Power Dissipation . . . .   | 40        |
| 3.3.4    | Flow Localization and Instability Parameters . . . . .  | 40        |
| 3.4      | Compression Testing of Ti-622Si Alloy with the $(\alpha+\beta)$ Microstructure . .  | 41        |
| 3.4.1    | Stress-Strain Rate Curves and Strain Rate Sensitivity . . . . .   | 41        |

|          |  |           |
|----------|--|-----------|
| 3.4.2    | Calculation of Parameters of Constitutive Equation . . . . .                                       | 43        |
| 3.5      | Macroscopic and Microscopic Observations of Specimens . . . . .                                    | 45        |
| 3.5.1    | Macroscopic Observation of Deformed Specimens of Ti-622Si With<br>$\beta$ Microstructure . . . . . | 45        |
| 3.5.2    | Microstructural Characterization of Specimens of Ti-622Si . . . . .                                | 45        |
| <b>4</b> | <b>RESULTS</b>   | <b>51</b> |
| 4.1      | Microstructural States of Ti-622Si Alloy . . . . .   | 51        |
| 4.1.1    | The $\beta$ transus temperature of Ti-622Si Alloy . . . . .  | 56        |
| 4.1.2    | Microstructure of Ti-622Si at Hot Working Temperatures . . . . .                                   | 56        |
| 4.2      | Flow Behaviour of Ti-622Si with $\beta$ Structure . . . . .  | 59        |
| 4.2.1    | Stress-Strain Behaviour . . . . .  | 59        |
| 4.2.2    | Temperature Correction of the Stress-Strain Curves . . . . .                                       | 61        |
| 4.2.3    | Temperature Corrected Stress-Strain Curves . . . . .   | 80        |
| 4.2.4    | Stress-Strain Rate Behaviour and Strain Rate Sensitivity . . . . .                                 | 80        |
| 4.2.5    | Phenomenological Description of Flow Behaviour at High Tem-<br>perature . . . . .                  | 81        |
| 4.2.6    | Instability Parameters . . . . .   | 90        |
| 4.2.7    | Structural Manifestations of Unstable Flow . . . . .   | 112       |

|          |  |            |
|----------|--|------------|
| 4.2.8    | Microstructural Changes in Ti-622Si with $\beta$ Microstructure During its Hot Deformation . . . . . | 122        |
| 4.2.9    | Microstructural Evolution of Ti-622Si During Deformation in the $\beta$ Phase Field . . . . .        | 132        |
| 4.3      | Flow behaviour of Ti-622Si With Equiaxed Structure . . . . .   | 132        |
| 4.3.1    | Constitutive Behaviour . . . . .   | 149        |
| 4.3.2    | Parameters of Constitutive Relationship for Region II . . . . .                                      | 149        |
| <b>5</b> | <b>DISCUSSION</b>  | <b>159</b> |
| 5.1      | Influence of Instability Parameters on the Flow Instability . . . . .                                | 160        |
| 5.2      | Mechanism of Microstructural Evolution . . . . .   | 164        |
| 5.3      | DMM Interpretation of Microstructural Evolution . . . . .  | 168        |
| 5.4      | Influence of Microstructural Evolution on Stress-Strain Behaviour and Flow Instability . . . . .     | 169        |
| 5.5      | Constitutive Behaviour of Ti-622Si with Equiaxed Microstructure . . . . .                            | 173        |
| 5.6      | Best Domain of Workability . . . . .   | 178        |
| <b>6</b> | <b>SUMMARY AND CONCLUSIONS</b>   | <b>189</b> |
|          | <b>Anexure-A</b>   | <b>196</b> |

# List of Figures

|     |  |    |
|-----|--|----|
| 1.1 | Phase diagrams for Ti-alloying element system . . . . .  | 4  |
| 1.2 | Inhomogeneous flow during uniaxial compression . . . . .   | 13 |
| 1.3 | Variation of $\gamma$ with strain for a typical flow softening material . . . . .  | 17 |
| 1.4 | G content and J co-content for a workpiece . . . . .   | 19 |
| 3 1 | As received microstructure of Ti-622Si alloy . . . . .   | 47 |
| 3 2 | Microstructure of Ti-622Si alloy in the TMT condition . . . . .  | 47 |
| 3.3 | Compression specimens for Ti-622Si alloy with $\beta$ -structure, with concentric grooves on the faces and hole for thermocouple insertion . . . . . | 48 |
| 3 4 | Specimen and platens surrounded by three zone furnace . . . . .  | 49 |
| 3 5 | Geometry of compression platens for compression of Ti-622Si with equiaxed microstructure . . . . .   | 50 |
| 4 1 | Ti-622Si alloy in $\beta$ microstructural state at (a) lower and (b) higher magnifications. . . . .  | 53 |



|      |  |    |
|------|--|----|
| 4.2  | Microstructure of Ti-622Si alloy in the conditions: (a) TMT (b) TMT-A1 and (c) TMT-A3 . . . . .  | 54 |
| 4.3  | Grain growth behaviour of Ti-622Si in TMT condition at 920°C . . . . .   | 55 |
| 4.4  | Microstructure of Ti-622Si in TMT-A3 condition, soaked at temperatures: (a) 970°C, (b) 975°C and (c) 980°C and subsequently water quenched . . . . .   | 57 |
| 4.5  | Microstructure of Ti-622Si with $\beta$ structure, soaked at temperatures: (a) 800°C (b) 900°C and (c) 950°C and subsequently water quenched . . . . . | 58 |
| 4.6  | Microstructure of Ti-622Si in TMT-A3 condition, soaked at 940°C and subsequently water quenched . . . . .  | 59 |
| 4.7  | Load-displacement curves obtained from compression test of Ti-622Si( $\beta$ ) at 750°C . . . . .  | 62 |
| 4.8  | True stress versus true plastic strain curves for Ti-622Si( $\beta$ ) at 750°C . . . . .   | 63 |
| 4.9  | True stress versus true plastic strain curves for Ti-622Si( $\beta$ ) at 800°C . . . . .   | 64 |
| 4.10 | True stress versus true plastic strain curves for Ti-622Si( $\beta$ ) at 850°C . . . . .   | 65 |
| 4.11 | True stress versus true plastic strain curves for Ti-622Si( $\beta$ ) at 900°C . . . . .   | 66 |
| 4.12 | True stress versus true plastic strain curves for Ti-622Si( $\beta$ ) at 950°C . . . . .   | 67 |
| 4.13 | True stress versus true plastic strain curves for Ti-622Si( $\beta$ ) at 1000°C . . . . .  | 68 |
| 4.14 | Variation of plastic strain corresponding to peak stress with strain rate for Ti-622Si( $\beta$ ) . . . . .  | 69 |
| 4.15 | Variation of recorded temperature rise at the end of compression test with strain rate for Ti-622Si( $\beta$ ) . . . . .                               | 71 |

|      |  |    |
|------|--|----|
| 4 16 | Schematic representation of boundary condition applied to equation 4.9 . . . . .   | 75 |
| 4 17 | Variation of $f$ with plastic strain for Ti-622Si( $\beta$ ) . . . . .   | 76 |
| 4.18 | Temperature dependency of true stress corresponding to strain level of<br>0.1 for Ti-622Si( $\beta$ ) . . . . .                                      | 79 |
| 4 19 | Variation of peak true stress with strain rate for Ti-622Si( $\beta$ ) . . . . .   | 82 |
| 4.20 | Variation of true stress with strain rate for Ti-622Si( $\beta$ ) at strain of 0.1 . . . . .   | 83 |
| 4 21 | Variation of temperature corrected true stress with strain rate for Ti-<br>622Si( $\beta$ ) at strain of 0.3 . . . . .                               | 84 |
| 4.22 | Variation of $m$ with strain rate for Ti-622Si( $\beta$ ) corresponding to strain of<br>$\epsilon_p$ . . . . .                                       | 85 |
| 4.23 | Variation of $m$ with strain rate for Ti-622Si( $\beta$ ) corresponding to strain of<br>0.3 . . . . .  | 86 |
| 4 24 | Plot of strain rate corresponding to fixed stress levels versus $(1/T) \times 10^4$<br>for Ti-622Si( $\beta$ ) . . . . .                             | 88 |
| 4.25 | Plot of $m$ calculated using equation 4.16 versus that obtained experiment-<br>ally for Ti-622Si( $\beta$ ) corresponding to strain of 0.1 . . . . . | 89 |
| 4.26 | Variation of true stress corresponding to strain level of 0.1 with Zener-<br>Holloman parameter for Ti-622Si( $\beta$ ) . . . . .                    | 91 |
| 4.27 | Variation of true stress corresponding to strain level of 0.3 with Zener-<br>Holloman parameter for Ti-622Si( $\beta$ ) . . . . .                    | 92 |
| 4.28 | Variation of true stress corresponding to strain level of 0.5 with Zener-<br>Holloman parameter for Ti-622Si( $\beta$ ) . . . . .                    | 93 |

|      |   |     |
|------|---|-----|
| 4.29 | Variation of $\psi$ with plastic strain at 750°C for Ti-622Si( $\beta$ ) . . . . .  | 95  |
| 4.30 | Variation of $\psi$ with plastic strain at 750°C for Ti-622Si( $\beta$ ) . . . . .  | 96  |
| 4.31 | Variation of $\psi$ with plastic strain at 800°C for Ti-622Si( $\beta$ ) . . . . .  | 97  |
| 4.32 | Variation of $\psi$ with plastic strain at 800°C for Ti-622Si( $\beta$ ) . . . . .  | 98  |
| 4.33 | Variation of $\psi$ with plastic strain at 850°C for Ti-622Si( $\beta$ ) . . . . .  | 99  |
| 4.34 | Variation of $\psi$ with plastic strain at 850°C for Ti-622Si( $\beta$ ) . . . . .  | 100 |
| 4.35 | Variation of $\psi$ with plastic strain at 900°C for Ti-622Si( $\beta$ ) . . . . .  | 101 |
| 4.36 | Variation of $\psi$ with plastic strain at 900°C for Ti-622Si( $\beta$ ) . . . . .  | 102 |
| 4.37 | Variation of $\psi$ with plastic strain at 950°C for Ti-622Si( $\beta$ ) . . . . .  | 103 |
| 4.38 | Variation of $\psi$ with plastic strain at 950°C for Ti-622Si( $\beta$ ) . . . . .  | 104 |
| 4.39 | Variation of $\psi$ with plastic strain at 1000°C for Ti-622Si( $\beta$ ) . . . . .   | 105 |
| 4.40 | Variation of $\psi$ with plastic strain at 1000°C for Ti-622Si( $\beta$ ) . . . . .   | 106 |
| 4.41 | Domains for different types of variation of $\psi$ with plastic strain for Ti-622Si( $\beta$ ) . . . . .  | 107 |
| 4.42 | Contour Map for $\zeta$ parameter corresponding to strain level of 0.1 for Ti-622Si( $\beta$ ) . . . . .  | 108 |
| 4.43 | Contour Map for $\zeta$ parameter corresponding to strain level of 0.3 for Ti-622Si( $\beta$ ) . . . . .  | 109 |
| 4.44 | Contour Map for $\zeta$ parameter corresponding to strain level of 0.1 for Ti-622Si( $\beta$ ) obtained from the temperature corrected stress-strain curves . . . . . | 110 |

|      |  |     |
|------|--|-----|
| 4 45 | Contour Map for $\zeta$ parameter corresponding to strain level of 0.3 for<br>Ti-622Si( $\beta$ ) obtained from the temperature corrected stress-strain curves | 111 |
| 4 46 | Variation of $\psi_c$ with plastic strain at 750°C for Ti-622Si( $\beta$ ) . . . . .   | 113 |
| 4 47 | Variation of $\psi_c$ with plastic strain at 750°C for Ti-622Si( $\beta$ ) . . . . .   | 114 |
| 4.48 | Variation of $\psi_c$ with plastic strain at 800°C for Ti-622Si( $\beta$ ) . . . . .   | 115 |
| 4.49 | Variation of $\psi_c$ with plastic strain at 800°C for Ti-622Si( $\beta$ ) . . . . .   | 116 |
| 4.50 | Variation of $\psi_c$ with plastic strain at 850°C for Ti-622Si( $\beta$ ) . . . . .   | 117 |
| 4 51 | Variation of $\psi_c$ with plastic strain at 900°C for Ti-622Si( $\beta$ ) . . . . .   | 118 |
| 4 52 | Variation of $\psi_c$ with plastic strain at 950°C for Ti-622Si( $\beta$ ) . . . . .   | 119 |
| 4 53 | Domains for different types of variation of $\psi_c$ with plastic strain for Ti-<br>622Si( $\beta$ ) . . . . .   | 120 |
| 4 54 | Specimen of Ti-622Si( $\beta$ ) deformed at 800°C and $10^2 \text{ s}^{-1}$ upto a strain of<br>0.5 . . . . .  | 122 |
| 4.55 | Schematic diagram for deformed specimen exhibiting inhomogeneous flow  | 123 |
| 4.56 | Schematic diagram for deformed specimen with misalignment in the centres<br>of the top and the bottom centres . . . . .  | 124 |
| 4.57 | Shear banding in specimens of Ti-622Si( $\beta$ ) deformed at: (a) 750°C/ $10$<br>$\text{s}^{-1}$ (b) 750°C/ $10^2 \text{ s}^{-1}$ . . . . .                   | 125 |
| 4.58 | Shear banding in specimens of Ti-622Si( $\beta$ ) deformed at: (a) 800°C/ $10^2$<br>$\text{s}^{-1}$ and (b) 900°C/ $10^2 \text{ s}^{-1}$ . . . . .             | 126 |
| 4.59 | Variation of $\delta$ with strain rate for Ti-622Si( $\beta$ ) . . . . .   | 127 |

|      |  |     |
|------|--|-----|
| 4 60 | Variation of $\lambda$ with strain rate for Ti-622Si( $\beta$ ) . . . . .  | 128 |
| 4 61 | Variation of $e$ with strain rate for Ti-622Si( $\beta$ ) . . . . .  | 129 |
| 4 62 | Microstructure of Ti-622Si( $\beta$ ) following deformation at $750^{\circ}\text{C}/10^{-3} \text{ s}^{-1}$<br>upto a strain of 0.5 . . . . .  | 133 |
| 4 63 | Microstructure of Ti-622Si( $\beta$ ) following deformation at $750^{\circ}\text{C}/10^{-2} \text{ s}^{-1}$<br>upto a strain of 0.5 . . . . .  | 133 |
| 4 64 | Microstructure of Ti-622Si( $\beta$ ) within shear band following deformation at<br>$750^{\circ}\text{C}/10 \text{ s}^{-1}$ upto a strain of 0.5 . . . . .                             | 134 |
| 4.65 | Microstructure of Ti-622Si( $\beta$ ) outside the shear band following deforma-<br>tion at $750^{\circ}\text{C}/10^2 \text{ s}^{-1}$ upto a strain of 0.5 (at low magnification) . . . | 134 |
| 4 66 | Microstructure of the shear band following deformation of Ti-622Si( $\beta$ ) at<br>$750^{\circ}\text{C}/10^2 \text{ s}^{-1}$ upto a strain of 0.5(at low magnification) . . . . .     | 135 |
| 4.67 | Microstructure of Ti-622Si( $\beta$ ) outside the shear band following deforma-<br>tion at $750^{\circ}\text{C}/10^2 \text{ s}^{-1}$ upto a strain of 0.5 . . . . .                    | 135 |
| 4.68 | Microstructure of Ti-622Si( $\beta$ ) within shear band following deformation at<br>$750^{\circ}\text{C}/10^2 \text{ s}^{-1}$ upto a strain of 0.5 . . . . .                           | 136 |
| 4.69 | Microstructure of Ti-622Si( $\beta$ ) within shear band (intense zone) following<br>deformation at $750^{\circ}\text{C}/10^2 \text{ s}^{-1}$ upto a strain of 0.5 . . . . .            | 136 |
| 4.70 | Microstructure of Ti-622Si( $\beta$ ) within shear band following deformation at<br>$800^{\circ}\text{C}/10^2 \text{ s}^{-1}$ upto a strain of 0.5 . . . . .                           | 137 |
| 4 71 | Microstructure of Ti-622Si( $\beta$ ) within shear band (intense zone) following<br>deformation at $800^{\circ}\text{C}/10^2 \text{ s}^{-1}$ upto a strain of 0.5 . . . . .            | 137 |

|      |  |     |
|------|--|-----|
| 4.72 | Microstructure of Ti-622Si( $\beta$ ) following deformation at $850^{\circ}\text{C}/10^{-3} \text{ s}^{-1}$<br>upto a strain of 0.5 . . . . .  | 138 |
| 4.73 | Microstructure of Ti-622Si( $\beta$ ) following deformation at $900^{\circ}\text{C}/10^{-1} \text{ s}^{-1}$<br>upto a strain of 0.5 . . . . .  | 138 |
| 4.74 | Microstructure of Ti-622Si( $\beta$ ) following deformation at $950^{\circ}\text{C}/10^{-3} \text{ s}^{-1}$<br>upto a strain of 0.5 . . . . .  | 139 |
| 4.75 | Microstructure of Ti-622Si( $\beta$ ) following deformation at $950^{\circ}\text{C}/1 \text{ s}^{-1}$ upto<br>a strain of 0.5 . . . . .  | 139 |
| 4.76 | Microstructure of Ti-622Si( $\beta$ ) following deformation at $950^{\circ}\text{C}/10^2 \text{ s}^{-1}$<br>upto a strain of 0.5 . . . . .   | 140 |
| 4.77 | Microstructure of Ti-622Si( $\beta$ ) following deformation at $1000^{\circ}\text{C}/10^{-3} \text{ s}^{-1}$<br>upto a strain of 0.5 . . . . .   | 140 |
| 4.78 | Microstructure of Ti-622Si( $\beta$ ) following deformation at $1000^{\circ}\text{C}/10^{-1} \text{ s}^{-1}$<br>upto a strain of 0.5 . . . . .   | 141 |
| 4.79 | Microstructure of Ti-622Si( $\beta$ ) following deformation at $900^{\circ}\text{C}/10^2 \text{ s}^{-1}$<br>upto a strain of 0.5 . . . . .   | 142 |
| 4.80 | Microstructure of Ti-622Si( $\beta$ ) following deformation at $1000^{\circ}\text{C}/10^2 \text{ s}^{-1}$<br>upto a strain of 0.5 at (a) lower and (b) higher magnifications . . . . . | 143 |
| 4.81 | Plot of true stress versus strain rate for Ti-622Si in TMT condition . . .   | 144 |
| 4.82 | Plot of true stress versus strain rate for Ti-622Si in TMT-A3 condition .  | 145 |
| 4.83 | Plot of strain rate sensitivity versus strain rate for Ti-622Si in TMT<br>condition . . . . .  | 146 |

|      |   |     |
|------|---|-----|
| 4.84 | Plot of strain rate sensitivity versus strain rate for Ti-622Si in TMT-A2 condition . . . . .                                 | 147 |
| 4.85 | Plot of strain rate sensitivity versus strain rate for Ti-622Si in TMT-A3 condition . . . . .                                 | 148 |
| 4.86 | Plot of $\log \frac{\dot{\epsilon}}{\sigma^n}$ versus $\log d$ at a temperature of 800°C for Ti-622Si . . . . .               | 151 |
| 4.87 | Plot of $\log \frac{\dot{\epsilon}}{\sigma^n}$ versus $\log d$ at a temperature of 850°C for Ti-622Si . . . . .               | 152 |
| 4.88 | Plot of $\log \frac{\dot{\epsilon}}{\sigma^n}$ versus $\log d$ at a temperature of 900°C for Ti-622Si . . . . .               | 153 |
| 4.89 | Plot of $\log \frac{\dot{\epsilon}}{\sigma^n}$ versus $\log d$ at a temperature of 920°C for Ti-622Si . . . . .               | 154 |
| 4.90 | Plot of $\log \frac{\dot{\epsilon}}{\sigma^n}$ versus $\log d$ at a temperature of 940°C for Ti-622Si . . . . .               | 155 |
| 4.91 | Plot of $\log \frac{\dot{\epsilon}}{\sigma^n}$ versus $\log d$ at a temperature of 950°C for Ti-622Si . . . . .               | 156 |
| 4.92 | Plot of $\log(\sigma^{-n} T E^{n-1} d^p)$ versus $(1/T)$ for Ti-622Si . . . . .   | 158 |
| 5.1  | Variation of $\frac{m}{m+1}$ with $m$ . . . . .   | 179 |
| 5.2  | Variation of $\ln \frac{m}{m+1}$ with $m$ . . . . .   | 179 |
| 5.3  | Schematic diagram of $\beta$ penetration into $\alpha$ plate . . . . .  | 180 |
| 5.4  | Efficiency map for Ti-622Si( $\beta$ ) corresponding to strain level of 0.1 . . . . .   | 180 |
| 5.5  | Efficiency map for Ti-622Si( $\beta$ ), corresponding to strain level of 0.3 . . . . .  | 181 |
| 5.6  | Efficiency map for Ti-622Si( $\beta$ ), corresponding to strain level of 0.5 . . . . .  | 182 |
| 5.7  | Efficiency map obtained after temperature correction, for Ti-622Si( $\beta$ ), corresponding to strain level of 0.1 . . . . . | 183 |

---

|      |   |     |
|------|---|-----|
| 5 8  | Efficiency map obtained after temperature correction, for Ti-622Si( $\beta$ ),<br>corresponding to strain level of 0.3 . . . . .  | 184 |
| 5 9  | Plot of extent of flow softening in Ti-622Si ( $\beta$ ) versus strain rate . . . . .   | 185 |
| 5 10 | Plot of extent of flow softening in Ti-622Si ( $\beta$ ) exhibited by the temper-<br>ature corrected stress-strain curves versus strain rate . . . . .  | 186 |
| 5 11 | Plot of extent of flow softening in Ti-622Si ( $\beta$ ) exhibited by the tem-<br>perature corrected stress-strain curves after normalization versus strain<br>rate . . . . .                   | 187 |
| 5 12 | Schematic diagram of primary $\alpha$ and prior $\beta$ grains, showing $\alpha$ - $\alpha$ and $\alpha$ - $\beta$<br>boundaries (a) at lower temperatures and (b) at higher temperatures . . . | 188 |



# List of Tables

|     |   |     |
|-----|---|-----|
| 1.1 | Grain size exponent, $p$ , reported for superplastic Ti-6Al-4V . . . . .                          | 11  |
| 3.1 | Chemical composition for Ti-622Si alloys . . . . .  | 35  |
| 4.1 | Grain size of Ti-622Si with $(\alpha+\beta)$ microstructure . . . . .                             | 60  |
| 4.2 | Values of $f$ assumed by Semiatin and Lahoti and Dadras and Thomas . .                            | 72  |
| 4.3 | Theoretically estimated (upper) and experimentally measured (lower)<br>temperature rise . . . . . | 77  |
| 4.4 | Grain size of Ti-622Si with $(\alpha+\beta)$ microstructure . . . . .                             | 150 |

---

|              |   |
|--------------|---|
| $K$          | constant in constitutive equation                   |
| $v$          | flow localization parameter (instability parameter) |
| $\zeta$      | thermodynamic instability parameter                 |
| $m$          | strain rate resistivity                             |
| $J, G$       | dissipator content, dissipator co-content           |
| $D$          | power dissipation                                   |
| $\gamma$     | normalized flow softening coefficient               |
| $\eta$       | efficiency  |
| $\epsilon$   | engineering strain                                  |
| $F$          | force   |
| $\epsilon$   | true strain   |
| $\dot{A}$    | rate of change of cross sectional area              |
| $A_0$        | constant  |
| $\epsilon_t$ | prestrain   |
| $\psi_s$     | flow localization parameter for shear bending       |
| $P$          | Power dissipated by the specimen per unit volume    |
| $J_{max}$    | maximum attainable value of J                       |
| $T_m$        | melting temperature                                 |
| $s$          | thermodynamic instability proposed by Gegel         |
| $S^s$        | entropy generated within specimen                   |

---

|              |  |
|--------------|--|
| $W$          | work done  |
| $\rho$       | density  |
| $C$          | specific heat  |
| $f$          | the fraction of heat generated that is retained by the specimen                      |
| $\Delta T$   | temperature rise   |
| $\epsilon_c$ | critical strain required for nucleation of strain free grains during hot deformation |
| $\epsilon_s$ | strain interval over which a cycle of dynamic recrystallization is completed         |
| $\epsilon_p$ | strain corresponding to peak stress, plastic strain                                  |
| $X(t)$       | stroke at time $t$   |
| $h_o$        | initial height   |
| $t$          | time   |
| $\Delta X_p$ | plastic component of displacement  |
| $\Delta X$   | displacement   |
| $L$          | Load   |
| $M$          | combined machine and specimen stiffness  |
| $A_o$        | initial area of cross section  |
| $v$          | crosshead speed  |
| $l$          | specimen length  |
| $l_o$        | initial length of specimen   |
| $d$          | grain size   |

---

|                  |  |
|------------------|--|
| $E$              | Young's modulus of elasticity  |
| $n$              | stress exponent  |
| $k$              | Boltzmann constant   |
| $\bar{d}_\alpha$ | average grain size of $\alpha$ phase                                     |
| $\bar{d}_\beta$  | average grain size of $\beta$ phase                                      |
| $N_{i\alpha}$    | number of linear intercepts on $\alpha$ phase                            |
| $N_{i\beta}$     | number of linear intercepts on $\beta$ phase                             |
| $L_{i\alpha}$    | intercept length of $\alpha$ phase                                       |
| $L_{i\beta}$     | intercept length of $\beta$ phase  |
| $K_g$            | constant   |
| $n_g$            | constant   |
| $\Delta T_a$     | $\Delta T$ under adiabatic condition                                     |
| $\Gamma$         | Thermal diffusivity  |
| $\kappa$         | Thermal conductivity   |
| $q$              | heat flux  |
| $T_a$            | ambient temperature  |
| $h$              | corrected heat transfer coefficient                                      |
| $\epsilon_m$     | emissivity   |
| $\sigma_s$       | Stiffen-Boltzmann constant   |
| $T_0$            | initial temperature during deformation                                   |
| $\sigma_c$       | Temperature corrected stress   |
| $\sigma_p$       | peak stress  |
| $\lambda$        | ratio of top to bottom diameters of deformed specimen                    |
| $e$              | ellipticity  |
| $\delta$         | misalignment in the centres of top and bottom faces of deformed specimen |
| $\sigma_l$       | Actual true stress   |
| $A_l$            | Actual cross sectiona area   |

|                         |   |
|-------------------------|---|
| $\epsilon_l$            | local strain  |
| $\gamma_{\alpha\alpha}$ | interfacial energy of $\alpha\alpha$ interface                                      |
| $\gamma_{\alpha\beta}$  | interfacial energy of $\alpha\beta$ interface                                       |
| $\theta$                | interfacial dihedral angle  |
| $\gamma_{cn}$           | average normalised strain hardening coefficient                                     |
| $\psi_c$                | flow localization parameter obtained from temperature corrected stress-strain curve |
| $\psi_{max}$            | maximum value of $\psi$   |
| $\psi_{smax}$           | maximum value of $\psi_s$   |
| $T_o$                   | initial temperature of specimen   |
| $\epsilon_m$            | emissivity  |
| $\sigma_s$              | Stefen-Boltzmann constant   |
| $K_1, K_2$              | constants   |
| $\lambda$               | ratio of top to bottom diameters of deformed specimen                               |

## List of Abbreviations

|     |                            |
|-----|----------------------------|
| PM  | Powder metallurgy          |
| DMM | Dynamic material modelling |
| DRY | Dynamic recovery           |
| DRX | Dynamic recrystallization  |
| SFE | Stacking fault energy      |

# Synopsis

The unique combination of properties like high strength to weight ratio even at elevated temperatures, good creep and fatigue properties and an excellent corrosion resistance has led to an extensive use of titanium alloys in the aerospace industry. Among these alloys the two phase ( $\alpha + \beta$ ) alloys are of special importance because by employing suitable combinations of deformation processing and heat treatment schedules their properties can be varied over a wide range. Two microstructural states of these alloys, namely (a) the structure in which the  $\alpha$  phase has plate like morphology [usually designated as  $\beta$  structure] and (b) the structure in which the  $\alpha$  phase has an equiaxed morphology [usually designated as the ( $\alpha + \beta$ ) structure], are of general interest because they not only display different combinations of mechanical properties but their hot working behaviours are also markedly different. The flow curves of ( $\alpha + \beta$ ) titanium alloys, in general, display dissimilar characteristics in these two microstructural states, with  $\beta$  structure displaying the tendency of undergoing the unstable flow over a wider range of temperature and strain rates. It is to be noted that since in their cast structure ( $\alpha + \beta$ ) titanium alloys possess the plate like morphology of the  $\alpha$  phase their primary working is carried out in the  $\beta$  microstructural state. Further working of  $\beta$  structure is also of primary concern as it is this structure which gives rise to the ( $\alpha + \beta$ ) structure by their deformation processing below the  $\beta$  transus temperature. Due to these requirements, hot working of ( $\alpha + \beta$ ) titanium alloys in their  $\beta$  microstructural state is often carried out over a wide strain rate range. In contrast, hot deformation of these alloys in their ( $\alpha + \beta$ ) microstructural condition is generally carried out during secondary working operation which

is best done by methods such as superplastic forming and hence at lower strain rates in a narrower range

The present work is concerned with the study of hot working behaviour of Ti-6 Al-2 Mo-1.5 Cr-0.4 Fe-0.3 Si alloy in its  $\beta$  as well as  $(\alpha + \beta)$  microstructural states. This alloy, hereafter referred to as Ti-622Si alloy, contains Al as  $\alpha$  stabilizer and Mo, Cr and Fe as  $\beta$  stabilizers with Si being added to form silicides so as to improve its creep resistance. It therefore, represents the family of typical  $(\alpha + \beta)$  titanium alloy.  $\beta$  transus temperature of the alloy was found to be 975°C. Hot working behaviour of Ti-622Si alloy was studied by carrying out compression tests on cylindrical specimen. For specimens with the  $\beta$  structure the constant strain rate tests were conducted on a computer controlled servohydraulic testing machine in the temperature range of 750°C - 1000°C with strain rate varying between  $10^{-3} \text{ s}^{-1}$  and  $10^2 \text{ s}^{-1}$  and the load displacement curves were converted to true stress-true strain curves. In contrast, the hot deformation behaviour of the alloy in  $(\alpha + \beta)$  structure was studied by step strain rate compression tests which were carried out between 750°C and 960°C in the strain rate range  $10^{-5} \text{ s}^{-1}$  -  $5 \times 10^{-2} \text{ s}^{-1}$ . Thus while deformation of the alloy in the  $\beta$  microstructural state was carried out in two phase as well as single phase field, that in the  $(\alpha + \beta)$  microstructural state was done in the two phase field only. In order to study the effect of grain size on the strain rate sensitivity,  $m$ , the tests were performed on specimens having mean grain sizes of 6  $\mu\text{m}$ , 8  $\mu\text{m}$ , 13  $\mu\text{m}$  and 15  $\mu\text{m}$  respectively. For their microstructural examinations deformed samples in most cases were metallographically prepared and were analysed by optical microscopy, and/or scanning electron microscopy.

Since the flow stress of titanium alloys is known to be very sensitive to the deformation temperature and an appreciable temperature rise,  $\Delta T$ , may occur during its course, the experimental stress strain curves of the alloy in the  $\beta$  microstructural state were subjected to temperature correction. For the purpose of calculation of temperature rise, the fraction of heat generated retained by the specimen,  $f$ , was estimated using the heat transfer analysis.

The temperature rise,  $\Delta T$ , predicted by the analysis was found to fairly match with the experimentally measured values for strain rates lower than  $10 \text{ s}^{-1}$ . At higher strain rates the experimentally measured  $\Delta T$  was found to be significantly less than the calculated  $\Delta T$ , possibly due to the relatively lesser time allowed for heat to transfer from specimen to the thermocouples embedded in test specimens.

The experimental stress-strain curves of the alloy in its  $\beta$  microstructural state exhibited flow softening in the two phase field, below the  $\beta$  transus temperature and steady state or strain hardening behaviour in the single  $\beta$  phase field. The corrected stress-strain curves at all strain rates in the  $\beta$  phase field and at high strain rates in the  $(\alpha + \beta)$  phase field were found to exhibit continuous strain hardening. Oscillations in flow stress in the experimental as well as corrected stress strain curves were observed at all temperatures in the strain rate interval of  $10 \text{ s}^{-1} - 10^2 \text{ s}^{-1}$ . The strain rate sensitivity,  $m$ , of the alloy under these conditions was found to decrease with strain rate and had little dependence on temperature correction or strain level. The strain rate sensitivity of the alloy was found to be different in single phase  $\beta$  field and two phase  $(\alpha + \beta)$  field at all strain rates. While it varied between 0.09 and 0.37 in the  $\beta$  phase field its value was lower in the two phase field and was found to vary between 0.03 and 0.27.

Phenomenological description of the flow behaviour over the entire range of temperature and strain rate was characterized using the relationship

$$\sigma = A(Z) \quad (0.1)$$

where  $Z$  is the Zener-Hollomon parameter defined as  $Z = \dot{\epsilon} e^{(Q/RT)}$ ,  $Q$  is the activation energy,  $R$  is the universal gas constant and  $A(z)$  is a function of  $Z$ . The activation energy for the deformation of Ti-622Si alloy in the  $\beta$  microstructural state was found to be 540 kJ



$$\text{mol}^{-1} \pm 20 \text{ kJ mol}^{-1}$$

Visual examination of compression samples deformed to about a true strain of 0.5 revealed that Ti-622Si alloy in the  $\beta$  microstructural state underwent stable flow under a limited domain of temperatures and strain rates. The flow instability manifested itself in three ways: (1) inhomogeneous flow along the compression axis resulting in a difference in the specimen cross sectional areas at the two ends (2) ellipticity in the cross sectional area and (3) shear banding. In addition, a significant drift in the centres of the two faces was also observed which was associated with shear banding. On the other hand, ellipticity was found to be associated with both shear banding as well as inhomogeneous flow.

Microstructural examination of deformed specimens revealed that the morphology of  $\alpha$  plates during the deformation in the  $(\alpha + \beta)$  field i.e below the  $\beta$  transus temperature of the alloy was also not stable and varied in the following manner

- (a) Those plates which were oriented favourably with respect to the compression axis underwent reorientation and plastic deformation. Thus their lengths increased and resulted into higher aspect ratio i.e higher  $L/t$  with respect to their mean value in the starting microstructure.
- (b) Plates, which were not favourably aligned to cause their reorientation due to the geometric constraint from neighbouring  $\alpha$  plates/grains, underwent kinking and banding. Kinked  $\alpha$  plates were found to undergo differential plastic strains in the sense their thickness was different in different regions.
- (c) Plates which underwent local plastic deformation of considerable extent were subjected to their primary fragmentation thus leading to equiaxed morphology of the  $\alpha$  phase.
- (d) Fragmented equiaxed  $\alpha$  phase underwent coarsening during deformation at high tem-

peratures and low strain rates. The coarsened equiaxed  $\alpha$  phase underwent further deformation and secondary fragmentation.

In addition, in regions of intense shear bands the microstructure of the alloy was found to comprise of equiaxed grains of prior  $\beta$  in which secondary  $\alpha$  phase had precipitated in the plate like morphology. Such features indicated significant rise in local temperature during deformation which resulted into dissolution of the primary  $\alpha$  phase and recrystallization of the  $\beta$  phase.

In order to correlate the flow instability in the alloy with microstructural changes occurring during their deformation, the variation of the two instability parameters namely  $\psi$  and  $\zeta$  with strain was obtained from the flow behaviour. For uniaxial compression specimen  $\psi$  parameter is given by

$$\psi = [1/\sigma(d\sigma/d\epsilon) - 1]/m \quad (0.2)$$

The  $\zeta$  parameter is given by

$$\zeta = m + (d\log[m/(m+1)]/d\log\dot{\epsilon}) \quad (0.3)$$

The flow is unstable when  $\psi > 0$  and  $\zeta < 0$ .

Since the flow instability in specimen during their deformation may occur due to (i) temperature rise and (ii) microstructural changes, both the experimental as well as temperature corrected stress strain curves were utilized to estimate the flow instability parameter,  $\psi$ . The variation of  $\psi$  with plastic strain was found to be of four types:

**Type – I** : At all plastic strains  $\psi < 0$  indicating that the stable flow occurs throughout deformation;

Type – II :  $\psi > 0$  up to a critical strain and then  $\psi < 0$  indicating that the flow remains unstable up to a critical strain after which it tends to be stable,

Type – III :  $\psi < 0$  up to a critical strain and then  $\psi > 0$  indicating that the flow is stable to begin with but becomes unstable after reaching a critical strain;

Type – IV :  $\psi$  oscillates between positive and negative values indicating that the flow becomes stable and unstable several times during the deformation.

The flow instability parameter calculated from the experimental stress-strain curves,  $\psi$  exhibited all the four types of behaviours. It was observed that the geometric manifestations of flow instability could be predicted from the variation of  $\psi$  with strain. The variation of Type II indicated inhomogeneous flow without the occurrence of shear band. Similarly, the variations of Type III and Type IV indicated shear banding, which in some cases was also accompanied with inhomogeneous flow. On the other hand, it was observed that the variation of  $\zeta$  could predict only the instability arising from the development of intense shear bands.

In contrast to  $\psi$ , which predicts the combined effect of temperature rise and microstructural changes, the flow instability parameter estimated from the corrected stress-strain curves,  $\psi_c$ , is expected to predict the flow instability due to microstructural changes alone. The variation of  $\psi_c$  with strain at different temperatures and strain rates, for deformation of Ti-622Si alloy with  $\beta$  structure revealed that the plots of Type-I and Type-II only were obtained. Such a variation of  $\psi_c$  with strain indicates that either the flow remains completely stable throughout the deformation in spite of microstructural changes or turns into a stable one from an unstable one. Further, in case of Type-II behaviour it was observed that the critical strain at which the transition from unstable to stable flow occurred, increased with increasing strain rates at the deformation temperature of 750°C. In contrast, at deformation temperatures of 850°C, 900°C and 950°C, the critical strain decreased with increasing the strain rate. Such a variation of  $\psi_c$  with strain could be reasonably correlated with changes

in the morphology of  $\alpha$  plates during the course of their deformation.

It is well known that the plate like  $\alpha$  structure in  $(\alpha + \beta)$  titanium alloys generally exhibits flow instability while that of equiaxed  $\alpha$  is relatively stable. Further, it is also well understood that the plate like  $\alpha$  structure is unstable during deformation and transforms into relatively more stable equiaxed  $\alpha$  structure. Thus transformation of  $\beta$  to equiaxed microstructure will contribute to the flow stability and cause the transition to stable flow to happen at lower strain. On the other hand coarsening contributes to flow softening and instability and will thus cause the transition to stable flow to occur at higher strain.

At 750°C coarsening is not significant whereas transformation to equiaxed structure was observed. As a result the strain for transition from unstable to stable flow decreased with increase in the extent of transformation, i.e. with decrease in strain rate. In contrast to it at higher temperature coarsening of  $\alpha$  was more prominent and its effect is expected to predominate over that of transformation of  $\beta$  structure to equiaxed structure. As the coarsening contributes to instability and thus will tend to increase the strain of the transition from unstable to stable flow, the transition strain increased with the extent of coarsening, i.e. with decrease in the strain rate.

The absence of Type III and Type IV behaviour in  $\psi_c$  versus strain plots, which was found to be associated with shear banding in  $\psi$  versus strain plots, clearly indicated that the formation of shear band in Ti-622Si alloy occurred primarily due to temperature rise. Such a conclusion was also supported by the microstructural features observed in the regions of intense shear bands.

Hot deformation behaviour of Ti-622Si alloy in the  $(\alpha + \beta)$  microstructural state was characterized by studying the variation of its strain rate sensitivity under different temperature and strain rate conditions. The strain rate sensitivity,  $m$ , was calculated by (i) step strain tests and (ii) from the slope of the  $\log \sigma - \log \dot{\epsilon}$  data points. In contrast to  $\beta$  microstructural

state the strain rate sensitivity in  $(\alpha+\beta)$  microstructural state varied over a wide range i.e 0.25 to 0.8. The range of strain rate of high strain rate sensitivity ( $m > 0.4$ ) was found to become narrower with increase in the grain size. In general, the strain rate sensitivity was found to decrease with strain rate. However for the case of grain size of  $6 \mu\text{m}$  at temperatures of  $900^\circ\text{C}$  -  $940^\circ\text{C}$ , it first increased with strain rate and then decreased. For obtaining the constitutive behaviour of the alloy in  $(\alpha+\beta)$  microstructure the entire strain rate domain could be divided into region I, II and III. A mean value of 0.5 for the strain rate sensitivity was taken for the region II and grain size exponent was estimated. It was found that the grain size exponent increased with the increase in the volume fraction of  $\beta$  phase from 1.0 to 2.5. The increase in the grain size exponent with temperature could be correlated with changes in the starting microstructure with temperature and relative ease of sliding of  $\alpha$ - $\alpha$ ,  $\alpha$ - $\beta$  and  $\beta$ - $\beta$  interfaces.

# Chapter 1

## INTRODUCTION

Development of titanium alloys throughout the world has been phenomenal during the last three decades. The stimulus for the development initially came from the aerospace industries where there was a need for new materials with good creep resistance and higher strength to weight ratio at elevated temperatures. High melting point of titanium ( $1678^{\circ}\text{C}$ ) was taken as strong indication that titanium alloys would show good creep resistance at very high temperatures. Although subsequent investigations revealed that the upper limit of temperature for application was lower than expected, these alloys have become indispensable for aircraft and missile industries. This is because they were found to have high strength to weight ratio and good mechanical properties at elevated temperatures (up to  $500^{\circ}\text{C}$ ). In the aerospace industry, titanium alloys are mainly used for manufacturing compressor blades and discs in the gas turbine engine and rocket motor. They are also used for manufacturing aircraft structural members like the under carriage components, flap and slat track in the wings, engine mounting and for making cryogenic parts of rockets.

Titanium alloys, due to their high corrosion resistance (in particular good stress corrosion cracking and corrosion fatigue) and good compatibility with liquid fuels, are used

in chemical and marine industries. In chemical industries equipments used for handling solutions of bleaching agents, hot brine, ferric chloride and chlorinated hydrocarbons are made of titanium and titanium alloys. They are also used in tubing in steam turbines and in construction of offshore oil rigs.

Owing to good mechanical properties ( in particular good strength to weight ratio), outstanding resistance to corrosion by body fluids and compatibility with biological cells, prosthetic devices like heart valve, artificial joints, plates and pins are made out of titanium alloys.

India is on the verge of producing its own jet planes with components made of titanium alloys and would require substantial quantity of titanium alloys. Thus, titanium alloys are also important material for the Indian defense industry.

Titanium alloys can be broadly classified into three types: (1)  $\alpha$  alloys (2)  $\beta$  alloys and (3) two phase ( $\alpha+\beta$ ) alloys. Among the three, ( $\alpha+\beta$ ) alloys are most commonly used. Hot working or high temperature deformation processing plays crucial role in fabrication of components of two phase titanium alloys and is the most important processing route for these alloys. The present work aims at evaluating the hot workability of ( $\alpha+\beta$ ) titanium alloys and the various factors influencing it.

Hot working operations are of various types and they can be classified into various categories on the basis of the state of stress (SOS). However, most of the hot working operations have compressive state of stress. Therefore, the evaluation of hot workability in the present work has been confined to the case of compressive state of stress.

Sections 1.1 to 1.3 review literatures on alloying of titanium and types of titanium alloys, processing of ( $\alpha+\beta$ ) titanium alloys and fundamentals of hot workability under compressive loading with special reference to ( $\alpha+\beta$ ) titanium alloys.

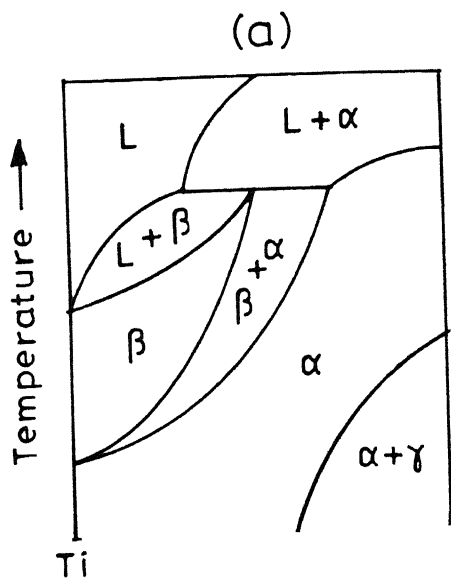
## 1.1 Alloying of Titanium and Types of Titanium Alloys[1, 2]

Titanium undergoes an allotropic transformation from a low temperature, hexagonal closed packed (HCP) structure ( $\alpha$ ) to a body centered cubic (BCC) structure ( $\beta$ ) at 882 °C. The  $\beta$  phase remains stable up to the melting point. The alloying of titanium is done in order to improve its mechanical properties. The phase diagram of titanium-alloying element systems are often complex. However, four types of titanium rich portion of different pseudo binary phase diagrams are common and are shown in Figure 1.1.

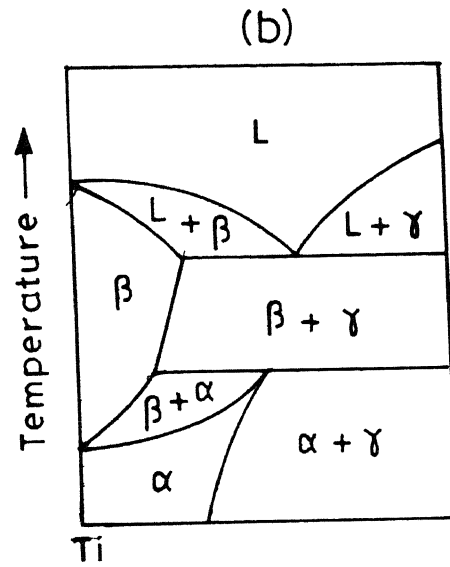
Elements that stabilize  $\alpha$  at higher temperatures are called  $\alpha$  stabilizers. Figure 1.1(a)-(b) show the pseudobinary phase diagram of the titanium  $\alpha$  stabilizer system.  $\alpha$  stabilizers giving rise to simple peritectic phase diagram are N and O. The  $\alpha$  stabilizers giving rise to  $\beta$ -peritectoid type of phase diagram are Al, Ge, C, Nd, Gd, Ce, La, Ga, Sc and B. Elements that preferentially dissolve in  $\beta$  phase and stabilize it at low temperatures are called  $\beta$  stabilizers. Two types of phase diagrams are obtained for titanium  $\beta$  stabilizers, i.e.  $\beta$  isomorphous type (shown in Figure 1.1(c)) and  $\beta$  eutectoid type (shown in Figure 1.1(d)).  $\beta$  stabilizers giving rise to isomorphous type of phase diagrams are Mo, V, Ta, Re, Hf, Nb and Zr and  $\beta$  stabilizers giving rise to eutectoid type of phase diagrams are Cu, W, Pd, Ag, Pt, Au, Mn, Fe, Cr, Fe, Ni, Co, W and H. However it should be noted that eutectoid reactions in a number of alloys are very sluggish and the alloys tend to behave as if this reaction did not occur. For example Ti-Fe and Ti-Mn systems behave as if they belong to the  $\beta$ -isomorphous type. Elements like Sn and Si are neutral in their effect in stabilizing either phase.

Titanium alloys are generally classified in three broad categories depending on the amount of  $\alpha$  and  $\beta$  stabilizers present in the alloy, i.e.  $\alpha$  alloys,  $\beta$  alloys and ( $\alpha+\beta$ ) alloys. Unalloyed titanium and alloys of titanium with  $\alpha$  stabilizers such as Al, Ga and

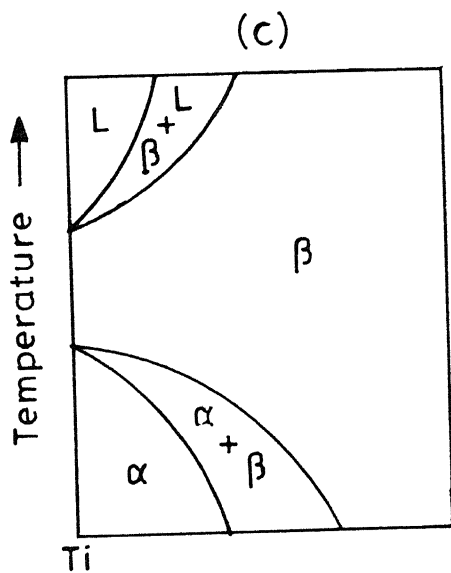




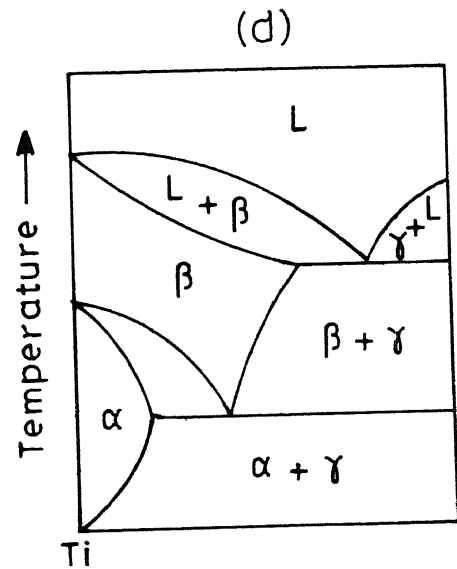
Simple peritectic  
N, O



$\beta$  - peritectoid  
B, Sc, Ga, La, Ce, Gd,  
Nd, Ge, Al, C



$\beta$  - isomorphous  
Mo, V, Zr, Nb, Hf, Ta, Re



$\beta$  - eutectoid  
Cr, Mn, Fe, Co, Ni, Cu,  
W, Pd, Ag, Pt

Figure 1.1: Phase diagrams for Ti-alloying element system

Sn either singly or in combination have HCP structures at ordinary temperatures and are termed as  $\alpha$  alloys. Examples of  $\alpha$  alloys are Ti-5Al-2.5 Sn and Ti-Al-Ga.  $\alpha$  alloys are characterized by satisfactory strength, toughness, creep resistance and weldability. Furthermore, due to the absence of ductile to brittle transformation at subzero temperatures,  $\alpha$  alloys are suitable for cryogenic applications. As the temperature rises above the room temperature,  $\alpha$  alloys rapidly lose their strength and are not suitable for elevated temperature applications.

$\beta$  alloys generally contain large amounts of one or more  $\beta$  isomorphous alloying elements like V, Nb, Ta (group five transition metals) and Mo (group six transition metals). These alloys are extremely formable. They are however prone to ductile to brittle transformation at subzero temperatures and hence unsuitable for cryogenic applications. Some  $\beta$  alloys also exhibit a metastable  $\beta$  phase at room temperature.

Two phase ( $\alpha+\beta$ ) titanium alloys combine the advantages of both  $\alpha$  and  $\beta$  alloys. At room temperature they contain 10-50%  $\beta$  phase and can be welded if the volume fraction of  $\beta$  phase is below 0.2. These alloys generally exhibit good fabricability and can be formed to near net shapes by superplastic forming. They have high strength at room temperature and moderate strength at elevated temperatures.

From the commercial point of view they are more important as compared to  $\alpha$  and  $\beta$  alloys. The most commonly used ( $\alpha+\beta$ ) titanium alloy is Ti-6Al-4V. In many two phase alloys Mo is used in the place of V as  $\beta$  stabilizer and Si is added to improve creep resistance at elevated temperatures.

## 1.2 Processing of ( $\alpha+\beta$ ) Titanium Alloys[1]

### 1.2.1 Casting

Casting of titanium and its alloys is relatively new in titanium industries. The high reactivity of titanium, especially in the molten stage presents a special challenge to the foundry. Expensive methods of melting, mold making and surface cleaning are required to maintain metal integrity. It is a common practice to melt titanium or its alloys as consumable electrode and the melt is collected in a water cooled copper crucible in vacuum chamber. The skull of solid titanium or titanium alloy initially formed on the water cooled Cu crucible protects it from the liquid melt. The melt is then immediately poured into molds from the container.

The melting point of Ti is very high. So limited superheat is achievable. This affects flowability of the liquid melt and consequently filling of the mold. Keeping these difficulties in view, it is a common practice to pour the liquid titanium centrifugally, thus forcing it into the cavities of the mold or to use preheated mold when the metal is poured statically. Molding are of two types: (a) rammed graphite molding and (b) lost wax investment molding. Through the casting route it is possible to make castings of the ( $\alpha+\beta$ ) titanium alloys with intricate shapes without any machining. But a great disadvantage of the process is that no microstructure apart from the cast structure can be obtained.

### 1.2.2 Powder Metallurgy Processing

Now a days due to availability of powders of sufficient purity (particularly low content of interstitial elements) products of titanium alloys are manufactured through the powder metallurgy (PM) route. PM products can be made to final size (nearnest shape) and thus

machining is not required. Powder consolidation is done by hot pressing and sintering and hot isostatic pressing. The sintering of ( $\alpha+\beta$ ) titanium alloys are carried out in  $\beta$  phase field. It has been observed that sintering is better when element powder is used rather than the prealloyed powder. Subsequent forging or extrusion is carried out in ( $\alpha+\beta$ ) phase field to produce the final components. This results in fine equiaxed microstructure. In hot isostatic pressing, the pressing and sintering which are sometimes accompanied by forging can be carried out in single operation. In powder metallurgy processing, the uniformity of composition is excellent because heterogeneity in cast billets is avoided. As there is no crystallographic texture and mechanical properties are isotropic. There are two disadvantages of powder metallurgy processing of titanium and its alloys: (a) the process of atomization for production of powders of titanium or its alloy is difficult due to low flowability of melt caused by non availability of high superheat. The second disadvantage is that components of big size cannot be made by this route.

### 1.2.3 Deformation Processing

The as cast structure of melted ingot of ( $\alpha+\beta$ ) titanium alloys is converted to wrought structure with the help of hot press forging. The forging is done at low strain rate as the cast structure is prone to cracking. The ingots are either forged to slabs which are subsequently hot rolled to plates or sheets, or they are pressed to round or square billets for processing to bars, rods, tubes, extruded sections or wires. Rough forging of ( $\alpha+\beta$ ) titanium alloys is carried out for making components such as gas turbine compressor discs. It is also done before closed die forging or hot rolling. Both open and closed dies are heated to avoid chilling and formation of dead zones. Sometimes forming operations like closed die forging or pressure blowing are carried out at very slow rates ( $10^{-6} \text{ s}^{-1}$ ) and are called creep forming.

In superplastic forming,  $(\alpha+\beta)$  titanium alloys having fine grained equiaxed microstructure is deformed under temperature and strain rate conditions of superplasticity. In case of superplastic forming, the load requirement is very low, no machining is involved as the forming is near net shape, and the metal flow is uniform. Also it does not result in residual stress and complex near net shapes can be formed. Superplastic forming is generally done through either superplastic forging or gas pressure techniques. In the gas pressure technique, which is the most common method of superplastic forming of titanium alloys pressures ranging between 100 to 1000 KPa are applied on the alloys which expands and fills mold cavity. The advantages of the superplastic forming of these alloys is enhanced by combining it with diffusion bonding, i.e. solid state joining. Both processes require similar condition, i.e. heat, pressure, clean surface and an inert environment. Diffusion bonding which is carried out with the superplastic forming eliminates the need for welding or brazing for manufacturing complex parts. The  $(\alpha+\beta)$  titanium alloys have been found to exhibit best superplasticity at temperatures varying between  $0.9T_\beta$  and  $0.93T_\beta$  [3]

Hot workability of a material is the relative ease with which that material can be shaped during high temperature deformation processing [4]. The relative ease refers to the stress required for the deformation as well as the extent of deformation that can be given to the material without giving rise to any undesirable change in it. The success of a forming operation depends on the good workability of the material. Therefore evaluation of hot workability of  $(\alpha+\beta)$  titanium alloys and various factors influencing it is necessary for designing a hot deformation process.

Hot workability is a strong function of the state of stress. For example during tensile deformation workability is limited due to necking which is absent during compression or torsion. Further, very high strain can be given to a material during torsion. In the present study we plan to evaluate the hot workability of  $(\alpha+\beta)$  titanium alloys under conditions of compressive stress. This study will be useful for most of the important

hot working operations like primary forging, superplastic forging, closed die forging, and rolling since the state of stress in all these operations is compressive.

## 1.3 Fundamentals of Hot Workability

### 1.3.1 Constitutive Equation

As mentioned in the previous section, workability or relative ease of shaping an alloy also refers to the flow stress that is needed to deform the alloy. The flow stress required to deform an alloy is given by the constitutive equation which mathematically describes the dependence of the flow stress upon strain, strain rate and temperature and can be established by simple laboratory tests. In case of high temperature deformation, the constitutive equation mostly gives the strain rate and temperature dependence of flow stress at steady state or selected strain. In few studies the constitutive equation giving the strain dependence of flow stress have been put forward [5].

It was found that a single constitutive equation describing the temperature and strain dependency of stress, over a wide range of temperature and strain rate can be given by expressing stress as a function of temperature compensated strain rate  $Z$ , as originally proposed by Zener and Hollomon [6, 7]

$$Z = \dot{\epsilon} \exp\left(\frac{Q}{RT}\right) \quad (1.1)$$

where  $Q$  and  $R$  are activation energy and gas constant respectively. The most widely used equation relating stress and Zener-Hollomon parameter has been found to be [6, 8, 9, 10]

$$Z = A(\sinh \alpha \sigma)^n \quad (1.2)$$

where  $A$ ,  $\alpha$  and  $n$  are temperature and strain rate independent constants. This constitutive equation is found to be valid for a number of pure metals and dilute al-

loys [6, 9, 11]. In pure aluminium, over a wide temperature and strain rate range, a single relation of the type given by equation (1.2) is adequate to express the interdependence of the flow parameters and the activation energy corresponds to that for self diffusion [6]. However, in complex alloys the analysis of data reveals large deviations from the strain rate predicted by above equations [11]

Constitutive equations have been obtained for two phase titanium alloys . The activation energy  $Q$  has been calculated in two ways for  $(\alpha+\beta)$  titanium alloys [5]:

- (a) from the slopes of  $\log \sigma - \frac{1}{T}$  plots (plots correspond to fixed values of strain rate) using the relationship [5]

$$Q = \frac{R \frac{d \ln \sigma}{d \frac{1}{T}}}{m} \quad (1.3)$$

where  $\sigma$ ,  $T$  and  $m$  are flow stress, deformation temperature and strain rate sensitivity respectively.

- (b) from the slope of  $\dot{\epsilon} - \frac{1}{T}$  plots (plots correspond to fixed stress levels) using the relationship [12]

$$\Delta(\ln \dot{\epsilon}) = -\frac{Q}{R} \Delta\left(\frac{1}{T}\right) \quad (1.4)$$

The activation energies calculated for two phase titanium alloys have been found to be much higher than that of self diffusion for both  $\alpha$  and  $\beta$  phases.

For micrograined superplastic alloys, the  $\log \sigma$  versus  $\log \dot{\epsilon}$  plots over wide ranges of strain rate show three distinct regions. For each region the general form of constitutive equation can be expressed as

$$\dot{\epsilon} = \frac{AD_o G b}{kT} \left(\frac{b}{d}\right)^p \left(\frac{\sigma}{G}\right)^n \exp\left(-\frac{Q}{RT}\right) \quad (1.5)$$

where  $D_o$  is the diffusivity coefficient,  $G$  is shear modulus,  $d$  is the grain size,  $p$  is the inverse grain size exponent,  $n$  is the stress exponent,  $k$  is the Stefan-Boltzman constant,

$b$  is atomic size or burger vector and  $A$  is a constant [13]. The values of  $n$ ,  $p$  and  $A$  are different for the three regions. Constitutive behavior of superplastic micrograined Ti-6Al-4V alloy is very well documented [14-24]. While superplastic behavior in few other  $(\alpha+\beta)$  titanium alloys have been reported [22], Ti-6Al-4V has received more attention because of its all round properties and users confidence.

The influence of grain size has been studied by number of investigators [25] for Ti-6Al-4V alloy. The grain size dependence of strain rate of deformation can be expressed by equation (1.5). Table 1.1 reports the values of grain size exponent,  $p$ , reported by several investigators.

Table 1.1: Grain size exponent,  $p$ , reported for superplastic Ti-6Al-4V

| Grain size range ( $\mu\text{m}$ ) | average exponent | range of exponent | reference |
|------------------------------------|------------------|-------------------|-----------|
| 6.6-19.8                           | 1.48             | 1.27-1.75         | [26]      |
| 6.4-20.0                           | 2.28             | 1.64-3.47         | [16]      |
| 4.5-9.0                            | 0.83             | 0.74-0.86         | [27]      |
| 14.0-24.0                          | 1.7              | -                 | [15]      |

Further grain size distribution has been found to significantly influence the flow stress and strain rate sensitivity [28]. Ti-6Al-4V having higher spread in the grain size was found to exhibit higher flow stress and strain rate sensitivity [18]. The influence of non uniformity in grain size has been explained by Ghosh and Raj [29] in terms of transition from dislocation creep to superplastic flow over a much wider range of strain rate. Apart from the grain size, grain aspect ratio is significant [18, 25] but few quantitative studies on its influence have been reported.

The self diffusivity of Ti in  $\beta$  phase in the  $(\alpha+\beta)$  titanium alloys is two orders of magnitude higher than that in  $\alpha$  phase [29]. Also  $\alpha$  phase has fewer slip system than



that of  $\beta$ . Both these differences in  $\alpha$  and  $\beta$  phases indicate that  $\alpha$  phase is harder than  $\beta$  phase. Thus the volume fraction of the  $\alpha$  phase, i.e.  $V_\alpha$  is expected to have significant influence on the flow stress and strain rate sensitivity,  $m$ , at a given temperature and strain rate. Some studies have been carried out to determine the influence of volume fraction on the flow stress [30]. In these study it has been observed that addition of  $\beta$  stabilizing elements like H improves the superplasticity at lower temperatures by increasing the volume fraction of  $\beta$  phase at these temperatures. But analyzing the effect of volume fraction of  $\alpha$  and  $\beta$  phases is difficult as the grain size distribution, which also significantly influences the stress, changes along with the volume fraction of the two phases.

Activation energy,  $Q$ , is the measure of the influence of temperature dependence of the flow stress. The value of activation energy often gives insight into the deformation mechanism of plastic deformation. In most superplastic alloys the activation energy is generally found close to that for grain boundary diffusion. But this is not the case for two phase titanium alloys for which the measured activation energy is higher than both that of self diffusion and consequently much higher than activation energy of grain boundary diffusion [14, 15, 27, 31]. The high values of activation energy of superplastic deformation remain unexplained.

### 1.3.2 Instability During Uniaxial Compression

As stated earlier, apart from its meaning of stress required to deform a material during hot working, workability also refers to the extent of deformation that can be given to a material or ductility. During the hot compression of two phase titanium alloys extent of deformation of the alloys or their workability is often limited by triggering of flow instability. Though defects like void formation and triple point cracking are also known to limit workability, these defects require the assistance of tensile stresses and thus not

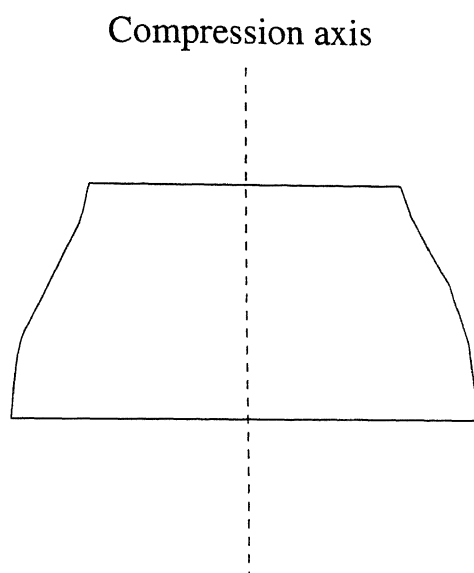


Figure 1.2 Inhomogeneous flow during uniaxial compression

of much significance for hot compression [12].

The flow instability manifests itself in various ways [12, 32, 33]. A very common manifestation of flow instability has been referred in the literature as inhomogeneous flow, and is shown schematically in Figure 1.2. Inhomogeneous flow has been reported for different alloys including two phase titanium alloys [32]. Although the extent of flow inhomogeneity has been correlated with instability parameters which are derived from the stress strain curves, it has been seldom quantified in terms of geometrical changes in the deformed specimen. Although the flow instability parameters also indicate the extent of flow instability, quantifying the extent of inhomogeneous flow in terms of the geometrical changes in the specimen during the deformation is direct method of doing so. Once the extent of flow instability is quantified, the influence of operational variables like temperature and strain rate on the same can be systematically. Thus it is desirable to quantify the flow inhomogeneity in  $(\alpha+\beta)$  titanium alloys.

During hot compression at very high strain rates ( $10\text{ s}^{-1}$ - $10^2\text{ s}^{-1}$ ) the cylindrical specimens undergo significant shear banding. The extent of shear banding has been also

correlated with the instability parameters [12]. However, the judgment of the intensity of shear banding has been done purely on the basis of visual observation of etched cross section of the deformed specimen. Thus, like in the case of inhomogeneous flow no attempt has been made to quantify shear banding from the geometry of the deformed specimens and systematically study its variation with temperature and strain rate of compression.

Microstructure within the shear band has been studied for different alloys including two phase titanium alloys [12]. The microstructure within the shear band is distinctly different from that in the remaining region of the specimen. The microstructural observations indicate that the structural transformation and thus deformation within the band is much higher as compared to the remaining region. However more detailed study of microstructure within the shear band is required.

The theories predicting flow inhomogeneity during compression from constitutive behavior can be classified into three categories: (1) Considere's criterion [34, 35], (2) based on flow localization parameter [12, 32, 35] and (3) models predicting the development of mechanical, metallurgical and geometrical defects [32]. Considere's criterion is based on the relation

$$F = \sigma A \quad (1.6)$$

$$dF = \sigma dA + A d\sigma \quad (1.7)$$

where  $F$  is force and  $A$  is area of cross section. According to this criterion flow instability occurs when  $dF=0$  (a load maximum is reached). This leads to the criterion for flow instability

$$\frac{d\sigma}{\sigma} = -\frac{dA}{A} = d\epsilon = \frac{de}{1+e} \quad (1.8)$$

or

$$\gamma = \frac{\frac{d\sigma}{d\epsilon}}{\sigma} = 1 \quad (1.9)$$

where  $\gamma$  is normalized strain hardening coefficient. Hart's criterion, which was originally proposed for tension test but also applicable to compression [35, 36] extends the Considere's approach to strain rate hardening materials. Hart considered mechanical defect resulting into inhomogeneity in cross section area along the vertical axis and the flow to be unstable if

$$\frac{\partial \ln \dot{A}}{\partial A} > 0 \quad (1.10)$$

where  $A$  is the cross sectional area and  $\dot{A}$  is the magnitude of rate of change of area. Thus unlike Considere, Hart did not arrive at flow instability criteria on the basis of load instability. Rather he assumed

$$\delta F = \sigma \delta A + A \delta \sigma = 0 \quad (1.11)$$

where  $\delta F$  is the variation of load within the workpiece along the compression axis. According to Hart criterion [35], flow instability occurs during compression at steady velocity when

$$\gamma > 1 + m \quad (1.12)$$

For the case of compression it is to be noted that load( $P$ ), true stress( $\sigma$ ), true strain( $\epsilon$ ), cross head speed( $L$ ) and strain rate( $\dot{\epsilon}$ ) are negative, and  $m, A, \dot{A}$  and  $L$  are positive. Thus for constant speed, loading is stable as long as  $[\gamma - (1 + m)] < 0$ , and unstable when  $[\gamma - (1 + m)] > 0$ . Similarly for constant strain rate testing loading is stable when  $\gamma < 1$ .

Jonas et al. [35] suggested a more fundamental definition of flow localization parameter based on the variation of the local strain within the material undergoing deformation. According to them flow localization parameter,  $\psi$  is given by

$$\psi = \frac{\partial \ln \dot{\epsilon}}{\partial \epsilon} \quad (1.13)$$

For uniaxial compression the localization parameter will be given by

$$\psi = \frac{\gamma - 1}{m} \quad (1.14)$$

It has been observed that when  $\psi > 5.0$  significant flow localization occurs during the compression of Ti-6242Si and Ti-10-2-3 [12, 32].

Jonas et al. [35] have calculated the variation of  $\gamma$  with strain for compression of material obeying the constitutive equation

$$\sigma = -A_j(-\dot{\epsilon})^m[1 - \exp(25\epsilon_t)](-\epsilon_t)^{-0.375} \quad (1.15)$$

where  $\epsilon_t$  is prestrain in the material and  $A_j$  is a constant. Figure 1.3 shows the variation of  $\gamma$  with strain. According to the figure the flow is initially stable. Beyond a critical strain, which is different according to different instability criteria, the flow becomes unstable and subsequently it becomes stable again. Flow instability due to development of the mechanical and geometric defects has been analyzed compression, though more extensively done for tension. It has been observed that geometric defects much more easily lead to flow localization [35]. Jonas et al. [35] have carried out the analysis of flow localization for the case of uniaxial compression. At 50% reduction they obtained very little flow localization for  $\psi > 1.0$ , up to a small extent for  $\psi = 3.0$  and up to a significant extent for 5.0 and 10.0. This confirms to the experimental results on Ti-6242Si and Ti-10-2-3 [35, 32]

For the case of shear banding the flow localization parameter is given by

$$\psi_s = \frac{\gamma}{m} \quad (1.16)$$

Semiatin and Lahoti [12] have systematically studied the effect of  $\psi_s$  on shear band formation during side pressing in Ti-6242Si alloy. They studied variation of  $\psi_s$  during the hot deformation of the alloy in its two microstructural states, i.e. equiaxed and Widmanstätten, with strain for different temperatures and strain rates. They have concluded that shear banding is significant when the  $\psi_s$  exceeds 5.0. Though the authors have not categorized the trends in the variation of  $\psi_p$  with strain, different trend can be seen from their data. At low strain rate the  $\psi$  was found to decrease with strain whereas

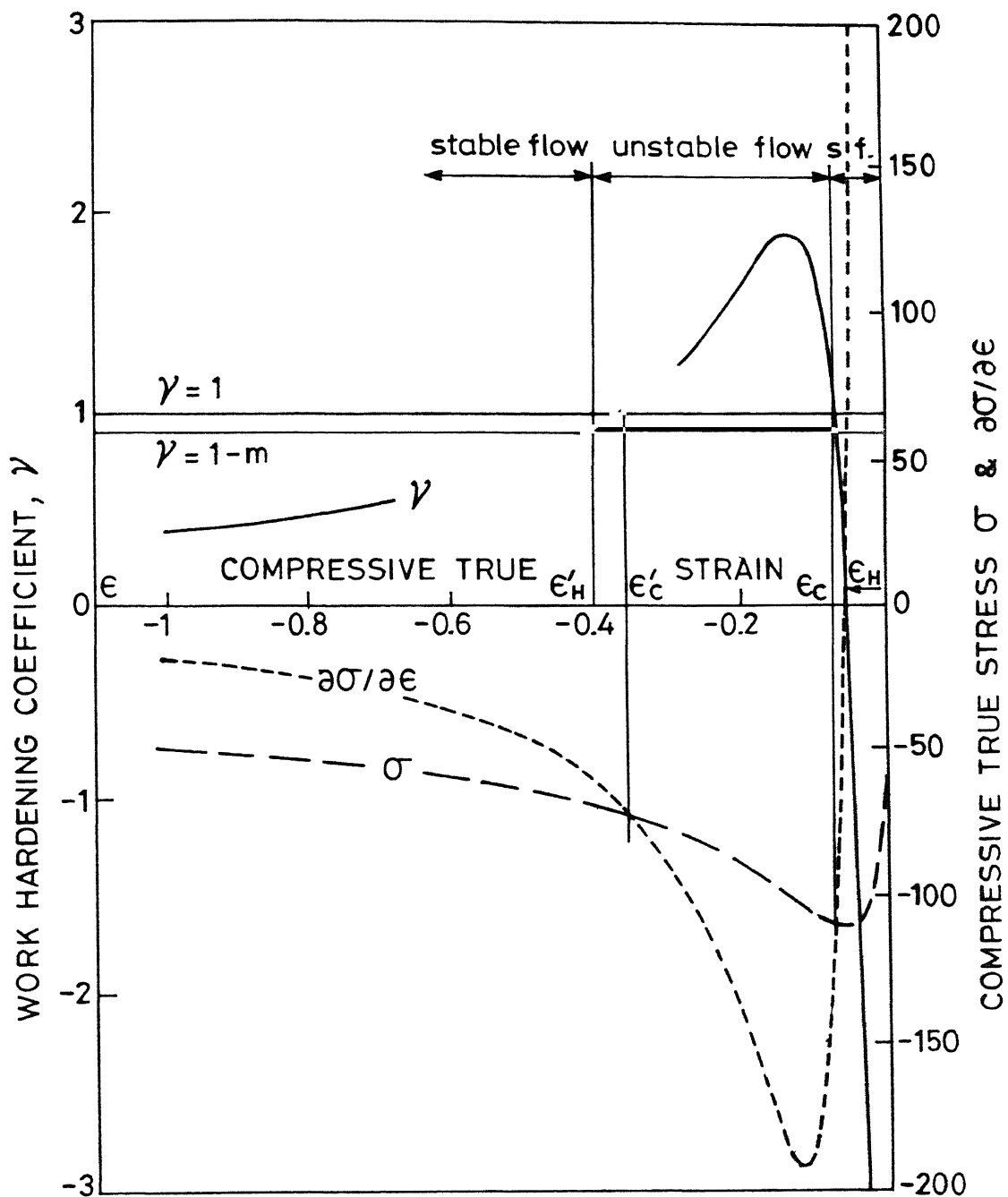


Figure 1.3. Variation of  $\gamma$  with strain for a typical flow softening material

at higher strain rates the variation was not monotonic and the localization parameter was found to oscillate.

### 1.3.3 Other Approaches to Workability

#### Dynamic Materials Modeling(DMM) [37-41]

Dynamic materials model (DMM) is a new approach to correlate the flow behavior to not only the hot workability but also with the microstructural evolution. This approach is based on thermodynamic principles of continuum mechanics of large plastic flow. The model uses the concepts of systems engineering. The workpiece undergoing hot working is considered to be a nonlinear dissipater of power and its constitutive behavior describes the manner in which energy is converted at any instant into thermal energy or into energy required by microstructural modification (both of which are not recoverable by the system). Total power dissipated by the workpiece per unit volume,  $P$ , is given by

$$P = \sigma \dot{\epsilon} \quad (1.17)$$

Figure 1.4 shows the variation of stress with strain rate for the case of a linear and nonlinear dissipater. The area under the stress-strain rate curve is denoted by  $G$ , where

$$G = \int_0^{\epsilon} \sigma d\dot{\epsilon} \quad (1.18)$$

$G$  has been termed as the dissipater content. This is the component, that according to DMM, causes temperature increase in the work piece. The complimentary part (the total power is given by the rectangle OABC in Figure 1.4 and complimentary part is the shaded region) which is denoted by  $J$ , where

$$J = \int_0^{\sigma} \dot{\epsilon} d\sigma \quad (1.19)$$

$J$  has been termed as the dissipater power co-content( $J$ ).  $J$  is the power utilized for structural changes.

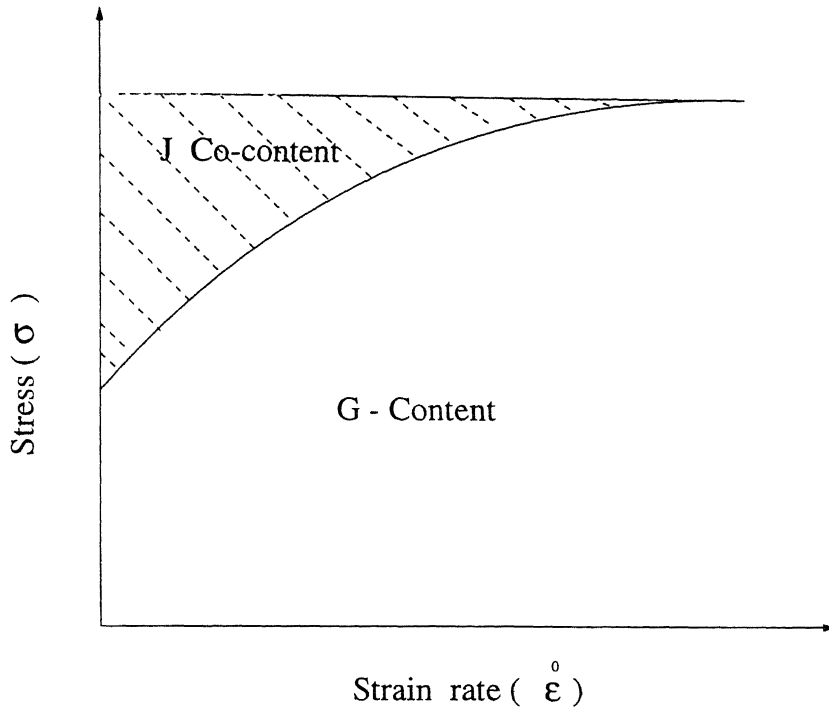


Figure 1.4: G content and J co-content for a workpiece

When the work piece material follows the constitutive equation

$$\sigma = K \dot{\epsilon}^m \quad (1.20)$$

where  $m$  is the strain rate sensitivity and  $K$  is constant, the dissipater co-content will be given by

$$J = \frac{\sigma \dot{\epsilon} m}{m + 1} \quad (1.21)$$

At one extreme,  $J$  can be as high as  $G$  when  $m=1$  and on the other hand  $J=0$  when  $m=0$ . The case of  $m=1$  has been considered to be the ideal case and a efficiency term has been defined as

$$\eta = \frac{J}{J_{max}} = \frac{2m}{m + 1} \quad (1.22)$$

which essentially describes the ability of the workpiece material to utilize power in structural changes. This is obtained from the variation of true stress with strain rate at a given true strain level, in iso-strain rate tests carried out at different temperatures and strain rate. The variation of efficiency parameter with temperature and strain rate



has been found to have relationship with the structural changes occurring during hot deformation. According to Prasad et al. [37] efficiency of dissipation ( $\eta$ ) is characteristic of the metallurgical process responsible for the dissipation. When two major dissipation processes having different characteristics occur simultaneously, the value of  $J$  will reach its maximum when the energy of dissipation of one process equals that of the other.

Following are the examples cited for the same.

- (a) At low temperature ( $T < 0.25 T_m$ ) and high strain rate ( $10 \text{ s}^{-1}$ - $100 \text{ s}^{-1}$ ) ductile fracture results from a void formation at hard particles. In the efficiency map (plot of  $\eta$  with respect to temperature and strain rate), the efficiency is very high and steeply varies with decrease in temperature and increase in strain rate within the temperature-strain rate domain for the void formation.
- (b) At high temperature ( $T > 0.75 T_m$ ) and low strain rates ( $< 0.001 \text{ s}^{-1}$ ), grain boundary sliding leads to wedge cracking. In the efficiency map the domain is characterized by very high value of efficiency which increases rapidly with decrease in strain rate.
- (c) Dynamic recrystallization becomes dominant at temperatures around  $0.75 T_m$  and strain rates varying between  $0.1$  to  $10 \text{ s}^{-1}$ . The efficiency in this domain ranges between 30 to 50% which are generally less than the processes mentioned in (a) and (b).
- (d) At very high strain rates ( $> 10 \text{ s}^{-1}$ ) and a relatively lower temperatures intense flow localization is commonly observed and the efficiency in this domain is very low.

These observations have been carried out in wide range of materials [38]. The dynamic materials model has been extended for arriving at criteria for flow instability. These criteria are based on the extremum principles of irreversible thermodynamics of

large plastic flow, proposed by Ziegler [42]. According to Ziegler, a system undergoing large plastic deformation will be unstable if

$$\frac{dD(\dot{\epsilon})}{d\dot{\epsilon}} < \frac{D(\dot{\epsilon})}{\dot{\epsilon}} \quad (1.23)$$

where  $D(\dot{\epsilon})$  is the power dissipation. Using the above relation Gegel et al. [39] have arrived at instability criteria which is given by

$$\frac{\partial s}{\partial \ln \dot{\epsilon}} \geq 0 \quad (1.24)$$

and

$$\frac{\partial \eta}{\partial \ln \dot{\epsilon}} \geq 0 \quad (1.25)$$

where

$$s = \frac{1}{T} \left[ \frac{\partial(\ln \sigma)}{\partial(\frac{1}{T})} \right] \quad (1.26)$$

. Kumar [37] assumed  $D=J$  and thus arrived at

$$\frac{dJ}{d\dot{\epsilon}} < \frac{J}{\dot{\epsilon}} \quad (1.27)$$

or

$$\zeta = \frac{\partial \ln(\frac{m}{m+1})}{\partial \ln \dot{\epsilon}} + m < 0 \quad (1.28)$$

Kumar's criterion has been tested for a wide variety of material and has been found to successfully predict the instability domain during hot compression.

Although the dynamic material model approach is successful in identifying different domains of microstructural evolution and instability, its theoretical foundation is debatable. Prasad et al. [37] have defined  $G$  term as "power dissipated by plastic work, most of which is converted into heat; the remaining small part is stored as lattice defect". This definition is not acceptable because  $P$ , which is the sum total of  $G$  and  $J$ , is the power dissipated by plastic work, most of which is converted into heat. The authors define the

term J as “related to the metallurgical mechanisms which occur dynamically to dissipate power”, and the examples of metallurgical mechanisms are dynamic recovery, dynamic recrystallization, internal fracture, dissolution or growth of particles, dynamic spheroidization of acicular structures and deformation induced phase transformations [37].

Though the meaning of metallurgical mechanisms is clear it is not clear as to what is meant by “dissipation of power through dynamic metallurgical processes”. Montheillet and Jonas [43] have pointed out that quality of dissipation should not be identified with G and dynamic metallurgical processes not to be identified with J. They have pointed out the importance of G and J in calculations based on variational principles in mechanics of solids. But they have not agreed with the employment of G and J to establish optimum conditions of hot working. According to them, given a driving force for localization, the strain rate sensitivity plays the role of mass while the acceleration is represented by the rate of flow localization. Thus in the presence of a fixed driving force higher values of  $m$  are directly responsible for lower rates of flow concentration. It follows that the best regime of hot working should correspond to highest possible value of  $m$  and the range that is identified in this way does not depend on whether  $m$  or  $\eta$  is maximized. Montheillet and Jonas [43] prefer to maximize  $m$  because of the physical insight provided by the theories of plastic instability.

Prasad [44] has replied to the objection made by them. He has cited thermodynamic principles of Malvern [45]. According to it the total power dissipated is related to the rate of entropy production as

$$P = \sigma \dot{\epsilon} = T \frac{dS^i}{dt} \geq 0 \quad (1.29)$$

where  $T$ =temperature,  $\frac{dS^i}{dt}$  rate of entropy production and inequality sign applies for irreversible deformation. Malvern has shown that this total rate of entropy production has two components, namely “internal” entropy rate and “thermal” entropy rate. Prasad has linked the internal entropy production rate to the term J. However the relationship

is not explicitly discussed.

Apart from this, Prasad et al. [37] have assumed that the flow of material obeys equation (1.20). However the equation of this type is valid only when  $m$  is constant over a wide range of strain rate, which is not the case with two phase titanium alloys [5]. Murty et al. [46] have thus suggested an improved method of calculating efficiency  $\eta$  using continuous piecewise polynomial fitted for  $\sigma$ - $\dot{\epsilon}$  data.

Though the physical interpretation of efficiency map and the instability map, which is also based on the same physical concepts, has been questioned, the approach of construction efficiency (or strain rate sensitivity) and instability maps have been found to be very useful in finding out the domains of various structural changes in the material and best domain of workability [47-70]. DMM approach of modeling deformation has been also applied to two phase titanium alloys by Prasad et al. [37]. They have explained peaks observed in Ti-6242Si alloy with equiaxed microstructure in terms of power dissipation due to  $(\alpha+\beta)$  to  $\beta$  phase transformation and dynamic recrystallization. For Ti-6242Si with  $\beta$  microstructure they have correlated the variation in efficiency at low strain rates with wedge cracking and transformations occurring in the  $\beta$  microstructure. Krishna et al. [70] have used the DMM approach to study the hot workability of near  $\alpha$  titanium alloy 685. They have reported domains of high efficiency (approximately 55% at low strain rate in the  $(\alpha+\beta)$  phase field and at strain rates above  $1 \text{ s}^{-1}$  in the  $\beta$  phase field, for this alloy. The two domains have been identified with breakup and spheroidization of  $\alpha$  plates and dynamic recovery of *beta* phase.

### Dislocation Population Model[71]

Recently, Bocek and Choi have evaluated the stability of plastic flow during high temperature deformation using dislocation population model. The ratio of the energy expended to that stored has been considered as the measure for the distance from the thermo-

dynamic equilibrium. According to the model, instability of the deformed structure (structural instability) which gives rise to macroscopic flow instability occurs at a critical model parameter. From the view point of the model, instability is a consequence of the exhaustion of energy storage capacity.

#### 1.3.4 Dynamic Changes Occurring During the Hot Deformation and Their Influence on the Flow Behavior and Flow Instability

As discussed in the previous section the flow instability during hot deformation depends on the extent of flow softening given by  $\gamma$  and the strain rate sensitivity,  $m$ .  $\gamma$  depends on the changes accompanying the deformation. It is well known [32] that two primary factors resulting into flow softening during the hot deformation are (1) temperature rise and (2) microstructural and textural changes occurring in the material. The strain rate sensitivity,  $m$ , depends on the mechanism of the plastic deformation.

##### Temperature Rise During Hot Deformation and its Influence on the Flow Behavior and Flow Instability

During hot deformation the plastic work ( $W$ ) which is a function of strain is given by

$$W = \int_0^\epsilon \sigma d\epsilon \quad (1.30)$$

and is converted into heat. A part of this heat is transferred to the surrounding and the remaining gets stored into the material resulting in temperature rise. Different investigators have calculated the temperature rise as a function of strain using the relation:

$$\Delta T(\epsilon) = \frac{f}{\rho C} \int_0^\epsilon \sigma d\epsilon \quad (1.31)$$

where  $\Delta T$  is the temperature rise as a function of strain ( $\epsilon$ ),  $\rho$  is the density,  $C$  is specific heat and  $f$  is the fraction of heat generated that is retained by the specimen. Investigators [5, 59] have assumed the fraction of heat generated that is stored in the material ( $f$ ) to be independent of strain and have assumed different values for different ranges of strain rates. However there appears no uniform basis for assuming the values of  $f$ . On the other hand by carrying out a rigorous heat transfer analysis the  $f$  as a function of strain and thus  $\Delta T$  as a function of strain can be estimated with reasonable accuracy. However no such analysis was found in the literature.

The temperature rise will result in flow softening [32], the extent of which increases with increase in temperature rise. In the case of ( $\alpha+\beta$ ) titanium alloys the flow stress is a strong function of temperature. Thus significant flow softening and consequent flow instability is expected for these alloys.

## Dynamic Recovery

During dynamic recovery (DRY), cross slip, climb and node unpining of dislocations, which permit the dislocations to unravel from hardening network and annihilate occur [10]. The salient features of dynamic recovery are as follows.

- (1) The extent of dynamic recovery during hot deformation decreases with decrease in the stacking fault energy (SFE) as the width of the faulted region between two partial components of a dislocation increases [10, 28].
- (2) Subgrains with low angle of orientation and equiaxed shape are formed.
- (3) The size of the subgrain increases with increase in temperature, decrease in strain rate and decrease in flow stress [6, 28].
- (4) Solute additions usually retard DRY, specially if they cause further increase in the faulted region between the two partials [10, 28].

- (5) It has been generally observed that the rate of dynamic recovery controls dynamic recrystallization [72].

When dynamic recovery is the only softening mechanism, the flow behavior is of the steady state type. Whereas significant flow softening is required for flow instability to set in during compression. Thus dynamic recovery does not contribute to the flow instability.

### Dynamic Recrystallization [6,10,73-75]

The dynamic recrystallization plays an important role in determining the workability of an alloy during the hot working. It influences the hot working of an alloy in two ways, stated as follows.

- (1) As mentioned earlier, crack nucleation and propagation is an important factor determining the ductility during hot working. The crack nucleation and propagation is usually retarded by dynamic recrystallization (DRX) [28, 76]. In the case of fatigue also, DRX inhibits the crack propagation [77]. Therefore dynamic recrystallization is many times very desirable during hot working.
- (2) It can cause substantial flow softening and consequently flow instability, and thereby is detrimental to hot workability. Since in the present study we are focusing on the flow instability we will discuss the influence of DRX on the stress-strain behavior, which is important from the point of view of plastic instability.

The occurrence of DRX under constant strain rate condition is shown to be often accompanied by steady drop in the flow stress as well as oscillations in the flow stress. The flow curves are characterized by stress oscillations at lower strains which gradually become damped to give an apparent steady state flow at high strains. Luton and

Sellari [78] rationalized the transition from oscillatory to single peak flow behavior by assuming that various cycles of recrystallization occur. According to them stress oscillations are observed when incubation strain or critical strain ( $\epsilon_c$ ) for initiation of DRX is greater than the strain interval over which a recrystallization cycle is completed ( $\epsilon_x$ ), i.e.  $\epsilon_c > \epsilon_x$ . On the other hand if  $\epsilon_c < \epsilon_x$  one cycle of recrystallization starts before the next one begins and the oscillation is suppressed.  $\epsilon_c$  is generally taken equal to the peak strain,  $\epsilon_p$  [10, 79].

The model by Sandstrom and Lagneborg [80] is based on the description of the volume distribution of dislocations produced as a result of the continuous recrystallization. With the help of the model, they have explained the transition from periodic to single peak behavior and the gradual disappearance of flow stress oscillations with strain. Recently, Rollet et al. [79] have developed a Monte Carlo model for DRX from earlier models used to simulate SRX and grain growth. The model simulates DRX by adding recrystallization nuclei and stored energy continuously with time and the simulations have reproduced many of the essential features of DRX. Derby and Ashby [81] have developed a model for DRX in which the nucleation rate is equated to a simple growth law such that a constant grain size is maintained. Experiments indicated [82] that the kinetics of DRX follows the Avrami kinetics.

For ( $\alpha+\beta$ ) titanium alloys DRX has been observed for both plate like microstructure as well as equiaxed microstructure [30, 83]. In the case of equiaxed microstructure it was found to coincide with superplasticity [30]. However it will lead to flow softening temperature strain rate conditions, which is away from the best condition for superplasticity, due to less contribution to plastic strain from grain boundary sliding and more contribution from slip by dislocation movement.



## Influence of Morphological Changes

Microstructure of  $(\alpha+\beta)$  titanium alloys can be broadly classified into: (a) platelike microstructure consisting of  $\alpha$  phase with plate morphology and (b) equiaxed microstructure. During the hot deformation of  $(\alpha+\beta)$  titanium alloys, the equiaxed microstructure exhibits grain growth at relatively lower strain rates. The effect of grain coarsening on the flow behavior depends on the mechanism of plastic deformation. Under superplastic condition when the grain boundary sliding is significant then strain hardening occurs as a result of grain coarsening. This results into a stable flow as the normalized strain hardening coefficient ( $\gamma$ ) and thus the  $\psi$  parameter is negative. In the non superplastic domain of temperature and strain rate coarsening of  $\alpha$  phase results into flow softening [32]. At higher strain rates due to the process of DRX and  $\beta$  pinching the coarse grains of  $\alpha$  in  $(\alpha+\beta)$  titanium alloys fragment into smaller ones and this process is associated with flow softening.

$(\alpha+\beta)$  titanium alloys with platelike microstructure exhibit more flow softening and thus are more prone to flow instability [12]. The  $\alpha$  plates undergo kinking, fragmentation into equiaxed morphology and coarsening. All these transformations are associated with flow softening [32].

Fragmentation, i.e. transformation of  $\alpha$  plates having high aspect ratio in  $(\alpha+\beta)$  titanium alloys into equiaxed  $\alpha$  grains (with low aspect ratio) has been studied for many  $(\alpha+\beta)$  titanium alloys. Peters et al. [84] started with a sample of Ti-6Al-4V having martensite microstructure and deformed them at 800°C, 960°C, 957°C and 990°C up to different strains. Following the deformation they water quenched the samples and subjected them to annealing treatment at 800°C for different times. They observed that both deformation as well as post deformation heat treatment played an important role in generation of equiaxed microstructure. The fraction of equiaxed  $\alpha$  phase increased with increasing heat treatment time. They also observed that transformation to equiaxed

structure more easily occurred at temperature closer to  $\beta$  transus, i.e. at 960°C, 975°C and 990°C.

Modification of plate morphology in Ti-6Al-4V to equiaxed morphology was investigated by Weiss et al. [83] with the aim of controlling the aspect ratio and final grain size of  $\alpha$  grains. They carried out measurement of average length, thickness and aspect ratio of  $\alpha$  plates in samples of Ti-6Al-4V having a starting microstructure of Widmanstätten type (with different average plate thickness), which were deformed at 955°C and at  $10^{-2} \text{ s}^{-1}$  up to different strains and followed by annealing at 925°C for two hours. They observed that the aspect ratio of  $\alpha$  lamellae decreases with increase in the forging strain upon subsequent isothermal annealing. For a given amount of deformation the starting microstructure with thinner  $\alpha$  plates transformed more easily to equiaxed  $\alpha$  grains, i.e. lower strain was required by the starting microstructure consisting of thinner plates.

Weiss et al. [83] also carried out TEM studies on the deformed samples in order to find out the mechanism of  $\alpha$  plate break up. They observed that the  $\alpha$  plate break up was due to penetration of  $\beta$  phase into the subboundaries of the subgrain formed in the  $\alpha$  plates. Under certain conditions where limited penetration of the  $\beta$  phase into the  $\alpha/\alpha$  subboundaries takes place, high angle  $\alpha/\alpha$  interphase are formed. The separation by  $\beta$  phase is easier in thin  $\alpha$  lamellae. In thick plate the  $\beta$  penetration is incomplete leading to aggregate of necklace like structure. Semiatin et al. [85] studied the microstructural evolution in Ti-6242Si having Widmanstätten structure at different temperatures and strain rates up to different strains. They observed increase in fraction of equiaxed  $\alpha$  with strain in hot worked material. On heat treating the deformed material at higher temperature the microstructure was found to be more equiaxed. They also studied the effect of strain rate on the microstructural evolution of Widmanstätten structure and found that at low strain rate the fraction of equiaxed  $\alpha$  at a given strain is higher.

## Chapter 2

# OBJECTIVE OF THE PRESENT STUDY AND PLAN OF THE WORK

$(\alpha+\beta)$  titanium alloys have unique combination of properties like high strength to weight ratio at elevated temperatures, good creep and fatigue properties and an excellent corrosion resistance. This has led to an extensive use of these alloys in aerospace, chemical and marine industries. Owing to its compatibility with biological cells  $(\alpha+\beta)$  titanium alloys are also used to manufacture surgical implants.

Two microstructures of  $(\alpha+\beta)$  titanium alloys: (a)  $\beta$  structure and (b) equiaxed structure, are of general interest because they not only display different combinations of mechanical properties but their hot working behaviors are also markedly different. Thus hot working of the two microstructural states are carried out in different temperature-strain rate domains. The  $\beta$  structure, which is the cast structure, exhibits flow softening and instability over a wide range of temperature (in the  $(\alpha+\beta)$  phase field) and strain rate. In contrast, hot deformation of  $(\alpha+\beta)$  titanium alloys with equiaxed microstructure

has very limited domain of flow instability, that is caused by temperature rise, at high strain rates and the alloys in this microstructural state can be formed to near net shapes under superplastic condition. Although  $\beta$  structure does not have good workability as compared to the equiaxed structure,  $\beta$  structure being the cast structure from which the equiaxed structure is obtained by hot working in the  $(\alpha+\beta)$  phase field, its hot workability is of primary concern.

Thus, in the present work our objective is to study the: (a) hot workability of Ti-622Si alloy, an  $(\alpha+\beta)$  titanium alloy with defense application, with  $\beta$  structure in the temperature-strain rate range for primary hot working and (b) that of the same alloy with equiaxed microstructure in the temperature-strain rate domain of superplasticity. Ti-622Si alloy contains Al as  $\alpha$  stabilizer and Mo, Cr and Fe as  $\beta$  stabilizers with Si being added to form silicides so as to improve its creep resistance. It therefore, represents the family of typical  $(\alpha+\beta)$  titanium alloy with good creep resistance. Keeping in the view, the importance of compressive state of stress during primary and secondary hot working operations it was decided to study the hot workability under compressive condition.

Hot workability refers to both the stress required as a function of temperature and strain rate, which is given by constitutive equations and the extent of possible deformation. Constitutive equations are useful in knowing the load required to carry out hot working operation. Hence, one of the major objectives of the present study is to determine the constitutive equations for Ti-622Si in both  $\beta$  and equiaxed microstructure. The hot workability, which also refers to the extent of deformation, is often limited by the flow instability. Thus another major objective of the study is to characterize the flow instability during compression of Ti-622Si( $\beta$ ) and the various factors influencing the same.

As pointed out in Chapter 1, flow instability during compression manifests itself in two ways:(a) inhomogeneous flow and (b) shear banding. However the extent of these

manifestations, whose variation with the parameters of hot working, i.e. temperature and strain rate will be useful in deciding the optimum conditions of hot working, have been seldom quantified. As a result proper correlation between the extent of these manifestations and the various factors influencing the flow instability was not found in literature. Thus in the present, attempts will be made to quantify the extent of inhomogeneous flow and shear banding and correlate them with various factors influencing the flow instability. One of the major factors influencing the flow instability is the stress-strain behavior. Different parameters which predict the triggering of flow instability have been put forward. In the present study we intend to calculate some of these parameters and correlate them with the extent of flow instability. In this was, we also plan to draw a comparison between the instability criteria based on flow localization parameters and those based on DMM.

It was discussed in the previous chapter that flow softening and instability in  $(\alpha+\beta)$  titanium alloys with plate like microstructure, is caused by temperature rise and microstructural changes in contrast to the equiaxed microstructure in which they arise mainly due to temperature rise. However no systematic study was found in the literature that correlates the microstructural changes in these alloys with the flow softening and flow instability. In order to do so the effect of temperature rise has to be eliminated by carrying out temperature correction of the stress-strain curves. However as pointed out in Chapter 1, the temperature corrections for compression tests reported in the literature were carried out without any rigorous estimation of the fraction of the heat generated that is retained by the compression specimen,  $f$ . So in the present chapter, one of the important objective is to estimate  $f$  and based on that, do the temperature correction of the stress-strain curves and subsequently correlate the flow softening and flow instability with the morphological changes occurring during the hot deformation. In correlating the flow instability with the microstructural changes, both flow localization parameters as well as the thermodynamic parameters (DMM approach) will be used.

DMM approach of predicting the efficiency of power dissipation and correlating it with microstructural changes is a relatively new approach to hot workability. Although it has been tested for a large number of alloys, its theoretical basis has been subject to criticism. In the present work, we intend to correlate the efficiency maps generated with the microstructural changes occurring during the hot working for Ti-622Si( $\beta$ ).

# Chapter 3

## EXPERIMENTAL PROCEDURE

### 3.1 Processing of Ti-622Si Alloy and its Characterization

#### 3.1.1 The As-Received Material

The two phase ( $\alpha+\beta$ ) titanium alloy Ti-6.4Al-2.6Mo-1.5Cr-0.4Fe-0.3Si, hereafter referred to as Ti-622Si alloy, was supplied by Midhani Ltd., Hyderabad, India. The alloy was manufactured using vacuum arc melting of electrode made from titanium sponge, aluminium shots and other elements. Ingots weighing about one ton were produced by double melting under the vacuum arc and were subjected to their forging in the  $\beta$  phase field. The forged billets were subsequently hot rolled first in the  $\beta$  phase field and then in the ( $\alpha+\beta$ ) phase field. The material received for the present study was supplied in the form of hot rolled bars of 30mm diameter.

The chemical composition of the alloy is given in Table 3.1 and the  $\beta$  transus temperature of the alloy, i.e. the temperature of transition from ( $\alpha+\beta$ )-phase field to  $\beta$

phase field during its heating was reported to be lying in between 960°C and 980°C.

Table 3.1: Chemical composition for Ti-622Si alloys

| Element        | Composition(wt%) |
|----------------|------------------|
| Al             | 6.4              |
| Mo             | 2.6              |
| Cr             | 1.5              |
| Fe             | 0.4              |
| Si             | 0.3              |
| Ni             | 0.02             |
| C              | 0.003            |
| Mn             | 0.001            |
| Zr             | 0.1              |
| N <sub>2</sub> | 0.01             |
| W              | 0.3              |
| Cu             | 0.003            |
| Ti             | Bal              |
| O <sub>2</sub> | 0.09             |
| N <sub>2</sub> | 0.01             |
| H <sub>2</sub> | 0.01             |

The microstructure of the as-received alloy, designated as condition AR, is shown in Figure 3.1. Thus the alloy in the as-received condition consisted of  $\alpha$  phase with two morphologies : (1) lamellar and (2) equiaxed, with the proportion of the lamellar  $\alpha$  being higher (approximately 70 %).



### 3.1.2 Modification of the As-Received Microstructure

As stated in Chapter 2, the aim of the present work was to study the hot deformation behaviour of Ti-622Si alloy in (a) Widmanstätten  $\alpha$  condition, i.e. the  $\beta$  microstructural state, both above and below the  $\beta$  transus temperature and (b) equiaxed  $\alpha$  condition, i.e. the  $(\alpha+\beta)$  microstructural state, below the  $\beta$  transus temperature. The as-received microstructure of Ti-622Si alloy was modified to Widmanstätten  $\alpha$  by air cooling the alloy from the  $\beta$  phase field. For this purpose the machined bars having diameter of 18mm and length of 10-15 cm were heated to 1050°C, i.e. in the  $\beta$  phase field, for 90 minute and subsequently air cooled.

In contrast, the equiaxed  $\alpha$  structure was obtained by subjecting the as-received material to further thermomechanical treatment in the two phase  $(\alpha+\beta)$  phase field. For this purpose the alloy was (1) hot rolled at 920°C from diameter of 30 mm to 14.5 mm in two passes and (2) subsequently annealed for 45 minutes at 920°C. This resulted into fine grained equiaxed  $\alpha$  microstructure which is shown in Figure 3.2 and is designated as TMT condition. As stated in the previous chapter, one of the objectives of the present study was to characterize the deformation behaviour of Ti-622Si with equiaxed  $\alpha$  microstructures of different grain sizes. Therefore, in order to obtain equiaxed microstructure with three successively higher grain sizes, rods of the hot rolled and annealed alloy were soaked at 920°C for 12 hour, 48 hour and 96 hour respectively.

### 3.1.3 Determination of the $\beta$ Transus Temperature

Though the  $\beta$  transus temperature of Ti-622Si alloy is reported to be 980°C, it is expected that the exact levels of interstitial elements present in the alloy may significantly influence the same. Therefore, the  $\beta$  transus temperature of the heat supplied was estimated by the metallography method. For this purpose specimens of the alloy were

soaked and equilibrated at the temperatures of 960°C, 970°C and 980°C respectively, i.e. at an interval of 10°C below the reported  $\beta$  transus temperature. The specimens were soaked by heating in a muffle furnace which had a constant temperature zone of 10 cm and within which the temperature was maintained  $\pm 2$  °C of the set temperature. An air atmosphere was maintained during the soaking. After soaking at the respective temperatures for a period of one hour specimens were quenched in water. These water quenched specimens were prepared for their microstructural examination by procedure outlined in section 3.5.2. The  $\beta$  transus, being the transition between the  $(\alpha+\beta)$  and  $\beta$  phase field, was taken to lie in between the maximum temperature at which  $\alpha$  phase was present and the minimum temperature at which  $\alpha$  was completely absent.

## 3.2 Preparation of Compression Specimens

Cylindrical compression specimens were machined from 18 mm bars having the  $\beta$  structure and from 14.5 mm bars having the  $(\alpha+\beta)$  structure. The machined specimens had diameter and height of 8 mm and 12 mm respectively and were provided with a chamfer of 1 mm at an angle of 45° at the edges of the specimen faces to avoid foldover during compression, if any. Since in the case of specimens having  $\beta$  microstructure, the lubricant used in order to minimize friction between the specimen faces and the platens was glass, which melts at deformation temperatures, the specimens were engraved with concentric grooves of about 0.2 mm depth on their faces for the retention of glass lubricant. In the case of compression specimens having  $(\alpha+\beta)$  structure, the lubricant used was boron nitrate powder, which does not melt at deformation temperatures and thus concentric grooves were not engraved on their faces.

The specimens having the  $\beta$  structure were deformed at relatively higher strain rates as compared to those having equiaxed microstructure. At higher strain rates, owing to higher rate of plastic work done on the specimens and shorter time duration available for

dissipation of heat to the surrounding, substantial temperature rise is expected. So the specimens having  $\beta$  structure, in addition to the concentric grooves were provided with a fine hole of 0.8mm at their mid-height in order to insert chromel-alumel thermocouple for measuring the temperature rise during deformation. These details of compression specimens are shown in Figure 3.3.

### 3.3 Compression Testing of Ti-622Si Alloy with the $\beta$ Structure

#### 3.3.1 Load-Displacement Curves

A DARTEC computer controlled servohydraulic testing machine was used for high temperature compression testing under iso-strain rate condition. Isothermal tests were conducted by compressing Ti-622Si specimens which were held in between IN-100 platens maintained at the testing temperature in a three zone muffle furnace shown schematically in Figure 3.4. Thus the temperature of the testing specimen was maintained within  $\pm 2^\circ\text{C}$  of the set temperature.

The testing machine had a load capacity of 100 KN and the actuator speed could be varied from a minimum of 0.003 mm/sec to a maximum of 1250 mm/sec, with a maximum stroke length of 50 mm. The amount and the direction of movement of the actuator was sensed by a linear variable differential transformer or the stroke transducer. The output from the stroke transducer was demodulated in the actuator electronic unit. The load cell of the machine was a resistance strain gauge device. The constant true strain rate was achieved by directly relating the strain of the specimen to the machine's stroke, i.e. actuator displacement, and producing an exponentially decaying stroke rate

to simulate true strain rate. The following relation was used for this purpose:

$$X(t) = -h_o[1 - \exp(\dot{\epsilon}t)] \quad (3.1)$$

where  $X(t)$  is the stroke at time  $t$ ,  $h_o$  is the initial height of the specimen and  $\dot{\epsilon}$  is the true strain rate. The strain rate was corrected in 150 stages while testing at strain rates lower than  $1.0 \text{ s}^{-1}$ , in 138 stages at  $10 \text{ s}^{-1}$  and in 13 stages at a strain rate of  $100 \text{ s}^{-1}$

Compression tests were carried out at temperatures of  $750^\circ\text{C}$ ,  $800^\circ\text{C}$ ,  $850^\circ\text{C}$ ,  $900^\circ\text{C}$ ,  $950^\circ\text{C}$  and  $1000^\circ\text{C}$  and at strain rates of  $10^{-3} \text{ s}^{-1}$ ,  $10^{-2} \text{ s}^{-1}$ ,  $10^{-1} \text{ s}^{-1}$ ,  $10^0 \text{ s}^{-1}$ ,  $10^1 \text{ s}^{-1}$  and  $10^2 \text{ s}^{-1}$ . Before heating, the specimens were covered with a slurry of borosilicate glass powder which melted at high temperature melted and acted as a lubricant. The adiabatic temperature rise of the samples was monitored with the help of a chromel-alumel thermocouple embedded with the help of a steel pin in the 0.8 mm hole located at mid height of the specimen. Each specimen was compressed to a true strain of 0.5 and the load stroke data was recorded. After the deformation the deformed specimens were water quenched within 10 seconds of stopping the test. Thus from the compression tests the load-displacement curves and the temperature rise at the end of the compression were obtained.

### 3.3.2 True Stress versus True Plastic Strain Curves

The variation of true stress with true plastic strain was obtained from the load-displacement curves. In order to obtain the variation of true stress with true plastic strain the elastic component of displacement was eliminated from the net displacement by using the relationship:

$$\Delta X_p = \Delta X - L/M \quad (3.2)$$

where  $\Delta X$  is the displacement,  $\Delta X_p$  is plastic component of the displacement,  $L$  is the load and  $M$  is the combined stiffness of the specimen and the machine assembly.

Subsequently true stress,  $\sigma$ , and true plastic strain,  $\epsilon_p$ , were calculated using equations:

$$\sigma = L/A_o(\Delta X/h_o + 1) \quad (3.3)$$

where  $A_o$  is initial cross sectional area and  $h_o$  is initial height of specimen.

$$\epsilon_p = -\ln\left(\frac{h_o}{h_o + \Delta X_p}\right) \quad (3.4)$$

### 3.3.3 Strain Rate Sensitivity and Efficiency of Power Dissipation

Strain rate sensitivity,  $m$ , of the material is defined as

$$m = \frac{\partial \log \sigma}{\partial \log \dot{\epsilon}} \quad (3.5)$$

From the stress-strain curves at different strain rates, the data between stress and strain rate corresponding to different strain levels was obtained. The data thus obtained was analyzed for the best fit curves. Strain rate sensitivity,  $m$ , as a function of strain rate was obtained from the slope of the best fit curves. Similarly  $\eta$  which is related to the  $m$  according to the relationship

$$\eta = \frac{2m}{m + 1} \quad (3.6)$$

was also calculated as a function of strain rate.

### 3.3.4 Flow Localization and Instability Parameters

To calculate the flow localization parameter  $\psi$ , (defined in Chapter 1) as a function of strain, value of slope of the stress-strain curve ( $d\sigma/d\epsilon$ ) was calculated by fitting high order polynomial functions through the stress-strain curves and calculating the slope

using the coefficients of the polynomial. This was done in order to eliminate the local fluctuations

The thermodynamic parameter  $\zeta$ , given by

$$\zeta = m + \frac{\partial \log \frac{m}{m+1}}{\partial \log \dot{\epsilon}} \quad (3.7)$$

was obtained as a function of strain rate from the slope of best fit line through the  $\log \frac{m}{m+1}$  -  $\log \dot{\epsilon}$  data points.

### 3.4 Compression Testing of Ti-622Si Alloy with the $(\alpha+\beta)$ Microstructure

#### 3.4.1 Stress-Strain Rate Curves and Strain Rate Sensitivity

The deformation characterization of Ti-622Si alloy with the  $(\alpha+\beta)$  microstructural state was carried out by establishing the variation of the flow stress as well as the strain rate sensitivity,  $m$ , with the strain rate at a given temperature. For this purpose, step strain rate tests were performed on a MTS (Material Testing System) machine.

MTS Machine used for the step strain rate compression tests was a servohydraulic testing machine. The machine had a load capacity of 100KN. It had a maximum stroke length of 100mm. The amount and the direction of movement of the actuator was sensed by a linear variable differential transformer or the stroke transducer. The output from the stroke transducer was demodulated in the actuator electronic unit. Isothermal compression tests were carried out by compressing the specimens in between compression platens, one of which was connected to the actuator and the other was held by the machine, as shown schematically in Figure 3.5. Compression platens, schematically shown in the figure, were made from rods of Superni 90 (a nickel based superalloy supplied

by Midhani, Hyderabad, India) having diameter of 2.5 inch. At first the platens were machined from bars of 2.5 inch diameter. To fit the platen with the machine, it was provided with threading on one end. The non threaded end (end facing the specimen) had a hole of 2.2 cm diameter and 2.2 cm depth. Subsequently, platens were heat treated at 700°C for 17 hours for precipitation hardening. Blocks of alumina having 2.2 cm diameter and 2.2 cm height were tightly fitted into the holes of the platens so that the stress from the compression specimen held between the platens is predominantly transmitted to alumina blocks. During the testing, the temperature of the specimen was maintained with the help of a 3 zone muffle furnace, that surrounded the two platens and the specimen held in between them, as shown in Figure 3.5. The temperature of specimen during deformation was maintained within  $\pm 2^\circ\text{C}$  of the set temperature. During the compression, the load applied to the specimen was measured with the help of a load cell which is a resistance strain gauge.

The step strain rate tests were carried out at temperatures of 750°C, 800°C, 850°C, 900°C, 920°C, 940°C, 950°C and 960°C and at each temperature the strain rate was varied by varying the actuator speed,  $v$ , which is related to the strain rate by the relation

$$\dot{\epsilon} = \frac{v}{l} \quad (3.8)$$

where  $l$  is the instantaneous length of the specimen. The values over which the actuator speed was varied were  $1.2 \times 10^{-4}$ ,  $6.25 \times 10^{-4}$ ,  $1.2 \times 10^{-3}$ ,  $6.25 \times 10^{-3}$ ,  $1.2 \times 10^{-2}$ ,  $6.25 \times 10^{-2}$ ,  $1.2 \times 10^{-1}$  and  $6.25 \times 10^{-1}$  respectively. For the specimen length of 12mm, i.e. the initial length of compression, these values of actuator speed correspond to strain rates of  $10^{-5}\text{s}^{-1}$ ,  $5.2 \times 10^{-5}\text{s}^{-1}$ ,  $10^{-4}\text{s}^{-1}$ ,  $5.2 \times 10^{-4}\text{s}^{-1}$ ,  $10^{-3}\text{s}^{-1}$ ,  $5.2 \times 10^{-3}\text{s}^{-1}$ ,  $10^{-2}\text{s}^{-1}$  and  $5.2 \times 10^{-2}\text{s}^{-1}$  respectively. However, since the length of the specimen varied during the compression, the actual strain rate values, though close to these values were different from them and were calculated using equation 3.8. At each actuator speed (or strain rate), the deformation was allowed to reach a steady state load and before stepping

up the deformation to higher cross head speed (or strain rate), the platen movement was arrested. The true stress corresponding to a cross head speed or strain rate was calculated from the steady state load value (P) using the relationship

$$\sigma = \frac{L}{A} \quad (3.9)$$

where A is the instantaneous cross sectional area of the specimen and given by

$$A = \frac{l_o A_o}{l} \quad (3.10)$$

where  $l_o$  and  $A_o$  are initial length and cross sectional area of specimen respectively.

After obtaining the strain rate and true stress values for different actuator speeds and thus the stress-strain rate curves, the strain rate sensitivity was directly obtained from the step strain rate tests using the relationship:

$$m = \frac{\log \frac{L_2}{L_1}}{\log \frac{v_2}{v_1}} \quad (3.11)$$

where  $L_1$  and  $L_2$  are loads corresponding to the actuator speeds of  $v_1$  and  $v_2$ .

### 3.4.2 Calculation of Parameters of Constitutive Equation

The experimental constitutive equation relating the flow stress, strain rate, temperature and the grain size during deformation of Ti-622Si with equiaxed microstructure, used in the present work, is given in the non dimensional form as

$$\dot{\epsilon} = \frac{AD_oEb}{kT} \left(\frac{b}{d}\right)^p \left(\frac{\sigma}{E}\right)^n e^{-\frac{Q}{RT}} \quad (3.12)$$

where E is the Young's modulus,  $D_o$  is the diffusivity coefficient,  $d$  is average grain size,  $b$  is the burgers vector or atom size,  $k$  is the Boltzmann constant,  $Q$  is activation energy,  $n$  is stress exponent,  $p$  is grain size exponent and A is dimensionless constant. In the case of Ti-622Si with equiaxed microstructure, the temperature-strain rate domain of deformation was divided into superplastic and non superplastic domains on the basis of



the value of strain rate sensitivity, i.e. domain with  $m > 0.4$  was taken as superplastic domain and that with  $m < 0.4$  was taken as non superplastic domain. The parameters of equation 3.12 was obtained for both the domains. First the representative values of strain rate sensitivity,  $m$  or inverse of stress exponent,  $n$  were assumed for the two domains and subsequently grain size exponent,  $p$ , for the superplastic domain and activation energy  $Q$  for superplastic as well as non superplastic domains were evaluated.

The grain size exponent in superplastic domain was calculated using the relationship

$$p = -\left[\frac{\partial \log(\frac{\epsilon}{\sigma^n})}{\partial \log d}\right]_T \quad (3.13)$$

Best fit line was drawn through the  $\log \frac{\epsilon}{\sigma^n}$  versus  $\log d$  plot and the slope was taken as the grain size exponent. The activation energy( $Q$ ) of equation (3.11) for superplastic domain can be obtained by the relationship:

$$Q = -R\left[\frac{\partial \log(\sigma^{-n} T E^{n-1} d^p)}{\partial (1/T)}\right]_\epsilon \quad (3.14)$$

In order to obtain  $Q$  using relationship 3.14 the  $\log(\sigma^{-n} T E^{n-1} d^p)$  was plotted against  $1/T$  and the best fit was drawn through the data points.  $Q$  is estimated from the slope of the best fit line. The activation energy for the non superplastic domain is given by

$$Q = -R\left[\frac{\partial \log(\sigma^{-n} T E^{n-1})}{\partial (1/T)}\right]_\epsilon \quad (3.15)$$

and was obtained from the slope of the best fit line between the  $\log(\sigma^{-n} T E^{n-1})$  and  $1/T$  data points.

Elastic modulus,  $E$  as a function of temperature is required to estimate  $Q$  using the relations 3.14 and 3.15. However the value of  $E$  for Ti-622Si was not available. Since  $E$  does not vary significantly with composition, the value of  $E$  as a function of temperature, reported for Ti-6Al-4V, was used for estimating  $Q$  in both superplastic and non superplastic domains. After  $p$  and  $Q$  were calculated for both superplastic and non superplastic domains, the non dimensional constant  $A$  was estimated by substituting the values of diffusivity  $D$  and atom size  $b$  in equation 3.12. The value of  $D$  and  $b$  used in the present study were also that of Ti-6Al-4V.

## 3.5 Macroscopic and Microscopic Observations of Specimens

### 3.5.1 Macroscopic Observation of Deformed Specimens of Ti-622Si With $\beta$ Microstructure

The deformed specimens of Ti-622Si with  $\beta$  structure were examined for the macroscopic changes in them during the compression. Photographs of side and perspective view of some of the deformed specimens were then taken with the help of a camera with close-up lenses. In order to quantify the non uniformity of deformation within the specimen, dimensions of the top and the bottom faces of the deformed specimens and misalignment in the centers of grooves inscribed on them were measured using a vernier caliper.

Further the deformed specimens were cut along vertical plane which is parallel to the maximum diameters of the two faces. The cut plane was at first polished using different grades of emery paper and then using alumina powder having particle sizes of  $1.0\ \mu\text{m}$  and  $0.3\ \mu\text{m}$  on a polishing cloth. The polished cross section was etched with Kroll's reagent and subsequently examined for non uniform plastic flow. Photographs of the etched cross sections of some of the specimens revealing non uniform plastic deformation were taken using camera with close up lenses.

### 3.5.2 Microstructural Characterization of Specimens of Ti-622Si

Microstructural characterization of undeformed as well as deformed specimens of Ti-622Si in its  $\beta$  microstructural state and that of undeformed specimens of the alloy in its  $(\alpha+\beta)$  microstructural state were carried out under a Leitz Metallux 3 optical microscope (Leitz Wetzlar, Germany) and a JEOL model ISI 60 scanning electron microscope

(JEOL, Japan). The specimens to be examined were cut and the cut cross sections were polished (as per the procedure given in Section 3.5.1), etched with Kroll's reagent and observed under microscope. In the case of deformed specimens exhibiting anisotropy in the horizontal cross section, the specimens were cut along the vertical plane which is parallel to the maximum diameters of the two faces. After the microstructural observations, photographs of some representative regions were taken using the cameras attached to the microscope

In the case of Ti-622Si with  $(\alpha+\beta)$  microstructure, measurement of the average grain size of the  $\alpha$  phase,  $\beta$  phase and the entire microstructure was done by the mean intercept length method. The average grain sizes were determined using the relations

$$\overline{d_\alpha} = 1.74 \frac{\sum N_{i\alpha} L_{i\alpha}}{\sum N_{i\alpha}} \quad (3.16)$$

$$\overline{d_\beta} = 1.74 \frac{\sum N_{i\beta} L_{i\beta}}{\sum N_{i\beta}} \quad (3.17)$$

$$\overline{d_{\alpha\beta}} = 1.74 \frac{\sum N_{i\alpha} L_{i\alpha} + \sum N_{i\beta} L_{i\beta}}{\sum N_{i\alpha} + \sum N_{i\beta}} \quad (3.18)$$

where  $d_\alpha$ ,  $d_\beta$  and  $d_{\alpha\beta}$  are the average grain sizes of  $\alpha$  phase,  $\beta$  phase and the entire microstructure respectively,  $N_{i\alpha}$  and  $N_{i\beta}$  are the number of linear intercepts on the  $\alpha$  phase and  $\beta$  phase respectively and  $L_{i\alpha}$  and  $L_{i\beta}$  are the intercept lengths of the  $\alpha$  phase and  $\beta$  phase respectively. However, it was not possible to reveal the  $\beta$   $\beta$  boundary in certain cases by ordinary etching. So in these cases over etching of these specimens was done in order to reveal the  $\beta$ - $\beta$  boundary and to carry out the grain size measurements.

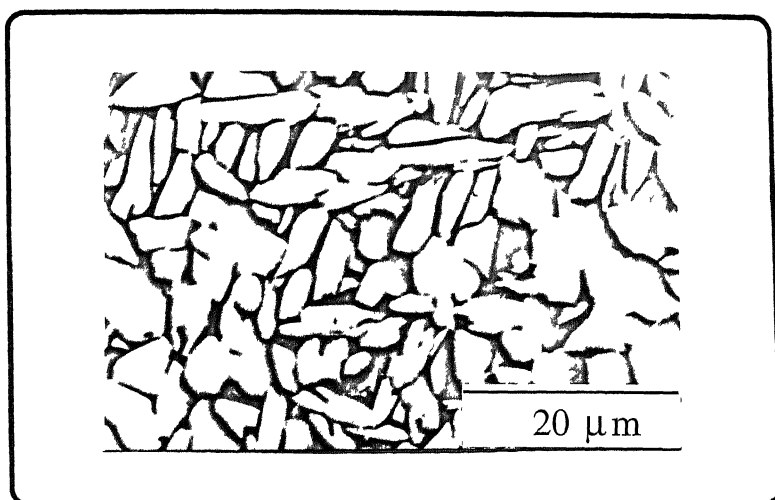


Figure 3.1: As received microstructure of Ti-622Si alloy

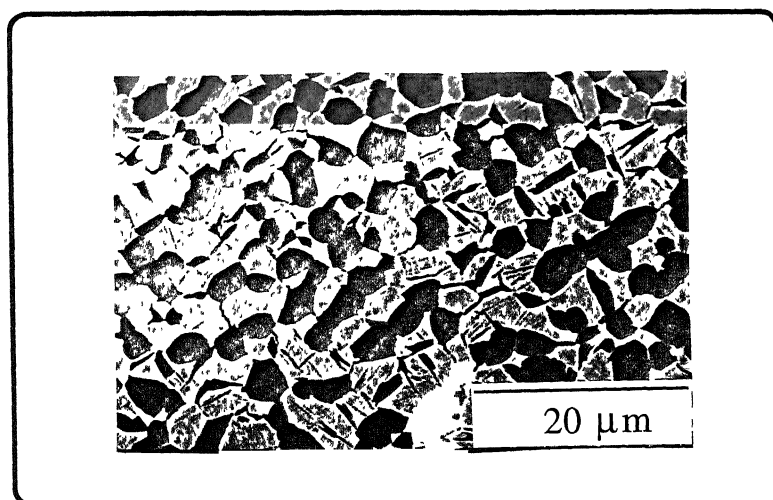


Figure 3.2: Microstructure of Ti-622Si alloy in the TMT condition

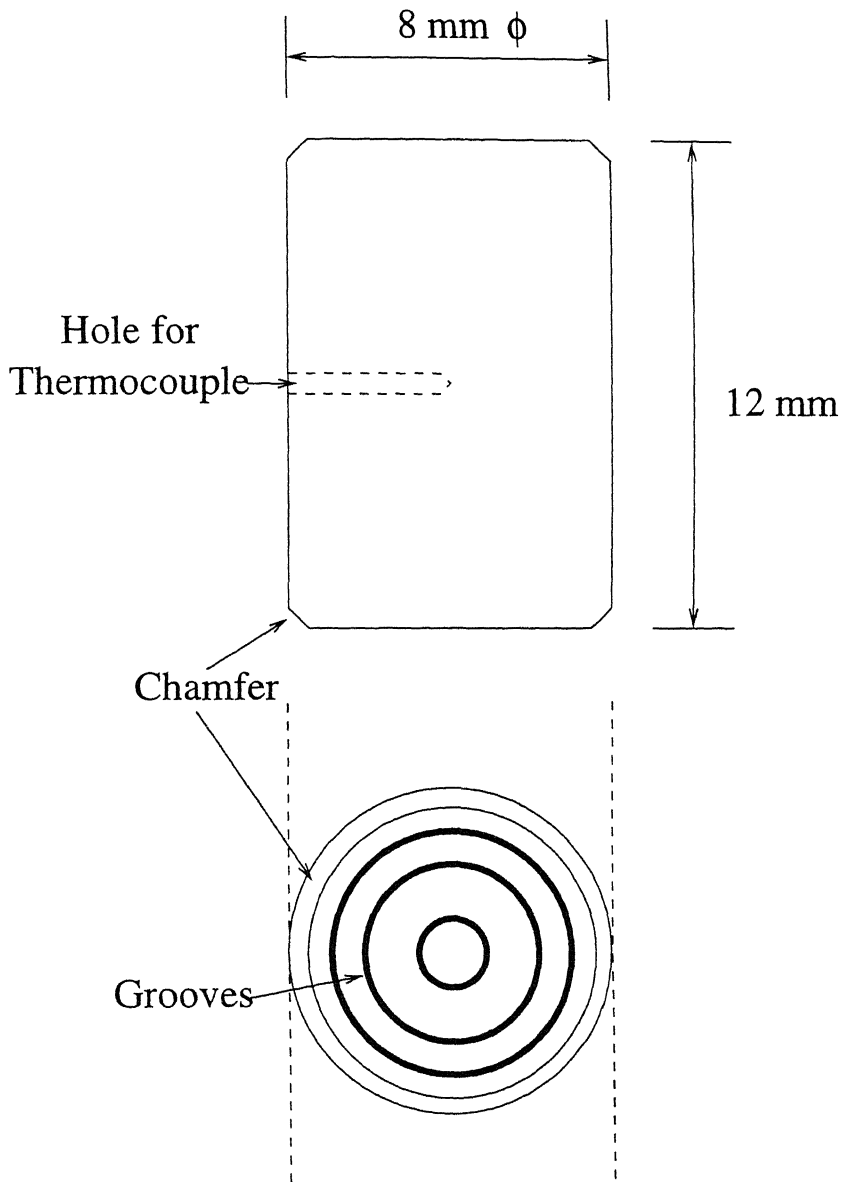


Figure 3.3: Compression specimens for Ti-622Si alloy with  $\beta$ -structure, with concentric grooves on the faces and hole for thermocouple insertion

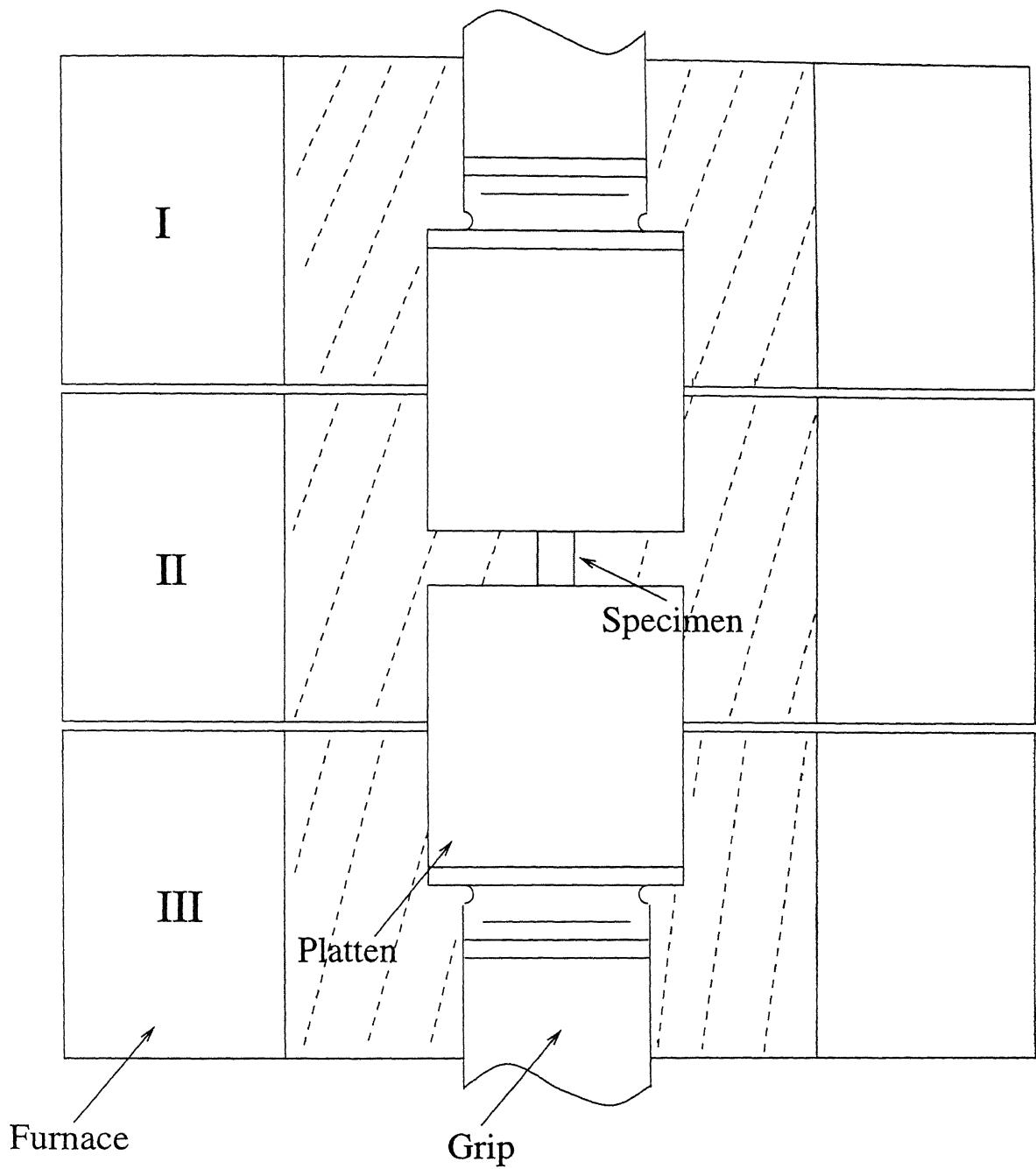


Figure 3.4: Specimen and platens surrounded by three zone furnace

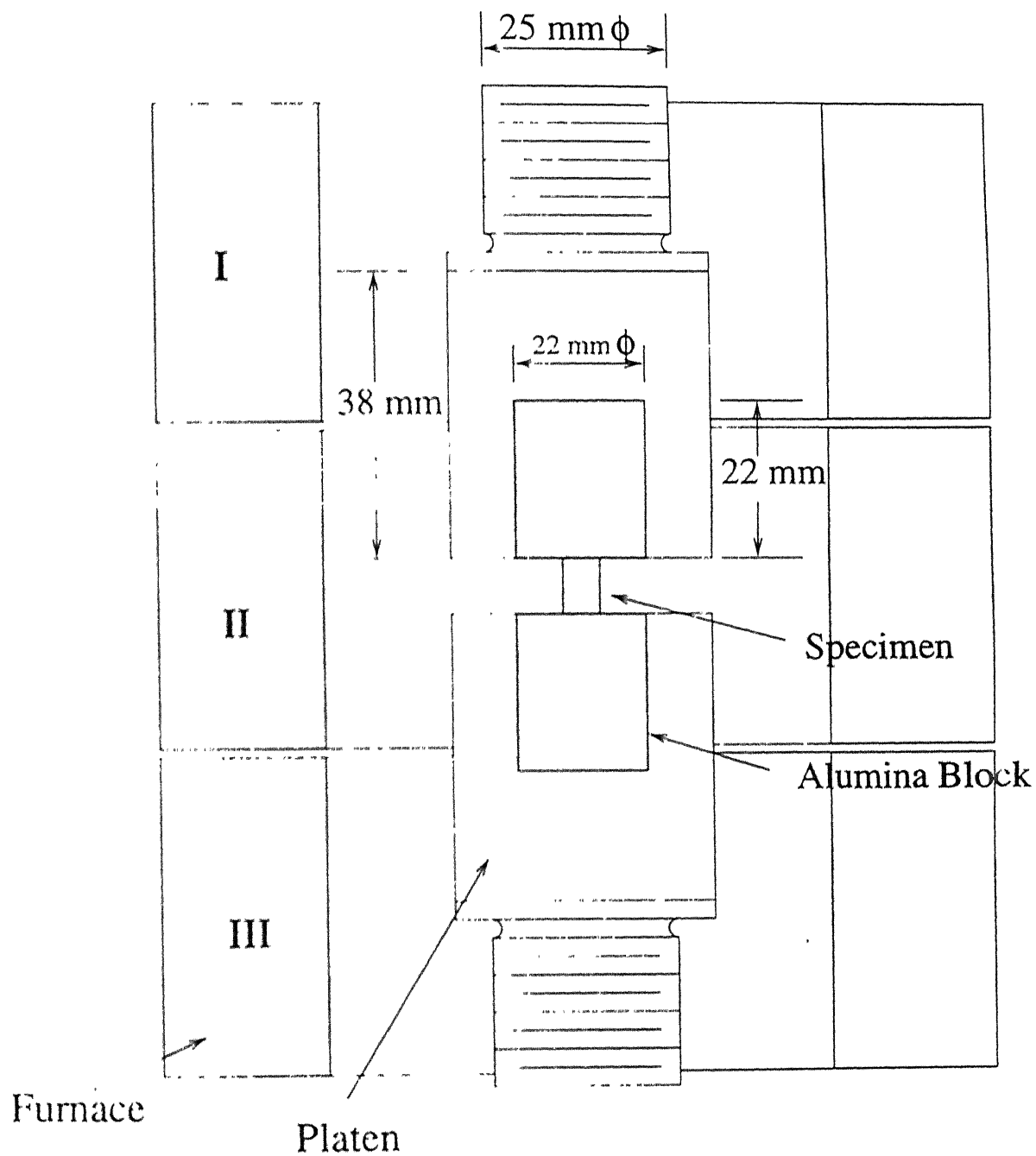


Figure 3.5: Geometry of compression platens for compression of Ti-622Si with equiaxed microstructure

# Chapter 4

## RESULTS

### 4.1 Microstructural States of Ti-622Si Alloy

As mentioned in Chapter 3 (Section 3.1.1), Ti-622Si alloy was received in the form of hot rolled bars of 30mm diameter (designated as condition AR). The microstructure of the alloy in condition AR has already been shown in Figure 3.1. As shown in the figure it consisted of  $\alpha$  phase with two morphologies : (1) coarse lamellar and (2) equiaxed, with the proportion of the lamellar  $\alpha$  being approximately 0.7. It is well known that coarse lamellar  $\alpha$  precipitates from  $\beta$  phase during slow cooling and that equiaxed  $\alpha$  is formed as a result of hot deformation of  $\alpha$  [1]. Thus the lower fraction of equiaxed  $\alpha$  in the microstructure suggests that most of the hot rolling was carried out either in the two phase field just below the  $\beta$  transus and/or was also partly carried out in the  $\beta$  phase field.

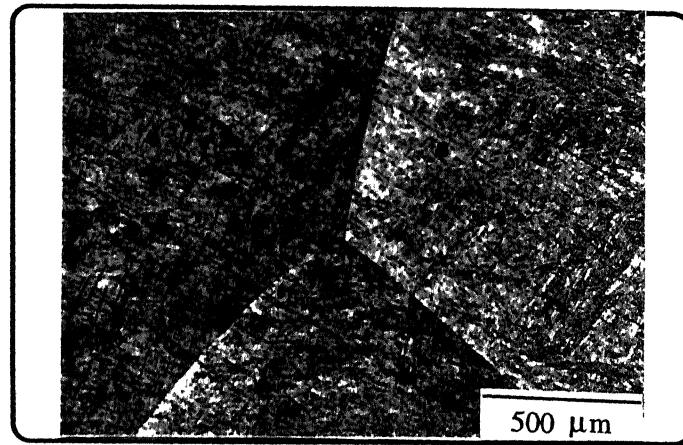
As mentioned in Chapter 2, the present study was carried out to investigate the hot working behaviour of Ti-622Si alloy in two microstructural states, namely (1) Widmanstätten or fine lamellar  $\alpha$  structure referred to as the  $\beta$  structure and (2) equiaxed  $\alpha$  structure referred to as  $(\alpha + \beta)$  structure. Since the alloy in AR condition consisted of



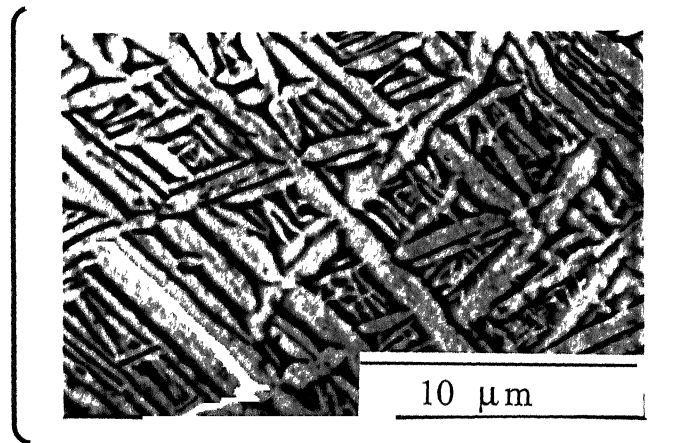
coarse lamellar as well as equiaxed morphologies of  $\alpha$ , the alloy was heated above the  $\beta$  transus temperature and subsequently aircooled to get purely Widmanstätten microstructure. The  $\beta$  structure thus obtained is shown in Figure 4.1. Figure 4.1(a) shows the microstructure at a low magnification while the same at higher magnification is shown in Figure 4.1(b). At low magnification very large equiaxed prior  $\beta$  grains can be observed. The microstructure at higher magnification consisted of a large fraction of  $\alpha$  phase in fine plate morphology with plate thickness less than  $1\ \mu\text{m}$  and a small fraction of  $\beta$  phase which was found to be present in between two adjacent  $\alpha$  plates.

Attempts were made to obtain equiaxed microstructure from the alloy in condition AR by heat treatment. However this was not possible. Therefore Ti-622Si alloy in AR condition was further hot rolled and annealed at  $920^\circ\text{C}$  in the two phase field as per the schedule described in Chapter 3. Microstructure of the alloy after hot rolling and annealing treatment, designated as condition TMT, was shown in Figure 3.2. The microstructure consisted of primary  $\alpha$  particles having volume fraction of 0.45 and prior  $\beta$  matrix in which Widmanstätten  $\alpha$  has precipitated, having volume fraction of 0.55. Though they were not fully equiaxed, most of the  $\alpha$  grains had aspect ratio close to 1.0. Few of the them were found to be clustered. The prior  $\beta$  matrix also consisted of equiaxed grains, whose aspect ratio was mostly close to 1.0. Thus it can be seen that as per the objective, equiaxed structure could be successfully achieved in the Ti-622Si alloy.

Further mill-annealing of the alloy in TMT condition was carried out at  $920^\circ\text{C}$  for 12 hour, 48 hour and 96 hour. The microstructures thus obtained, some of which are shown in Figure 4.2, will be hereafter referred to as TMT, TMT-A1(12 hour) and TMT-A3(96 hour). The figure suggests that grain growth had occurred in the alloy during the mill annealing. Grain sizes of the alloy in these conditions were measured as per procedure outlined in Section 3.5.2. The average grain-sizes in condition TMT-A1, TMT-A2 and TMT-A3 were found to be  $8.3\ \mu\text{m}$ ,  $12.7\ \mu\text{m}$  and  $14.6\ \mu\text{m}$  respectively.



(a)



(b)

Figure 4.1: Ti-622Si alloy in  $\beta$  microstructural state at (a) lower and (b) higher magnifications.

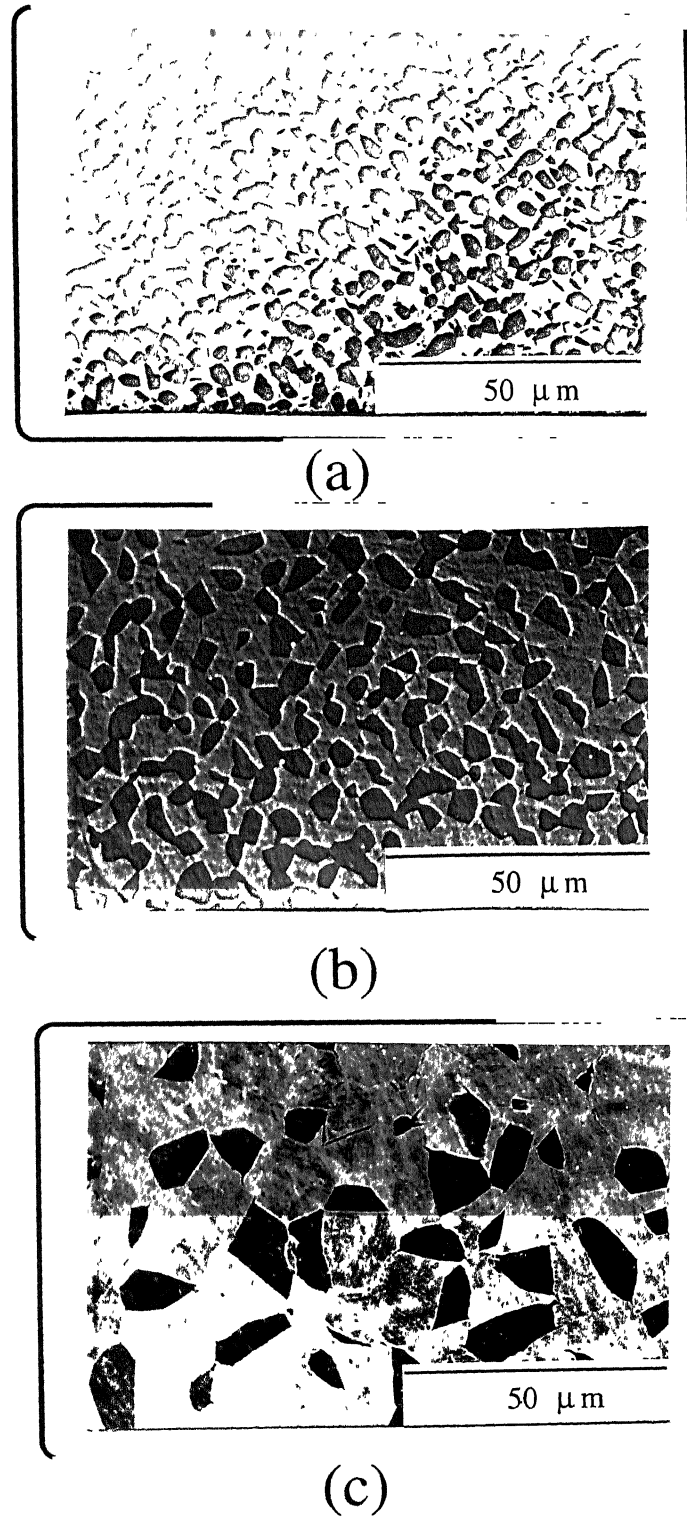


Figure 4.2: Microstructure of Ti-622Si alloy in the conditions: (a) TMT (b) TMT-A1 and (c) TMT-A3

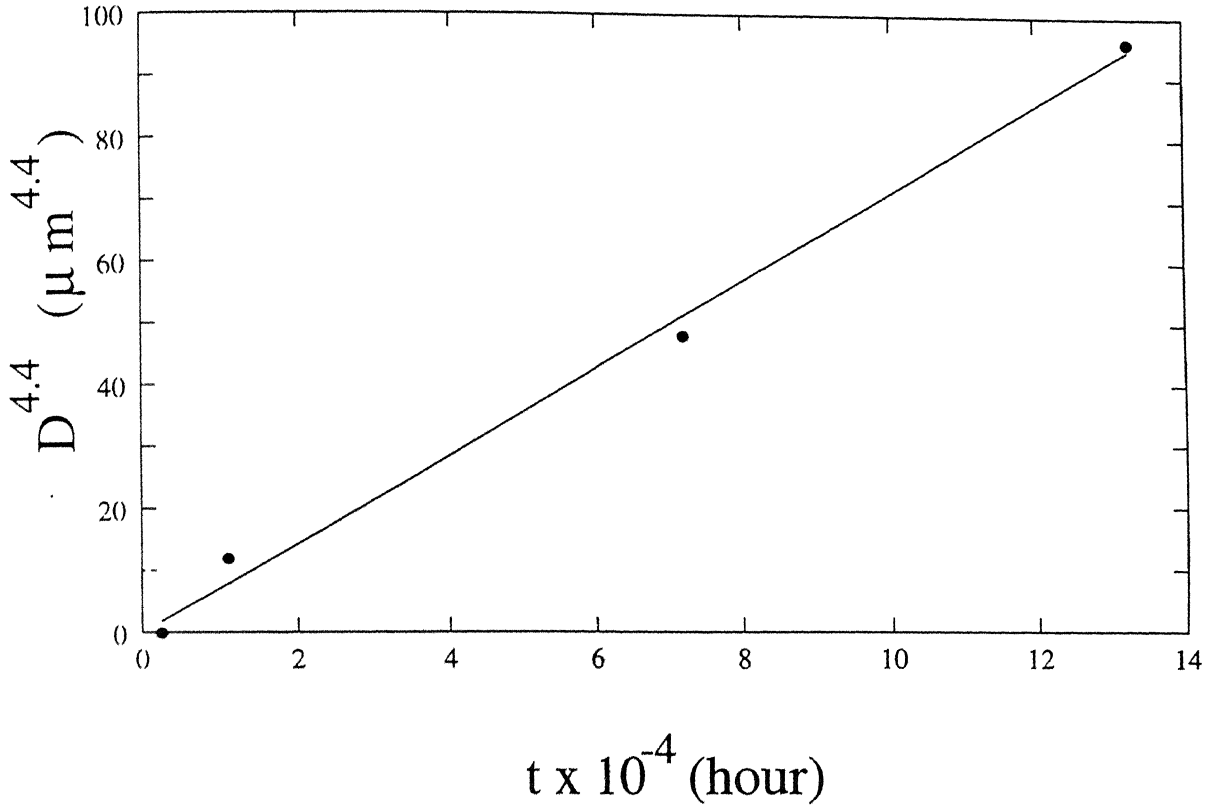


Figure 4.3: Grain growth behaviour of Ti-622Si in TMT condition at 920°C

Figure 4.3 shows the variation of grain-size with time of mill annealing. The grain growth was found to obey a parabolic law of the form

$$d^{n_g} - d_0^{n_g} = K_g t \quad (4.1)$$

where  $d$  is grain-size ( $\mu m$ ),  $d_0$  is initial grain-size ( $\mu m$ ),  $t$  is time(hour), and  $K_g$  ( $\mu m^{n_g} \text{ hour}^{-1}$  and  $n_g$  are constants.  $n_g$  and  $K_g$  were found to be 4.4 and  $1342.0 \mu m^{n_g} \text{ hour}^{-1}$  (or  $0.37 \mu m^{n_g} \text{ s}^{-1}$ ) respectively. The value of  $n_g$  is close to that of 4.8 reported by Ghosh and Hamilton [16] for Ti-6Al-4V at 927°C and that of 3.2 reported by Arieli et al. [15] for the same alloy at 950°C.  $K_g$  for the present alloy, i.e.  $0.37 \mu m^{n_g} \text{ s}^{-1}$  matched well with the value of  $0.24 \mu m^{n_g} \text{ s}^{-1}$  reported by Arieli et al. but was two order of magnitude higher than value of  $10^{-3} \mu m^{n_g} \text{ s}^{-1}$  observed by Ghosh and Hamilton.

#### 4.1.1 The $\beta$ transus temperature of Ti-622Si Alloy

In order to know the phase field of hot deformation of Ti-622Si, the knowledge of its  $\beta$  transus temperature is required. Although the  $\beta$  transus temperature of Ti-622Si alloy is reported in the range of 960°C-980°C by the suppliers, a closer estimate of the same is needed because the deformation behaviour in the two phase field critically depends on the relative proportions of  $\alpha$  and  $\beta$  phases which, in turn vary rapidly with temperature below and close to the  $\beta$  transus temperature. In the present study the  $\beta$  transus was estimated by water quenching the specimens in TMT-A3 condition from different temperatures. Microstructures of specimens water quenched from soaking temperatures of 970°C and 980°C are shown in Figures 4.4(a) and 4.4(c). It can be seen from these micrographs that while the specimen quenched from 970°C showed primary  $\alpha$ , the specimen quenched from 980°C showed no primary  $\alpha$ . It could be thus concluded that the  $\beta$  transus temperature of the alloy lies between 970°C and 980°C. For getting a still closer estimate of the  $\beta$  transus temperature another specimen was therefore water quenched after soaking it for 45 minutes at 975°C. In this specimen  $\alpha$  phase was absent as can be seen from Figure 4.4(b). Thus it can be concluded that the  $\beta$  transus temperature lies in between 970°C and 975°C.

#### 4.1.2 Microstructure of Ti-622Si at Hot Working Temperatures

Figures 4.5(a)-(c) show the microstructures of Ti-622Si alloy with  $\beta$  structure after soaking at 800°C, 900°C and 950°C for 45 minutes, followed by water quenching. The microstructures indicate that the morphology of  $\alpha$  plates remained the same in the two phase field but the amount of  $\alpha$  phase decreased with temperature.

The ( $\alpha+\beta$ ) microstructures with different grain-sizes also underwent changes with temperature. As the temperature was increased from room temperature to 920°C, the

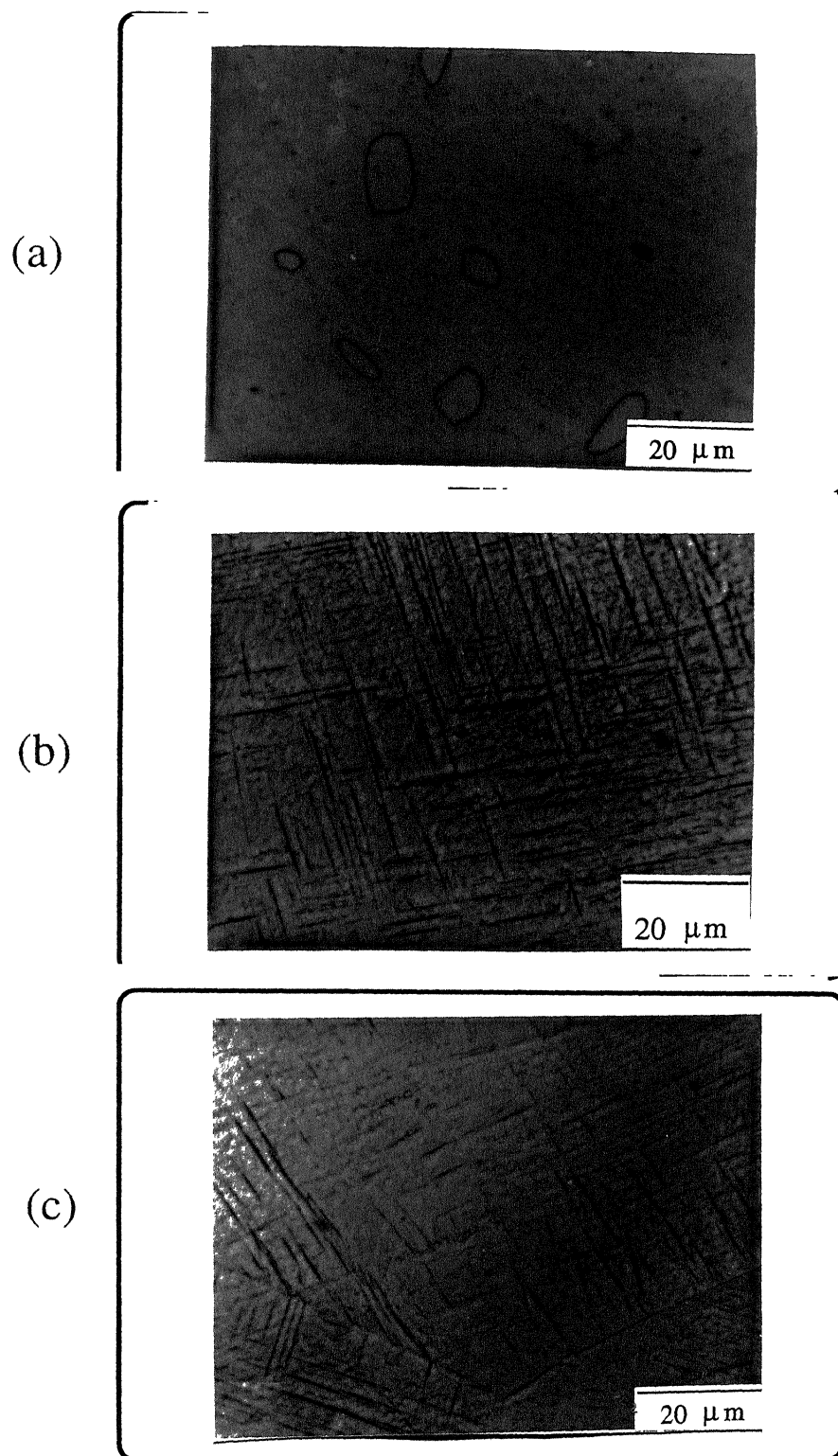


Figure 4.4: Microstructure of Ti-622Si in TMT-A3 condition, soaked at temperatures: (a) 970°C, (b) 975°C and (c) 980°C and subsequently water quenched

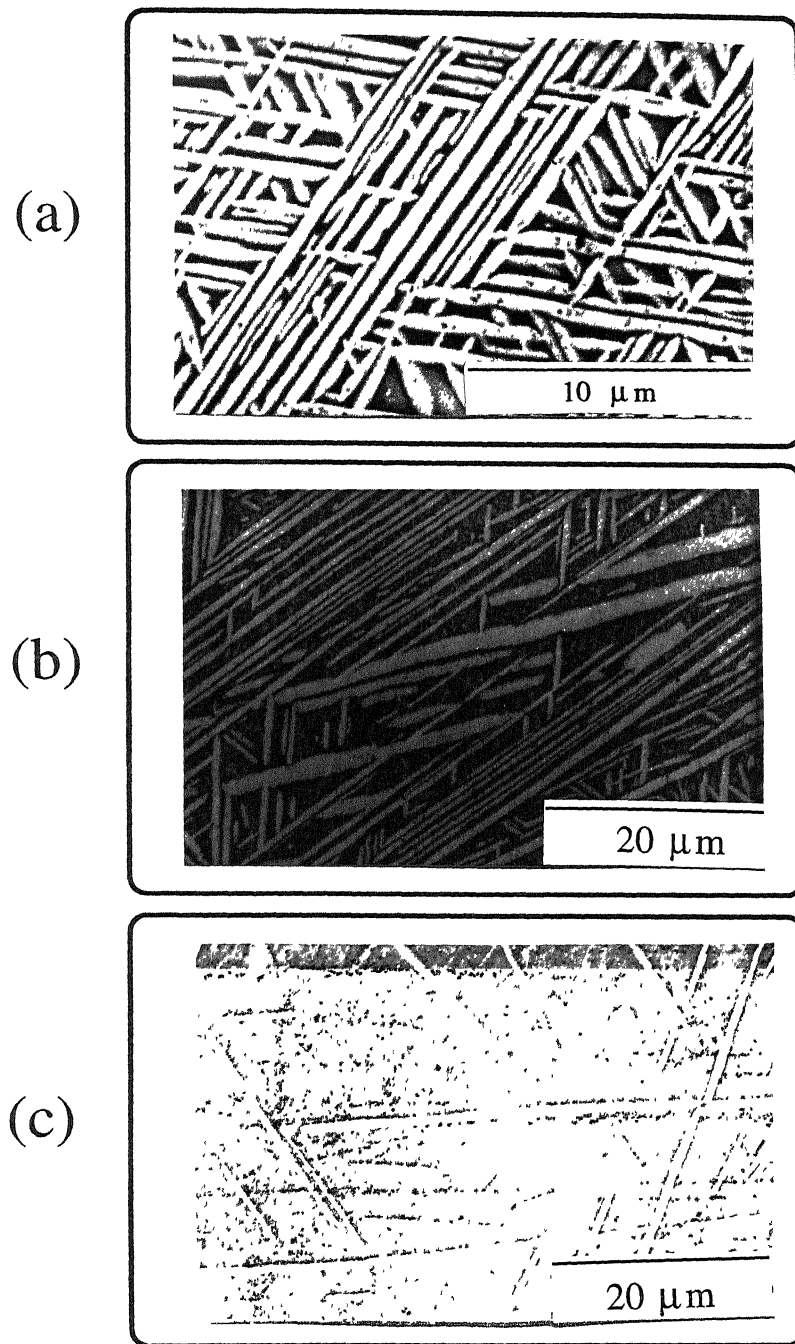


Figure 4.5: Microstructure of Ti-622Si with  $\beta$  structure, soaked at temperatures: (a) 800°C (b) 900°C and (c) 950°C and subsequently water quenched

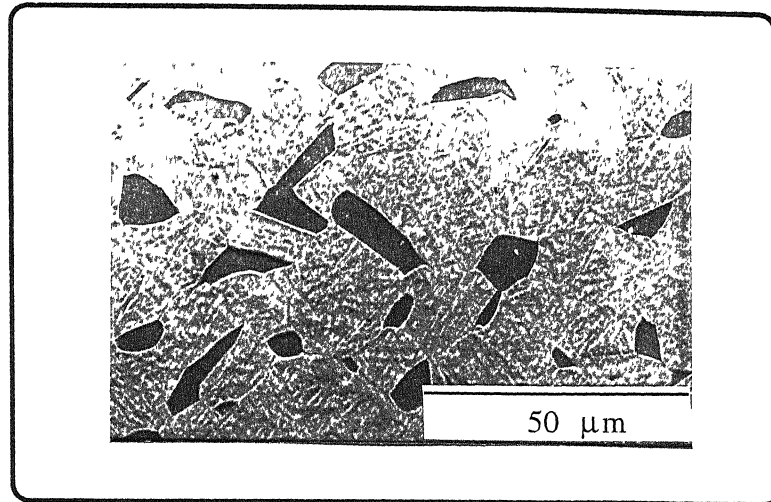


Figure 4.6 Microstructure of Ti-622Si in TMT-A3 condition, soaked at 940°C and subsequently water quenched

content of Widmanstätten  $\alpha$  within the prior  $\beta$  grains decreased and very less change occurred in the fraction of primary  $\alpha$ . Thus the average sizes of primary  $\alpha$  and prior  $\beta$  grains didn't vary significantly in this temperature range. Above 920°C, the quantity of primary  $\alpha$  decreased significantly with temperature. As a result, the average  $\alpha$  grain size was found to increase. This is evident from Figure 4.6 which shows microstructure of Ti-622Si in TMT-A3 condition which was soaked at 940°C and subsequently water quenched. Table 4.1 gives the average grain sizes of  $\alpha$  phase,  $\beta$  phase and of the entire microstructure at different temperatures.

## 4.2 Flow Behaviour of Ti-622Si with $\beta$ Structure

### 4.2.1 Stress-Strain Behaviour

Constant strain rate compression tests of Ti-622Si with  $\beta$  structure were carried out at temperatures varying from 750°C to 1000°C and at strain rates lying between  $10^{-3} \text{ s}^{-1}$  to  $10^2 \text{ s}^{-1}$ . Load displacement curves of the type shown in Figure 4.7 was obtained from



Table 4.1. Grain size of Ti-622Si with  $(\alpha+\beta)$  microstructure

| Specimen | T(°C)   | $d_{\alpha}(\mu\text{m})$ | $d_{\beta}(\mu\text{m})$ | $d_{\alpha\beta}(\mu\text{m})$ | $\sigma_{\alpha-\beta}$ |
|----------|---------|---------------------------|--------------------------|--------------------------------|-------------------------|
| TMT      | 750-920 | 6.6                       | 5.5                      | 5.9                            | 3.1                     |
|          | 940     | 4.9                       | 7.9                      | 6.7                            | 3.8                     |
|          | 950     | 4.1                       | 8.8                      | 7.8                            | 3.2                     |
| TMT-A1   | 750-920 | 8.3                       | 8.3                      | 8.3                            | 4.0                     |
|          | 940     | 5.8                       | 11.4                     | 9.3                            | 4.2                     |
|          | 950     | 5.2                       | 12.4                     | 10.4                           | 3.0                     |
| TMT-A2   | 750-920 | 11.6                      | 13.8                     | 12.7                           | 5.8                     |
|          | 940     | 7.9                       | 18.0                     | 14.2                           | 5.9                     |
|          | 950     | 6.9                       | 19.5                     | 15.2                           | 4.3                     |
| TMT-A3   | 750-920 | 12.6                      | 14.8                     | 14.6                           | 5.6                     |
|          | 940     | 8.9                       | 19.1                     | 16.2                           | 6.1                     |
|          | 950     | 7.6                       | 21.0                     | 16.9                           | 4.5                     |

these tests.

As mentioned in Chapter 3 (Section 3.3.2), true stress and true plastic strain were calculated from the values of load and displacement by eliminating the elastic component of displacement and assuming the compression to be uniform through out the specimen. The variation of true stress with true plastic strain thus obtained is shown in Figures 4.8-4.13 as dashed lines. It is to be recalled that the  $\beta$  transus temperature of the alloy was found to be lying in between  $970^{\circ}\text{C}$  and  $975^{\circ}\text{C}$ . Therefore, while the deformation of the alloy upto  $950^{\circ}\text{C}$  had occurred in the two phase, i.e.  $(\alpha+\beta)$  field, the deformation at  $1000^{\circ}\text{C}$  occurred in the single phase, i.e.  $\beta$  field.

At the deformation temperature of  $1000^{\circ}\text{C}$ , i.e. in the  $\beta$  phase field, steady state type of stress-strain behaviour was observed at strain rates ranging from  $10^{-3} \text{ s}^{-1}$  to  $10 \text{ s}^{-1}$ . In contrast at the strain rate of  $10^2 \text{ s}^{-1}$ , continuous strain hardening was observed in the alloy. Stress oscillations were observed at strain rates of  $10 \text{ s}^{-1}$  and  $10^2 \text{ s}^{-1}$ .

During deformation in the  $(\alpha+\beta)$  phase field, at all strain rates, flow softening was observed, which is typical of materials such as Cu-Zn alloys [51] and  $(\alpha+\beta)$  titanium alloys like Ti-6242Si [33]. The strain corresponding to the peak stress,  $\epsilon_p$ , varied with temperature and strain rate as shown in Figure 4.14. A minima in the values of  $\epsilon_p$  was observed in the strain rate interval  $10^{-2} \text{ s}^{-1}$ - $10^{-1} \text{ s}^{-1}$ . At strain rates of  $10 \text{ s}^{-1}$  and  $10^2 \text{ s}^{-1}$ ,  $\epsilon_p$  was considerably higher as compared to that at lower strain rates. At higher strain rates the softening in the  $(\alpha+\beta)$  phase field was accompanied by stress oscillation.

### 4.2.2 Temperature Correction of the Stress-Strain Curves

Titanium alloys have poor thermal conductivity. Therefore, these alloys are more prone to temperature rise during their hot deformation. The temperature rise results into flow softening and thus the value of flow stress obtained experimentally is less than that cor-

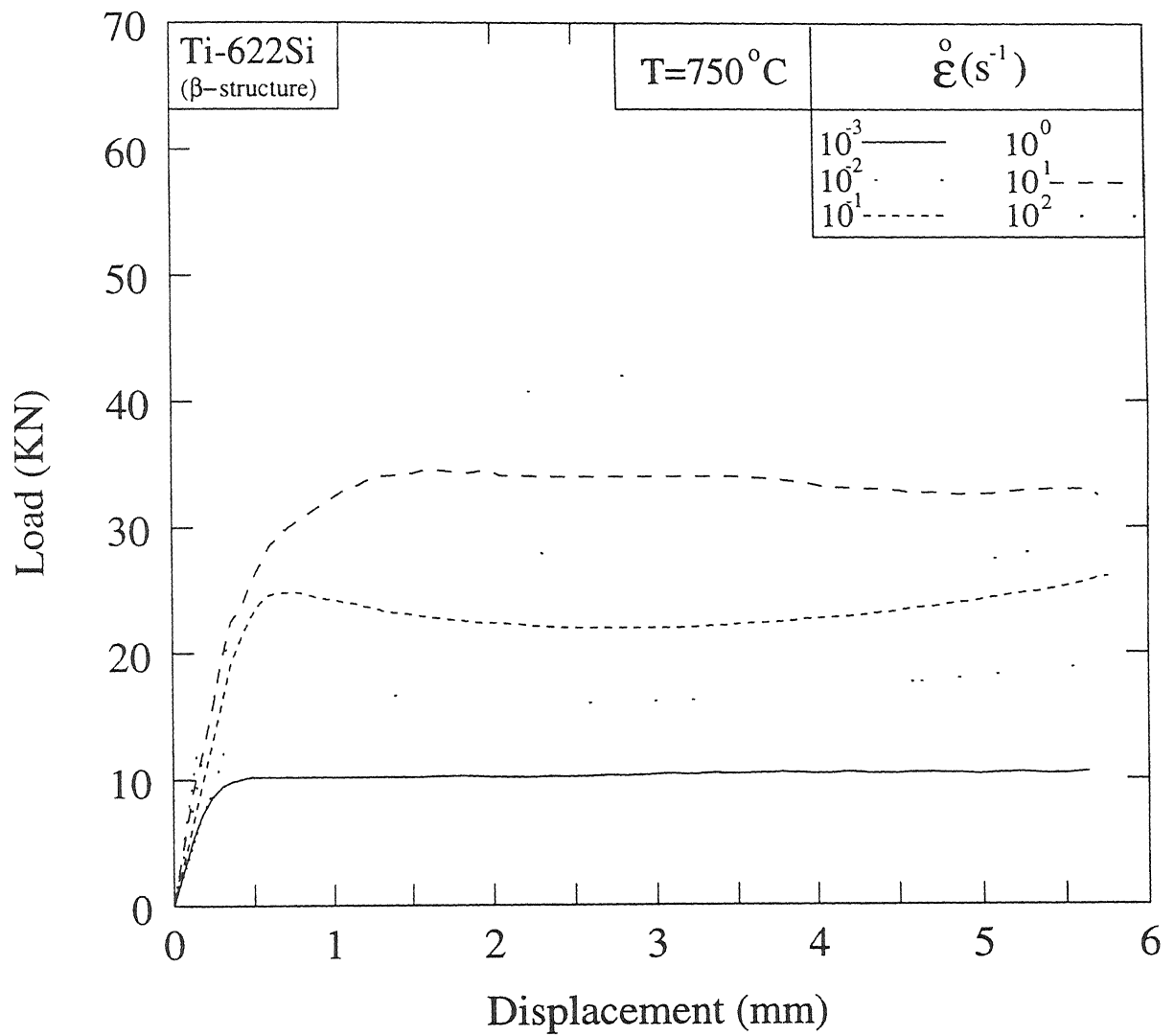


Figure 4.7: Load-displacement curves obtained from compression test of Ti-622Si( $\beta$ ) at  $750^{\circ}\text{C}$

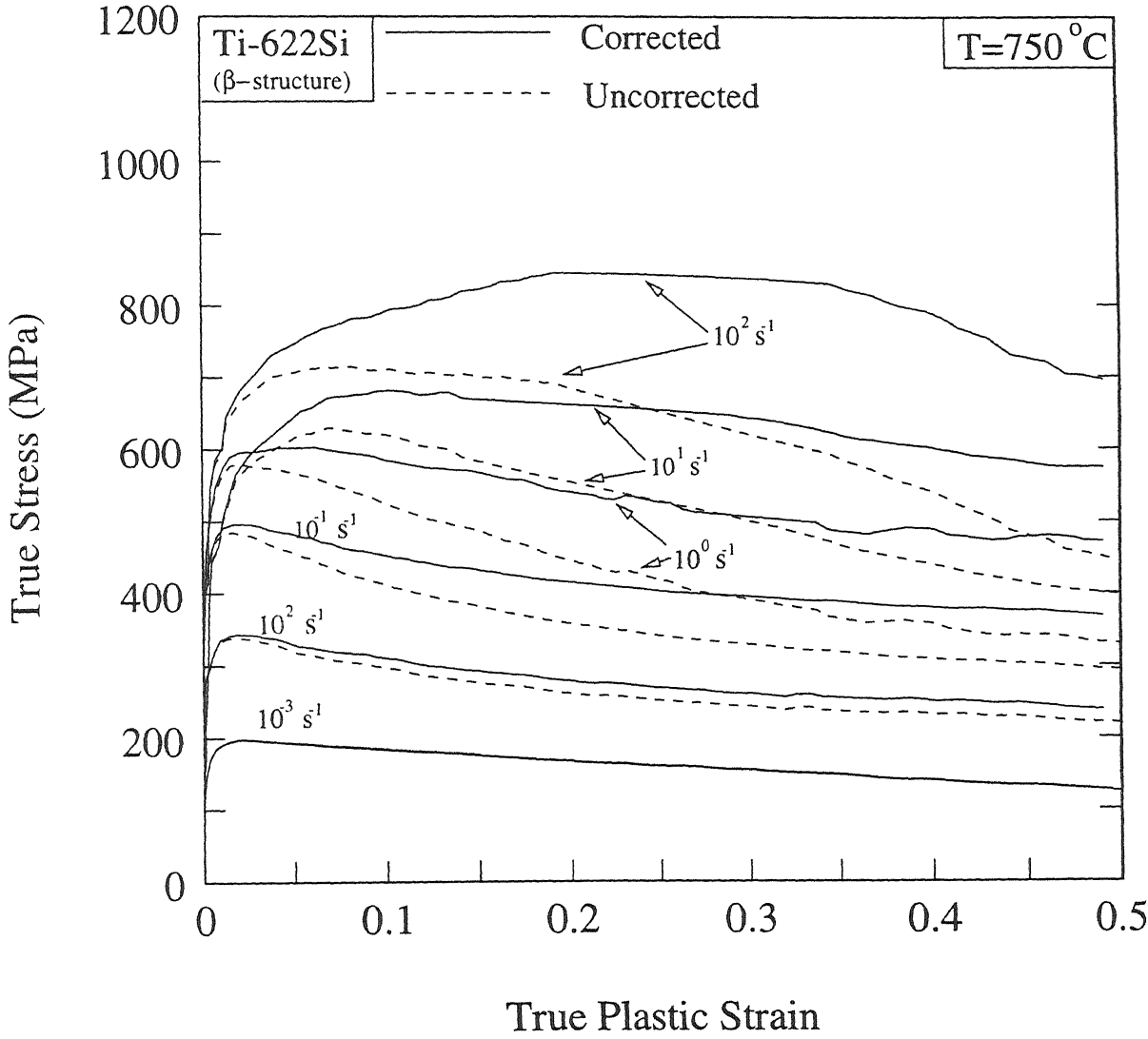


Figure 4.8: True stress versus true plastic strain curves for Ti-622Si( $\beta$ ) at 750°C

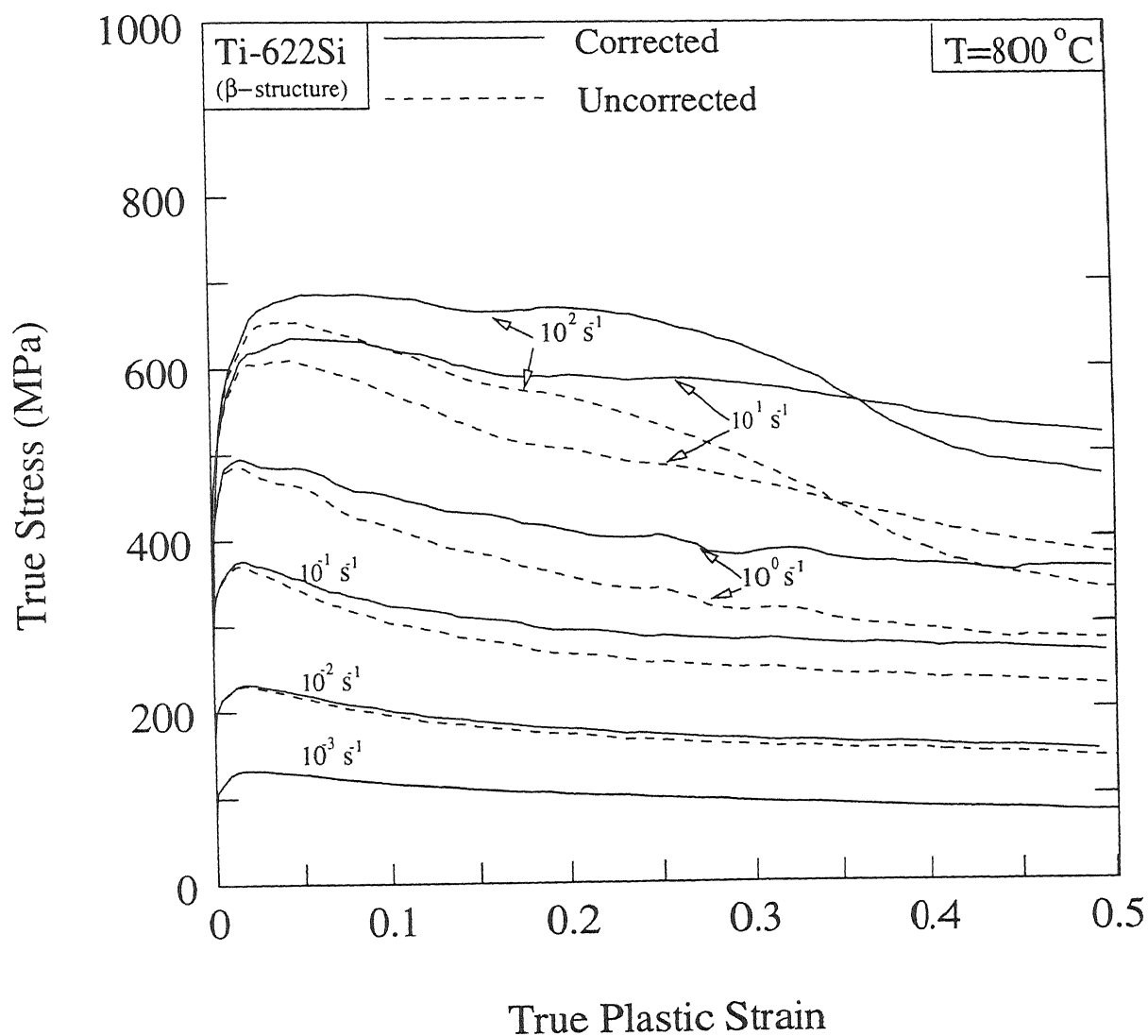


Figure 4.9: True stress versus true plastic strain curves for Ti-622Si( $\beta$ ) at  $800^\circ\text{C}$

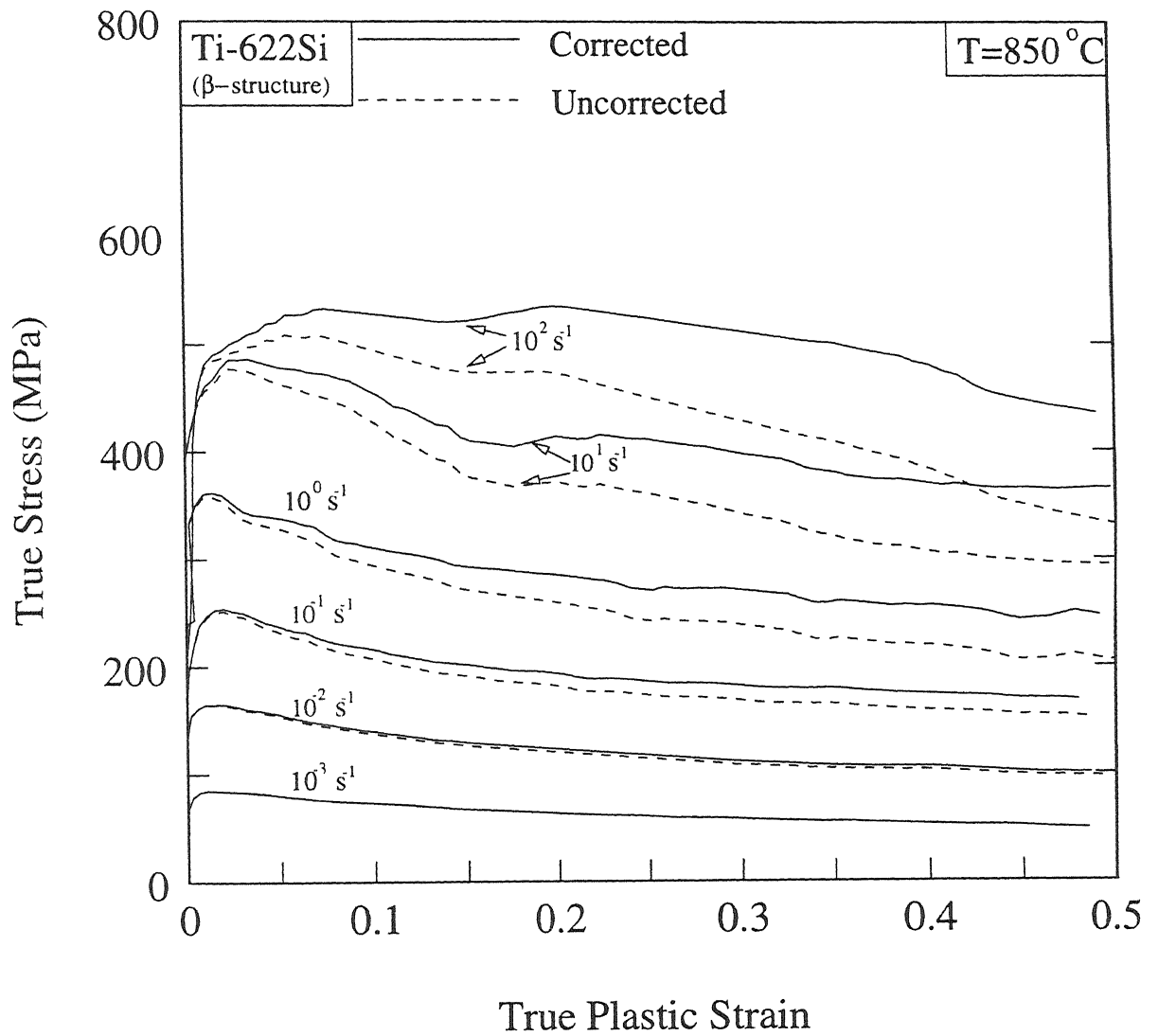


Figure 4.10: True stress versus true plastic strain curves for Ti-622Si( $\beta$ ) at  $850^{\circ}\text{C}$

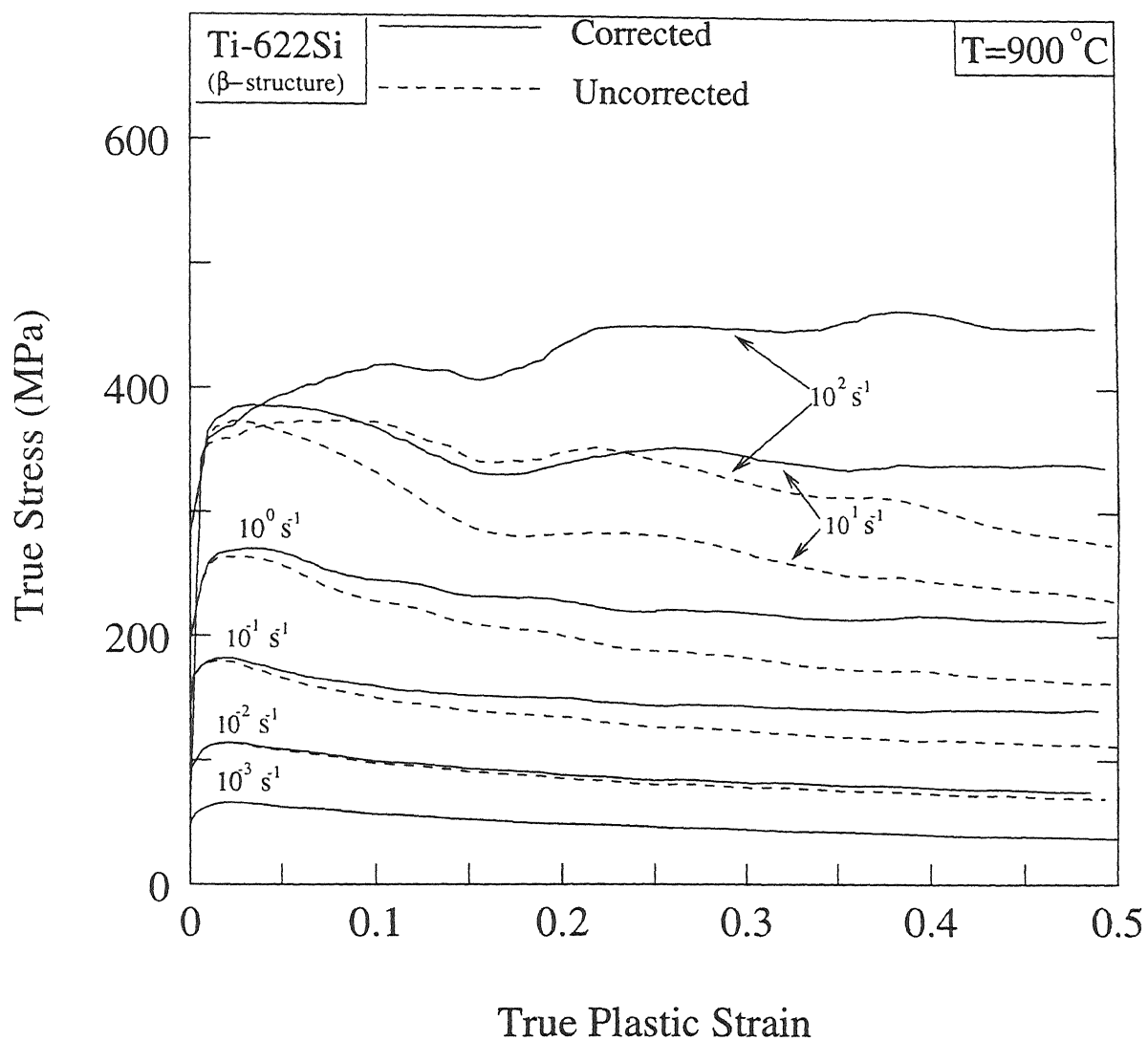


Figure 4.11: True stress versus true plastic strain curves for Ti-622Si( $\beta$ ) at  $900^\circ\text{C}$

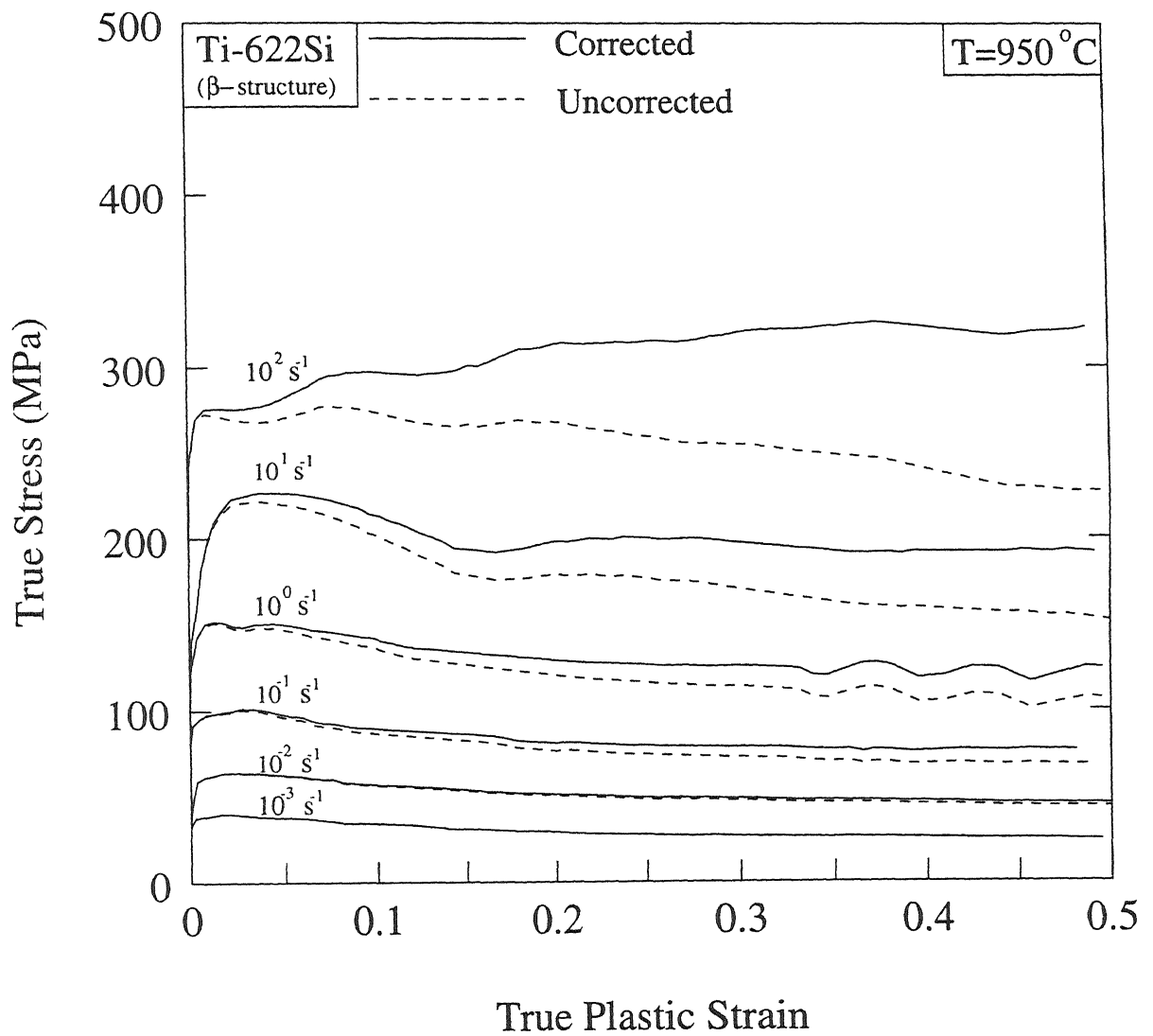


Figure 4.12. True stress versus true plastic strain curves for Ti-622Si( $\beta$ ) at  $950^{\circ}\text{C}$



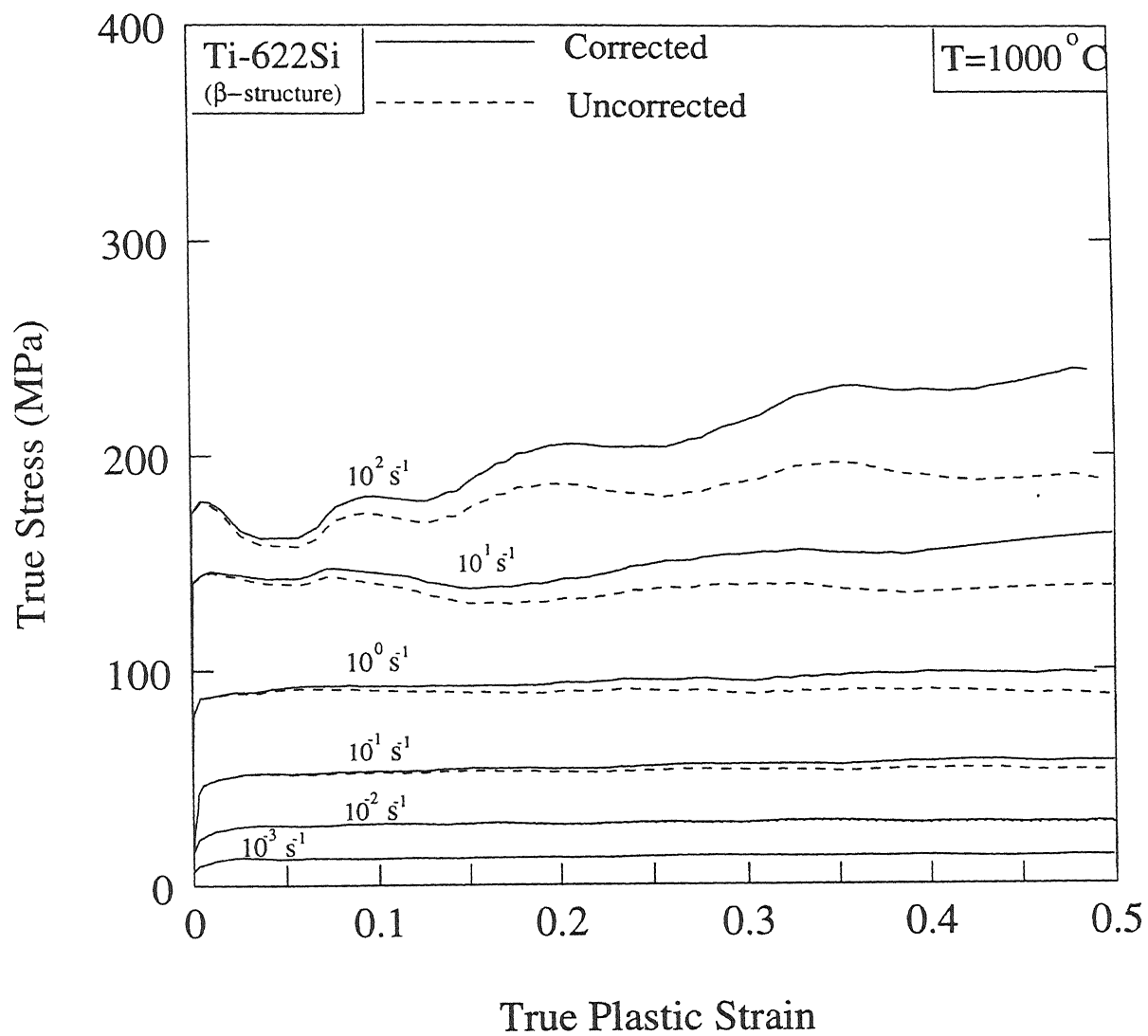


Figure 4.13: True stress versus true plastic strain curves for Ti-622Si( $\beta$ ) at  $1000^{\circ}\text{C}$

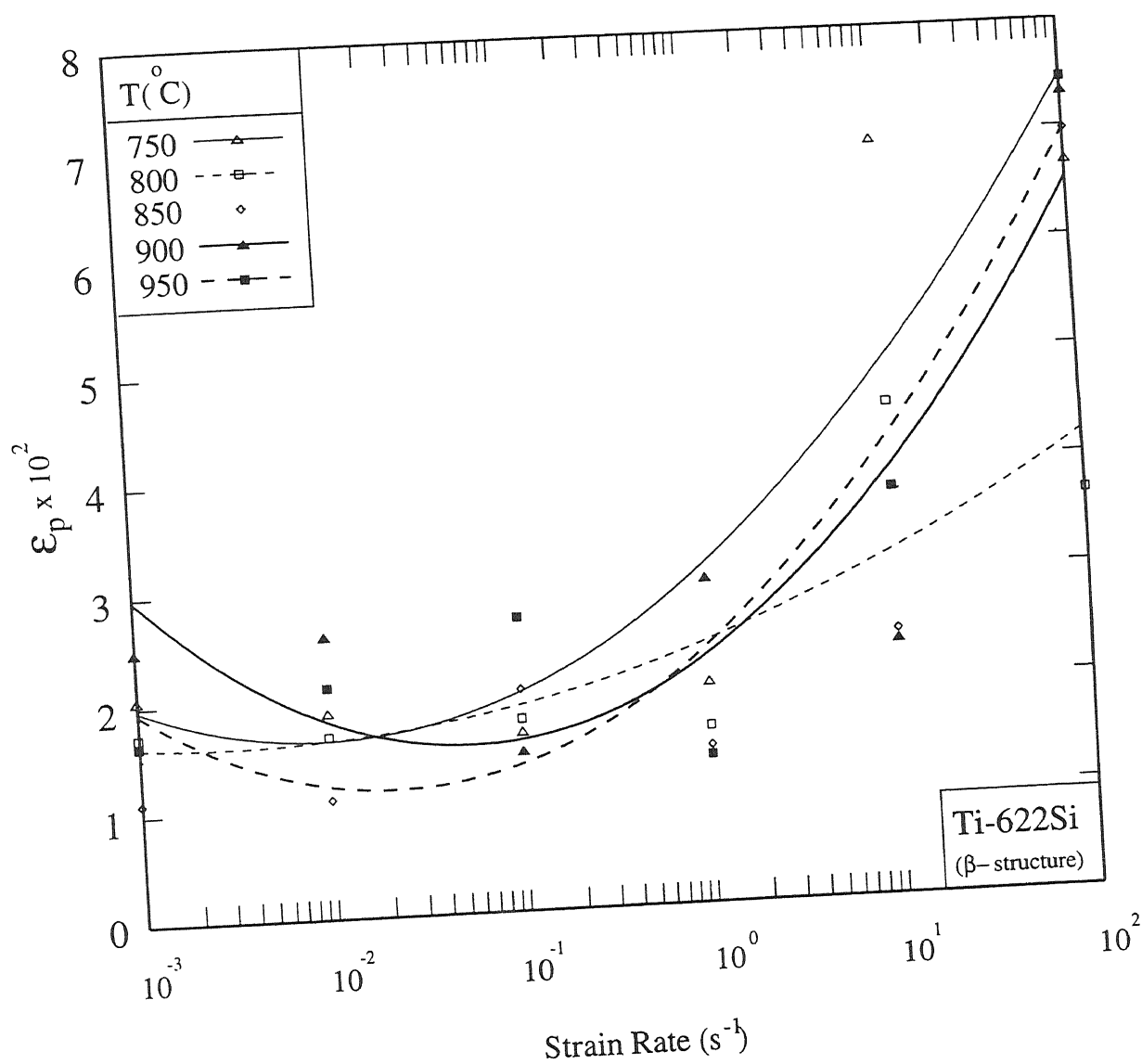


Figure 4.14: Variation of plastic strain corresponding to peak stress with strain rate for Ti-622Si( $\beta$ )

responding to the set deformation temperature. The softening is significant in titanium alloys due to strong temperature dependence of flow stress. Therefore temperature correction, i.e. estimation of stress values corresponding to the set deformation temperatures at all strains, was carried out from the (1) experimental stress-strain curves, (2) variation of specimen temperature with strain and (3) temperature dependency of flow stress. The variation of specimen temperature was found out experimentally (as per the procedure mentioned in section 3.3.1) as well as theoretically.

The experimentally measured variation in temperature rise of the specimens at the end of compression tests,  $\Delta T$ , with strain rate at different deformation temperatures is shown in Figure 4.15. It is clear from the figure that barring few cases, the experimentally measured rise in temperature,  $\Delta T$ , increased with increase in the strain rate at a given deformation temperature and also with decrease in the deformation temperature at a fixed strain rate. However, error in the measurement is expected as the temperature of the specimen changes continuously and thus insufficient time is given to the thermocouple to equilibrate with the specimen. Therefore the temperature of the specimens as a function of strain was estimated by theoretical method for the purpose of temperature correction.

The temperature of specimens as a function of strain can be theoretically estimated from the relationship

$$T(\epsilon) = T_0 + \Delta T(\epsilon) = T_0 + 0.42f \int_0^\epsilon \sigma d\epsilon \quad (4.2)$$

where  $T(\epsilon)$  and  $\Delta T$  are temperature and temperature rise of specimen respectively as a function of strain ( $\epsilon$ ),  $T_0$  is initial temperature of the specimen and  $f$  is the fraction of the heat generated that is retained by the specimen.  $f$  is equal to the ratio of the average temperature rise within the specimen to the average temperature rise calculated by assuming adiabatic condition. Thus  $f$  is given by the relation

$$f = \frac{\rho C A \int_0^\epsilon \Delta T(\epsilon, x) dx}{\rho C A \int_0^\epsilon \Delta T_a(\epsilon, x) dx} \quad (4.3)$$

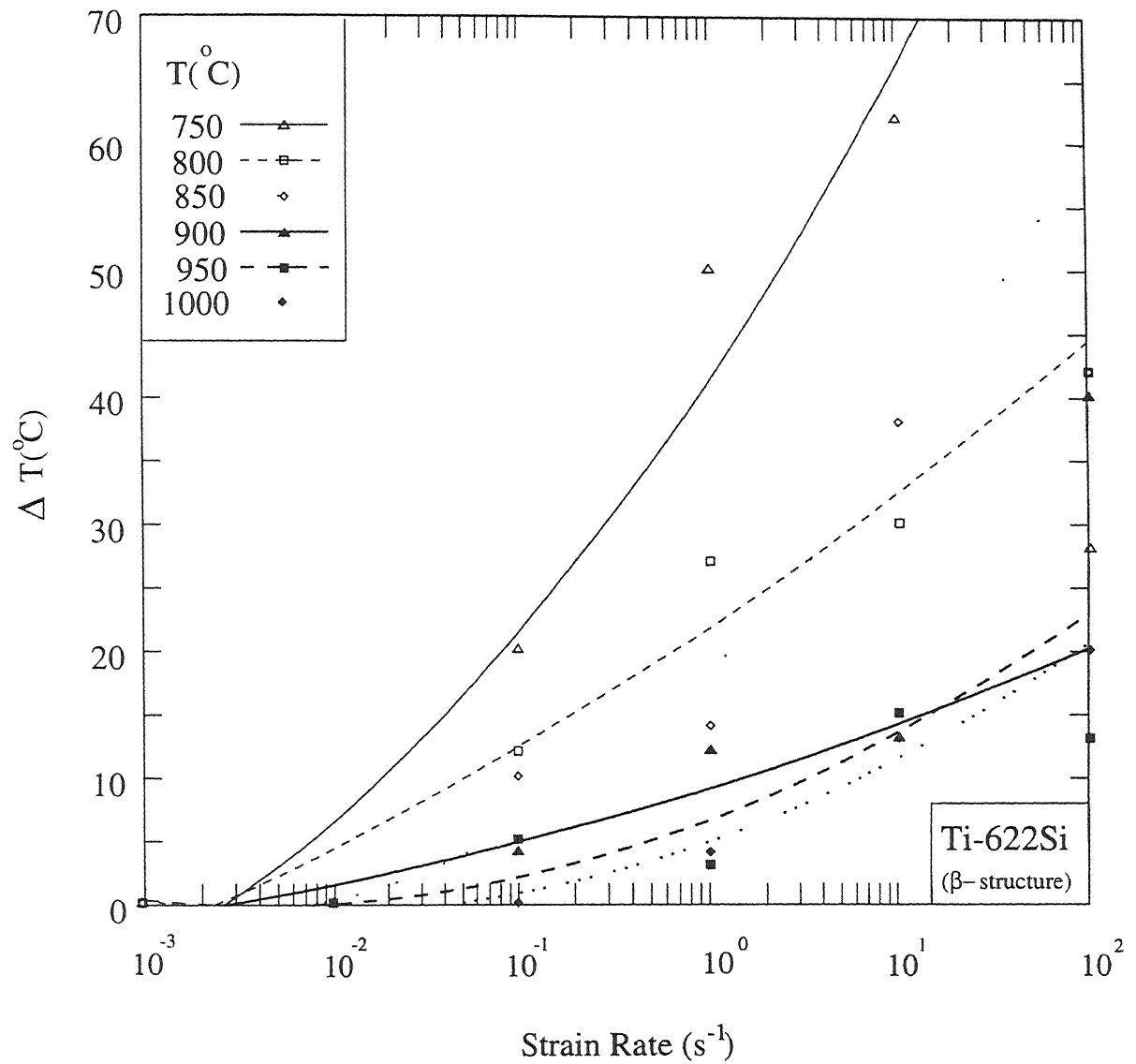


Figure 4.15. Variation of recorded temperature rise at the end of compression test with strain rate for Ti-622Si( $\beta$ )

Table 4.2: Values of  $f$  assumed by Semiatin and Lahoti and Dadras and Thomas

| Strain Rate $s^{-1}$ | Dadras and Thomas | Semiatin and Lahoti |
|----------------------|-------------------|---------------------|
| $10^{-3} s^{-1}$     | 0                 | -                   |
| $10^{-2} s^{-1}$     | 0.25              | -                   |
| $10^{-1} s^{-1}$     | 0.5               | 1.0                 |
| $10^0 s^{-1}$        | -                 | 1.0                 |
| $10^1 s^{-1}$        | -                 | 1.0                 |

or

$$f = \frac{\int_0^l \Delta T(\epsilon, x)}{\int_0^l \Delta T_a(\epsilon, x)} \quad (4.4)$$

where  $\Delta T(\epsilon, x)$  is the temperature rise within the specimen as a function of plastic strain ( $\epsilon$ ) and the distance from one end of the specimen ( $x$ ), and  $\Delta T_a(\epsilon, x)$  is the same, assuming no heat loss from the specimen or adiabatic condition.

Semiatin and Lahoti and Dadras and Thomas [5] chose different values of  $f$  for  $(\alpha+\beta)$  titanium alloys which have been given in Table 4.2. It can be seen that these values differ considerably from each other and thus there appears no unanimity in the criterion for choosing the value of  $f$ . However these differences may cause significant changes in the estimation of  $\Delta T$  and temperature correction.

Therefore in order to get a realistic estimate of  $f$ , the temperature distribution within the specimen and thus the average specimen temperature as a function of strain was done with the help of calculations involving heat transfer analysis. The value of  $f$  was then calculated using relationship 4.4. For calculating the temperature distribution in the specimen during the hot compression, the heat generated within the specimen and that lost to the surrounding during the deformation were considered. Heat generated (plastic work done) within the specimen per unit volume and per unit time is given by

$$P = \sigma \dot{\epsilon} \quad (4.5)$$

where  $H_i$  is the heat generated per unit volume and per unit time. Heat transfer from the specimen to surrounding or the heat loss takes place by (1) conduction through the platens, (2) convection through the ambient atmosphere of furnace and (iii) radiation, the governing equations for which are as follows

(1) heat conduction through the platens is governed by the equation

$$\nabla^2 T + \frac{P}{\kappa} = \frac{1}{\Gamma} \frac{\partial T}{\partial t} \quad (4.6)$$

where  $\Gamma$  is thermal diffusivity given by  $\kappa/\rho C$ , in which  $\kappa$  is the thermal conductivity,  $\rho$  is the density and  $C$  is the specific heat of the alloy.

(2) convection of heat through the ambient atmosphere of the furnace which is governed by the equation

$$q = h(T - T_a) \quad (4.7)$$

where  $q$  is the convective heat flux,  $h$  is the convective heat transfer coefficient,  $T$  is the specimen temperature and  $T_a$  is the ambient temperature

(3) radiative heat transfer to the ambient atmosphere and furnace walls is given by the relationship

$$q = e_m \sigma_s T^4 \quad (4.8)$$

where  $q$  is the convective heat flux,  $e_m$  is the emissivity, and  $\sigma_s$  is the Stefan-Boltzmann constant.

A rough calculation of the rate of heat loss from the specimen by (1) conduction through platens, (2) convection through the ambient atmosphere of the furnace and (3) radiation was carried out using Equations 4.6, 4.7 and 4.8 and realistic values of  $\Gamma$ ,  $h$ ,  $e$  and temperature difference between the specimen and the surrounding. From the calculations it was concluded that the heat transfer from the specimen through the platens was much higher as compared to that occurring by radiation and convection.

Thus in the present calculation the heat loss to the surrounding by convection and radiation was ignored. Since the platens extract heat from the two ends of the specimen the heat flow was assumed to be one-dimensional. Thus heat transfer in the specimen and platen was assumed to be governed by the one-dimensional conduction equation:

$$\frac{\partial^2 T}{\partial x^2} + \frac{P}{\kappa} = \frac{1}{\Gamma} \frac{\partial T}{\partial t} \quad (4.9)$$

Since sufficient time for reaching an uniform temperature was given to the specimens before the compression was carried out, an initial condition of temperature being equal to the set temperature through out the specimen and platen was applied to the Differential Equation 4.9. Essential boundary condition of  $T=T_a$  (ambient temperature) was applied at distance of 12mm away from the specimen ends, within the platens, as shown schematically in Figure 4.16. Finite difference method was used to solve Equation 4.9. The specimen length was discretized into hundred intervals and the same was done for the solution domain in both platens. Time step was varied from  $10^{-5}$ s to 1s depending on the strain rate of deformation. After each time step the length of the specimen and the grid layout within the specimen was updated. The value of  $\kappa, \rho, C$  and  $\Gamma$  for the specimen at different temperatures used in the present study were that of Ti-6Al-4V [1]. The  $\kappa$  and  $C$  at different temperatures for the IN-100 was estimated from the data available for IN-100 and other similar alloys.

The computer program for solving the differential equation by finite difference method is given in Annexure A. Using the computer program, the temperature distribution within the specimen and platen at different periods of time (strain) during hot compression at different set temperatures and strain rates was obtained. From the temperature distribution at different time periods (strain),  $f$  as a function of time (strain) was calculated using Equation 4.4.

It was found that  $f$  varied with plastic strain and strain rate. The variation of  $f$  with the strain at different strain rates is shown in Figure 4.17. On the other hand the deformation temperature and flow stress had no effect on the  $f$ . Variation in rise

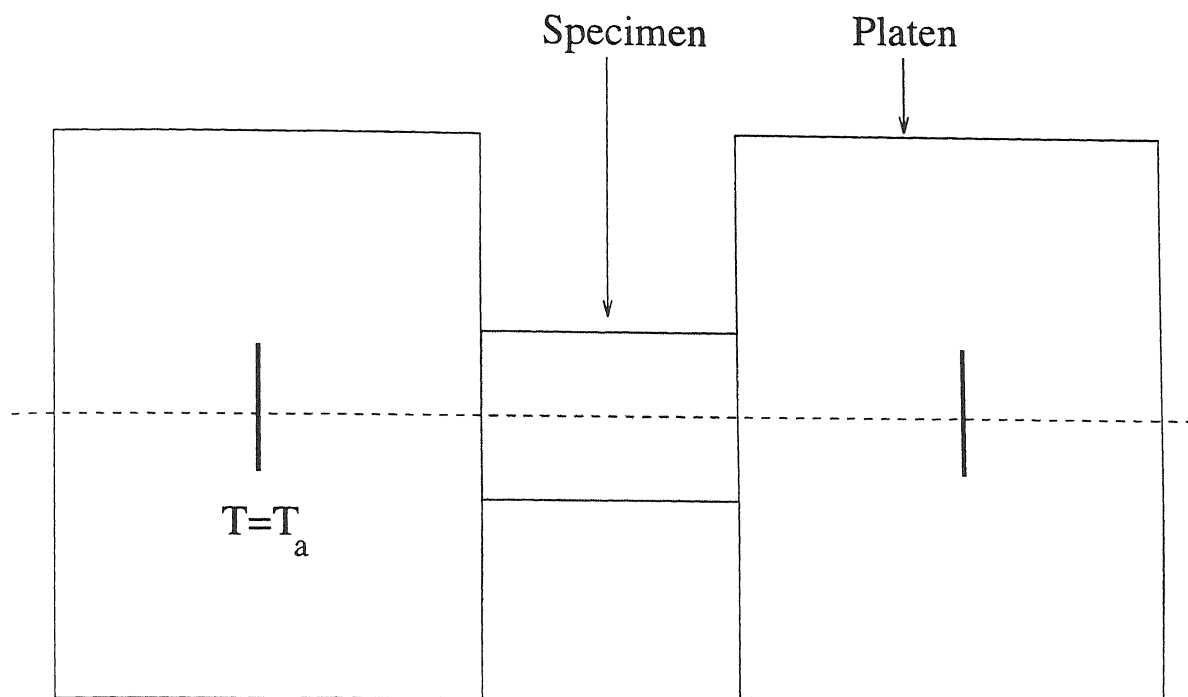


Figure 4.16. Schematic representation of boundary condition applied to equation 4.9

in temperature of specimen after a strain of 0.5 at different deformation temperature and strain rates is shown in Table 4.3 along with experimentally measured  $\Delta T$ . It can be seen that theoretically calculated  $\Delta T$  is generally much higher than  $\Delta T$  obtained experimentally.

The temperature rise accompanying the hot deformation results into flow softening and thus the value of flow stress obtained experimentally is less than that corresponding to the set deformation temperature. However, as mentioned previously the stress values and thus the stress-strain curves corresponding to the set deformation temperatures (temperature corrected stress-strain curves) can be obtained from the experimental stress-strain curves from the knowledge of (1) the temperature of specimen as a function of strain and (2) temperature dependency of flow stress. The values of  $f$  as a function of strain thus known, the temperature of specimen as a function of strain can be obtained using Equation 4.2. Thus in order to carry out the temperature correction the temperature dependency of flow stress was obtained from the experimental stress-strain



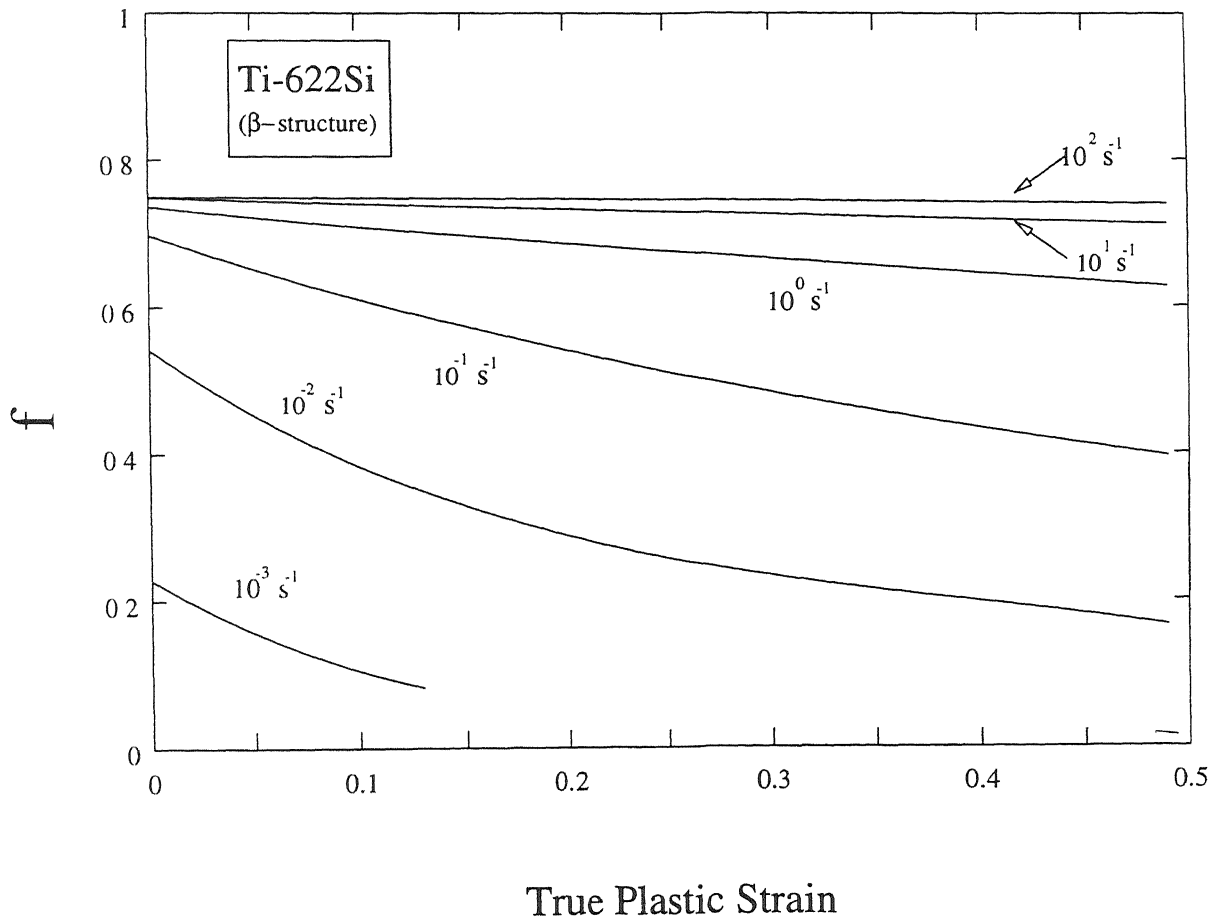


Figure 4.17: Variation of  $f$  with plastic strain for Ti-622Si( $\beta$ )

Table 4.3: Theoretically estimated (upper) and experimentally measured (lower) temperature rise

|                          | 750 °C | 800 °C | 850 °C | 900 °C | 950 °C | 1000 °C |
|--------------------------|--------|--------|--------|--------|--------|---------|
| $10^2 \text{ s}^{-1}$    | 96.0   | 78.0   | 67.6   | 51.0   | 39.0   | 28.0    |
|                          | 28.0   | 42.0   | 42.0   | 40.0   | 13.0   | 20.0    |
| $10^1 \text{ s}^{-1}$    | 77.0   | 73.0   | 54.6   | 42.0   | 26.0   | 20.8    |
|                          | 62.0   | 30.0   | 38.0   | 13.0   | 15.0   | 13.0    |
| $10^0 \text{ s}^{-1}$    | 57.0   | 46.0   | 34.0   | 26.0   | 16.0   | 11.0    |
|                          | 50.0   | 27.0   | 14.0   | 12.0   | 3.0    | 4.0     |
| $10^{-1} \text{ s}^{-1}$ | 29.0   | 22.0   | 15.0   | 11.0   | 6.0    | 4.4     |
|                          | 20.0   | 12.0   | 0.0    | 4.0    | 5.0    | 0.0     |
| $10^{-2} \text{ s}^{-1}$ | 9.0    | 6.0    | 4.2    | 2.9    | 1.8    | 0.9     |
|                          | 0.0    | 0.0    | 0.0    | 0.0    | 0.0    | 0.0     |
| $10^{-3} \text{ s}^{-1}$ | 0.5    | 0.3    | 0.2    | 0.17   | 0.1    | 0.05    |
|                          | 0.0    | 0.0    | 0.0    | 0.0    | 0.0    | 0.0     |

curve. The values of flow stress at low strain level of 0.1 were considered for obtaining the temperature dependency.

Figure 4.18 shows the temperature dependencies of true stress corresponding to strain level of 0.1, at different strain rates. In the figure, the true stresses are plotted in logarithmic scale with respect to  $1/T \times 10^4 \text{ K}^{-1}$ . Two regimes of temperature, i.e.  $750^\circ\text{C} < T < 900^\circ\text{C}$ , and  $T > 900^\circ\text{C}$  in which the variation of true stress, in logarithmic scale, with  $1/T (\times 10^4)$  is linear at all strain rates was identified and using regression analysis straight lines were fitted through the data points in both the regimes. The variation in the two regimes can be expressed by the equation

$$\log \sigma = K_1 + \frac{K_2}{T} \quad (4.10)$$

where  $K_1$  is the intercept and  $K_2$  is  $10^4$  times the slope of the fitted line.  $K_2$  is higher in regime I than in regime II. Similar trend has been reported by Dadras and Thomas for Ti-6242Si alloy with  $\beta$  structure.

The corrected value of stress,  $\sigma_c$ , corresponds to the set deformation temperature  $T_o$  and the experimentally obtained value of stress,  $\sigma$  corresponds to the raised temperature,  $T_o + \Delta T$ . Thus, from Equation 4.10 we obtain

$$\log \sigma_c = K_1 + \frac{K_2}{T_o} \quad (4.11)$$

and

$$\log \sigma = K_1 + \frac{K_2}{T_o + \Delta T} \quad (4.12)$$

Combining Equations 4.11 and 4.12 we get

$$\log \sigma_c - \log \sigma = K_2 \left[ \frac{1}{T_o} - \frac{1}{T_o + \Delta T} \right] \quad (4.13)$$

The exponential form of Equation 4.13 is

$$\sigma_c = e^{[\log \sigma + \left( \frac{1}{T_o} - \frac{1}{T_o + \Delta T} \right) K_2]} \quad (4.14)$$

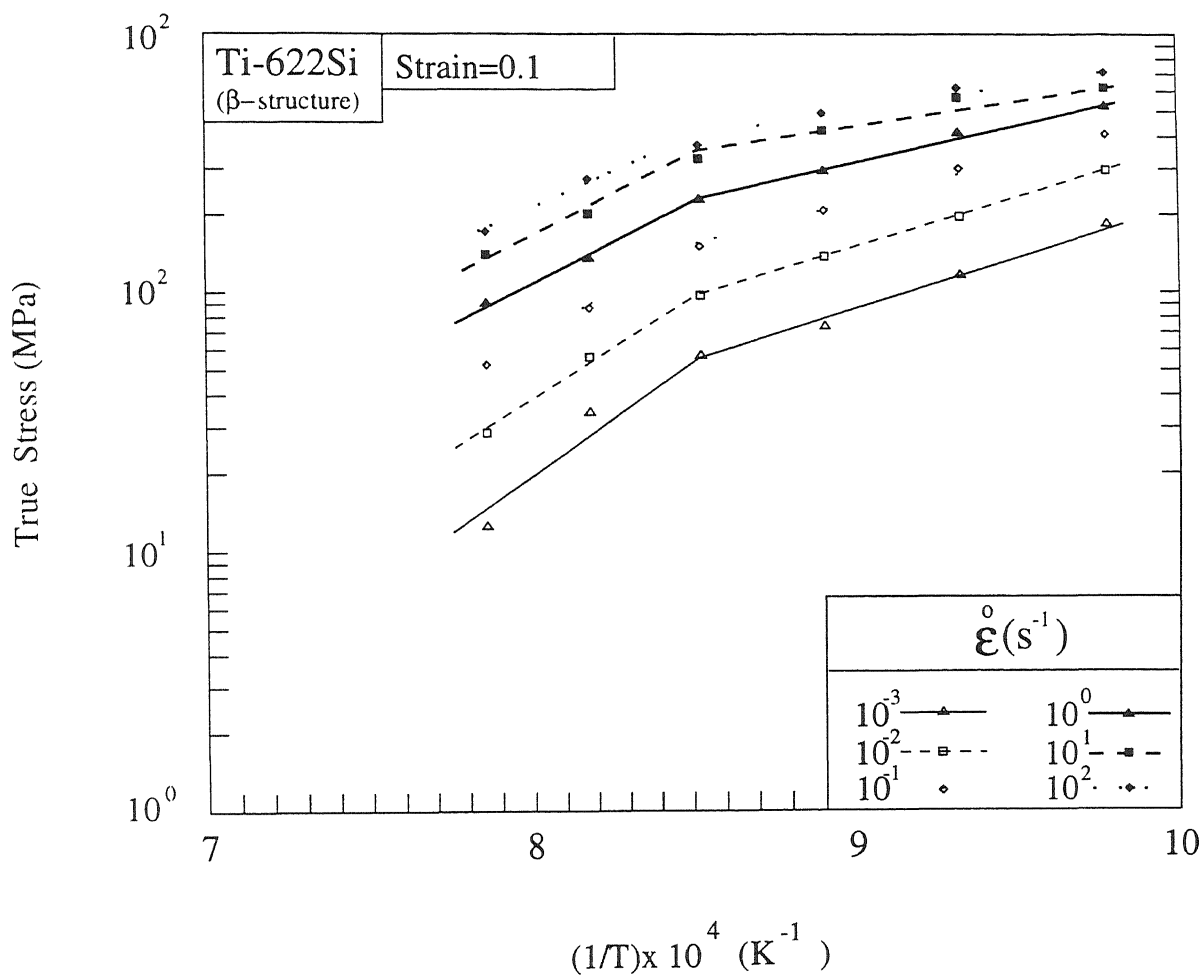


Figure 4.18: Temperature dependency of true stress corresponding to strain level of 0.1 for Ti-622Si( $\beta$ )

where  $\sigma_c$  denotes the corrected stress value. For temperature correction of the stress-strain curves in the temperature interval 750°C -850°C,  $K_2$  value corresponding to regime I was used and that of regime II was used for correcting the stress-strain curves at higher temperatures.

### 4.2.3 Temperature Corrected Stress-Strain Curves

The experimentally obtained as well as temperature corrected stress-strain curves (solid lines) are shown in Figure 4.8- 4.13. The effect of temperature correction on the stress-strain behaviour was found to vary with the strain, temperature and strain rate of deformation. The difference between experimentally obtained and temperature corrected flow stress, i.e.  $(\sigma - \sigma_c)$  was found to increase with strain at all temperatures and strain rates, as a result of increase in the specimen temperature with strain. It is clear from the Figure 4.8-4.13 that, like  $\Delta T$ , at strain rates of  $10^{-3} \text{ s}^{-1}$   $(\sigma - \sigma_c)$  tended to be zero and increased with the strain rate. It can be also seen from this figure that the value of  $(\sigma - \sigma_c)$  at a given strain rate increased with decrease in the set deformation temperature as per the variation in  $\Delta T$ . While flow softening during deformation in the  $(\alpha + \beta)$  phase field was still observed at lower strain rates, though lesser in extent, strain hardening was observed at higher strain rates. In contrast, in the  $\beta$  phase field, at higher strain rates, the temperature corrected flow curves exhibited strain hardening.

### 4.2.4 Stress-Strain Rate Behaviour and Strain Rate Sensitivity

Data between true stress and strain rate corresponding to set deformation temperature and strains of  $\epsilon_p$ , 0.1, 0.3 and 0.5 were obtained from the experimental as well as temperature corrected stress-strain curves. True peak stress,  $\sigma_p$ , and true stress at the strain of 0.3 as a function of strain rate at various deformation temperatures are

shown in Figures 4.19- 4.20 respectively. Similar behaviour was observed at strains of 0.3 and 0.5. Data obtained from the corrected flow curves for 0.3 strain is shown in Figure 4.21.

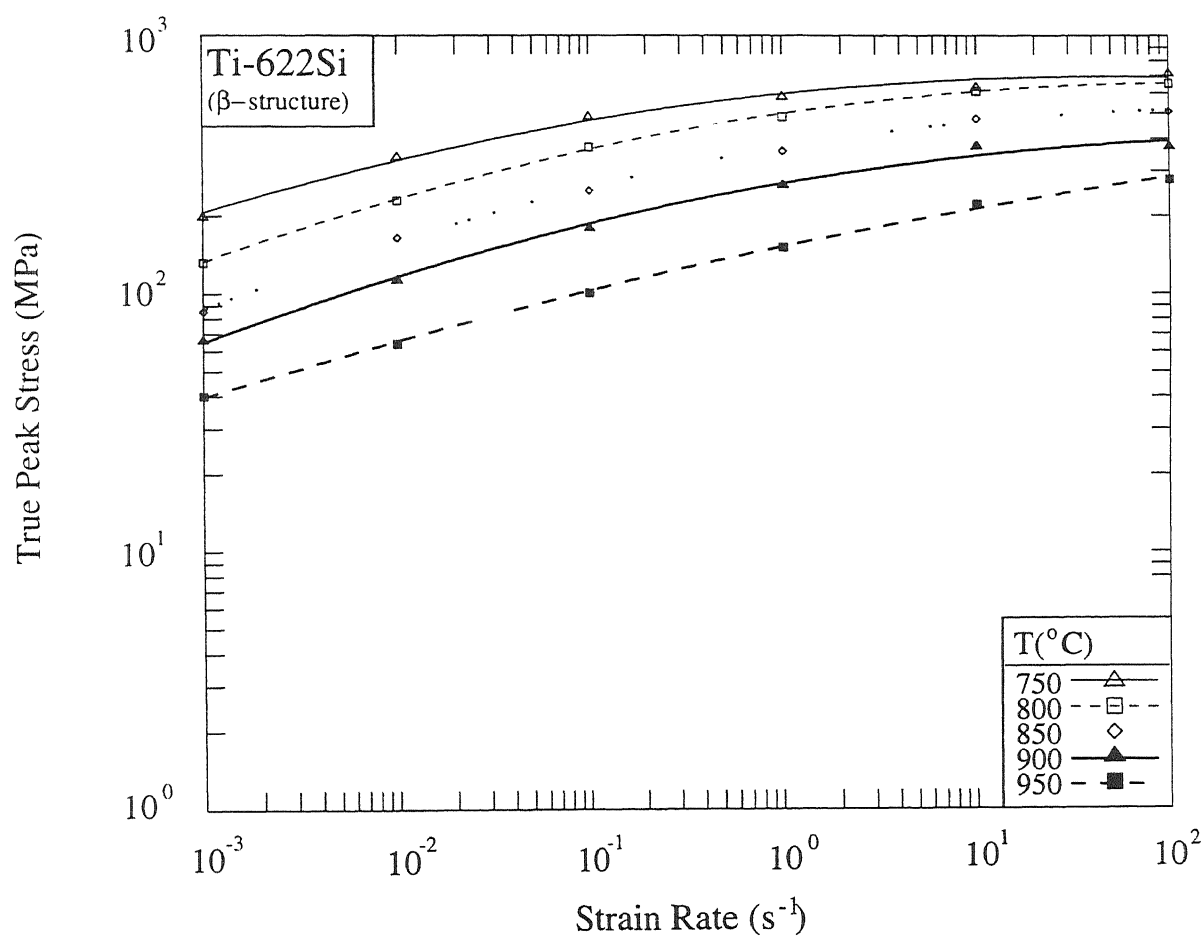
The strain rate sensitivity,  $m$ , corresponding to strains of  $\epsilon_p$ , 0.1, 0.3 and 0.5, of Ti-622Si alloy was calculated at different temperatures and strain rates from the slope of stress-strain curves. The variation of  $m$ , corresponding to strains of  $\epsilon_p$  and 0.3, with strain rate at different temperatures thus obtained is shown in Figures 4.22- 4.23. The  $m$  values of the  $\beta$  microstructure in the  $(\alpha+\beta)$  varied between 0.2 and 0.3 at the lowest strain rate of  $10^{-3} \text{ s}^{-1}$  and decreased with strain rate. At the highest strain rate, i.e.  $10^2 \text{ s}^{-1}$ , it ranged from 0.01 to 0.11. Similar trend has been reported by Dadras and Thomas [5]. The strain rate sensitivity in the  $\beta$  phase field was found to be higher than that in the two phase field at low strain rates. At  $10^{-3} \text{ s}^{-1}$  it was close to 0.4 and decreased with strain rate, similar to what was observed in the  $(\alpha+\beta)$  phase field. The values of  $m$  had little dependence on temperature and strain rate.

#### 4.2.5 Phenomenological Description of Flow Behaviour at High Temperature

In the past there has been various attempts to describe the flow behaviour during the hot working, over a wide range of temperature and strain rate using a single mathematical expression that relates the flow stress with the temperature and strain rate. In order to do so various expressions relating the flow stress with the temperature compensated strain rate or the Zenner-Holloman parameter,  $Z$ , given by

$$Z = \dot{\epsilon} e^{(Q/RT)} \quad (4.15)$$

where  $Q$  is the activation energy and  $R$  is the universal gas constant, have been proposed [7]. In the present study also, the variation of stress was described as a function

Figure 4.19: Variation of peak true stress with strain rate for Ti-622Si( $\beta$ )

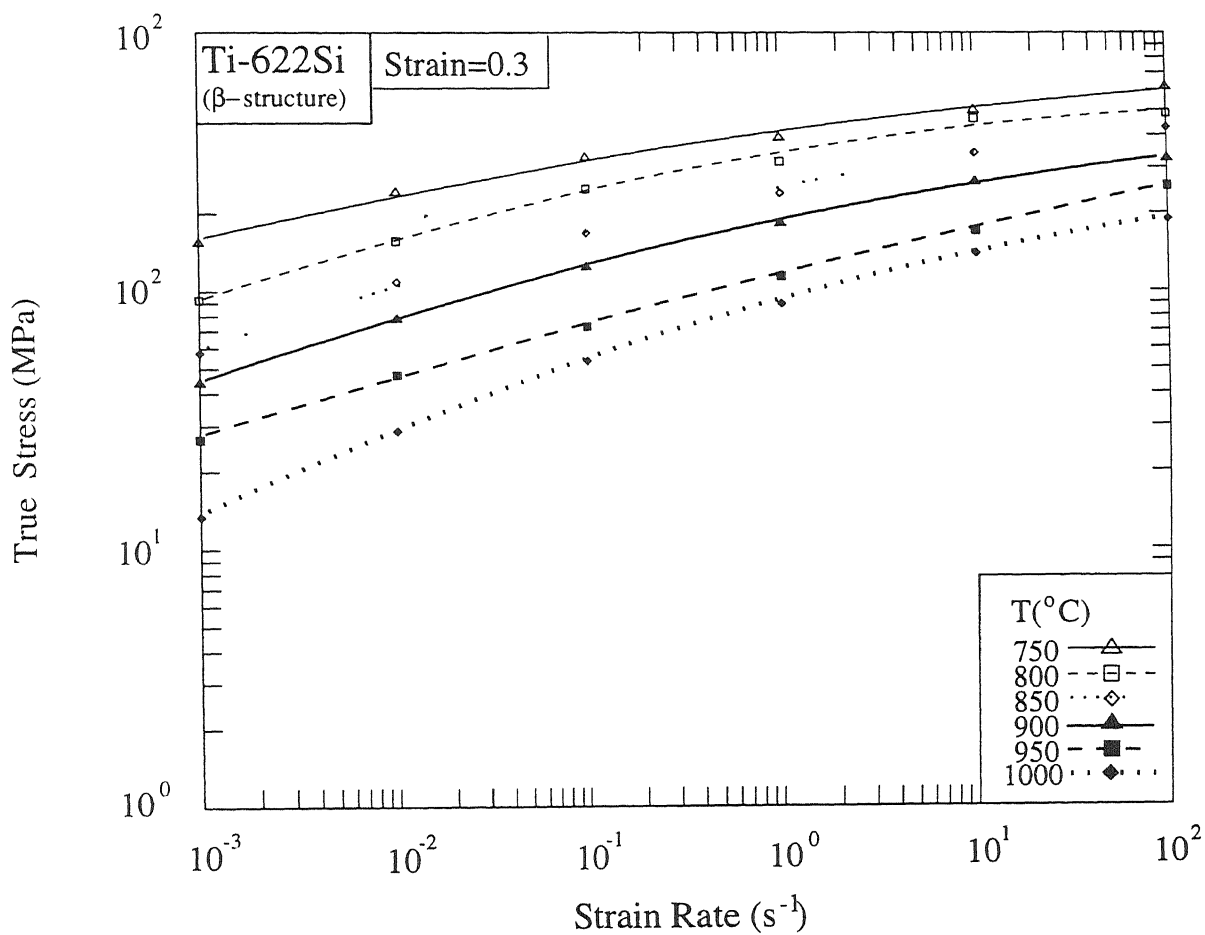


Figure 4.20. Variation of true stress with strain rate for Ti-622Si( $\beta$ ) at strain of 0.1



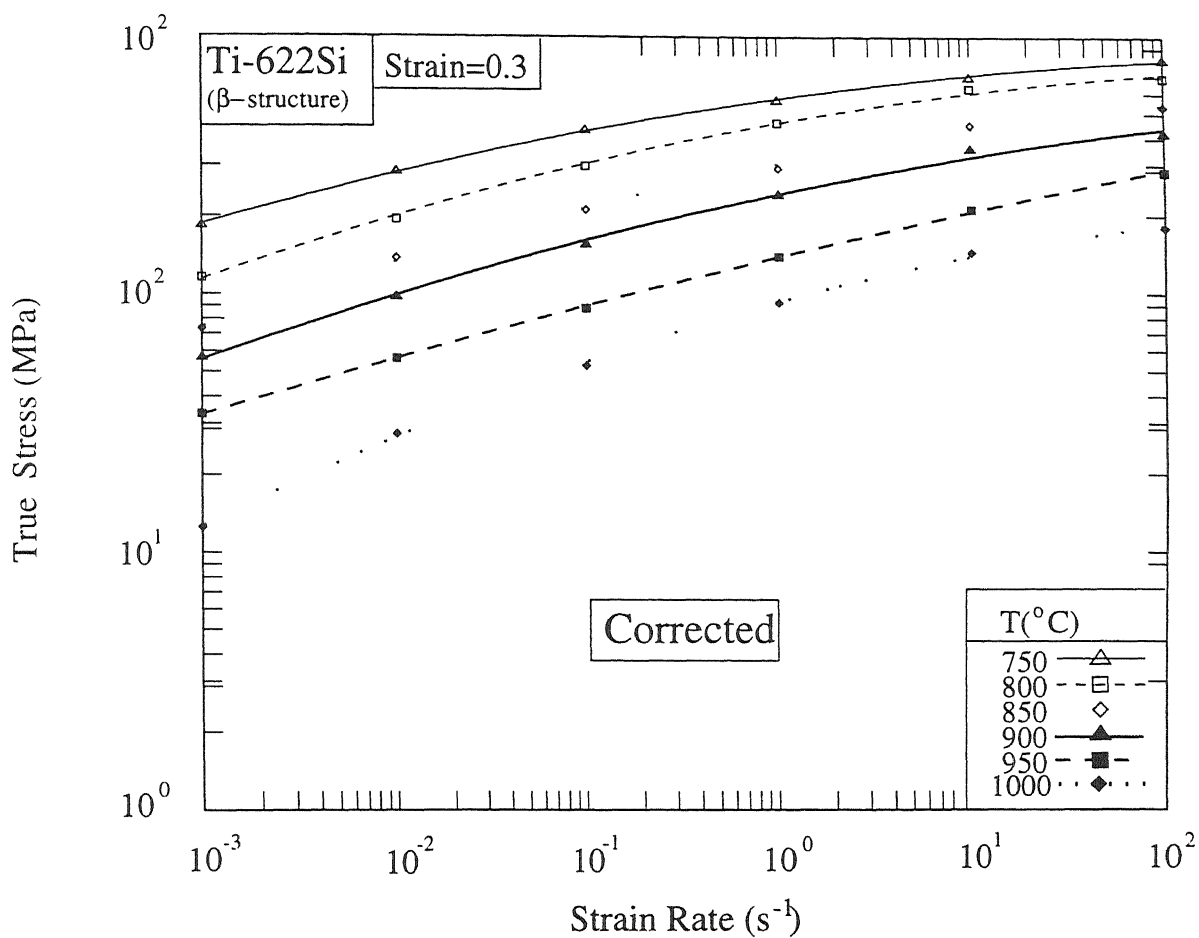


Figure 4.21: Variation of temperature corrected true stress with strain rate for Ti-622Si( $\beta$ ) at strain of 0.3

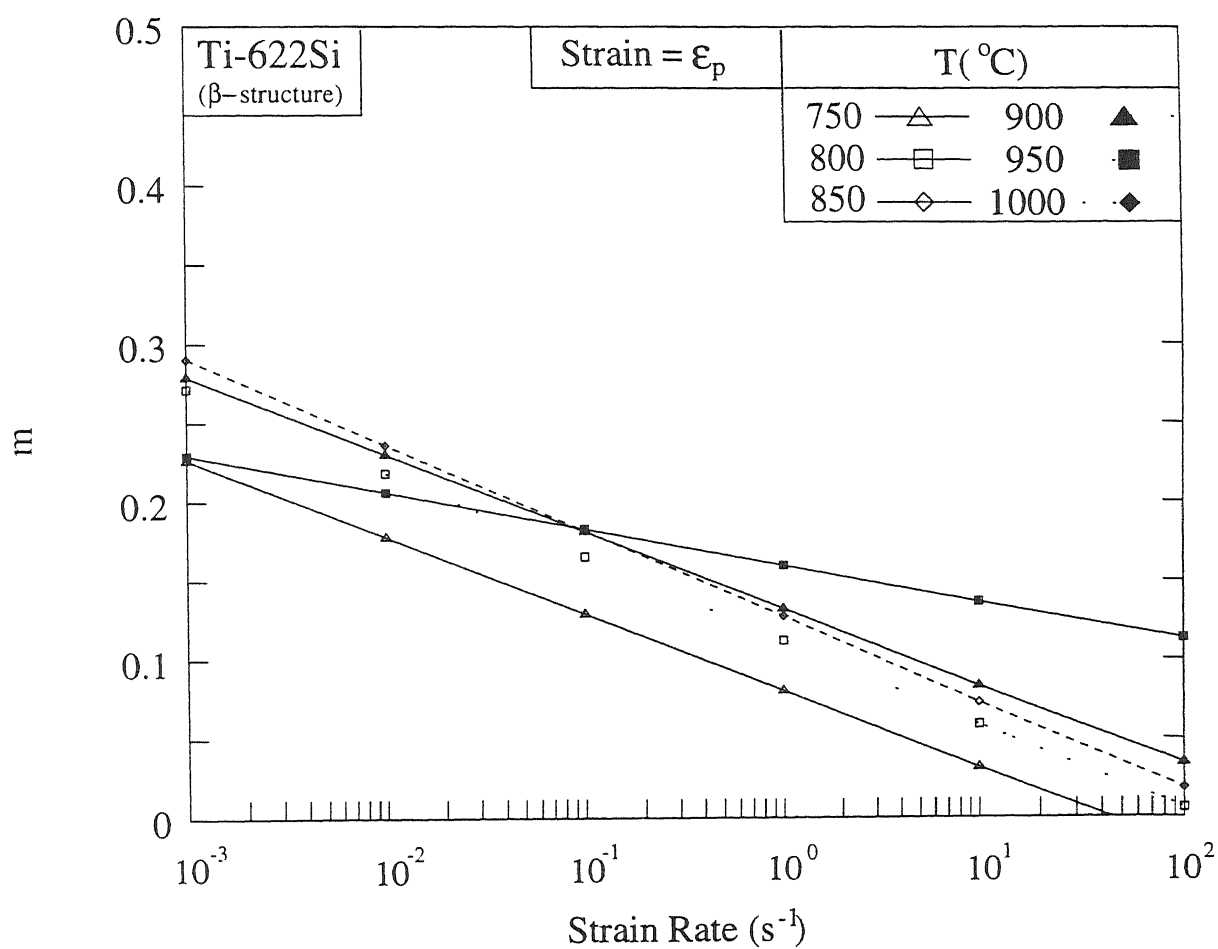


Figure 4.22: Variation of  $m$  with strain rate for Ti-622Si( $\beta$ ) corresponding to strain of  $\epsilon_p$

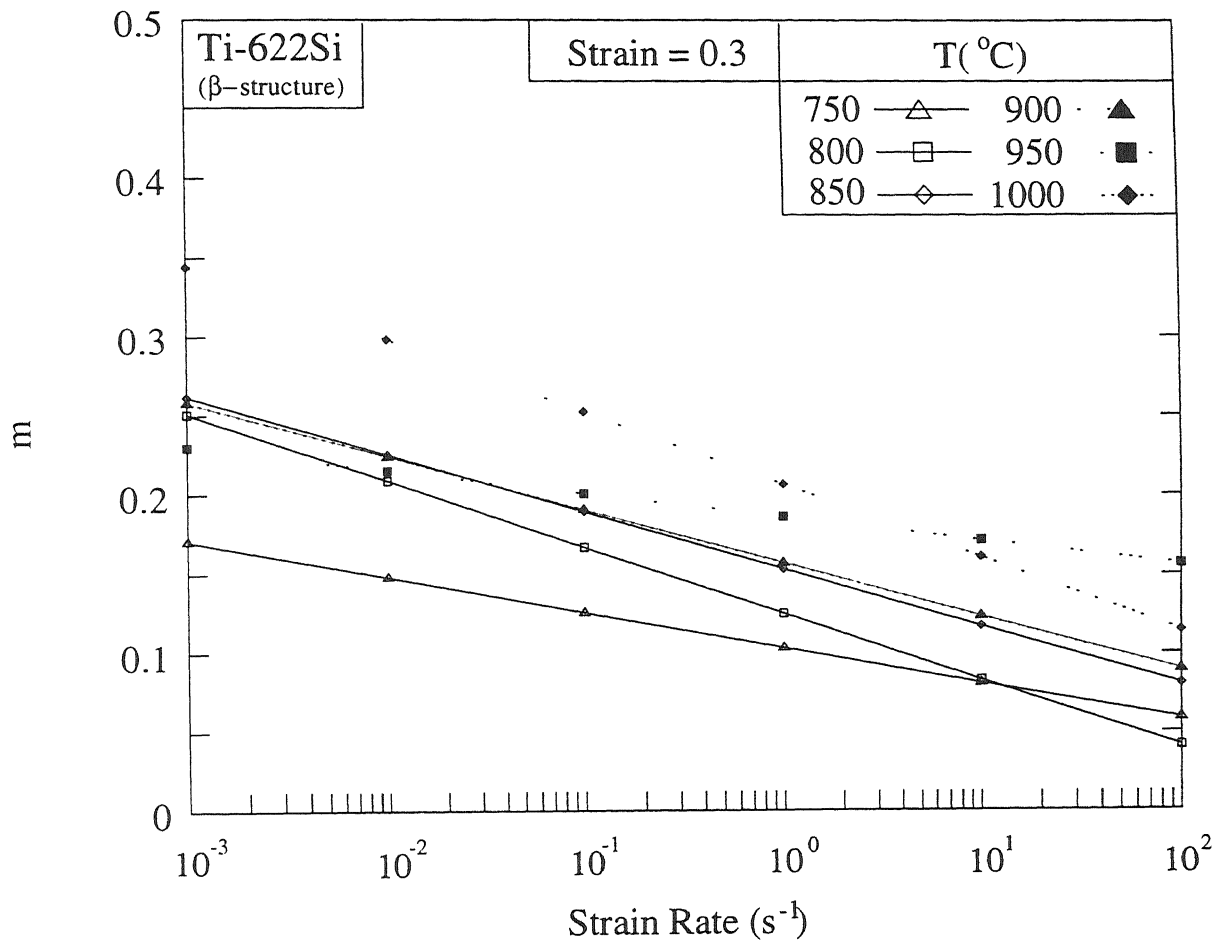


Figure 4 23: Variation of  $m$  with strain rate for Ti-622Si( $\beta$ ) corresponding to strain of 0.3

of the temperature compensated strain rate. In order to do so : (1) the activation energy was calculated and subsequently (2) the variation of flow stress as a function of the temperature compensated strain rate,  $Z$ , was obtained.

The activation energy of hot deformation of Ti-622Si in its  $\beta$  microstructural state was estimated from the variation of stress with temperature. Using the best fit lines in Figure 4.18, the data between  $1/T$  and strain rate corresponding to stress levels of 90 MPa and 245 MPa were obtained. The strain rate (in logarithmic scale) was then plotted against  $1/T$  as shown in Figure 4.24 and the activation energy was obtained from the slope of the best fit line. The activation energy corresponding to 90MPa and 245 MPa were very close to each other, i.e. 520 KJ mol<sup>-1</sup> and 560 KJ mol<sup>-1</sup> respectively. The value of activation energy shows close match with that obtained by Semiatin and Lahoti [12] for Ti-6242Si with  $\beta$ -structure and by Andres et al. [86] for near  $\alpha$  alloy IM1834 with lamellar structure.

For further analysis the activation energy was assumed to be independent of stress and its value was taken as 540 KJ mol<sup>-1</sup>, which is the average of the values corresponding to stress levels of 90 MPa and 245 MPa.

In order to ascertain the value of  $Q$ , the strain rate sensitivity,  $m$  was recalculated using the relationship between  $m$  and  $Q$  which has been derived by Semiatin and Lahoti [33], i.e.

$$m = -\frac{RT}{Q\sigma} \left[ \frac{d\sigma}{dT} \right]_e \quad (4.16)$$

Figure 4.25 shows the  $m$  corresponding to strain of 0.1, estimated by taking  $Q$  as 540 KJmol<sup>-1</sup>, plotted against that obtained experimentally. The match was found to be good, barring few points indicating that the value of activation energy is acceptable.

Figures 4.26- 4.28 show the variation of true stresses corresponding to strain levels of 0.1, 0.3 and 0.5 (in logarithmic scale) with the Zener-Hollomon parameter  $Z$  (in

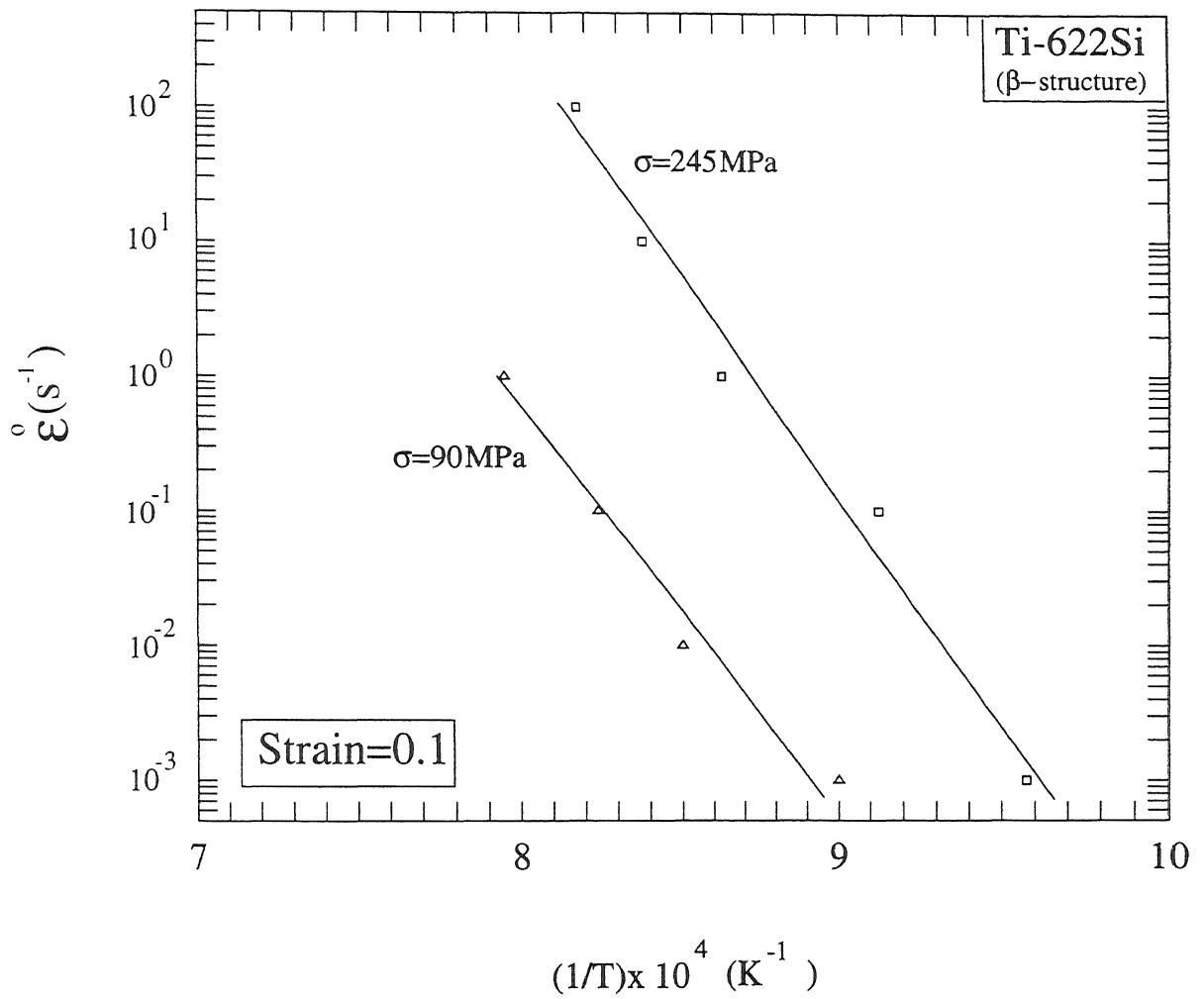


Figure 4.24: Plot of strain rate corresponding to fixed stress levels versus  $(1/T) \times 10^4$  for Ti-622Si( $\beta$ )

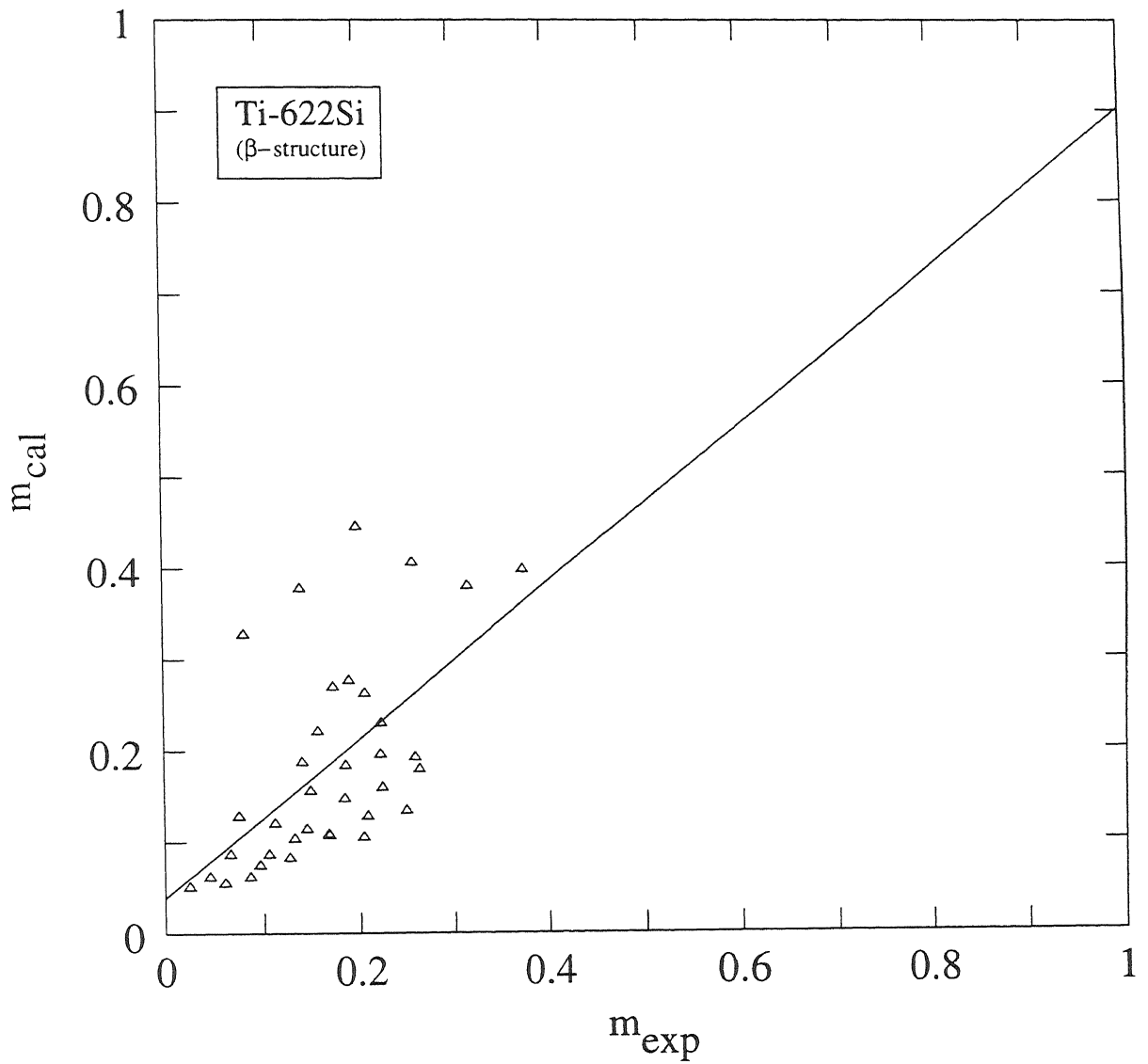


Figure 4.25: Plot of  $m$  calculated using equation 4.16 versus that obtained experimentally for Ti-622Si( $\beta$ ) corresponding to strain of 0.1

logarithmic scale). A second order polynomial was found to fit well through the data points

#### 4.2.6 Instability Parameters

The different instability criteria for predicting plastic instability that are obtained from the stress-strain and stress-strain rate data, have been discussed in Chapter 1. The two criteria that are very commonly used are: (1) based on flow localization parameter  $\psi$  [32] and (2) based on thermodynamic parameter,  $\zeta$  [37]. These criteria were used in the present study to predict flow instabilities during the uniaxial compression of Ti-622Si alloy with  $\beta$  structure.

Flow localization was quantified by the flow localization parameter,  $\psi$ , defined as

$$\psi = \frac{-\delta \ln \dot{\epsilon}}{\delta \epsilon} \quad (4.17)$$

where  $-\delta \ln \dot{\epsilon}$  is the difference in the strain rate and  $\delta \epsilon$  is the difference in plastic strain between two adjacent positions within the material undergoing deformation and separated by a distance of  $\delta x$ . Positive values of the parameter  $\psi$  indicates flow localization or instability whereas  $\psi < 0$  indicates stable flow. For the case of uniaxial compression  $\psi$  is given by the relationship

$$\psi = \frac{\gamma - 1}{m} \quad (4.18)$$

where  $\gamma$  is the normalized strain hardening rate, given by

$$\gamma = \frac{d\sigma}{\sigma d\epsilon} \quad (4.19)$$

The values of  $\psi$  were estimated at different temperature and strain rates. In order to eliminate the effect of local fluctuation in the stress-strain curves, the experimental data were fitted with smooth curves of a high order polynomial. Using the coefficients of the polynomial, the strain hardening rate, normalized with respect to true stress,  $\gamma$

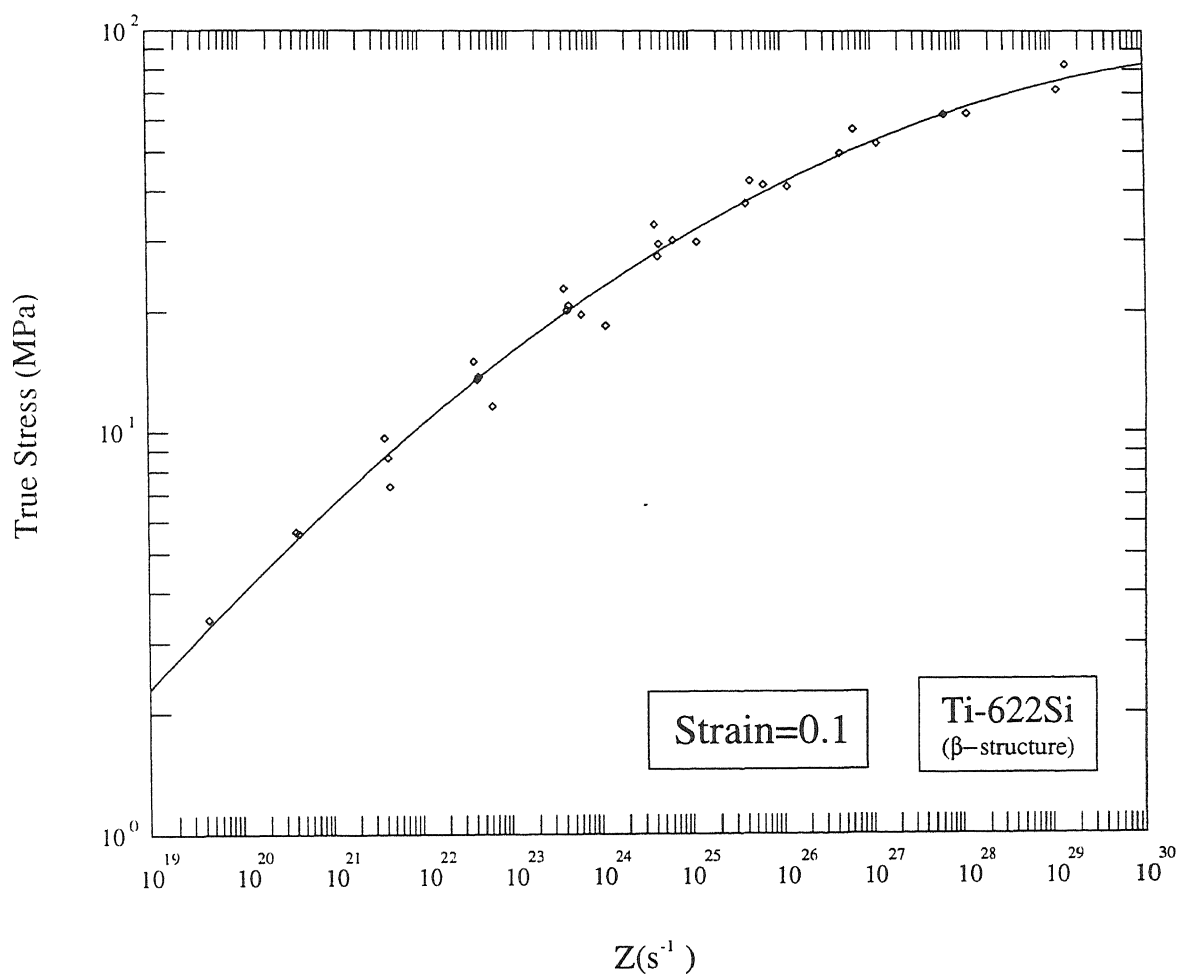


Figure 4.26: Variation of true stress corresponding to strain level of 0.1 with Zener-Holloman parameter for Ti-622Si( $\beta$ )



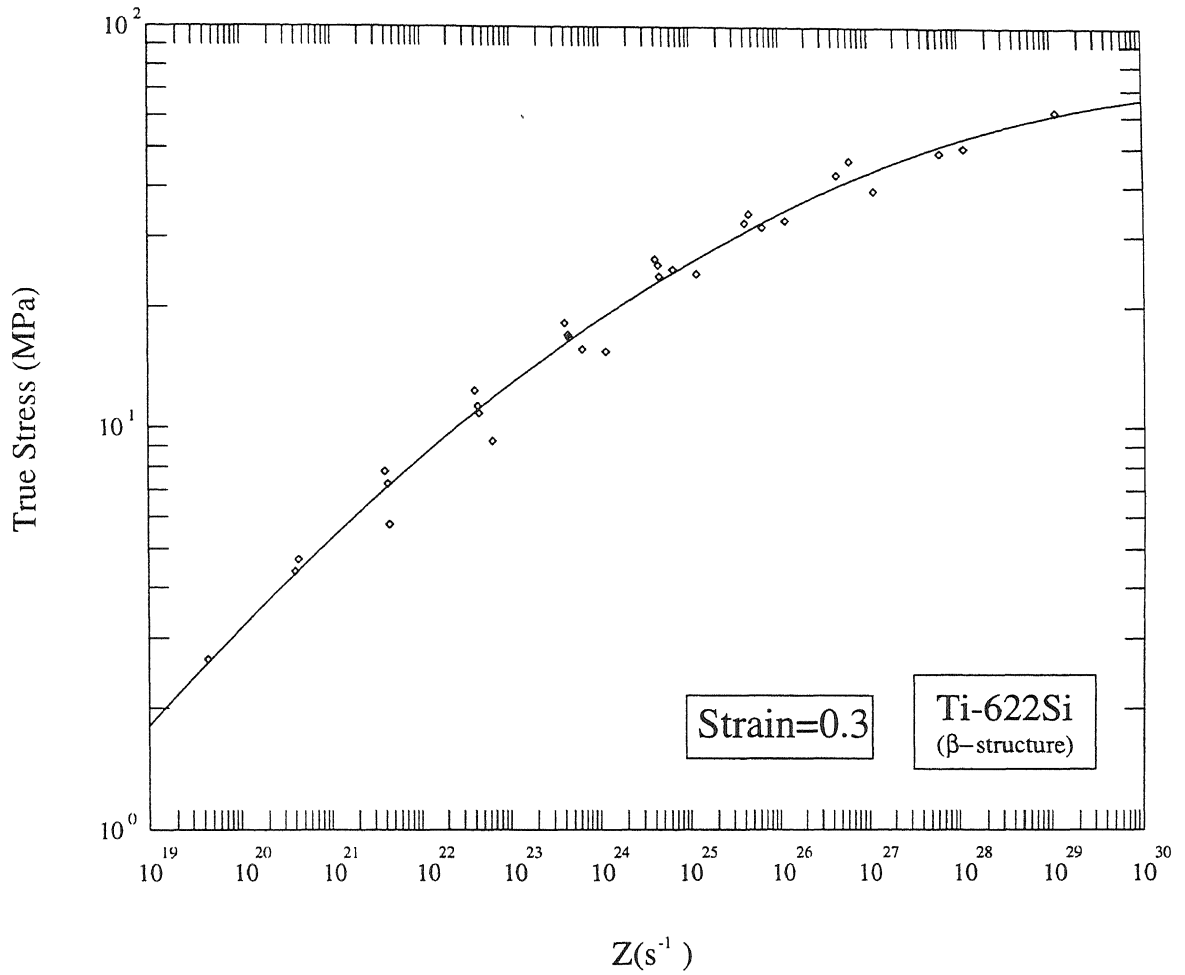


Figure 4.27: Variation of true stress corresponding to strain level of 0.3 with Zener-Holloman parameter for Ti-622Si( $\beta$ )

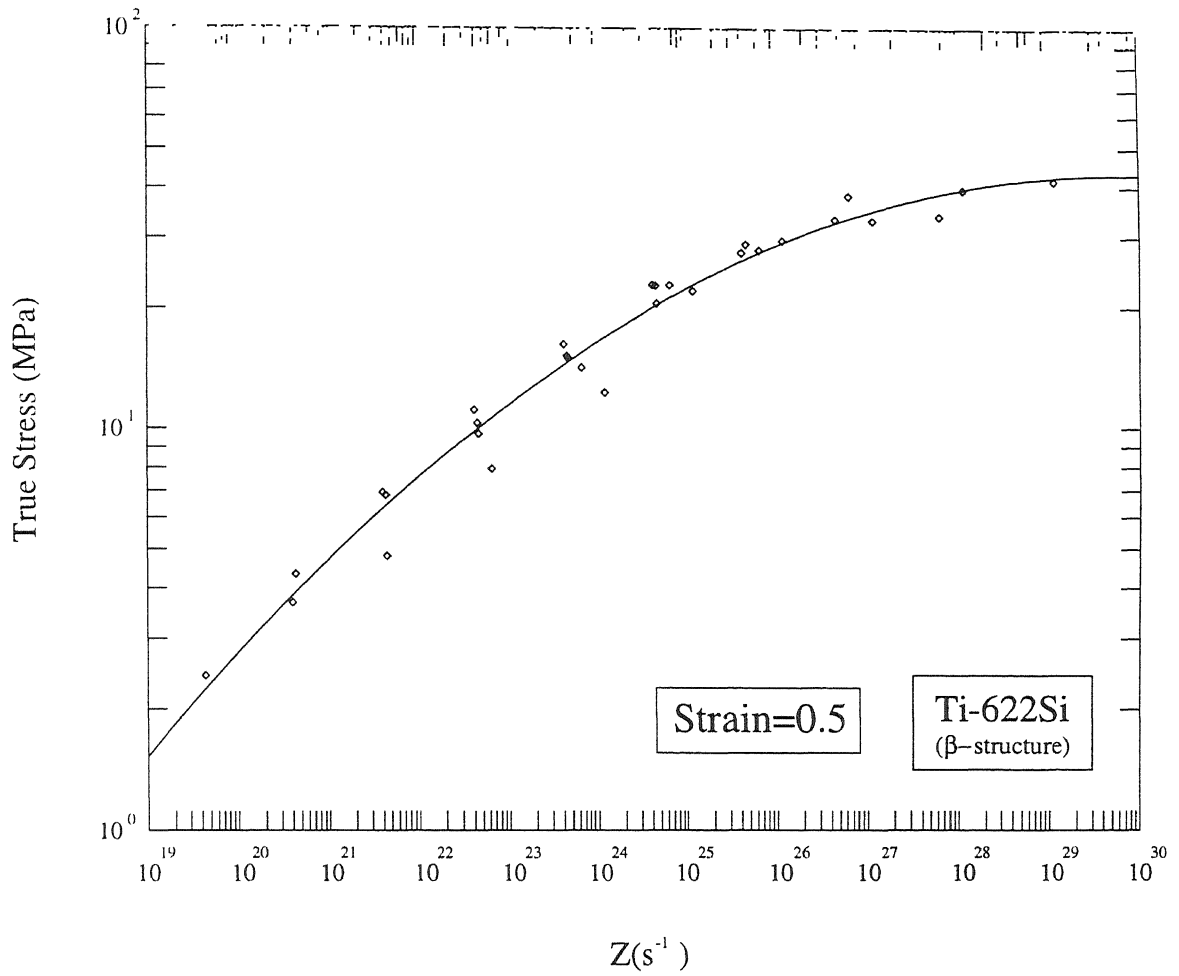


Figure 4.28: Variation of true stress corresponding to strain level of 0.5 with Zener-Holloman parameter for Ti-622Si( $\beta$ )

was calculated as a function of strain. Value of  $\psi$ , as a function of strain were obtained using the  $m$ -value corresponding to strain of 0.1. The variation of  $\psi$  as a function of plastic strain for deformation at different temperatures and strain rates as estimated from experimental stress-strain curves is shown in Figures 4.29- 4.40. The variation of  $\psi$  with plastic strain was found to be of four types:

- Type – I** At all plastic strains  $\psi < 0$ , indicating that the stable flow occurs throughout the deformation,
- Type – II**  $\psi > 0$  up to a critical strain and then  $\psi < 0$  indicating that the flow remains unstable up to a critical strain after which it tends to be stable;
- Type – III** :  $\psi < 0$  up to a critical strain and then  $\psi > 0$  indicating that the flow is stable to begin with but becomes unstable after reaching a critical strain;
- Type – IV** :  $\psi$  oscillates between positive and negative values indicating that the flow becomes stable and unstable several times during the deformation.

The temperature-strain rate domain for the four types of variation in  $\psi$  calculated from the experimental stress-strain curve is shown in Figure 4.41. The domain of Type-I variation in  $\psi$  is the domain of stable flow and in the remaining temperature-strain rate regime the variation of  $\psi$  indicates unstable flow at some stage of compression.

Flow instability was also predicted using the criteria based on irreversible thermodynamics and DMM, according to which the flow is unstable when the parameter  $\zeta$ , defined as

$$\zeta = m + \left( \frac{d \log[m/(m+1)]}{d \log \dot{\epsilon}} \right) \quad (4.20)$$

exceeds 0. Figure 4.42- 4.43 gives the contour plots for  $\zeta$  corresponding to plastic strains of 0.1 and 0.3. It can be seen that instability domain predicted by the thermodynamic criteria is smaller than that predicted from the flow localization parameter  $\psi$  and excludes regimes of low strain rates.

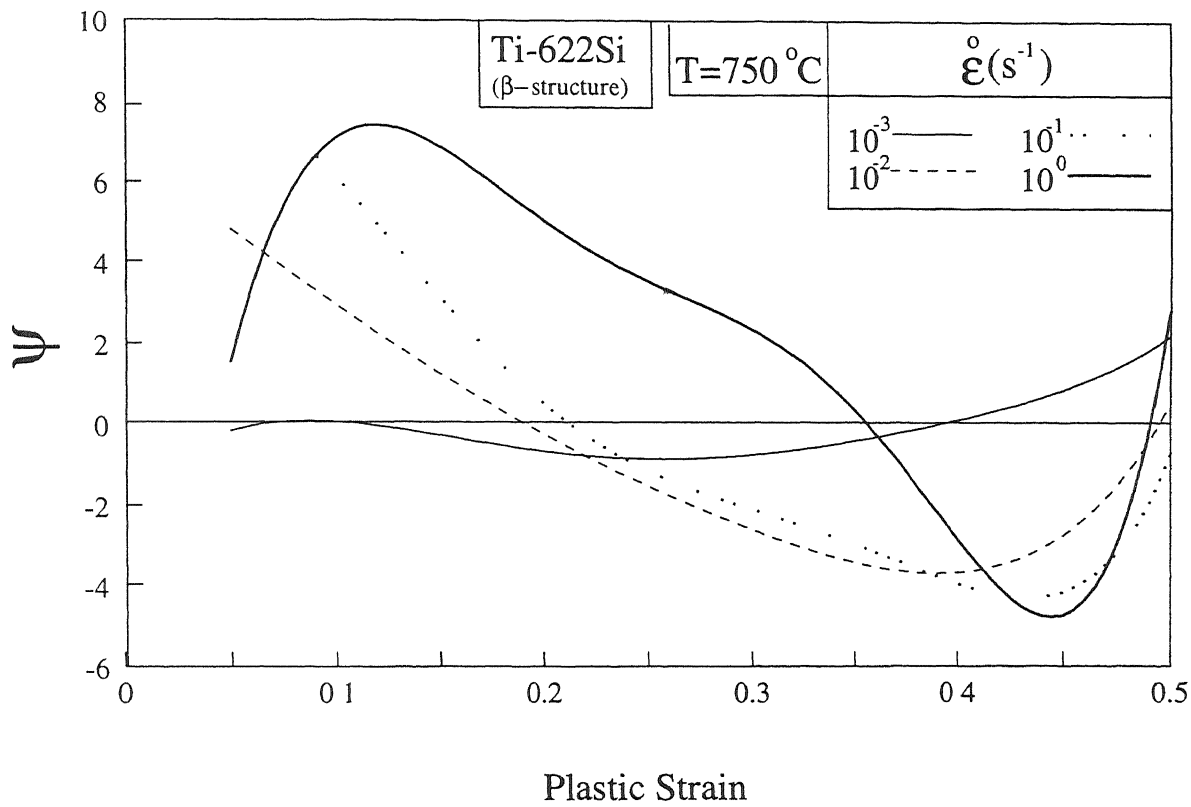


Figure 4.29: Variation of  $\psi$  with plastic strain at  $750^\circ\text{C}$  for Ti-622Si( $\beta$ )

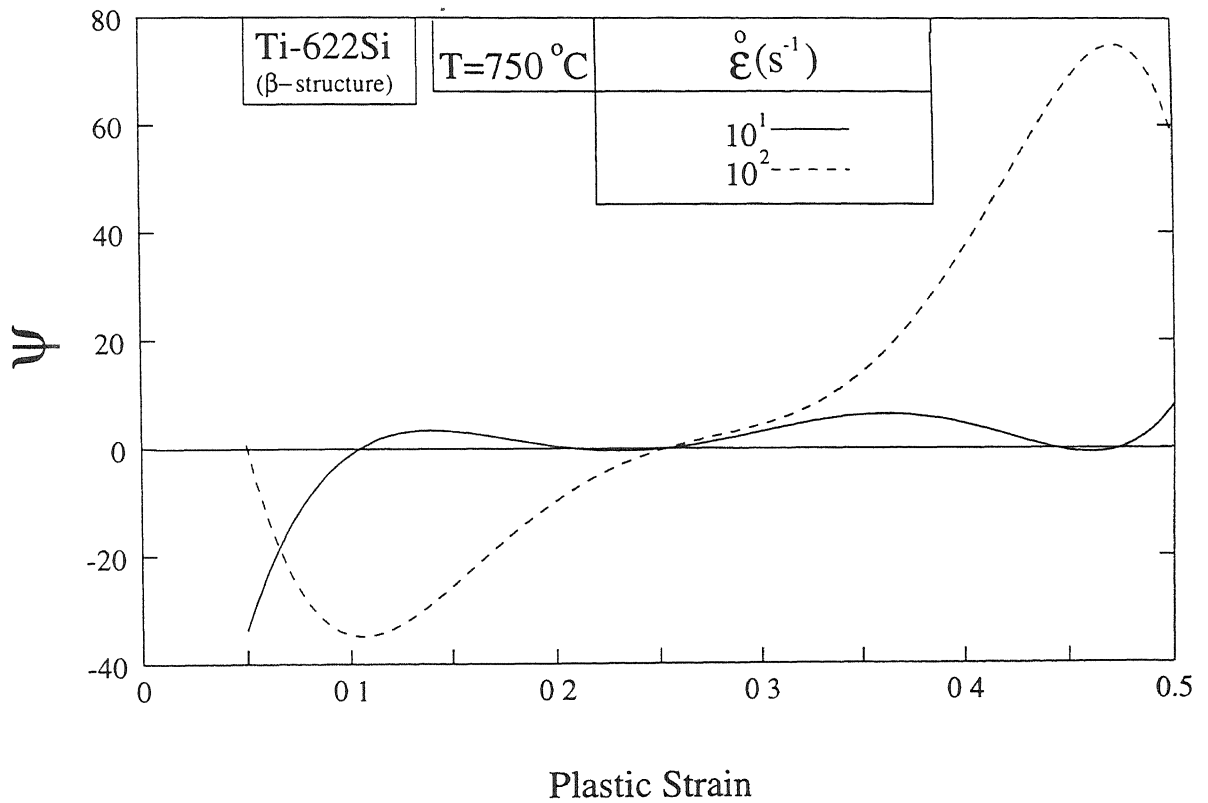


Figure 4.30: Variation of  $\psi$  with plastic strain at 750°C for Ti-622Si( $\beta$ )

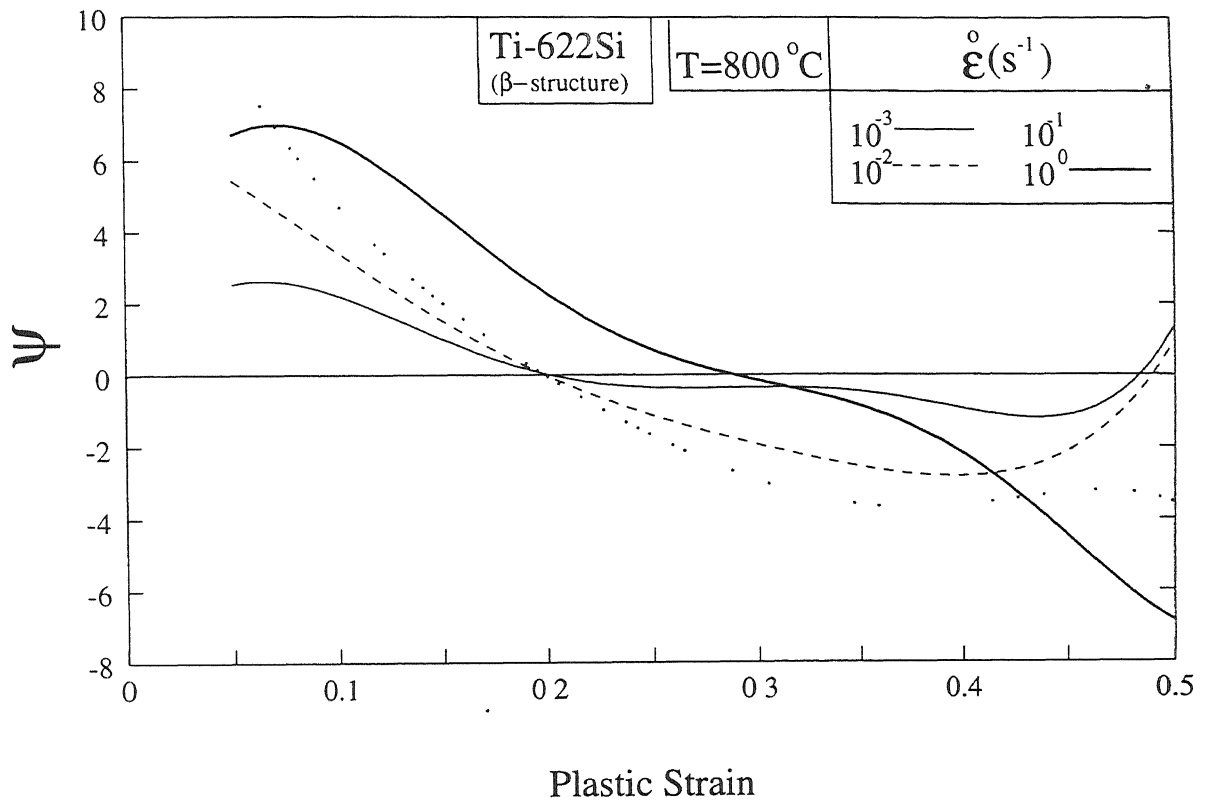


Figure 4.31: Variation of  $\psi$  with plastic strain at 800°C for Ti-622Si( $\beta$ )

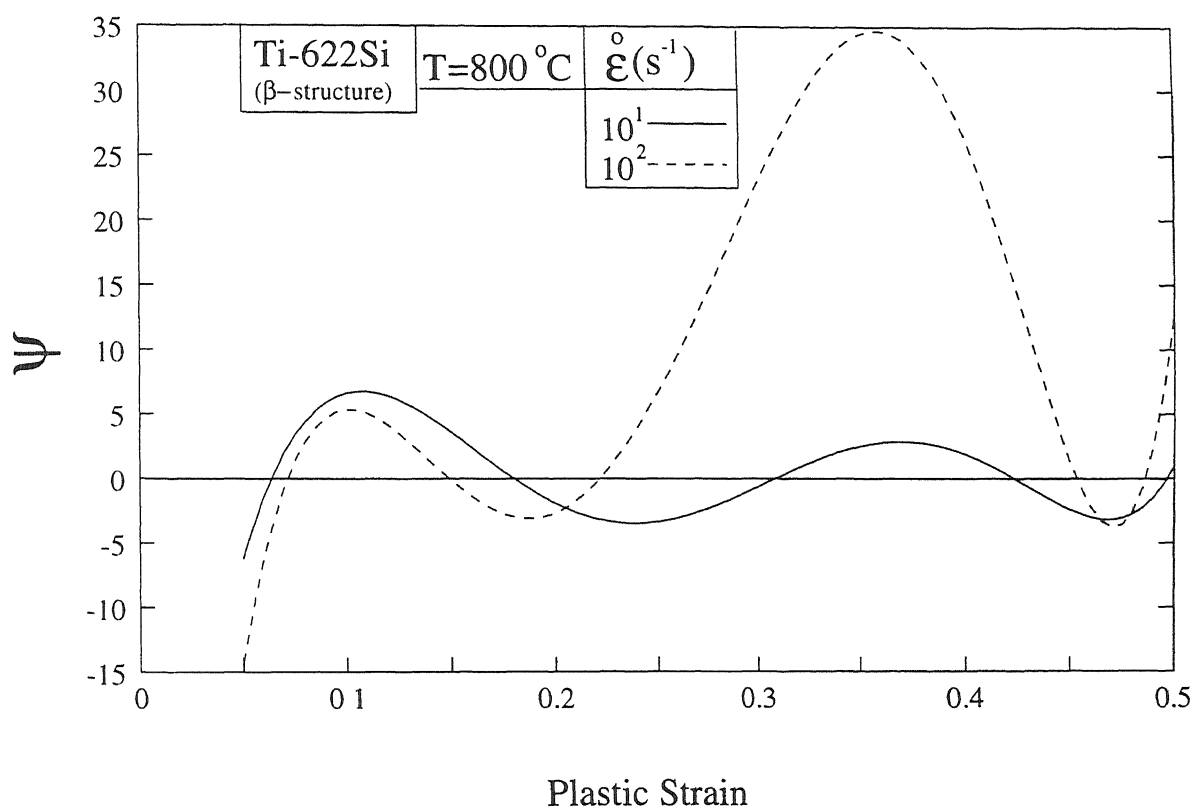


Figure 4.32: Variation of  $\psi$  with plastic strain at 800°C for Ti-622Si( $\beta$ )

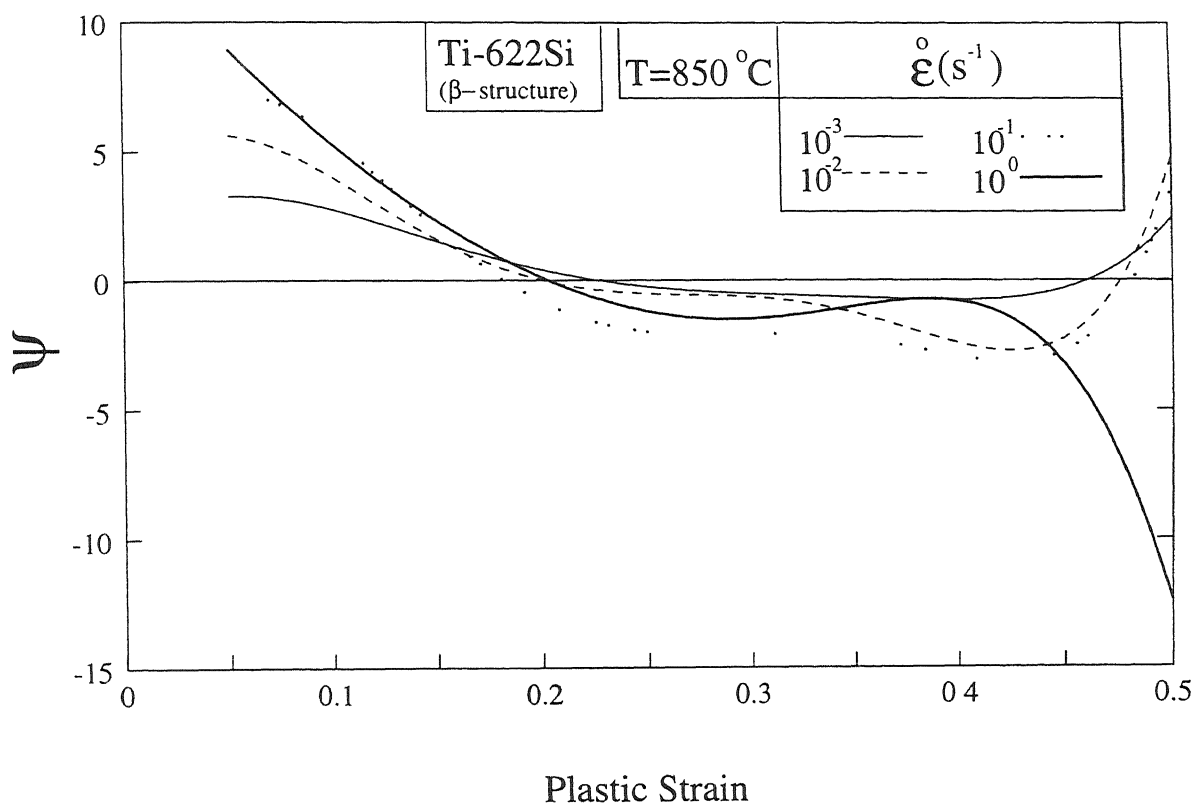


Figure 4.33: Variation of  $\psi$  with plastic strain at 850°C for Ti-622Si( $\beta$ )



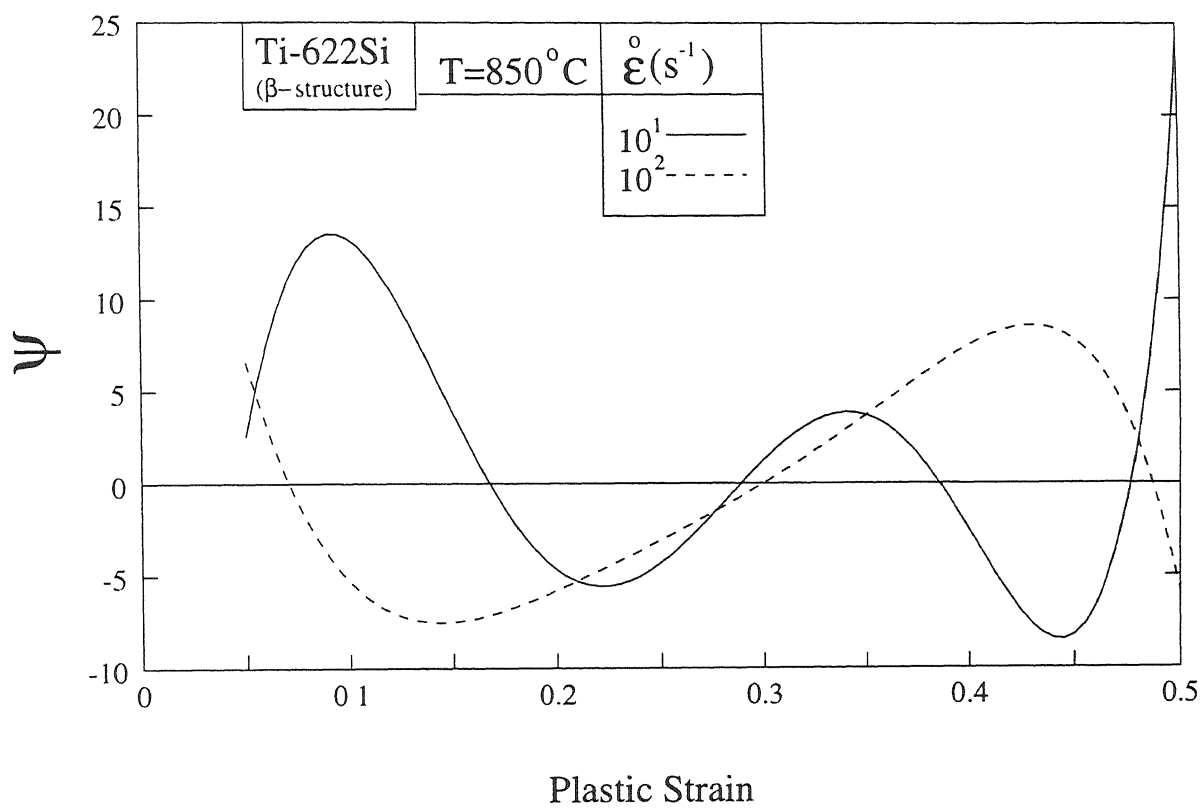


Figure 4.34: Variation of  $\psi$  with plastic strain at 850°C for Ti-622Si( $\beta$ )

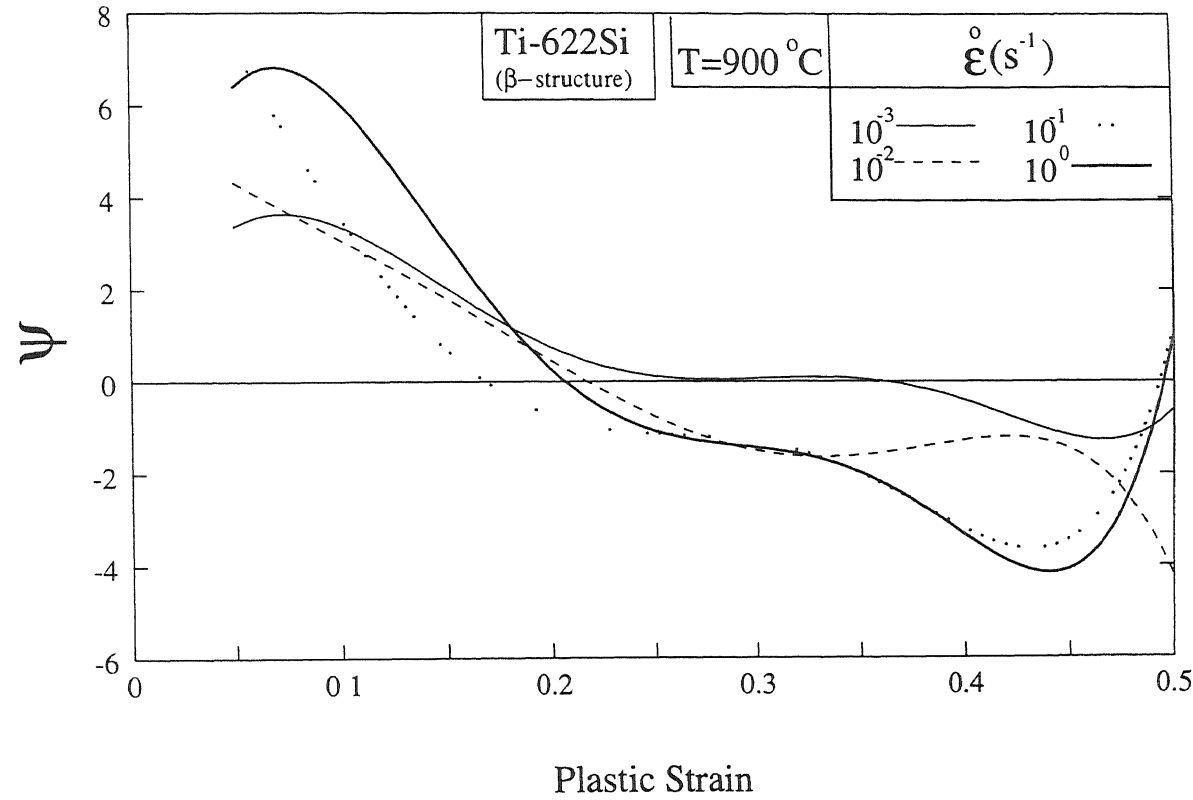


Figure 4.35: Variation of  $\psi$  with plastic strain at  $900^\circ\text{C}$  for Ti-622Si( $\beta$ )

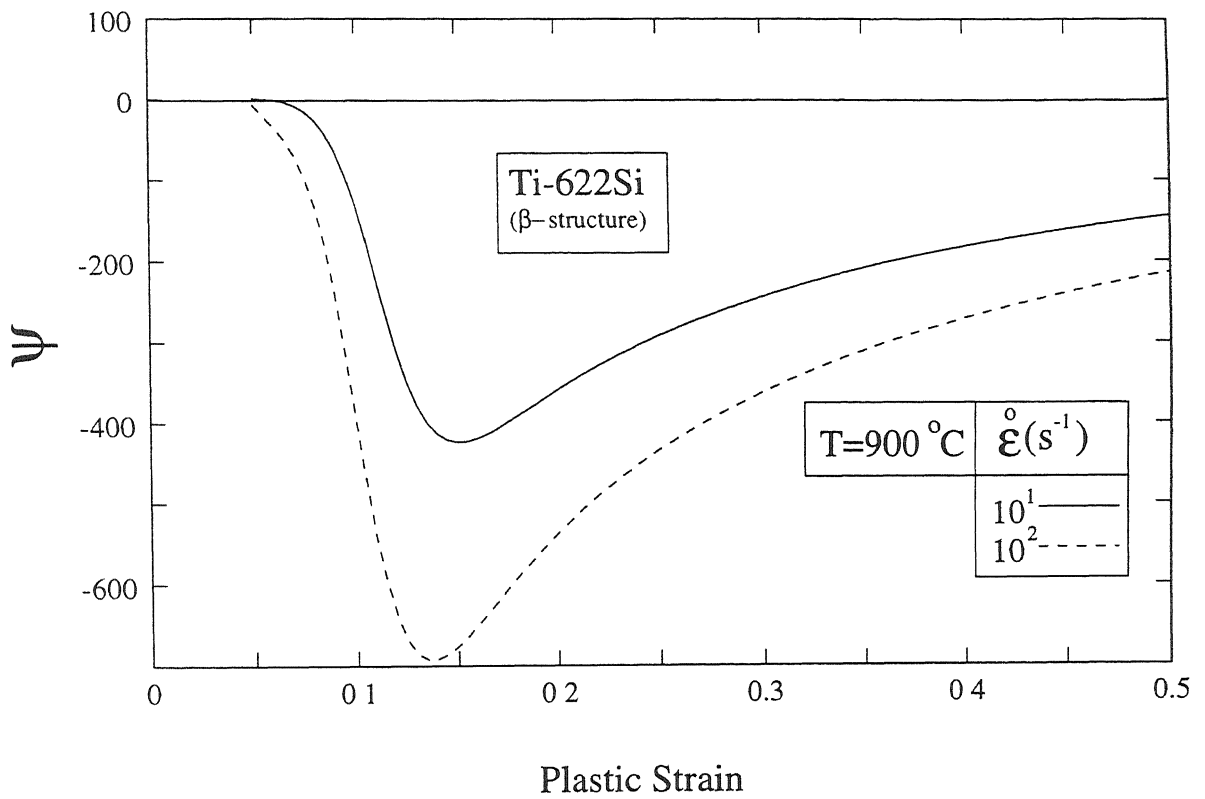


Figure 4.36: Variation of  $\psi$  with plastic strain at  $900^\circ\text{C}$  for Ti-622Si( $\beta$ )

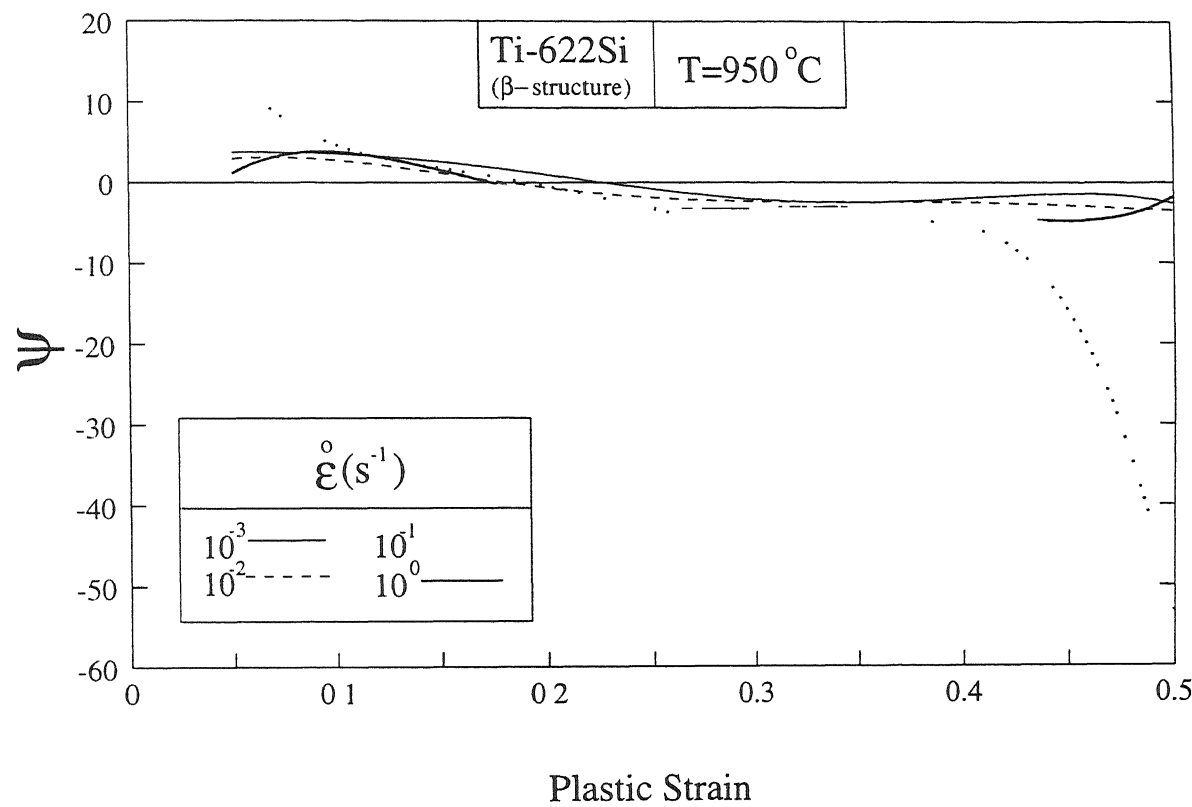


Figure 4.37. Variation of  $\psi$  with plastic strain at  $950^\circ\text{C}$  for Ti-622Si( $\beta$ )

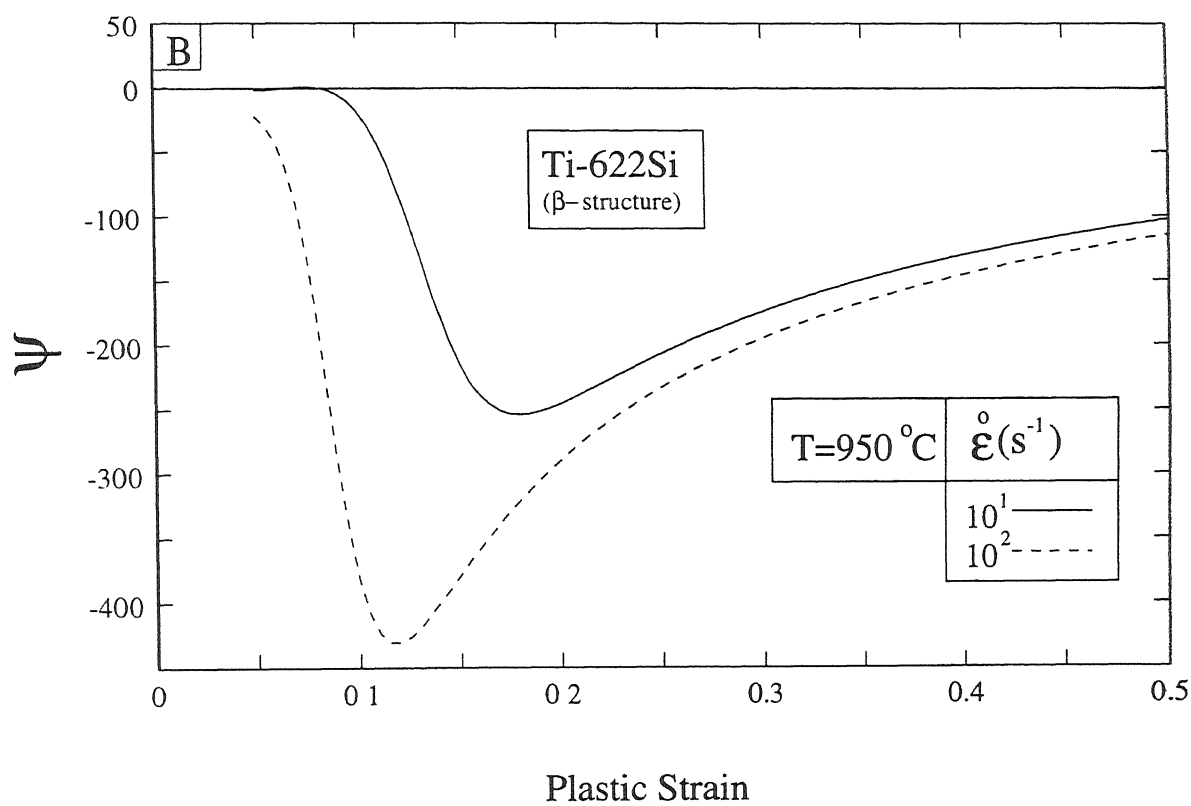


Figure 4.38: Variation of  $\psi$  with plastic strain at 950°C for Ti-622Si( $\beta$ )

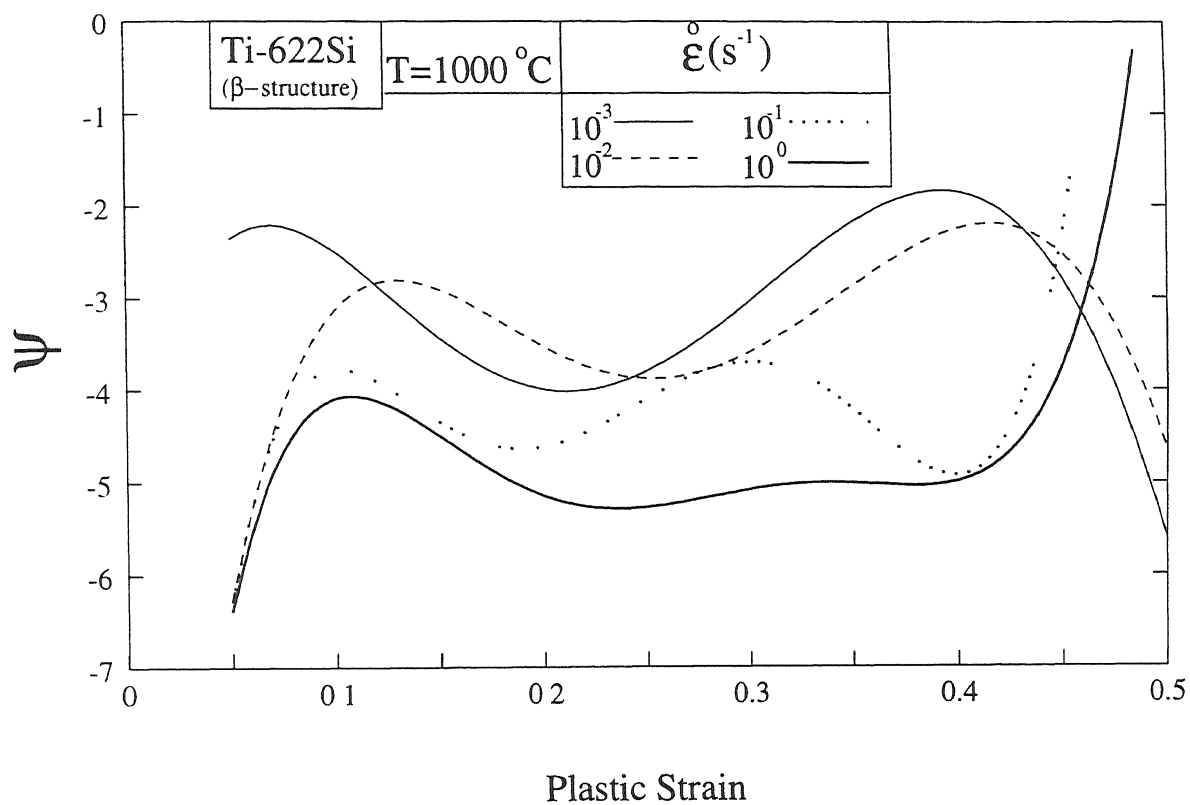


Figure 4.39: Variation of  $\psi$  with plastic strain at 1000°C for Ti-622Si( $\beta$ )

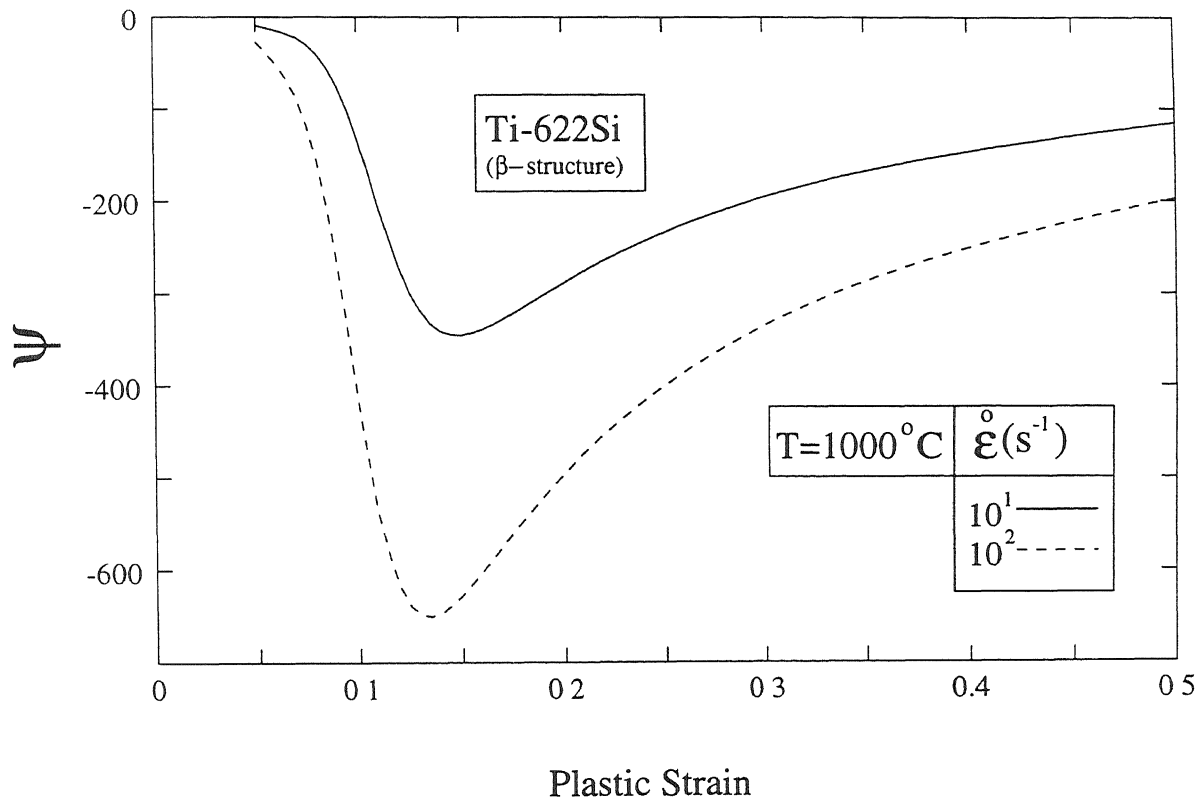


Figure 4.40: Variation of  $\psi$  with plastic strain at  $1000^\circ\text{C}$  for Ti-622Si( $\beta$ )

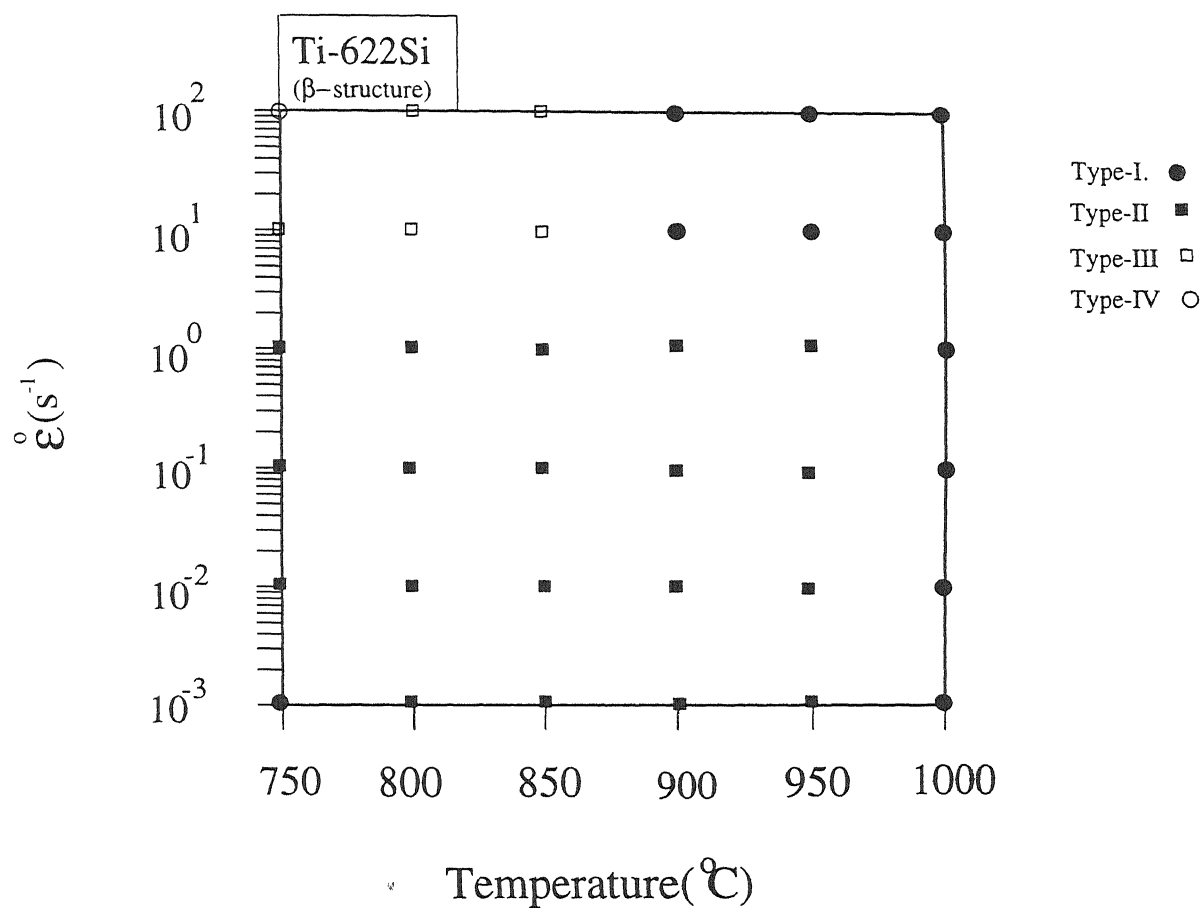


Figure 4.41: Domains for different types of variation of  $\psi$  with plastic strain for Ti-622Si( $\beta$ )



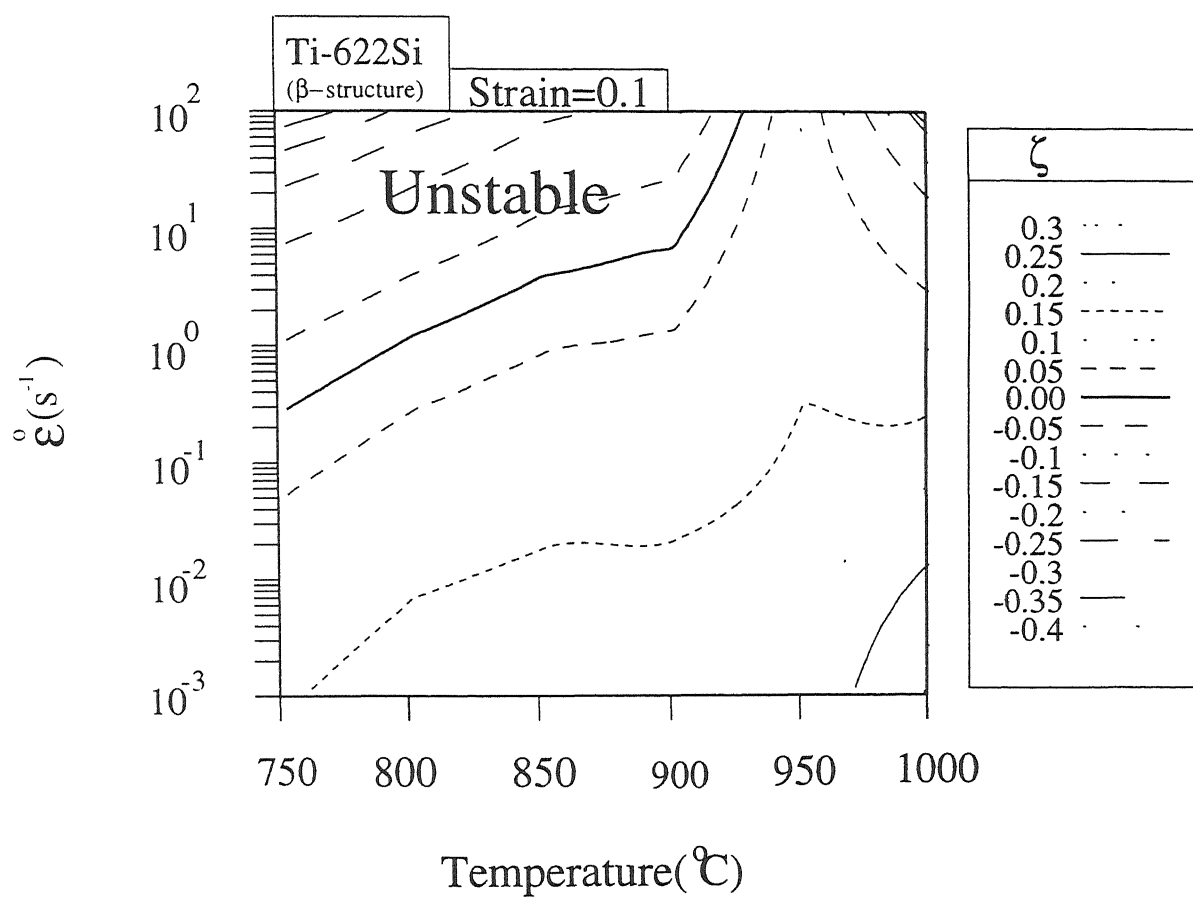


Figure 4.42: Contour Map for  $\zeta$  parameter corresponding to strain level of 0.1 for Ti-622Si( $\beta$ )

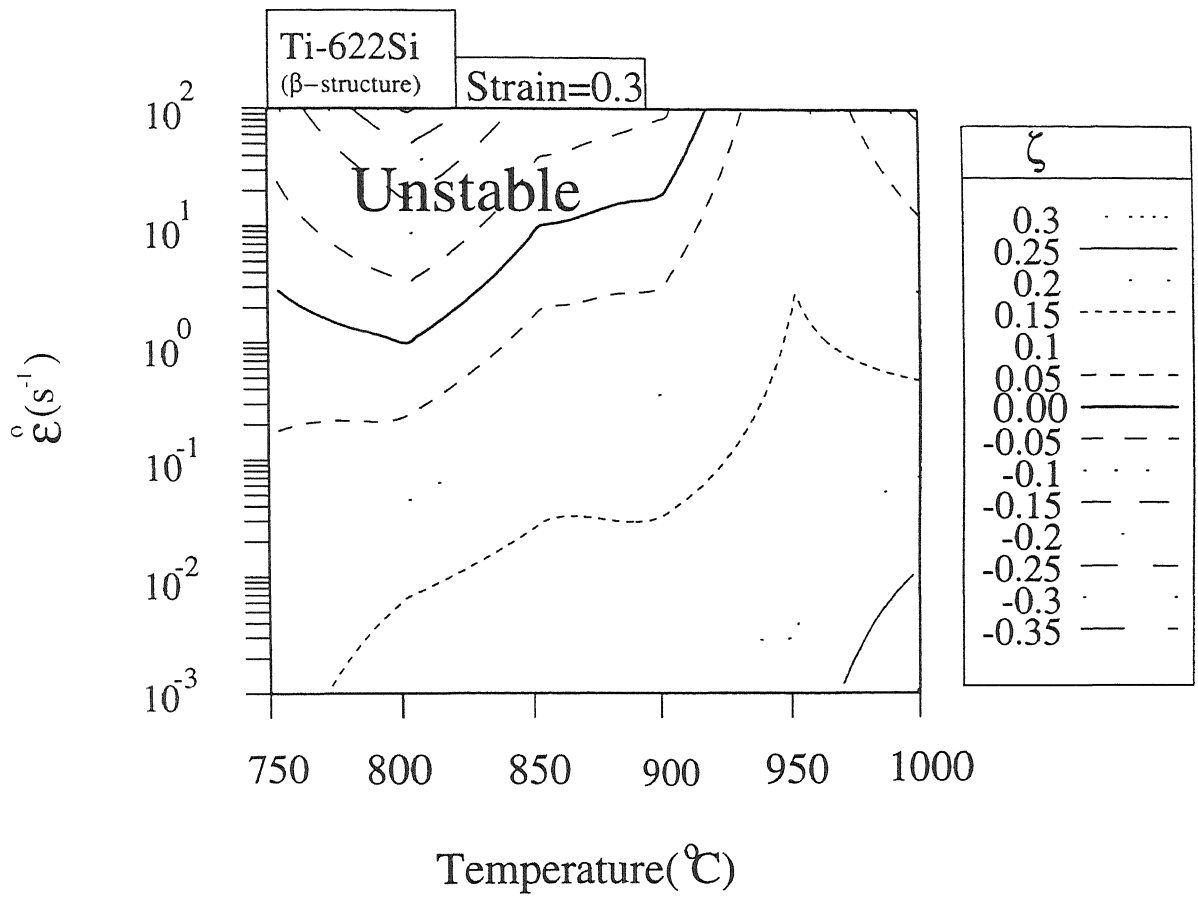


Figure 4.43: Contour Map for  $\zeta$  parameter corresponding to strain level of 0.3 for Ti-622Si( $\beta$ )

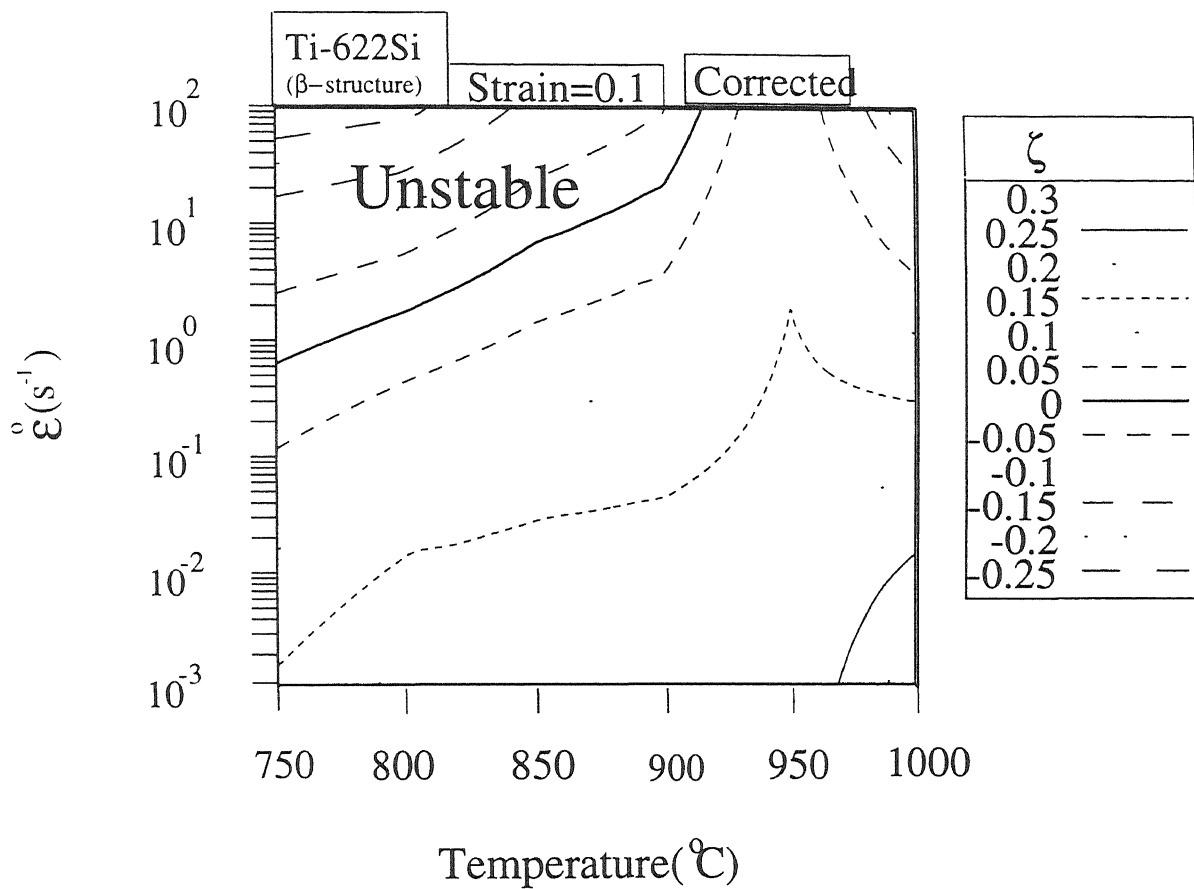


Figure 4.44 Contour Map for  $\zeta$  parameter corresponding to strain level of 0.1 for Ti-622Si( $\beta$ ) obtained from the temperature corrected stress-strain curves

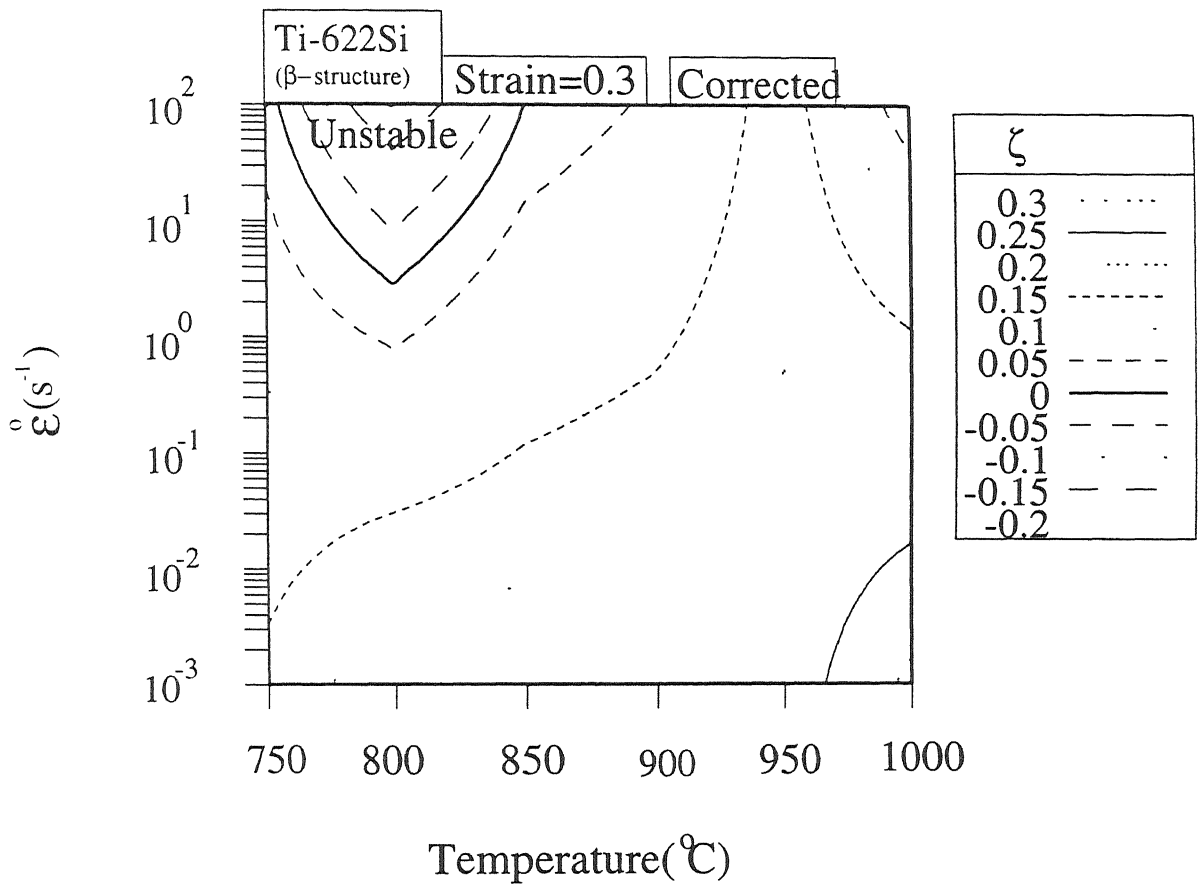


Figure 4.45. Contour Map for  $\zeta$  parameter corresponding to strain level of 0.3 for Ti-622Si( $\beta$ ) obtained from the temperature corrected stress-strain curves

As discussed in Chapter 1, flow instability is triggered by both temperature rise as well as microstructural and textural evolution in the alloy during its deformation. In order to eliminate the contributions of temperature rise in flow instability, parameter  $\psi$  and  $\zeta$  were also calculated from the temperature corrected stress-strain and stress-strain rate curves

The variation of  $\psi$  obtained from the temperature corrected stress-strain curves,  $\psi_c$  is shown in Figure 4.46- 4.52. The variation of  $\psi_c$  with strain for different temperatures and strain rates of deformation of  $\beta$  structure of Ti-622Si alloy revealed that the plots of Type-I and Type-II only were obtained. The temperature and strain rate domain of the two types of variation in  $\psi_c$  is shown in Figure 4.53. It can be seen that the domain for flow instability or the domain in which the variation in  $\psi$  is either of the three, i.e. Type-II, Type-III and Type-IV, becomes narrower as a result of temperature correction. Further, in case of Type-II behaviour of  $\psi_c$  it was observed that the critical strain at which the transition from unstable to stable flow occurred, increased with increasing strain rates at the deformation temperature of 750°C. In contrast, at deformation temperatures of 850°C, 900°C and 950°C, the critical strain decreased with increasing the strain rate.

The contour map of  $\zeta_c$ , i.e.  $\zeta$  obtained after temperature correction, is shown Figure 4.44- 4.45. It can be seen that at strain level of 0.3, the instability domain predicted from the values of  $\zeta_c$  is narrower than that predicted from that of  $\zeta$ .

#### 4.2.7 Structural Manifestations of Unstable Flow

The triggering of plastic instability during the compression of Ti-622Si alloy with  $\beta$  structure was predicted from the knowledge of its flow behaviour in the previous section. Observations on the manifestations of the unstable flow in the alloy as indicated by the shape distortion of compression specimens are reported in the present section. Unstable

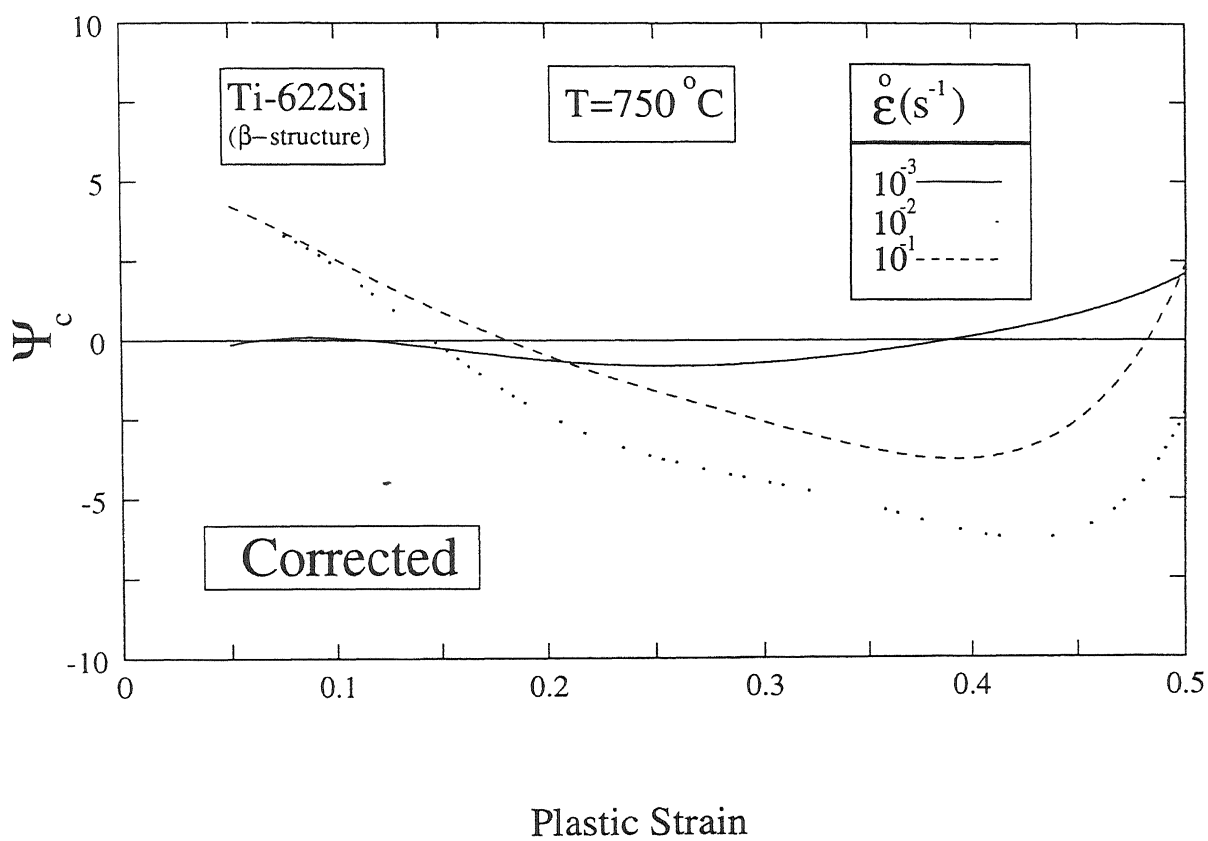


Figure 4.46: Variation of  $\psi_c$  with plastic strain at  $750^\circ\text{C}$  for Ti-622Si( $\beta$ )

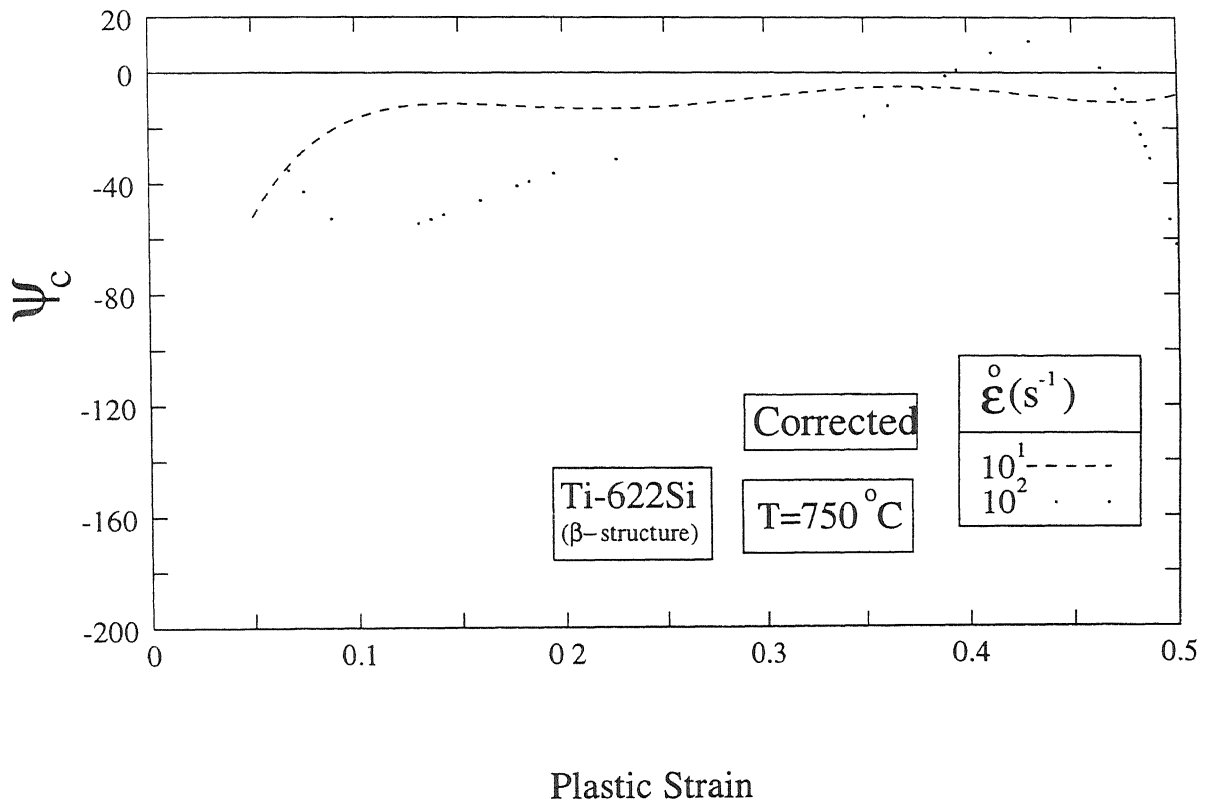


Figure 4.47: Variation of  $\psi_c$  with plastic strain at  $750^\circ\text{C}$  for Ti-622Si( $\beta$ )

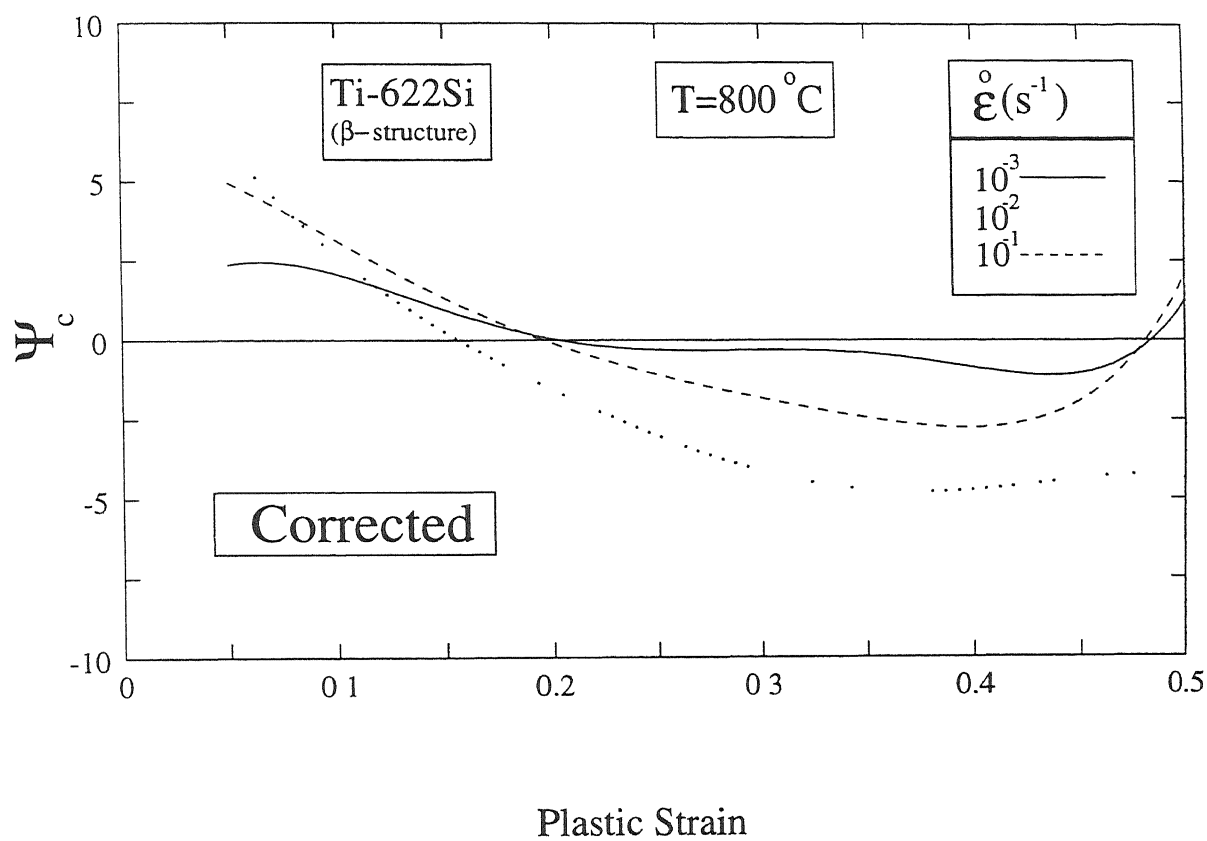


Figure 4.48. Variation of  $\psi_c$  with plastic strain at  $800^\circ\text{C}$  for Ti-622Si( $\beta$ )



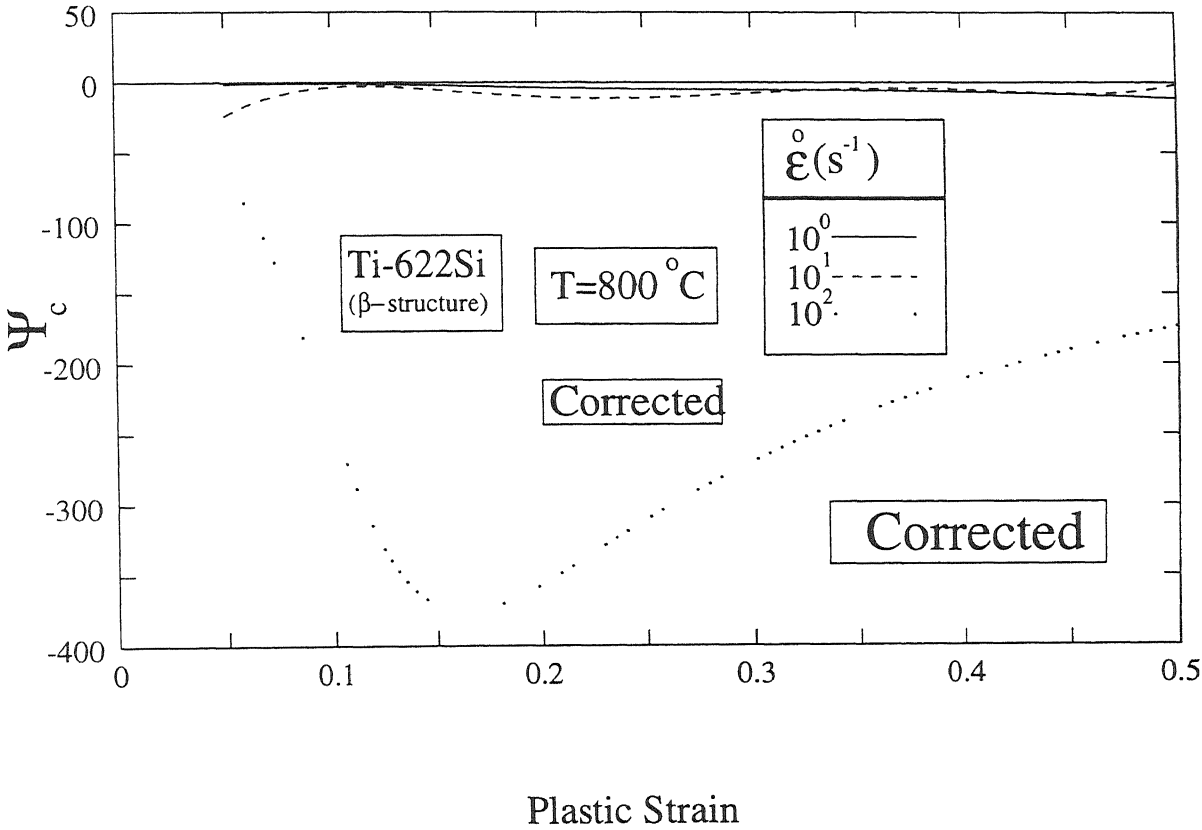


Figure 4.49: Variation of  $\psi_c$  with plastic strain at  $800^\circ\text{C}$  for Ti-622Si( $\beta$ )

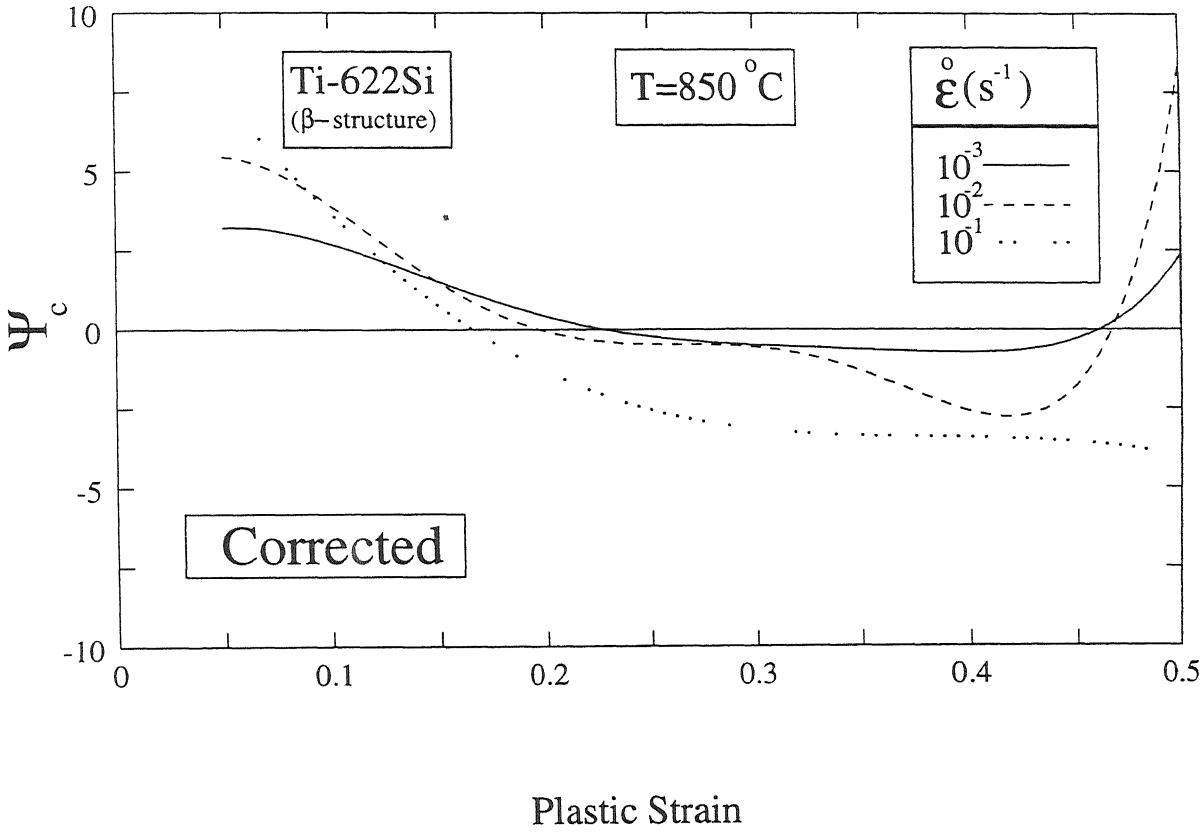


Figure 4.50. Variation of  $\psi_c$  with plastic strain at 850°C for Ti-622Si( $\beta$ )

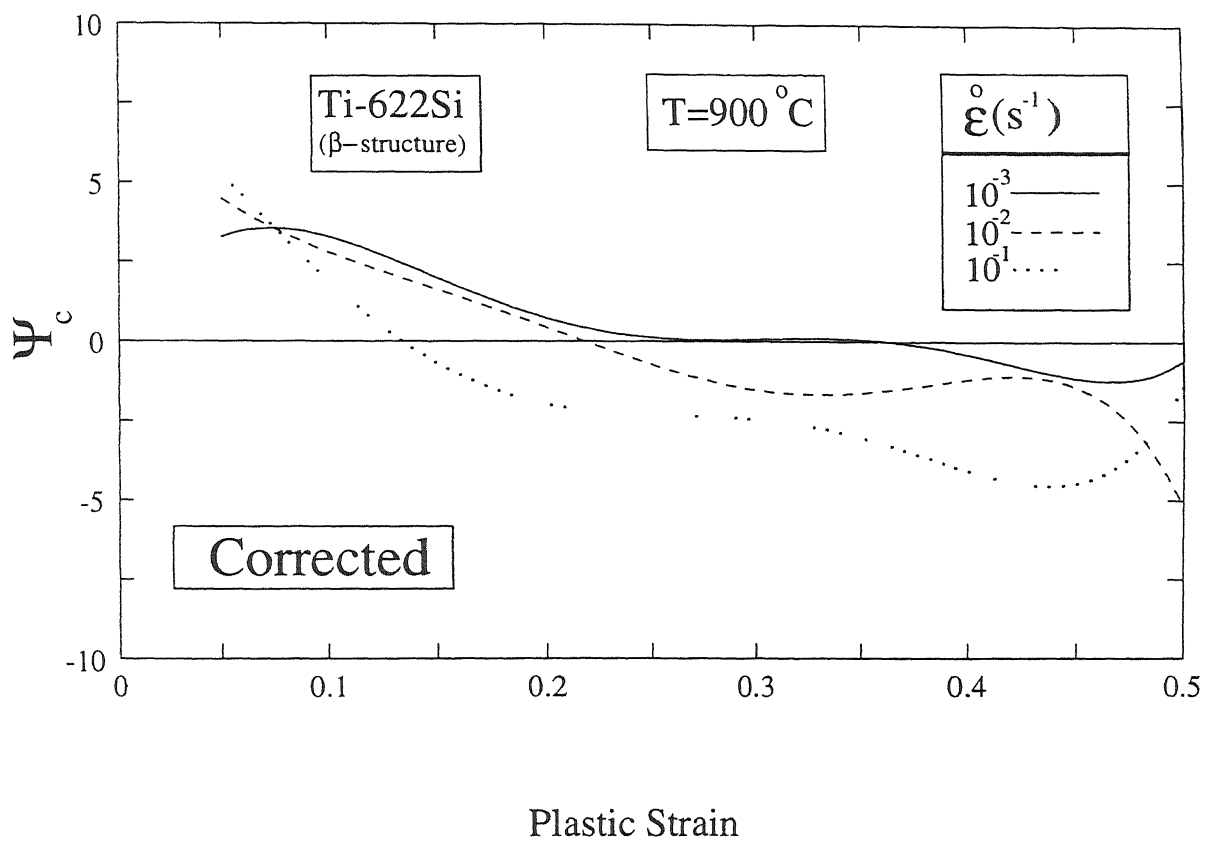


Figure 4.51: Variation of  $\psi_c$  with plastic strain at 900°C for Ti-622Si( $\beta$ )

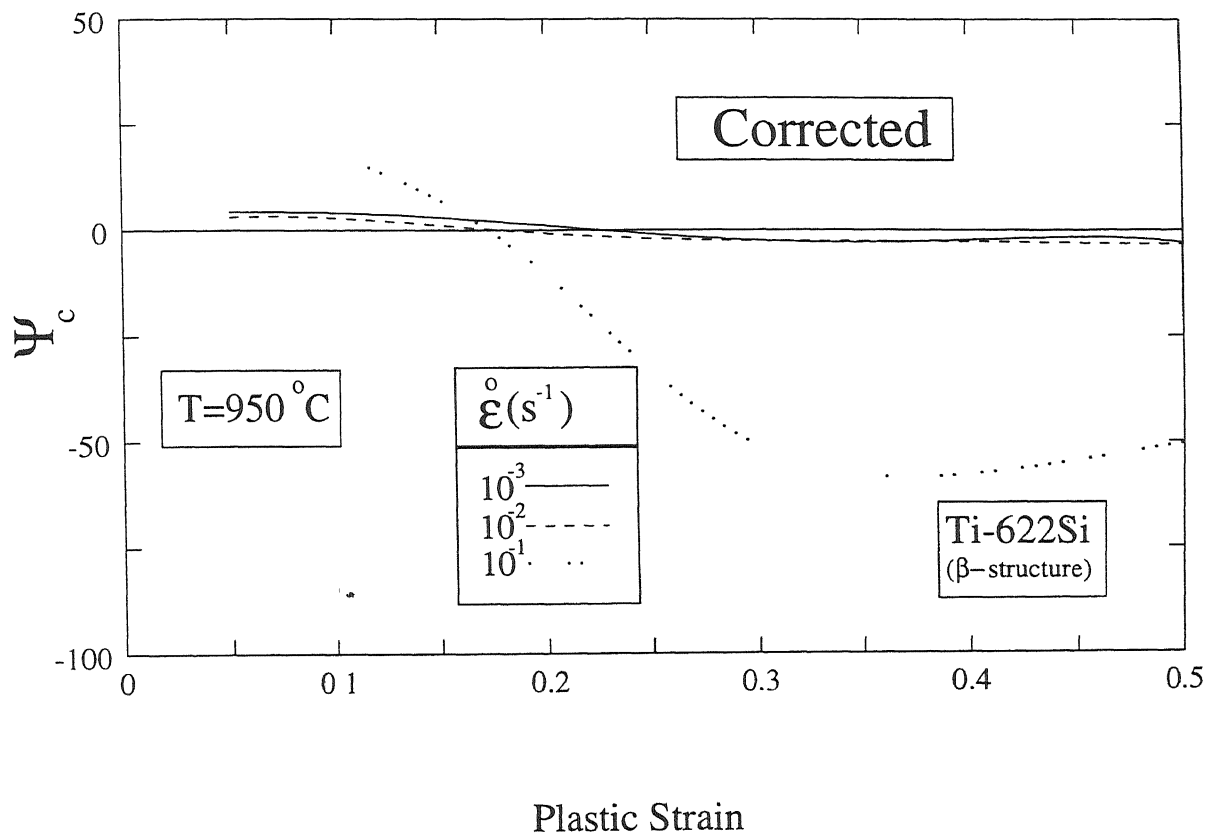


Figure 4.52. Variation of  $\psi_c$  with plastic strain at  $950^\circ\text{C}$  for Ti-622Si( $\beta$ )

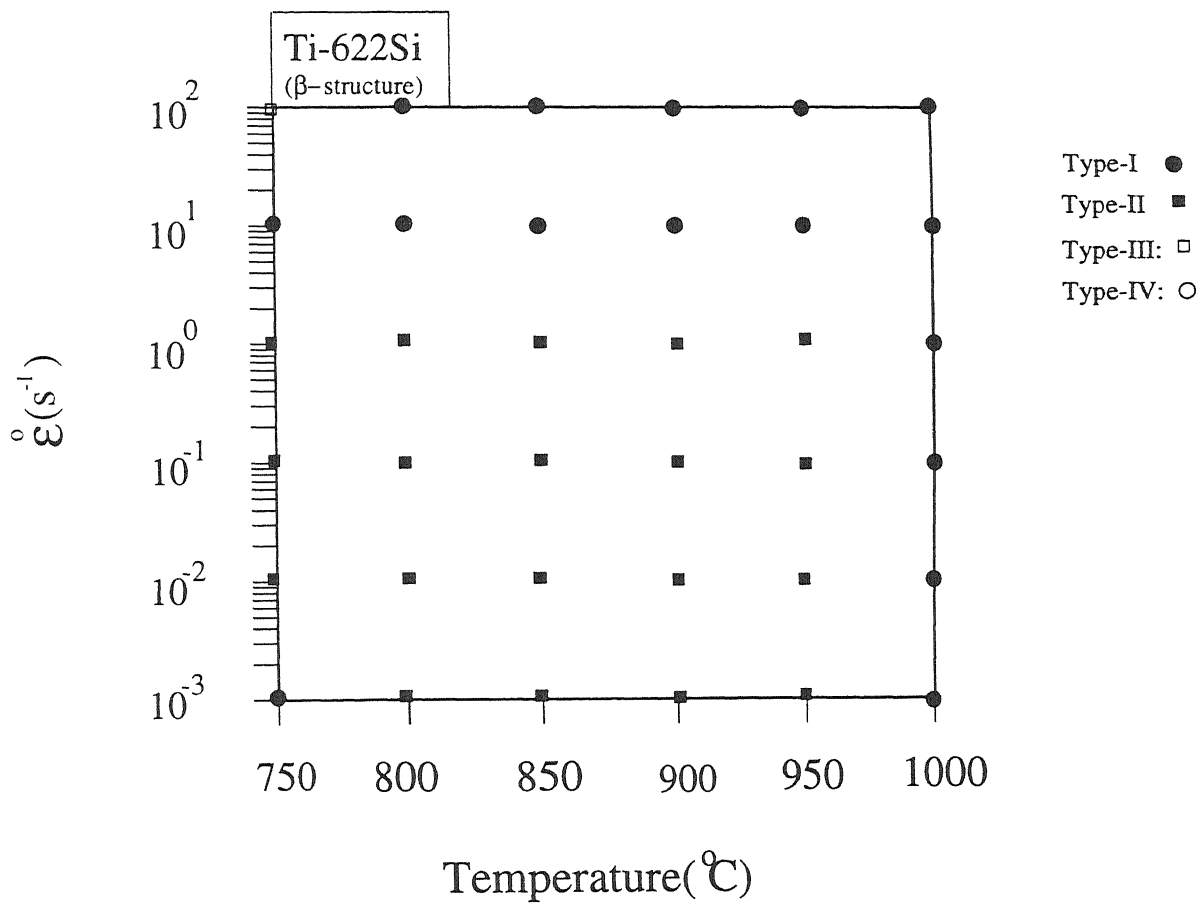


Figure 4 53: Domains for different types of variation of  $\psi_c$  with plastic strain for Ti-622Si( $\beta$ )

flow in Ti-622Si alloy with  $\beta$  microstructure was observed to manifest in the following ways

- (1) Lateral strain inhomogeneity along the compression axis as shown in Figure 4.54 (also shown schematically in Figure 4.55).
- (2) Anisotropic lateral strain leading to an elliptical cross section (shown schematically in Figure 4.55)
- (3) Shear banding (shown in Figures 4.57- 4.58 resulting into mutually opposite drift of the two face centers away from the compression axis (shown schematically in Figure 4.56).

The above mentioned changes were quantified by the parameters  $\lambda$ ,  $e$  and  $\delta$  respectively.  $\lambda$  is defined as

$$\lambda = \frac{D_1}{D_2} \quad (4.21)$$

where  $D_1$  and  $D_2$  are diameter of the the cross-section of the smaller and larger faces respectively (shown schematically in Figure 4.55).  $e$  is defined as

$$e = \frac{D_{min}}{D_{max}} \quad (4.22)$$

where  $D_{min}$  and  $D_{max}$  are the minimum and the maximum diameters of cross section of the top face in mutually orthogonal direction. The shear banding is quantified by the parameter  $\delta$  which is obtained after normalizing the measured drift by the change in the height of the specimen during the compression.

$$\delta = \frac{\delta_p}{\Delta H} \quad (4.23)$$

where  $\delta_p$  and  $\Delta H$  are the measured drift (shown schematically in Figure 4.56) and the change in the height of specimen during compression.

The variation of  $\lambda$  with strain rate at different temperatures is shown in Figure 4.60.  $\lambda$  was found to be close to 1.0 at temperatures of 950°C and 1000°C and at all strain rates.

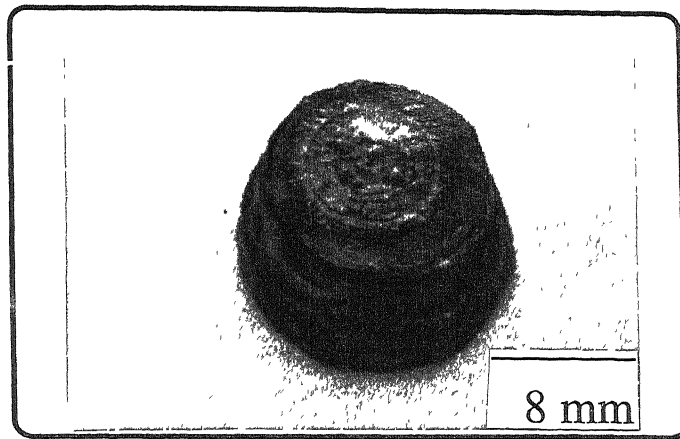


Figure 4.54. Specimen of Ti-622Si( $\beta$ ) deformed at 800°C and  $10^2 \text{ s}^{-1}$  up to a strain of 0.5

At lower temperatures  $\lambda$  was found to be minimum or the lateral strain inhomogeneity was maximum, at intermediate strain rates. On the other hand no particular trend was observed for  $\epsilon$  (Figure 4.61) except the fact that its value was high at lower temperatures and higher strain rates.

$\delta$  was found to increase with increase in strain rate and decrease with increase in temperature, as shown in Figure 4.59. The specimens with high  $\delta$  exhibited shear banding as shown in Figure 4.57- 4.58.

#### 4.2.8 Microstructural Changes in Ti-622Si with $\beta$ Microstructure During its Hot Deformation

The  $\beta$  microstructure of Ti-622Si alloy during the compression in the ( $\alpha+\beta$ ) phase field was found to be unstable and underwent changes including partial transformation to stable ( $\alpha+\beta$ ) microstructure depending upon the temperature and strain rate of the deformation. These changes were identified by comparing the microstructure of deformed specimens with that of undeformed specimens which were equilibrated at different tem-

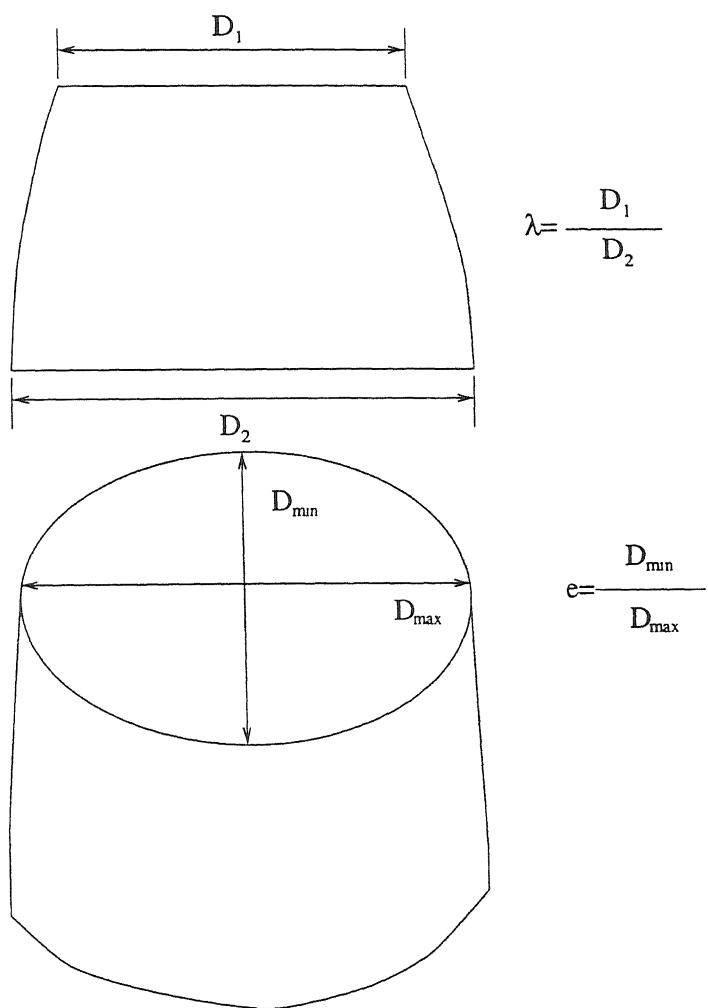


Figure 4.55. Schematic diagram for deformed specimen exhibiting inhomogeneous flow



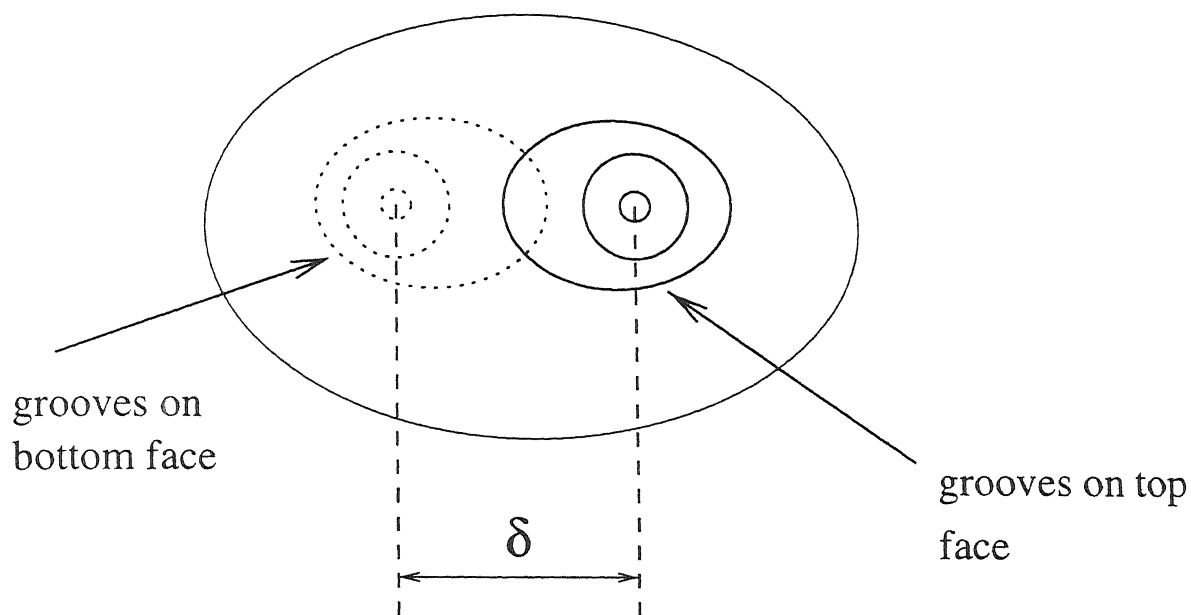


Figure 4.56. Schematic diagram for deformed specimen with misalignment in the centres of the top and the bottom centres

penetrations and were shown in Figure 4.5. The changes that were identified are as follows.

- (1) The straight  $\alpha$  plates underwent bending and kinking. This feature can be observed in Figures 4.62- 4.73.
- (2) Initially the  $\alpha$  plates had more or less uniform thickness along their lengths. However after the compression, thicknesses of some of the  $\alpha$  plates were found to vary along their lengths as shown in Figure 4.62- 4.63.
- (3)  $\beta$  phase penetrated into  $\alpha$  plates resulting into their fragmentation. In Figures 4.75- 4.76 the  $\beta$  penetration into  $\alpha$  is indicated. The  $\beta$  penetration was found to be of two types. In certain cases the penetration resembled pits which were occasionally found to become wider with the depth of penetration as the one shown in Figure 4.63. On the other hand the penetration resembled a wedge in Figure 4.75- 4.76. The fragmentation of the  $\alpha$  plates occurring due to the  $\beta$  penetration led to the formation of small fraction of equiaxed  $\alpha$  and thus partial

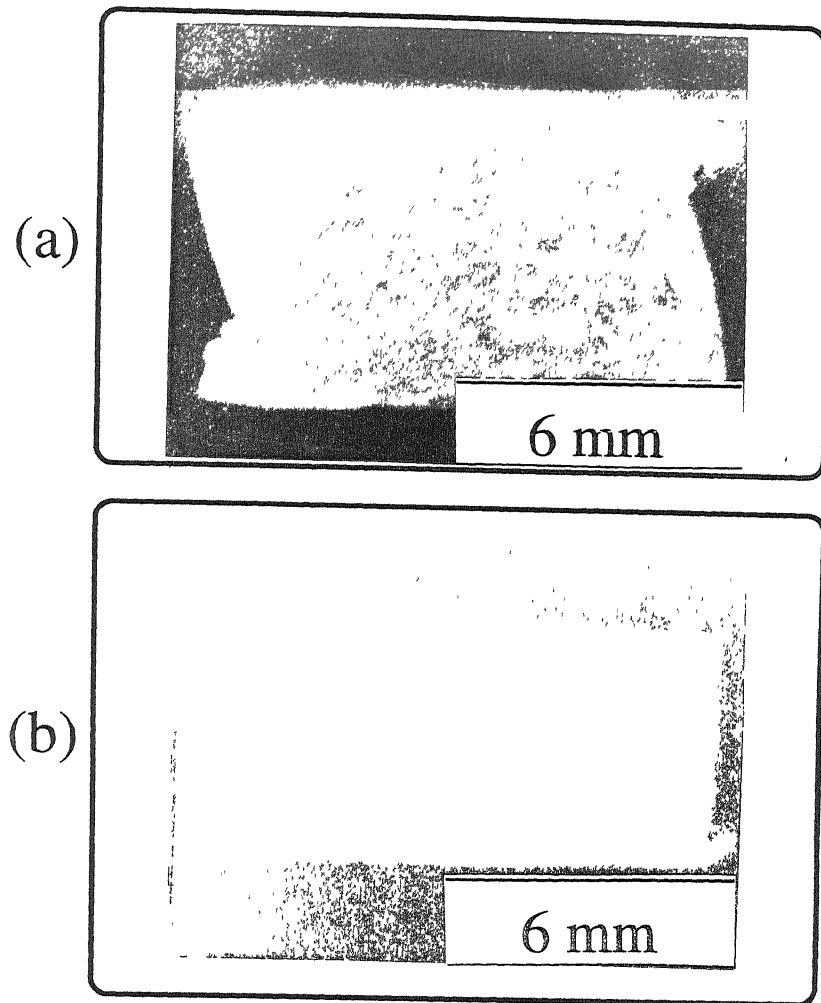


Figure 4.57: Shear banding in specimens of Ti-622Si( $\beta$ ) deformed at: (a)  $750^{\circ}\text{C}/10\text{ s}^{-1}$   
(b)  $750^{\circ}\text{C}/10^2\text{ s}^{-1}$

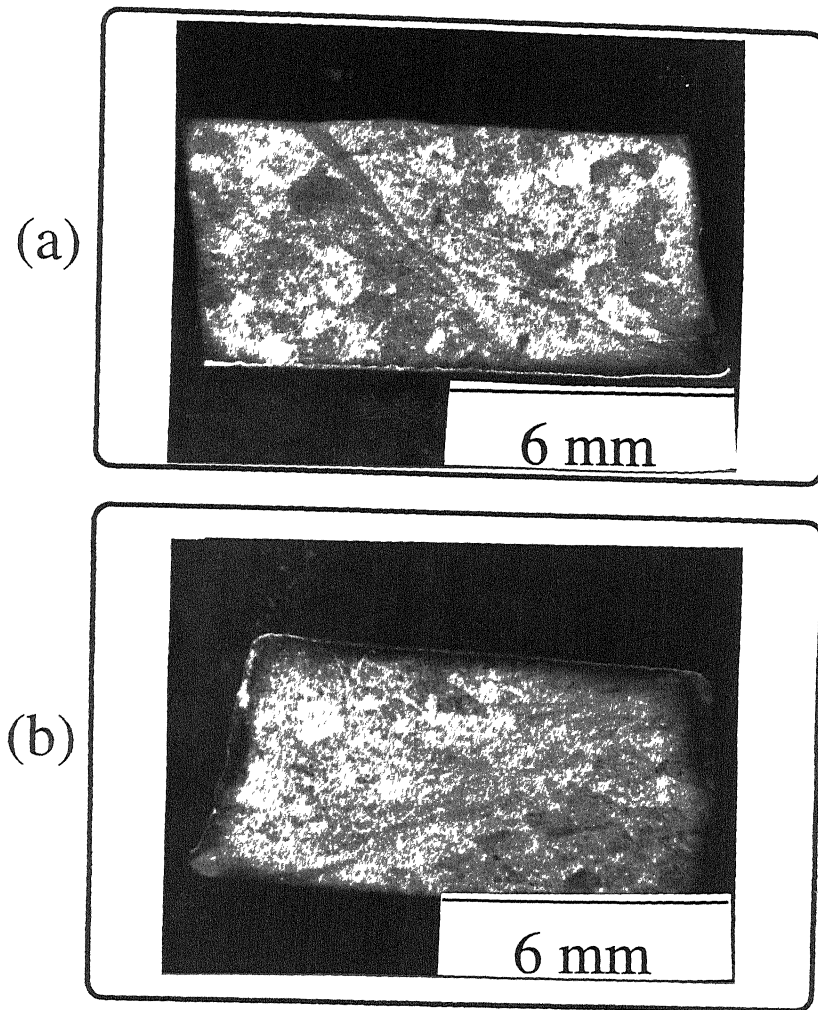


Figure 4.58: Shear banding in specimens of Ti-622Si( $\beta$ ) deformed at: (a)  $800^{\circ}\text{C}/10^2 \text{ s}^{-1}$  and (b)  $900^{\circ}\text{C}/10^2 \text{ s}^{-1}$

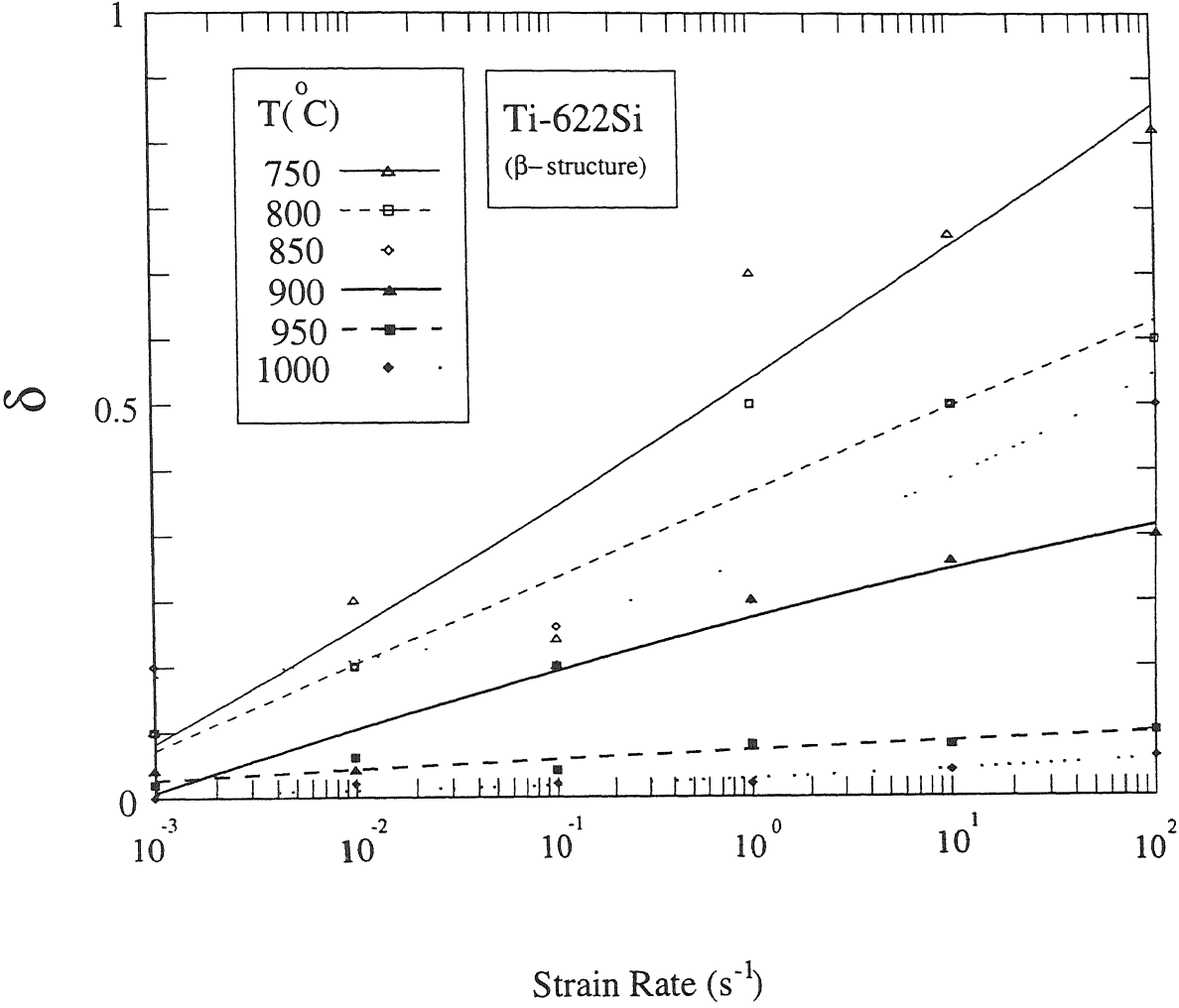
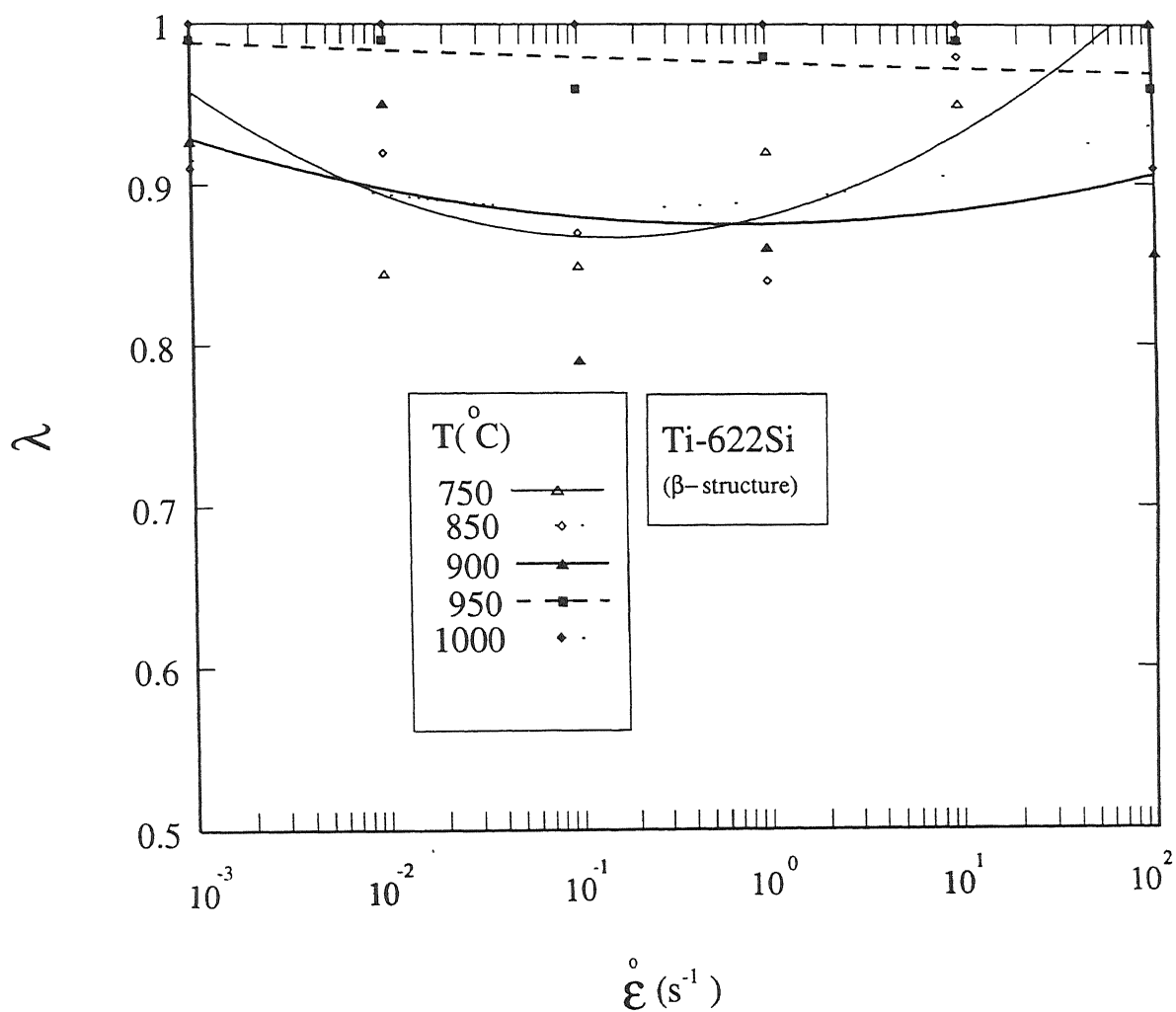
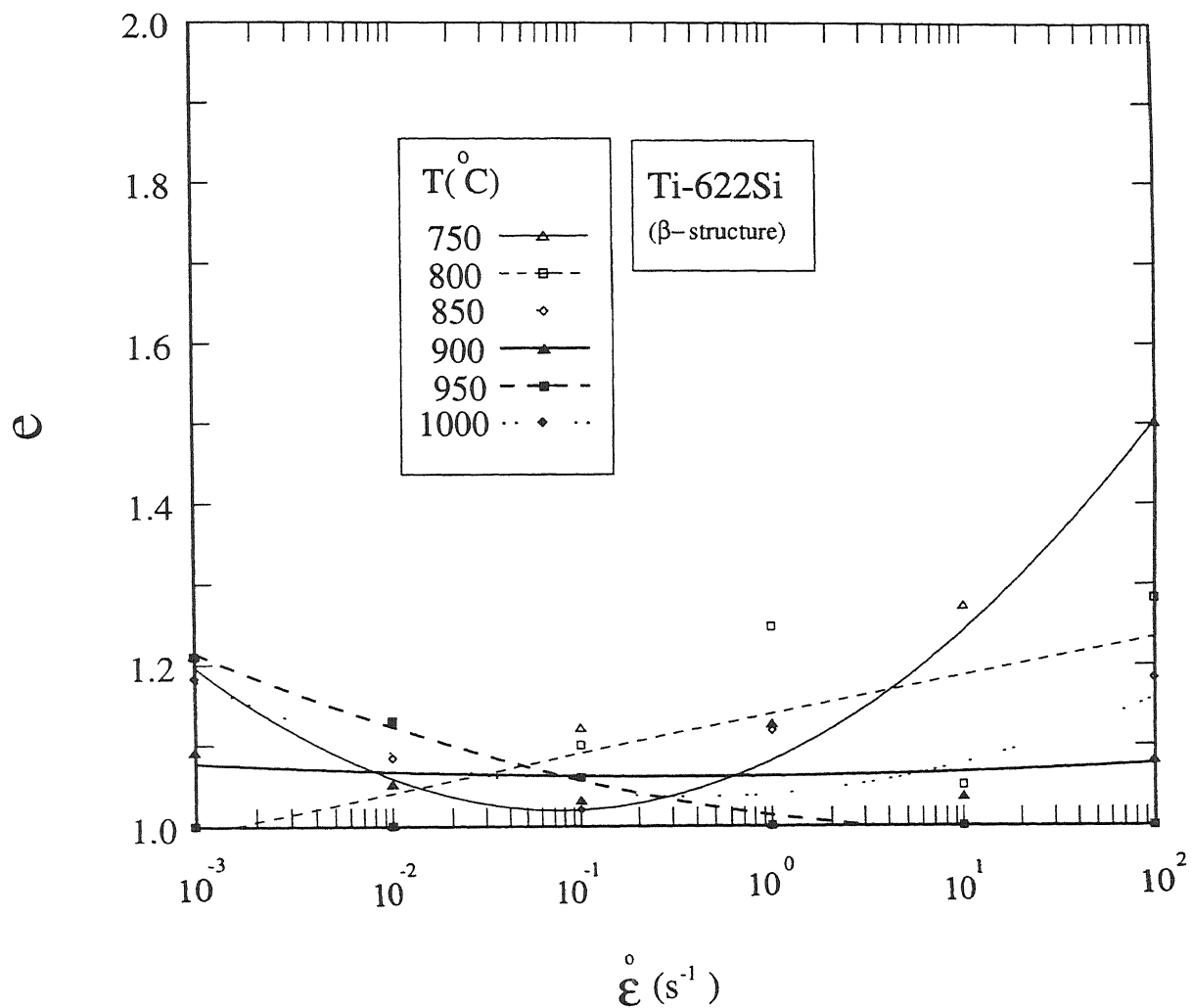


Figure 4.59: Variation of  $\delta$  with strain rate for Ti-622Si( $\beta$ )

Figure 4.60: Variation of  $\lambda$  with strain rate for Ti-622Si( $\beta$ )

Figure 4.61: Variation of  $e$  with strain rate for Ti-622Si( $\beta$ )

transformation to  $(\alpha+\beta)$  microstructure.

- (4) Cross linking between two adjacent  $\alpha$  plates occurred during the deformation as indicated in Figures 4.62- 4.63.
- (5) Coarsening of  $\alpha$  plates occurred. This is evident from by comparing the  $\alpha$  plate thickness in Figure 4.5 and Figure 4.74.

The extent of the above mentioned changes occurring in the  $\alpha$  plates varied with the temperature as well as the strain rate of deformation and will be discussed separately. Special microstructural features were observed in the intense shear bands of the specimens deformed at 750°C and 800°C and at a strain rate of  $10^2\text{s}^{-1}$ . These features as well as the microstructural evolution in the  $\beta$  phase field will be also separately discussed.

### Effect of Temperature on the Microstructural Evolution in the $(\alpha+\beta)$ Phase Field

With the increase in deformation temperature the extent of fragmentation and coarsening of the  $\alpha$  plates was found to increase at all strain rates. This is evident from the microstructures of the specimens deformed at the temperatures of 750°C, 850°C and 950°C and at strain rates of  $10^{-3}\text{s}^{-1}$  and  $10^2\text{s}^{-1}$ , which are shown in Figures 4.62, 4.72, 4.74, 4.68 and 4.76. During deformation at low strain rates and low deformation temperatures, the plate thicknesses in the specimens deformed at low strain rates was highly uneven along their lengths as shown in Figure 4.62. However with the increase in the deformation temperature the plate thickness in the deformed specimen tended to become uniform along their lengths. The  $\beta$  penetration into the  $\alpha$  plates was also found to vary with the temperature of deformation. At lower temperatures the penetration resembled pit formation whereas at high temperature wedge like  $\beta$  cusp was formed.

## Effect of Strain Rate on the Microstructural Evolution in the $(\alpha+\beta)$ Phase Field

With the increase in strain rate, the extent of  $\beta$  penetration and thus the fragmentation of  $\alpha$  plates, as well as the coarsening of  $\alpha$  was found to decrease. At temperatures varying between 750°C and 850°C the fragmentation of  $\alpha$  was absent and plate thickness was found to reduce during the deformation at high strain rates, except within the intense shear bands in the specimens deformed at 750°C and 800°C and at a strain rate of  $10^2\text{s}^{-1}$ . On increasing the strain rate the non uniformity in the plate thickness along the length of the  $\alpha$  plates that were observed at lower temperatures tended to disappear.

### Microstructural Changes within the Shear Bands

At lower temperatures and high strain rates the deformation within the specimens was highly nonuniform and shear banding occurred. The extent of deformation outside the shear band was less. Thus very little change in the Widmanstätten morphology as well as the plate thickness could be observed in the regions of the specimen outside the shear band, as can be seen from Figures 4.65 and 4.67. Figures 4.64, 4.66, 4.68, 4.70 and 4.79 shows the microstructure within shear band in specimens deformed at  $750^\circ\text{C}/10\text{s}^{-1}$ ,  $750^\circ\text{C}/10^2\text{s}^{-1}$ ,  $800^\circ\text{C}/10^2\text{s}^{-1}$  and  $900^\circ\text{C}/10^2\text{s}^{-1}$ . The microstructure within the shear band in the specimens consisted of  $\alpha$  plates which have either got oriented along the band or were found to be kinked in the direction perpendicular to shear band.

Within shear bands of specimen deformed at  $800^\circ\text{C}/10^2\text{s}^{-1}$  and  $750^\circ\text{C}/10^2\text{s}^{-1}$  separate and more intense bands were observed. The microstructure of the intense band in the specimen deformed at  $750^\circ\text{C}/10^2\text{s}^{-1}$  is shown in Figure 4.69. It consists of very low volume fraction of primary equiaxed  $\alpha$  which have been fragmented into very small size (1-2  $\mu\text{m}$ ). Apart from it, equiaxed prior  $\beta$  grains having size of 1-2  $\mu\text{m}$ , within which



secondary  $\alpha$  had precipitated, constituted the major fraction of microstructure. A small fraction of secondary equiaxed  $\beta$  grains without any presence of precipitated secondary  $\alpha$  were also observed. Along the prior  $\beta$ - $\beta$  boundaries relatively coarser  $\alpha$  plates were precipitated. The microstructure in the fold over region was also similar to more intense band. Microstructure of intense band in the specimen deformed at  $800^{\circ}\text{C}/10^2\text{s}^{-1}$  is shown in Figure 4.71. It indicates the fragmentation resulting into formation of  $(\alpha+\beta)$  structure had occurred having ultrafine size of  $\alpha$ .

#### 4.2.9 Microstructural Evolution of Ti-622Si During Deformation in the $\beta$ Phase Field

Figures 4.77- 4.80 shows the microstructure of Ti-622Si in the  $\beta$  phase field at strain rates of  $10^{-3}\text{ s}^{-1}$ ,  $10^{-1}\text{ s}^{-1}$  and  $10^2\text{ s}^{-1}$  respectively. At strain rates of  $10^{-3}\text{ s}^{-1}$  and  $10^{-1}\text{ s}^{-1}$  bulges at the grain boundaries can be observed. However recrystallization near the prior  $\beta$  grain boundaries could be observed at the higher strain rates, i.e.  $10\text{ s}^{-1}$  and  $10^2\text{ s}^{-1}$ .

### 4.3 Flow behaviour of Ti-622Si With Equiaxed Structure

Ti-622Si alloy in conditions TMT, TMT-A1, TMT-A2 and TMT-A3 were subjected to step strain rate tests at temperatures ranging from  $750^{\circ}\text{C}$  to  $960^{\circ}\text{C}$  and in the strain rate range of  $10^{-5}\text{ s}^{-1}$  to  $5\times 10^{-2}\text{ s}^{-1}$ . The variation of true stress with strain rate at different temperatures, for TMT and TMT-A3 are shown in Figure 4.81- 4.82. The true stresses as well as the strain rates in these figures were plotted in logarithmic scale. The strain rate sensitivity ( $m$ ) at different strain rates, for the alloy in TMT, TMT-A1, TMT-A2

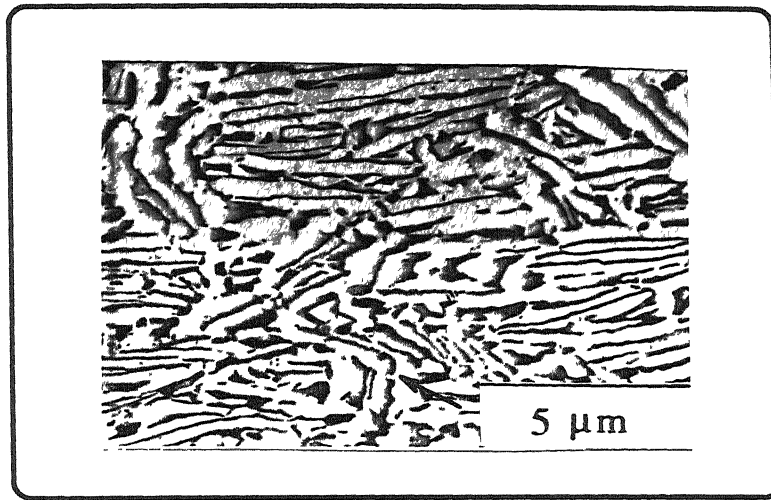


Figure 4.62. Microstructure of Ti-622Si( $\beta$ ) following deformation at 750°C/10<sup>-3</sup> s<sup>-1</sup> upto a strain of 0.5

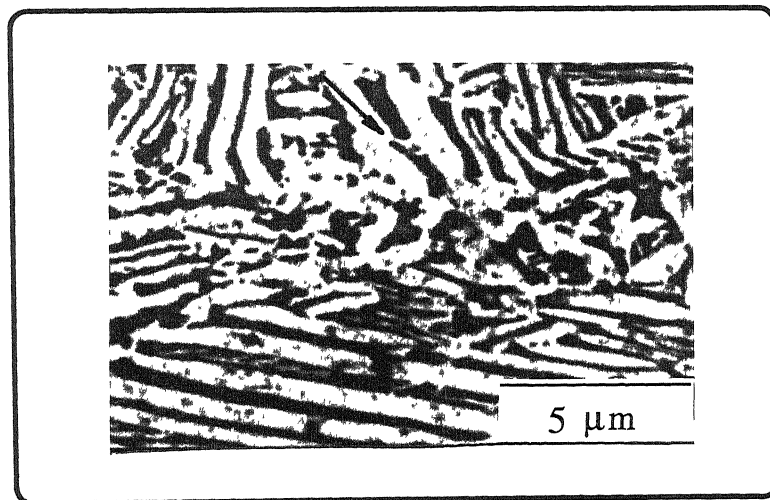


Figure 4.63: Microstructure of Ti-622Si( $\beta$ ) following deformation at 750°C/10<sup>-2</sup> s<sup>-1</sup> upto a strain of 0.5

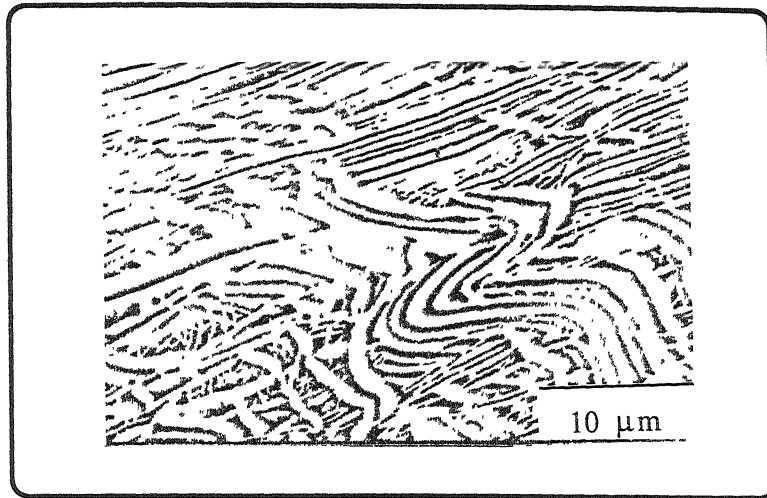


Figure 4.64 Microstructure of Ti-622Si( $\beta$ ) within shear band following deformation at  $750^{\circ}\text{C}/10\text{ s}^{-1}$  upto a strain of 0.5

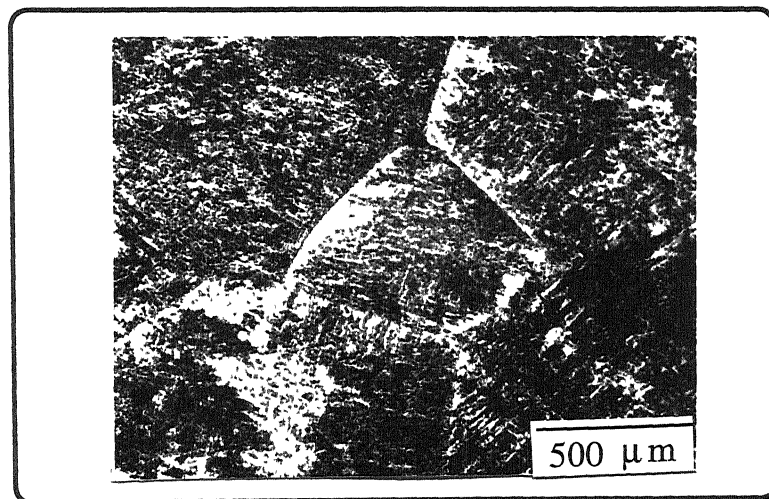


Figure 4.65: Microstructure of Ti-622Si( $\beta$ ) outside the shear band following deformation at  $750^{\circ}\text{C}/10^2\text{ s}^{-1}$  upto a strain of 0.5 (at low magnification)

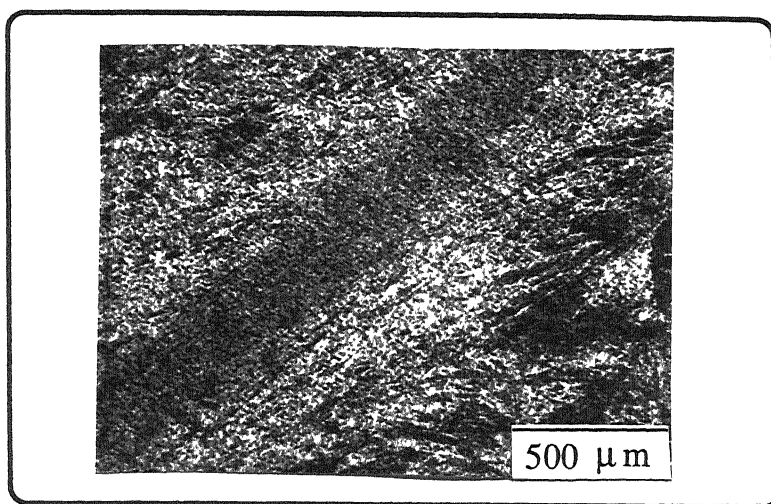


Figure 4.66 Microstructure of the shear band following deformation of Ti-622Si( $\beta$ ) at  $750^\circ\text{C}/10^2 \text{ s}^{-1}$  upto a strain of 0.5 (at low magnification)

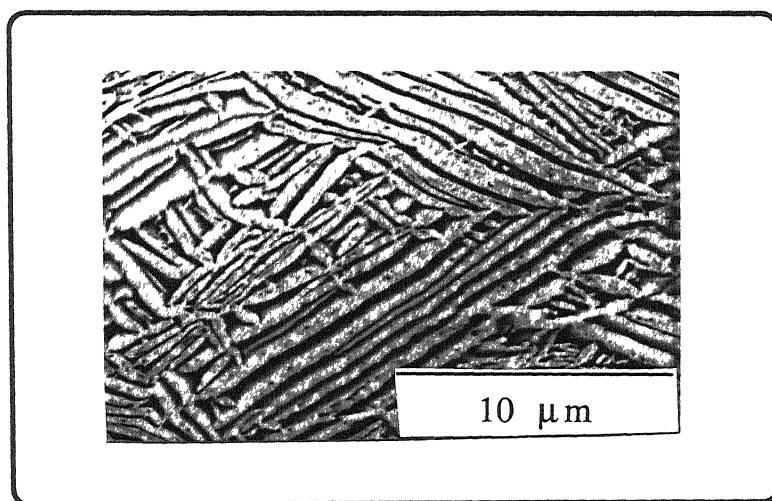


Figure 4.67: Microstructure of Ti-622Si( $\beta$ ) outside the shear band following deformation at  $750^\circ\text{C}/10^2 \text{ s}^{-1}$  upto a strain of 0.5

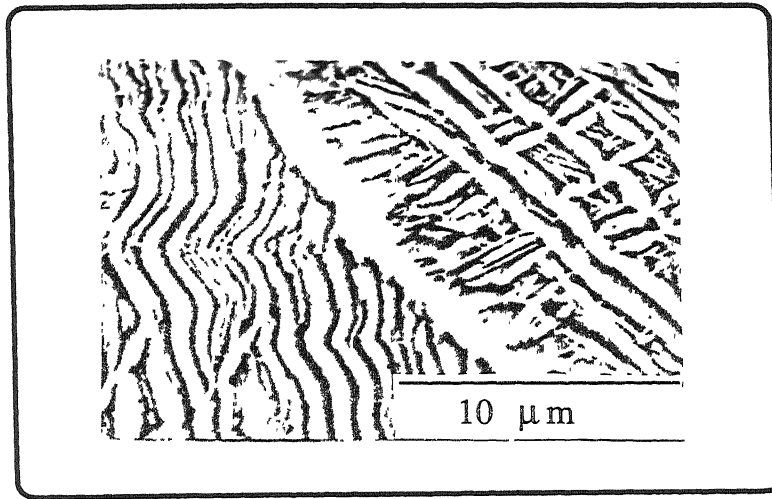


Figure 4.68: Microstructure of Ti-622Si( $\beta$ ) within shear band following deformation at  $750^{\circ}\text{C}/10^2 \text{ s}^{-1}$  upto a strain of 0.5

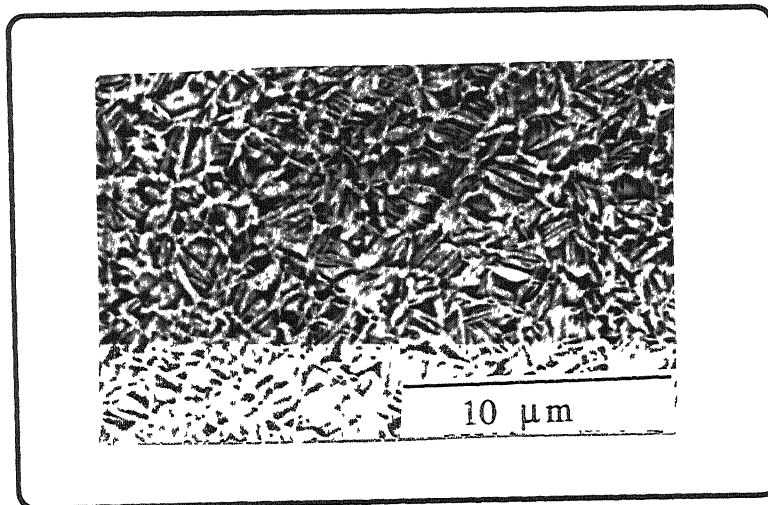


Figure 4.69: Microstructure of Ti-622Si( $\beta$ ) within shear band (intense zone) following deformation at  $750^{\circ}\text{C}/10^2 \text{ s}^{-1}$  upto a strain of 0.5

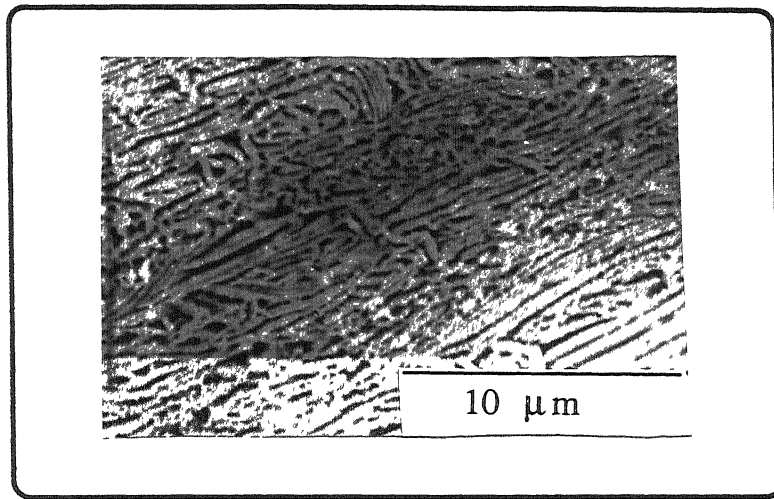


Figure 4.70: Microstructure of Ti-622Si( $\beta$ ) within shear band following deformation at  $800^{\circ}\text{C}/10^2 \text{ s}^{-1}$  upto a strain of 0.5

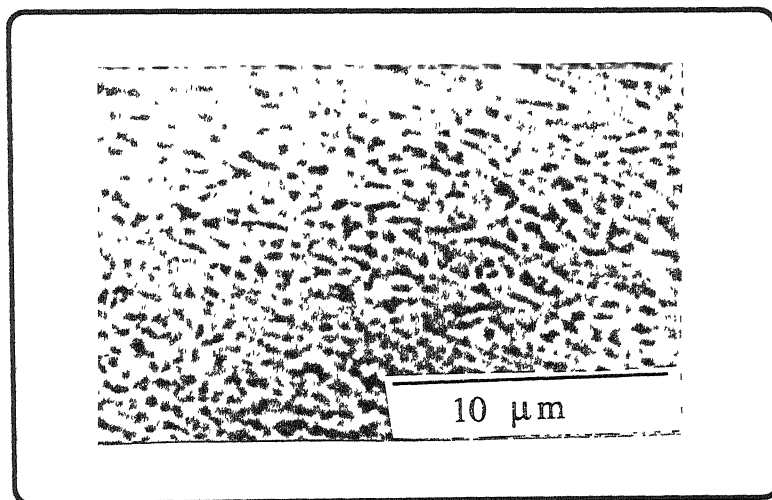


Figure 4.71: Microstructure of Ti-622Si( $\beta$ ) within shear band (intense zone) following deformation at  $800^{\circ}\text{C}/10^2 \text{ s}^{-1}$  upto a strain of 0.5

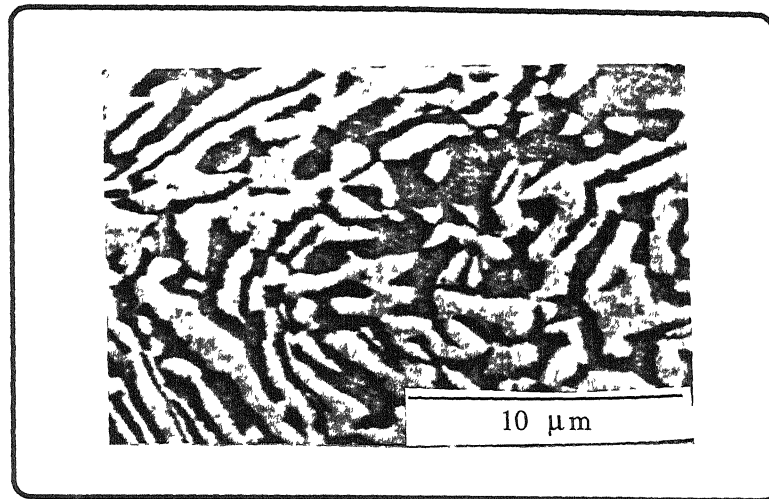


Figure 4.72: Microstructure of Ti-622Si( $\beta$ ) following deformation at  $850^{\circ}\text{C}/10^{-3} \text{ s}^{-1}$  upto a strain of 0.5

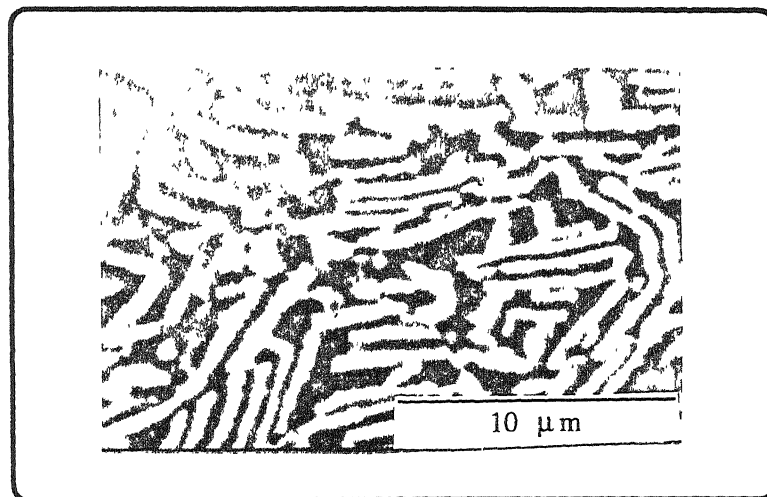


Figure 4.73: Microstructure of Ti-622Si( $\beta$ ) following deformation at  $900^{\circ}\text{C}/10^{-1} \text{ s}^{-1}$  upto a strain of 0.5

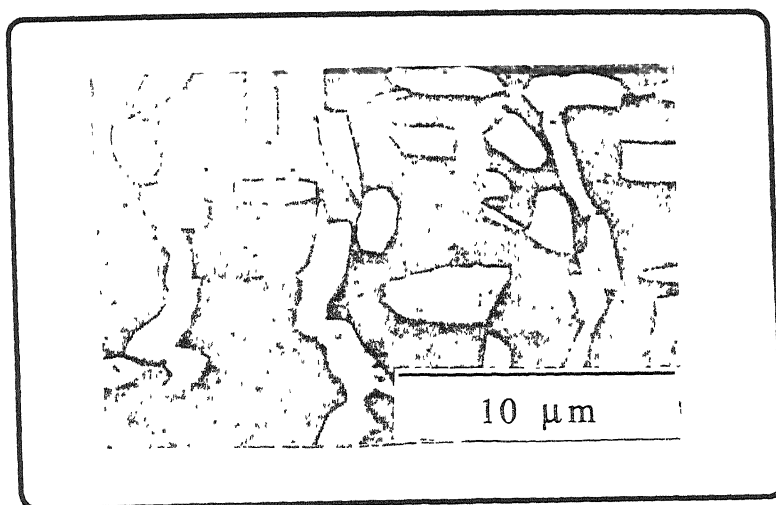


Figure 4.74: Microstructure of Ti-62.2Si( $\beta$ ) following deformation at 950°C/10<sup>-3</sup> s<sup>-1</sup> upto a strain of 0.5

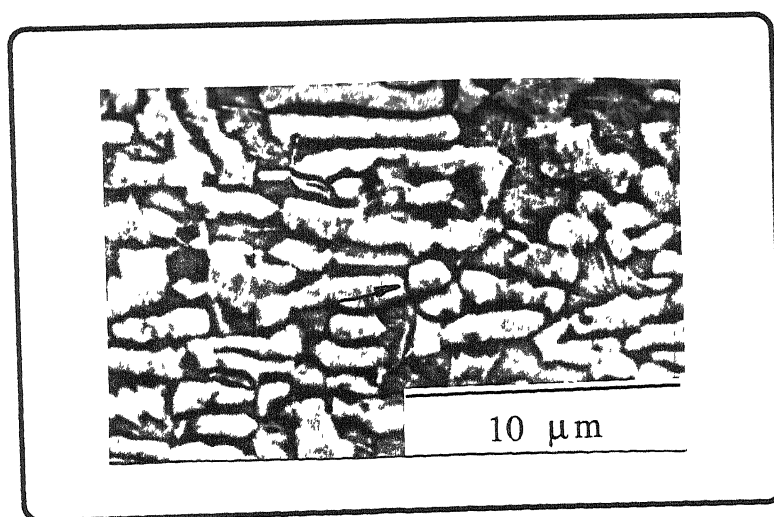


Figure 4.75: Microstructure of Ti-62.2Si( $\beta$ ) following deformation at 950°C/1 s<sup>-1</sup> upto a strain of 0.5



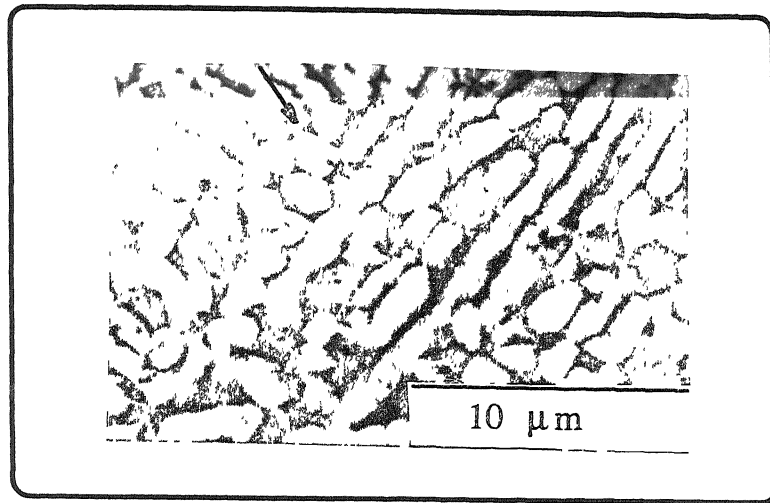


Figure 4.76: Microstructure of Ti-622Si( $\beta$ ) following deformation at  $950^{\circ}\text{C}/10^2\text{ s}^{-1}$  upto a strain of 0.5

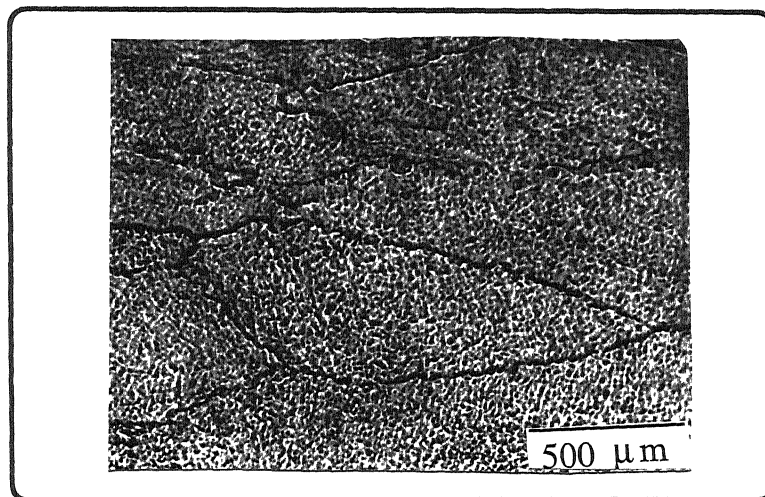


Figure 4.77: Microstructure of Ti-622Si( $\beta$ ) following deformation at  $1000^{\circ}\text{C}/10^{-3}\text{ s}^{-1}$  upto a strain of 0.5

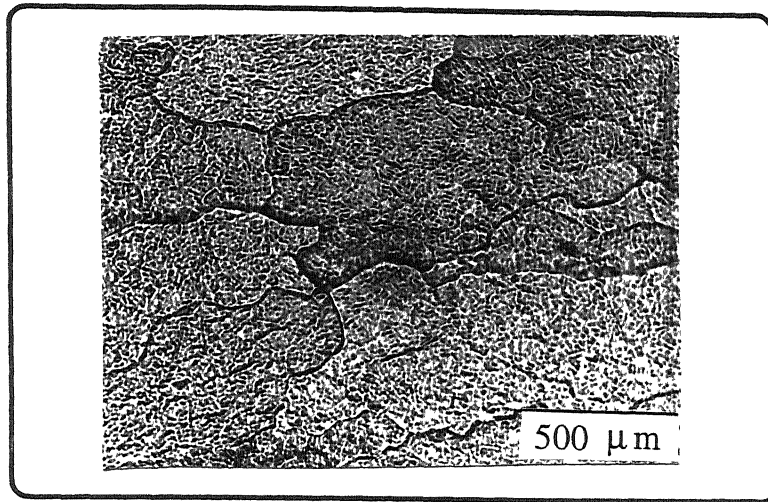


Figure 4.78: Microstructure of Ti-622Si( $\beta$ ) following deformation at  $1000^{\circ}\text{C}/10^{-1} \text{ s}^{-1}$  upto a strain of 0.5

and TMT-A3 was obtained directly from the step strain rate tests using the relationship

$$m = \frac{\log(\frac{L_2}{L_1})}{\log(\frac{v_2}{v_1})} \quad (4.24)$$

where  $L_1$  and  $L_2$  are steady state loads corresponding to cross-head speeds of  $v_1$  and  $v_2$  respectively and  $m$  is the strain rate sensitivity at strain rate corresponding to cross-head speed of  $v_1$ . Figure 4.83- 4.85 shows the variation of  $m$  with strain rate at different temperatures, for the alloy in conditions TMT, TMT-A2 and TMT-A3.

From the observed variation of strain rate sensitivity with strain rate for all the four conditions the following was concluded.

- (1) Ti-622Si alloy in conditions TMT-A1, TMT-A2 and TMT-A3 exhibited region II and III of superplasticity.
- (2) Ti-622Si alloy in conditions TMT condition exhibits region II and region III, at temperatures varying between  $750^{\circ}\text{C}$  to  $850^{\circ}\text{C}$  and at temperatures above  $940^{\circ}\text{C}$ . Best fit line was drawn through the

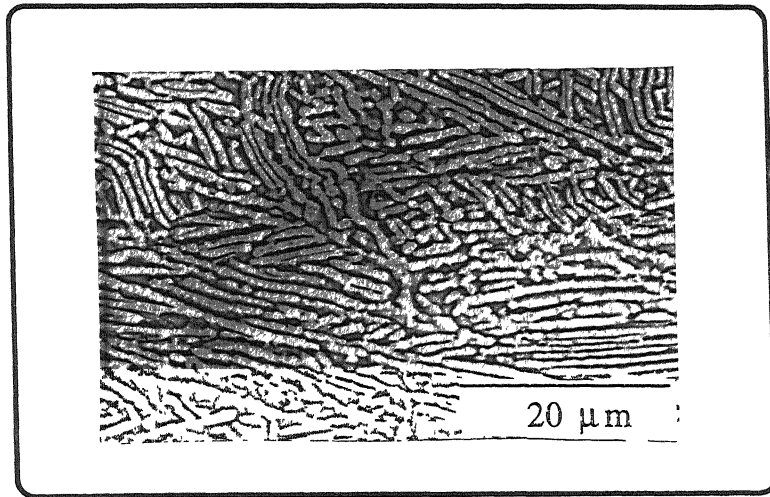


Figure 4.79. Microstructure of Ti-622Si( $\beta$ ) following deformation at  $900^{\circ}\text{C}/10^2 \text{ s}^{-1}$  upto a strain of 0.5

- (3) However, the alloy in TMT condition exhibited region I at strain rates varying between  $10^{-5} \text{ s}^{-1}$ - $5 \times 10^{-4} \text{ s}^{-1}$   $\log \frac{\dot{\epsilon}}{\sigma^n}$  versus  $\log d$  plot and the slope was taken as the grain-size exponent. and region II and III at higher strain rates.
- (4) The transition strain rate between regions II and III varied with grain size and temperature. It was observed to increase with increase in the test temperature for any grain size and decrease in grain size at given temperature.
- (5) The strain rate sensitivity in region II mostly varied from 0.4 to 0.6 except at few points. On the whole the strain rate sensitivity was found to increase with increase in temperature for a given strain rate. Similarly in region III it varied from 0.22 to 0.28.

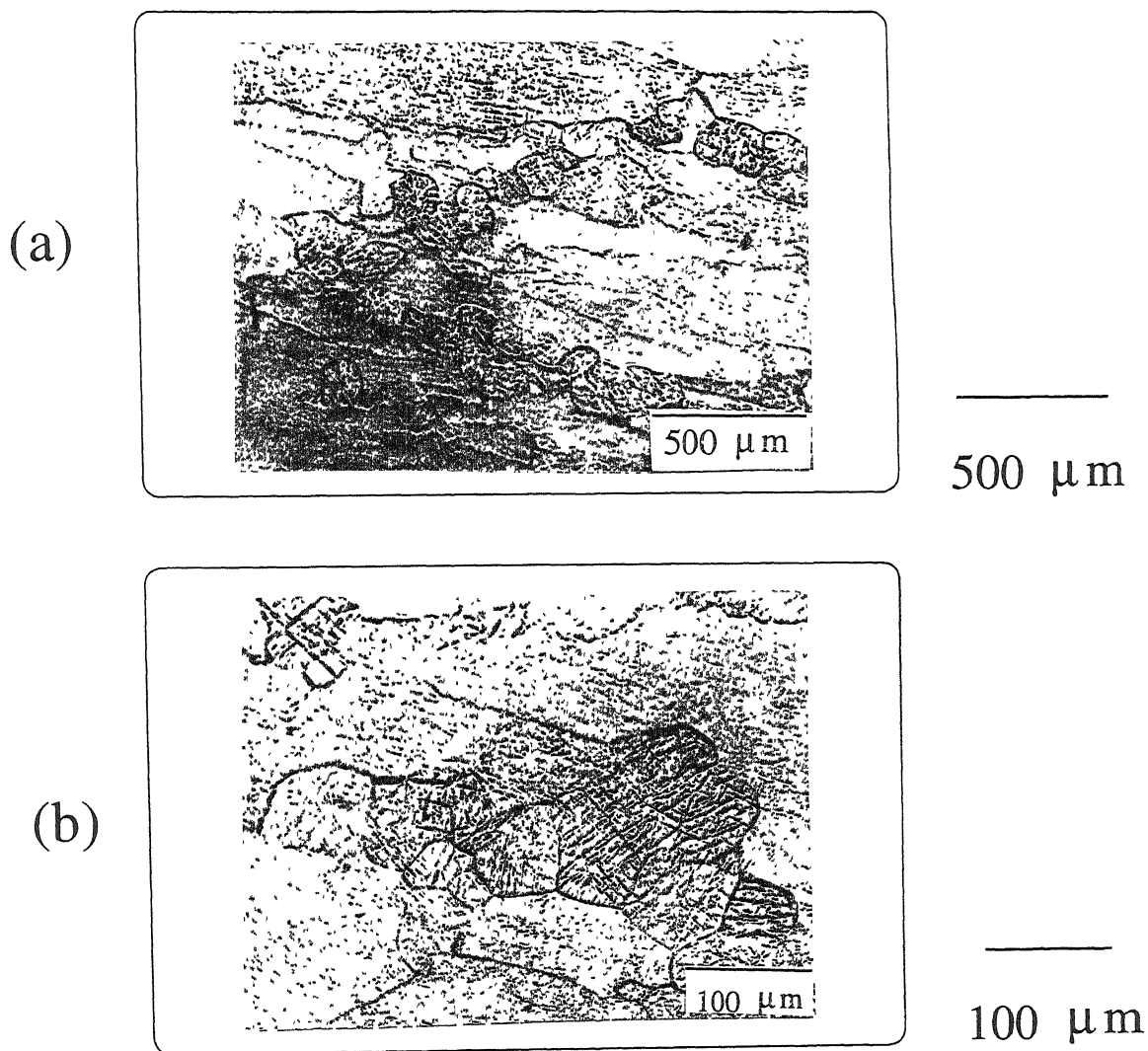


Figure 4.80: Microstructure of Ti-622Si( $\beta$ ) following deformation at  $1000^{\circ}\text{C}/10^2 \text{ s}^{-1}$  upto a strain of 0.5 at (a) lower and (b) higher magnifications

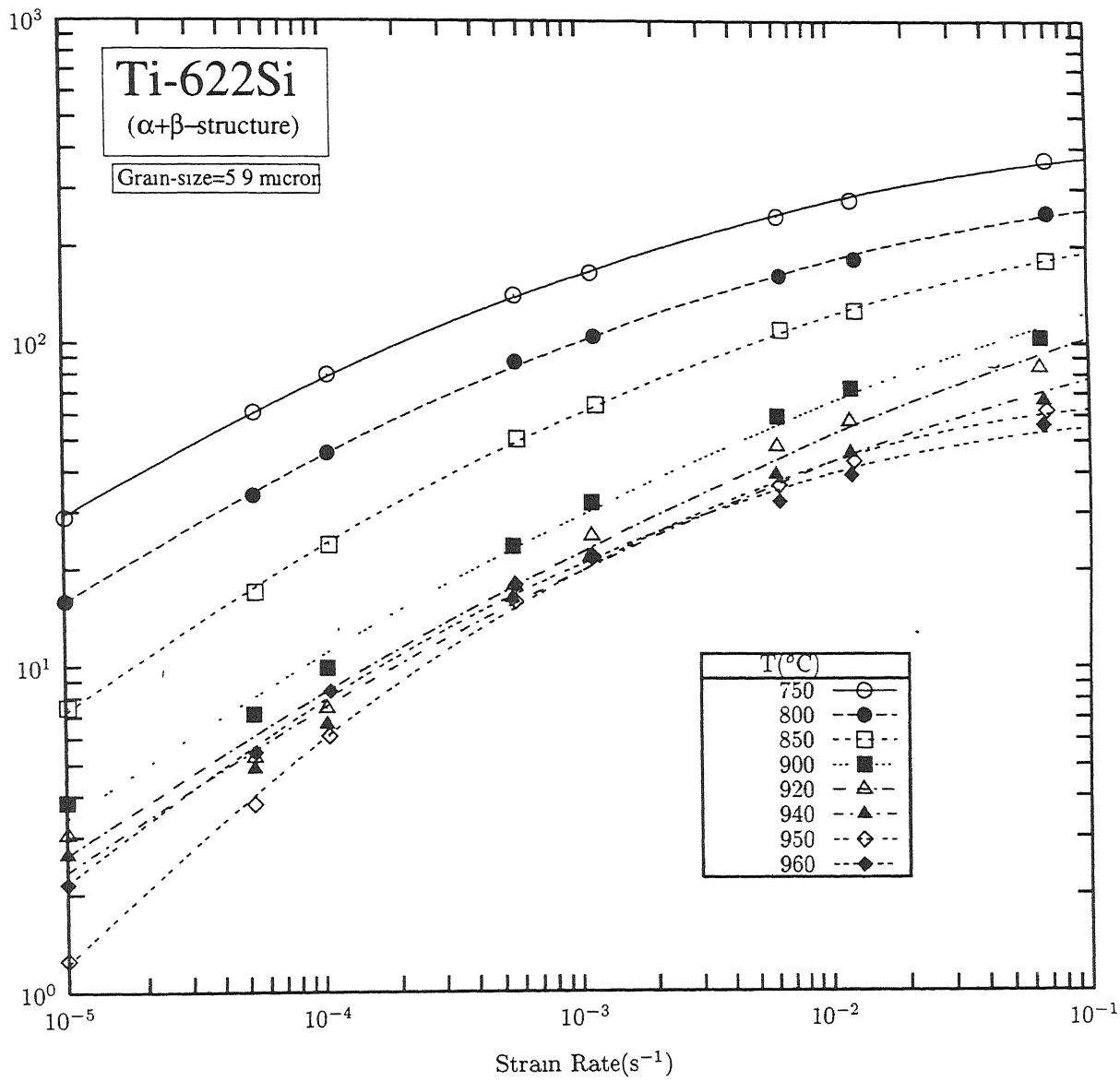


Figure 4.81: Plot of true stress versus strain rate for Ti-622Si in TMT condition

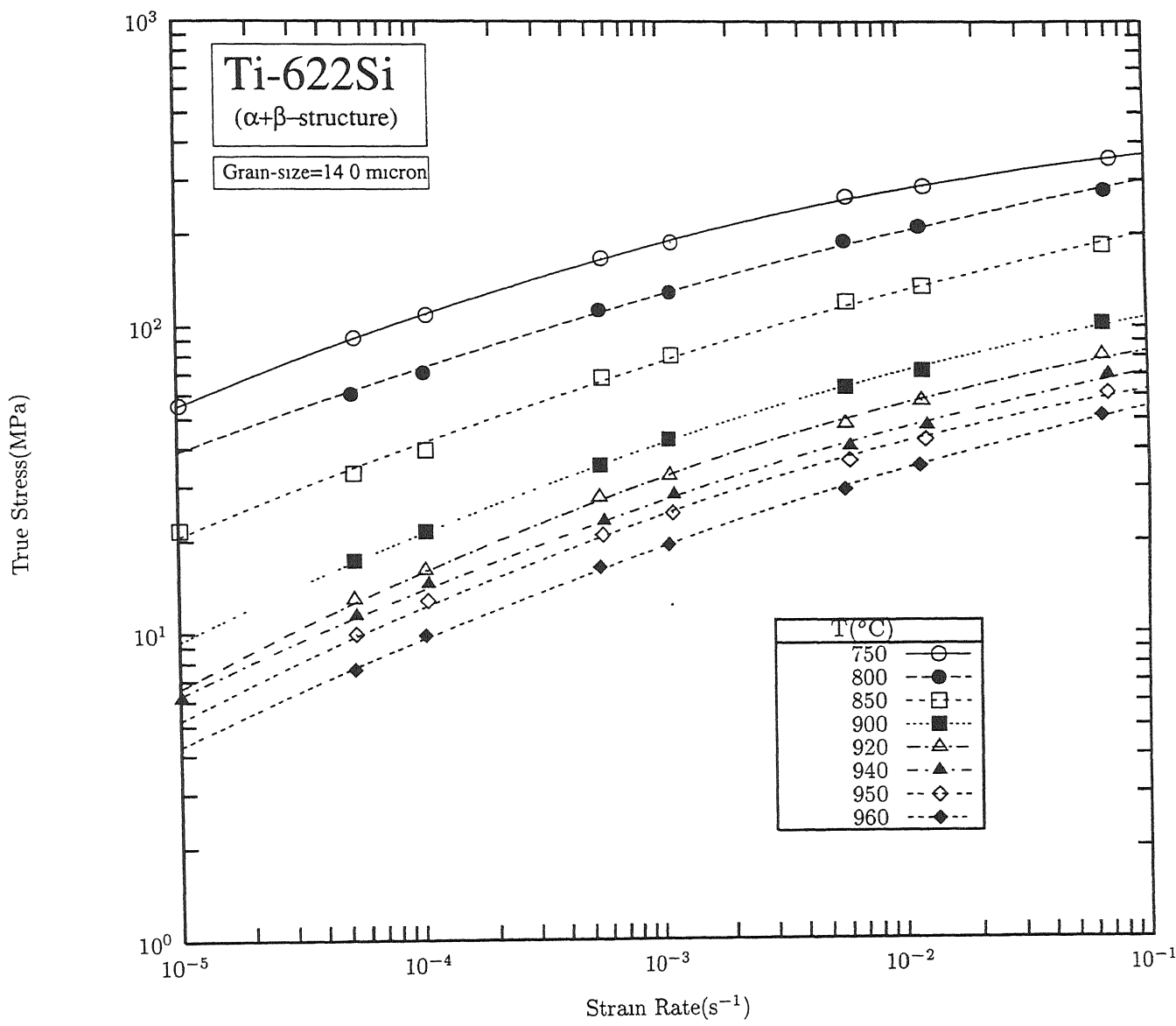


Figure 4.82: Plot of true stress versus strain rate for Ti-622Si in TMT-A3 condition

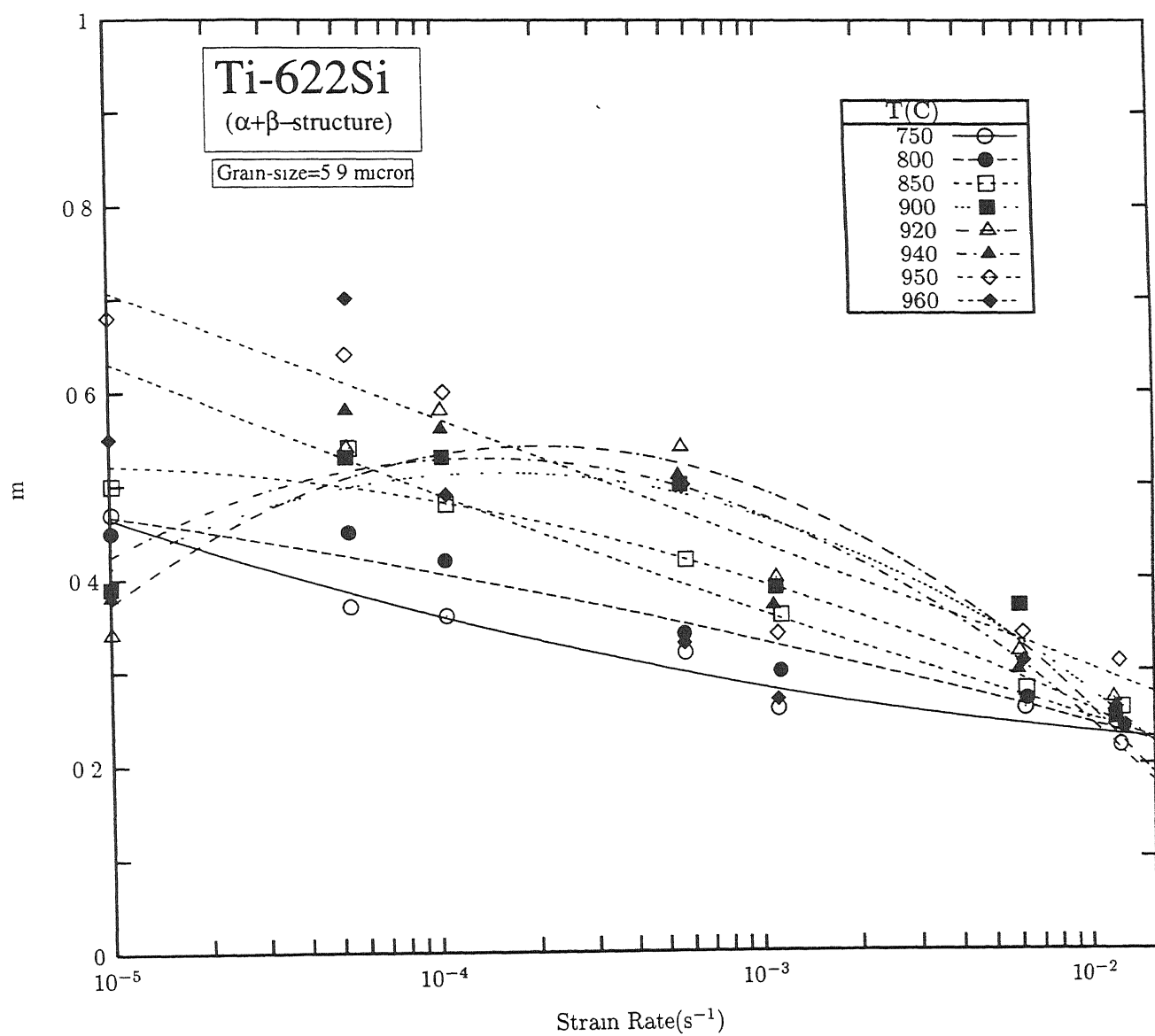


Figure 4.83: Plot of strain rate sensitivity versus strain rate for Ti-622Si in TMT condition

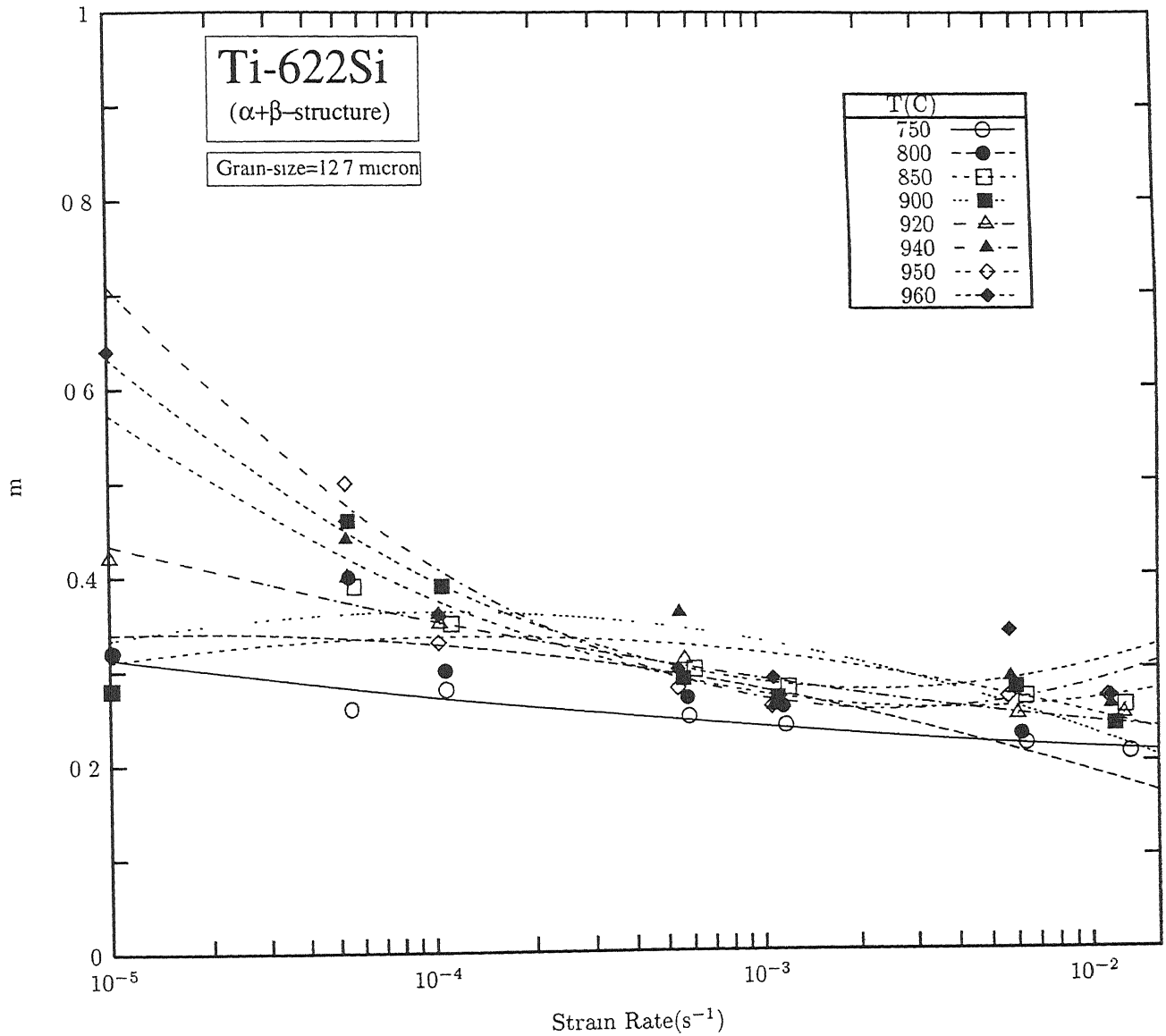


Figure 4.84: Plot of strain rate sensitivity versus strain rate for Ti-622Si in TMT-A2 condition



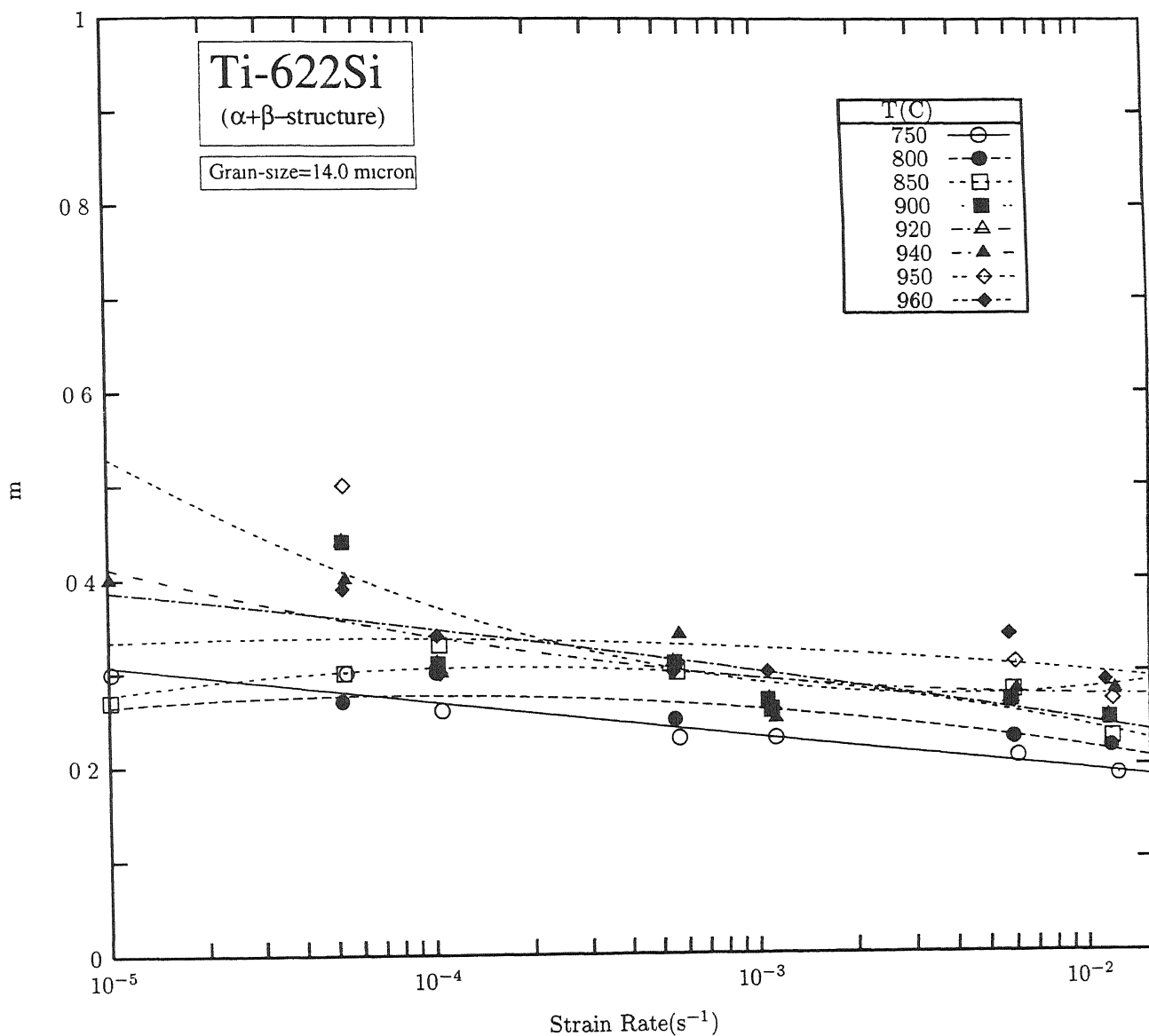


Figure 4.85: Plot of strain rate sensitivity versus strain rate for Ti-622Si in TMT-A3 condition

### 4.3.1 Constitutive Behaviour

As mentioned in Chapter 1 [13], the empirical relationship governing the steady state deformation of superplastic materials in the region I,II and III is written in the non-dimensional form as

$$\dot{\epsilon} = \frac{AD_oEb}{kT} \left(\frac{b}{d}\right)^p \left(\frac{\sigma}{E}\right)^n e^{-\frac{Q}{RT}} \quad (4.25)$$

where E is the Young's modulus,  $D_o$  is the diffusivity coefficient, d is average grain size, b is the burgers vector or atom size, k is the Boltzmann constant and A is dimensionless constant. The parameters of the constitutive relationship in the regions II and III have been calculated from the stress-strain rate data at different temperatures for Ti-622Si specimens with different grain sizes(at room temperature) This has not been attempted for region I due to lack of data over a wide range of strain rate, temperature and grain size.

### 4.3.2 Parameters of Constitutive Relationship for Region II

It was mentioned in the previous section that the strain rate sensitivity in the region II of superplasticity varied within a narrow range, i.e.  $0.5 \pm 0.1$ , barring few points. Therefore the sensitivity can be assumed to be independent of strain rate, temperature and grain size in this region and equal to 0.5.

The grain size exponent according to Equation (4.25) can be given by

$$p = -\left[\frac{\partial \log\left(\frac{\dot{\epsilon}}{\sigma^n}\right)}{\partial \log d}\right]_T \quad (4.26)$$

It can be seen from Equation (4.26) that the value of p is sensitive to that of n or m. Thus, p was estimated for three values of n, i.e. 1.66 (m=0.6), 2.0 (m=0.5) and 2.5 (m=0.4). The value of the  $\log \frac{\dot{\epsilon}}{\sigma^n}$  corresponding to a given grain size was calculated using the value of true stress at strain rate corresponding to crosshead speed of 6.25 x

$10^{-4} \text{ mm s}^{-1}$  (approximately  $5 \times 10^{-5} \text{ s}^{-1}$ ) Figure 4.86- 4.91 shows the variation of  $\log \frac{\dot{\epsilon}}{\sigma^n}$  at a strain rate of approximately  $5 \times 10^{-5} \text{ s}^{-1}$  with  $\log d$  calculated by assuming the value of  $n$  to be 0.4, 0.5 and 0.6 as well as that measured from step strain rate tests, at different temperatures. It can be seen from these figures that the scatter of data points around the best fit line is minimum in case of  $m=0.5$ . Thus,  $p$  calculated using  $m=0.5$  was taken as the grain size exponent and given in Table 4.4. The value of  $p$  was found to increase with increase in temperature, from 1.0 at  $800^\circ\text{C}$  to 2.5 at  $950^\circ\text{C}$ .

Table 4.4. Grain size of Ti-622Si with  $(\alpha+\beta)$  microstructure

| Temp. ( $^\circ\text{C}$ ) | $p$  |
|----------------------------|------|
| 800                        | 1.05 |
| 850                        | 1.32 |
| 900                        | 1.94 |
| 920                        | 2.59 |
| 940                        | 1.76 |
| 950                        | 2.54 |

The activation energy( $Q$ ) of equation (4.2) for region II can be obtained by the relationship:

$$Q = -R \left[ \frac{\partial \log(\sigma^{-n} T E^{n-1} d^p)}{\partial (1/T)} \right]_t \quad (4.27)$$

In order to obtain  $Q$  using relationship 4.27 the  $\log(\sigma^{-n} T E^{n-1} d^p)$  was plotted against  $1/T$  and the best fit was drawn through the data points (Figure 4.92).  $Q$  is estimated from the slope of the best fit line. The  $E$  for Ti-622Si was taken to be that of Ti-6Al-4V as the effect of composition on  $E$  is not significant. The plotted values correspond to the combined data points of all grain sizes at strain rate close to  $5 \times 10^{-5} \text{ s}^{-1}$  and were calculated by incorporating  $n=2.0$  and the values of  $p$  given in Table 4.4. However the

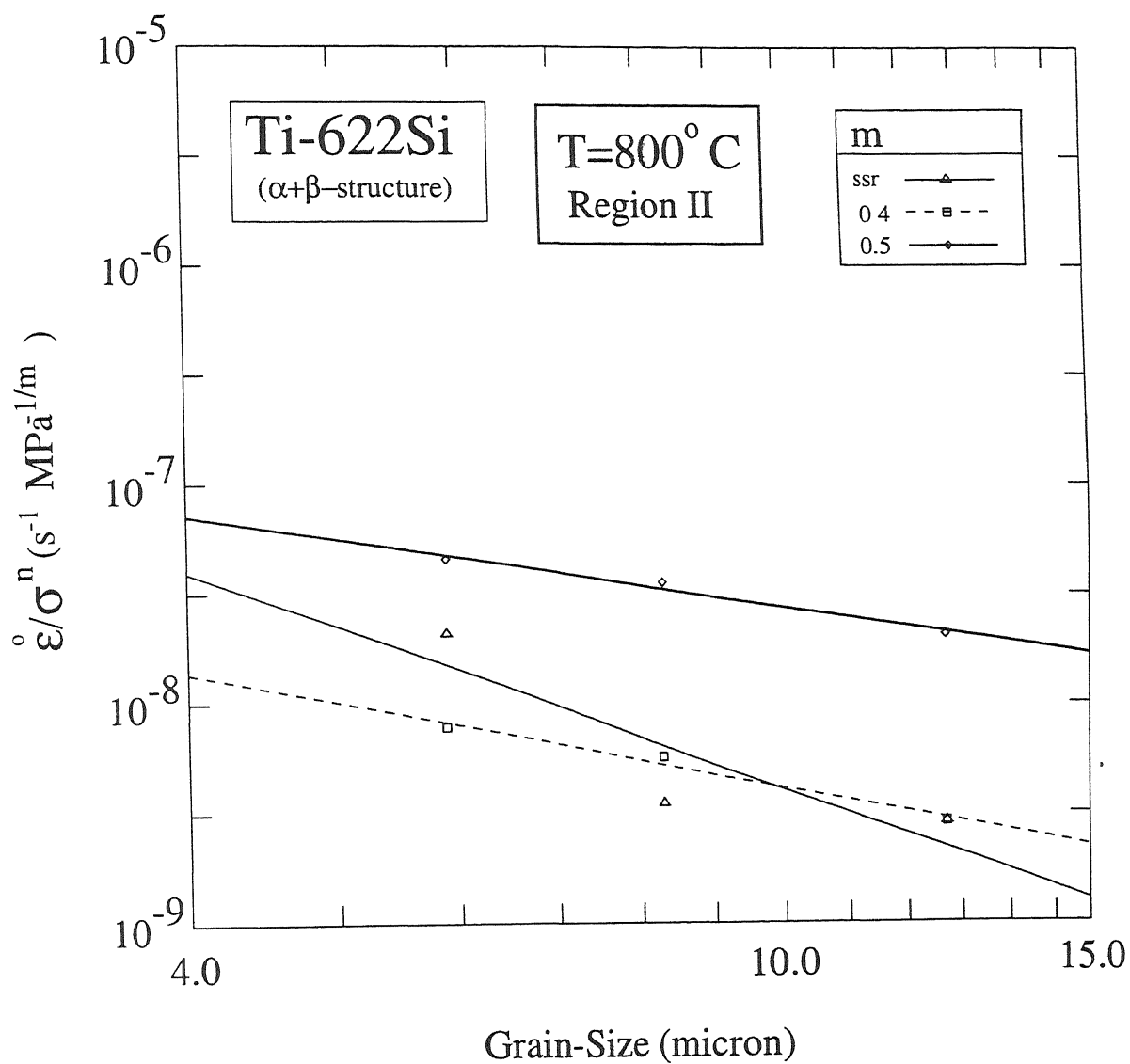


Figure 4.86. Plot of  $\log \frac{\dot{\epsilon}}{\sigma^n}$  versus  $\log d$  at a temperature of 800°C for Ti-622Si

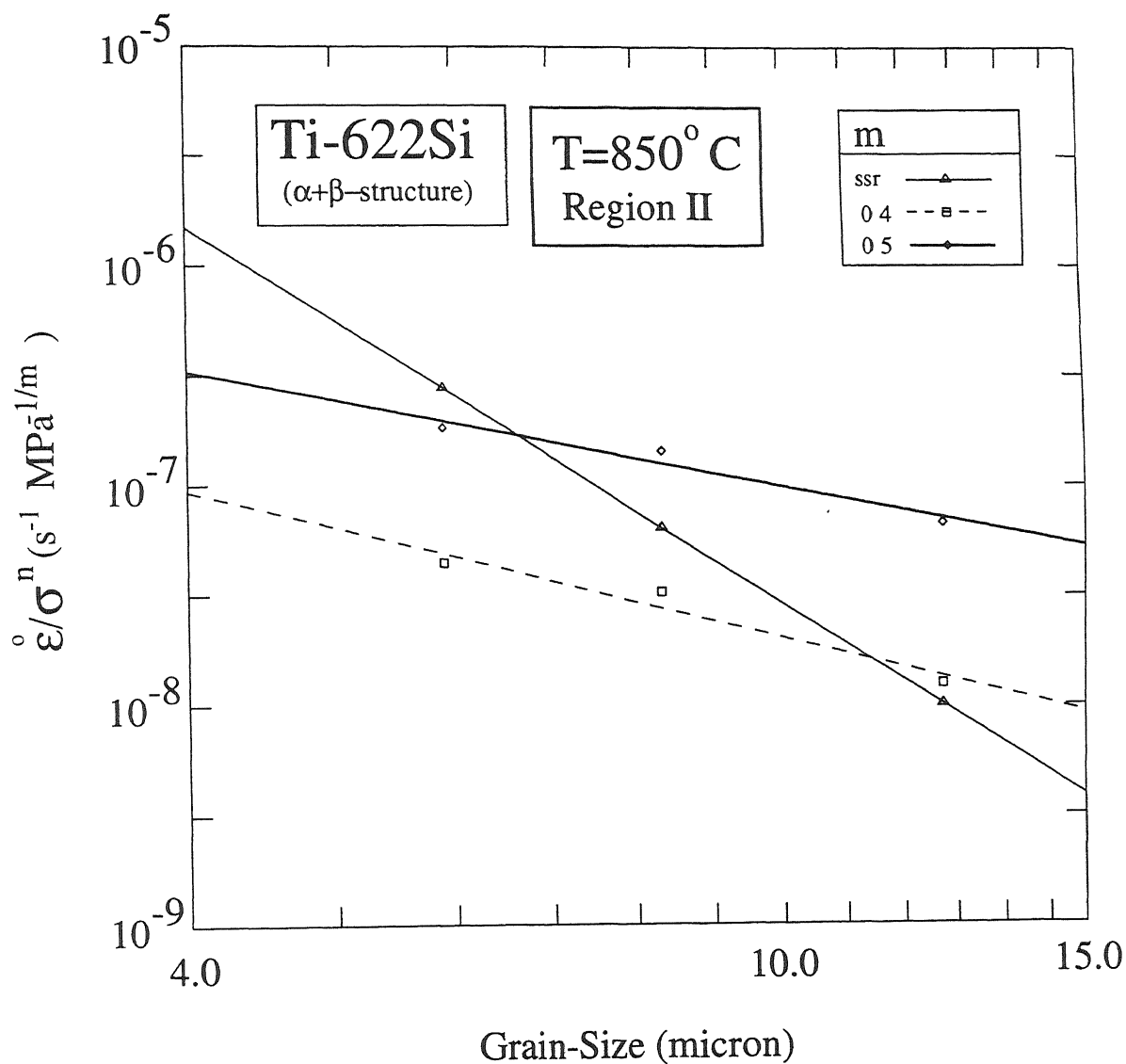


Figure 4.87: Plot of  $\log \frac{\dot{\epsilon}}{\sigma^n}$  versus  $\log d$  at a temperature of 850°C for Ti-622Si

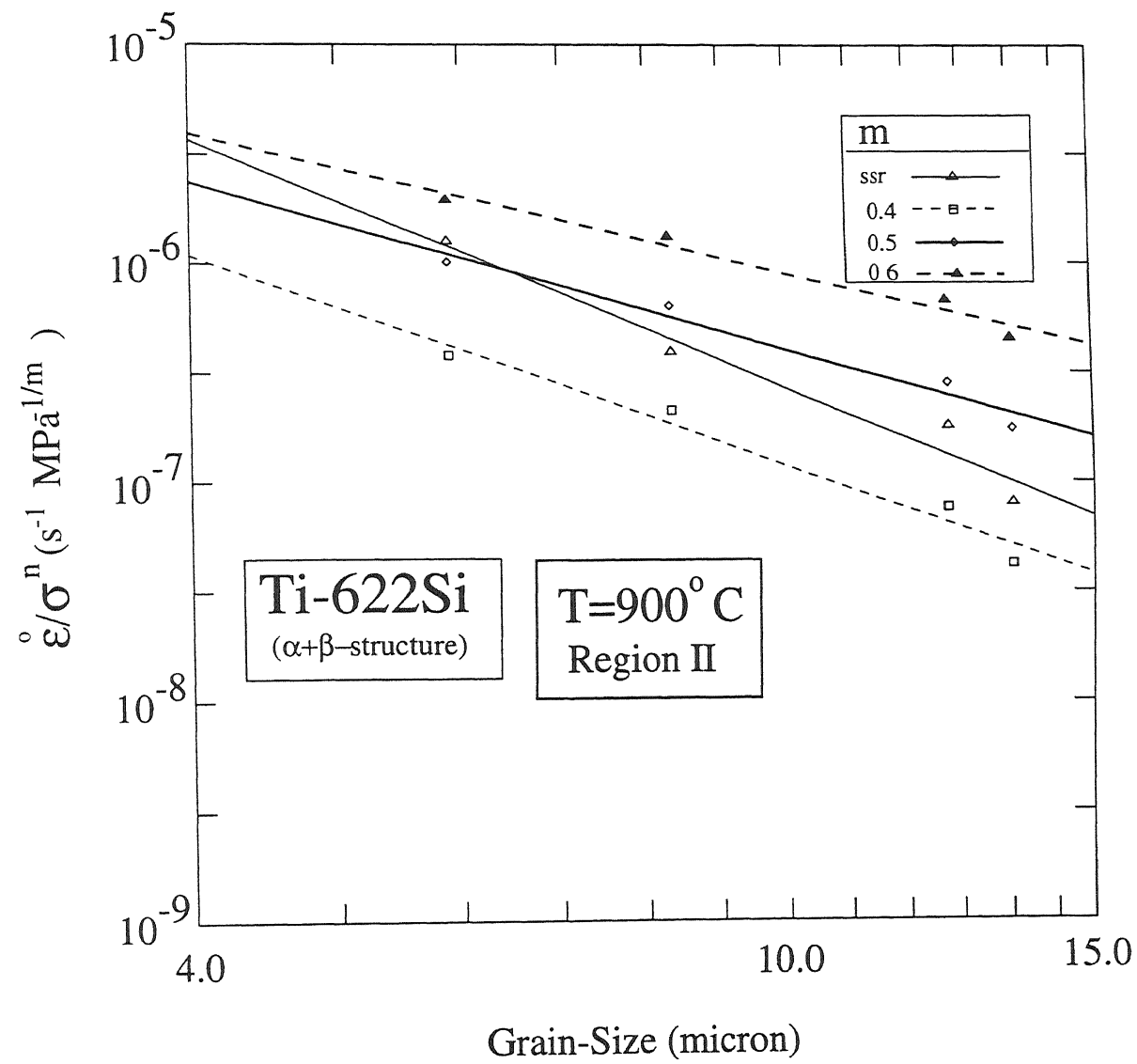


Figure 4.88: Plot of  $\log \frac{\epsilon}{\sigma^n}$  versus  $\log d$  at a temperature of 900°C for Ti-622Si

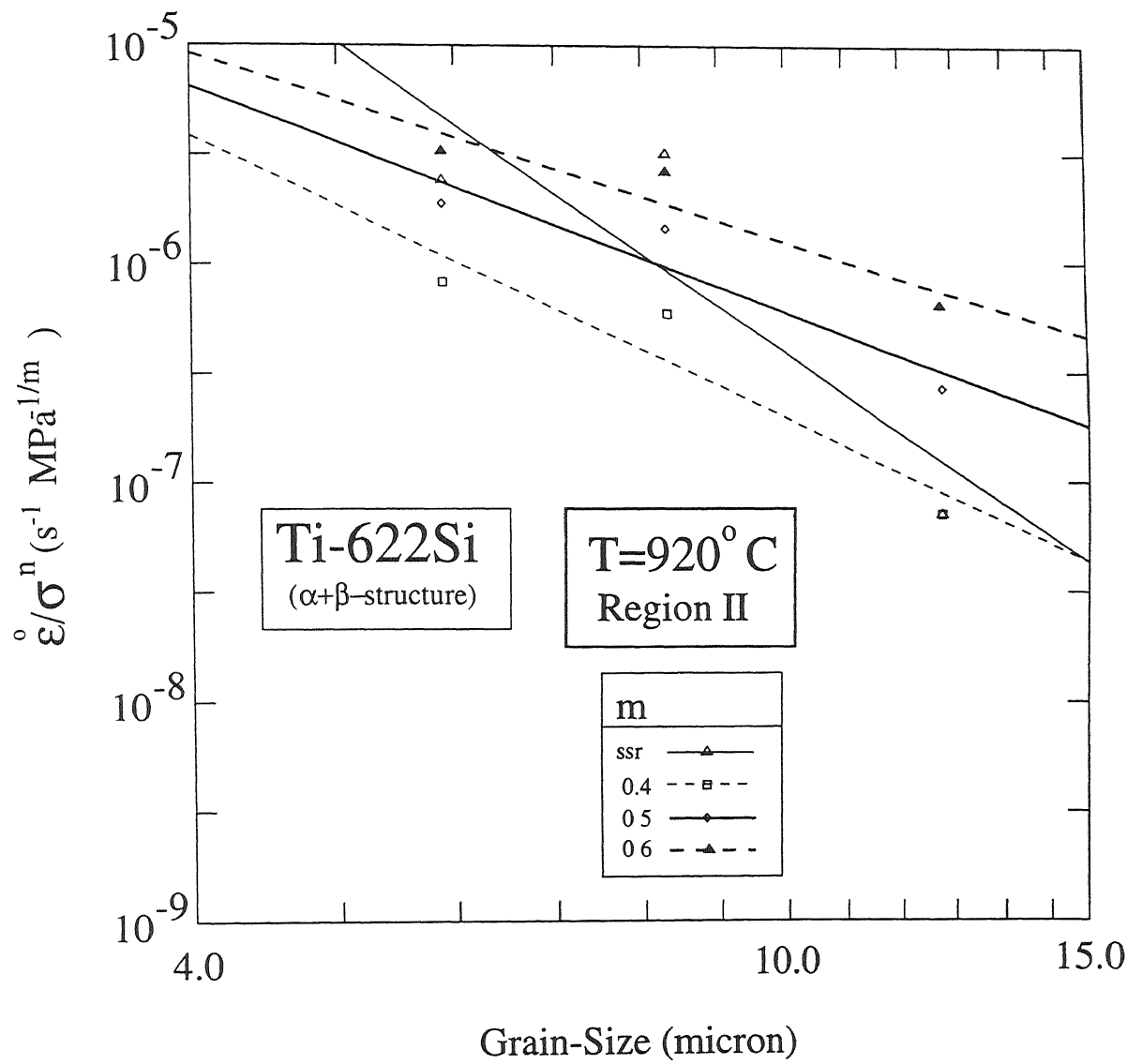


Figure 4.89: Plot of  $\log \frac{\dot{\epsilon}}{\sigma^n}$  versus  $\log d$  at a temperature of 920°C for Ti-622Si

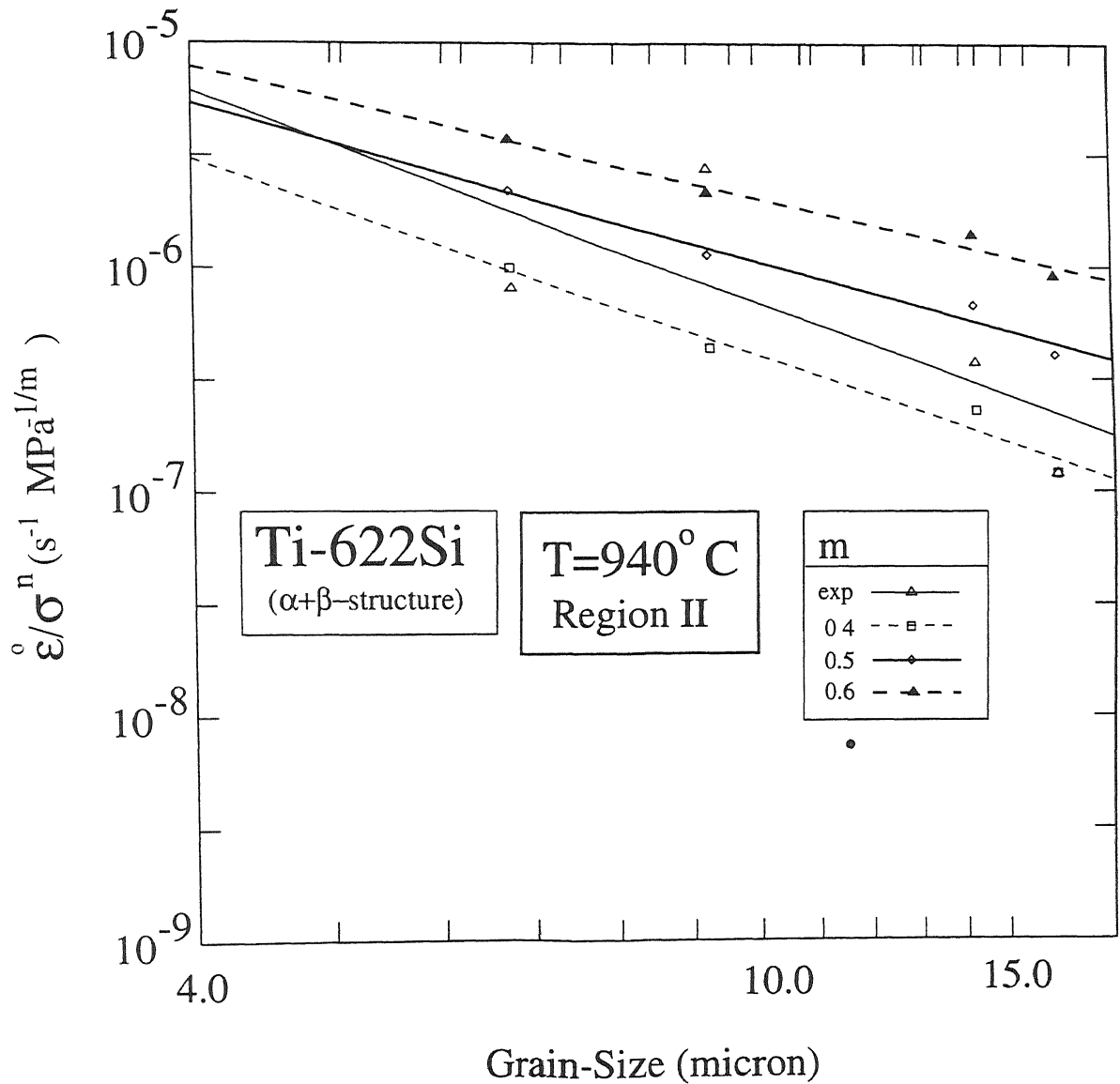


Figure 4.90: Plot of  $\log \frac{\dot{\epsilon}}{\sigma^n}$  versus  $\log d$  at a temperature of  $940^\circ C$  for Ti-622Si



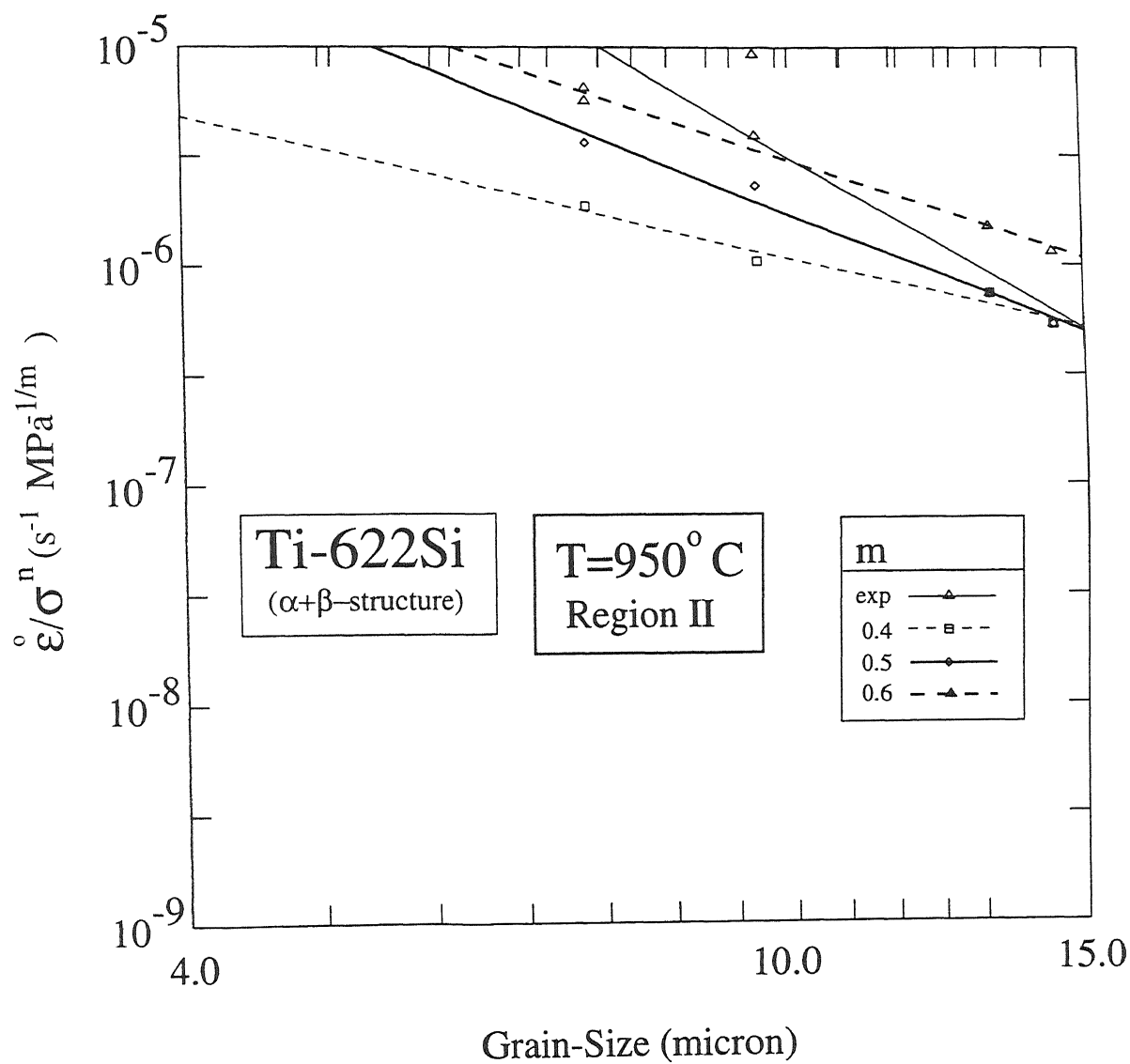


Figure 4.91: Plot of  $\log \frac{\dot{\epsilon}}{\sigma^n}$  versus  $\log d$  at a temperature of 950°C for Ti-622Si

variation of  $\log(\sigma^{-n} T E^{n-1} \dot{\epsilon}^p)$  above 900°C was found to be complex for all the values of strain rate sensitivity. Thus the calculation of activation energy was limited to the temperature range 750° C to 900°C. The activation energy value was found to be 249.8 KJ mol<sup>-1</sup>.

The constant A of the relationship 4.2 was determined using the values obtained for p and Q corresponding to region II and taking b value as the the atomic radius or pure titanium. Diffusivity value for both  $\alpha$  and  $\beta$  phases were considered. The values of A thus obtained by assuming D to be that of  $\beta$  phase and  $\alpha$  phase were approximately  $1.6 \times 10^8$  and  $1.6 \times 10^{10}$  respectively

In the region III, the true stress was found to be almost independent of the grain size. Thus the parameter p was taken as zero. The activation energy for the non-superplastic domain is given by

$$Q = -R \left[ \frac{\partial \log(\sigma^{-n} T E (n-1))}{\partial (\frac{1}{T})} \right] \quad (4.28)$$

and was obtained from the slope of the best fit line between the  $\log(\sigma^{-n} T E (n-1))$  and  $\frac{1}{T}$  data points. The activation energy for the nonsuperplastic region, i.e. region III was found to be  $290 \text{ KJ mol}^{-1} \pm 12.0 \text{ KJ mol}^{-1}$ .

Specimens of Ti-622Si( $\alpha+\beta$ ) were deformed upto strain of 0.5 under constant cross head speed condition, at different temperatures and at strain rates of approximately  $10^{-3} \text{ s}^{-1}$  and  $5 \times 10^{-1} \text{ s}^{-1}$ . Unlike Ti-622Si( $\beta$ ) it didn't exhibit inhomogenous flow.

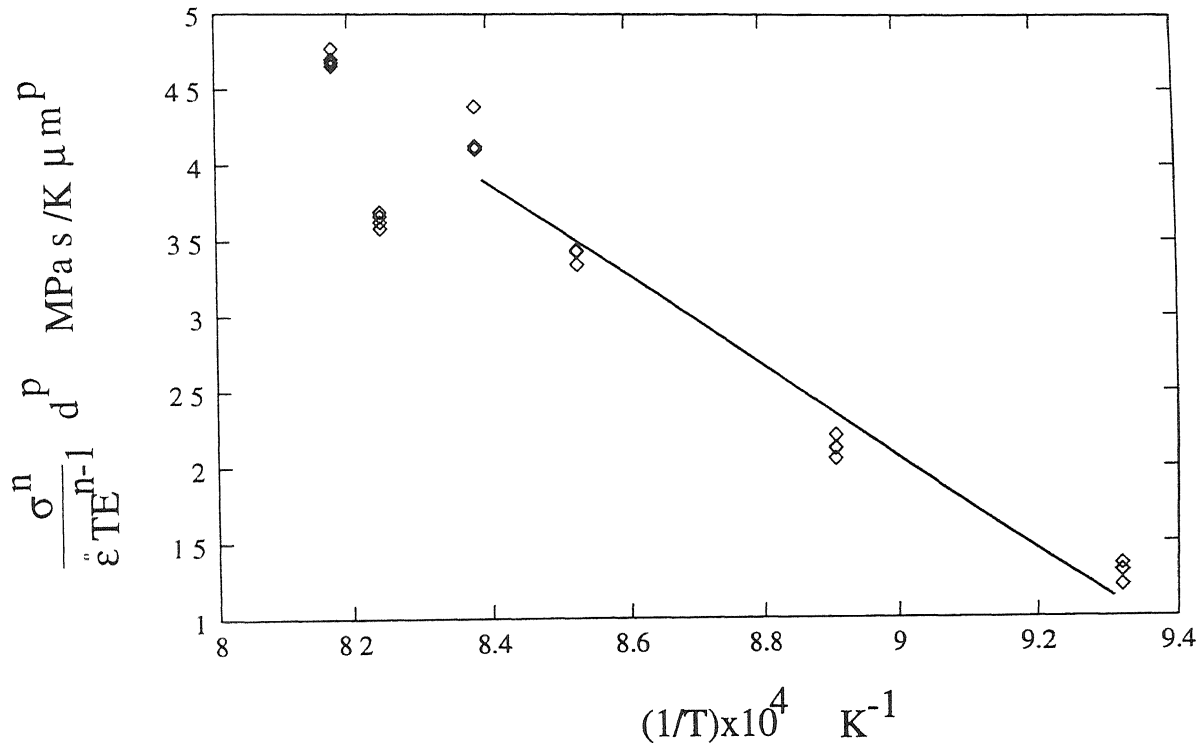


Figure 4.92. Plot of  $\log(\sigma^{-n} T E^{n-1} d^p)$  versus  $(1/T)$  for Ti-622Si

# Chapter 5

## DISCUSSION

Hot workability of  $(\alpha+\beta)$  titanium alloys with  $\beta$  structure [12, 70] is limited by flow instability. The flow instability in turn depends on stress-strain and stress-strain rate behaviour, temperature rise during deformation, presence of mechanical, geometrical and metallurgical defects and microstructural evolution. In this chapter, the influence of some of these factors on the flow instability of Ti-622Si( $\beta$ ) has been discussed.

In section 5.1, the influence of stress-strain and stress-strain rate behaviour on the flow instability, which is manifested as inhomogeneous flow and shear banding, has been analyzed using various instability parameters [32, 37, 40]. At first, the different instability criteria, using different instability parameters were tested for hot deformation of Ti-622Si( $\beta$ ). Further the influence of these parameters on the extents of flow inhomogeneity and shear banding, which have been quantified, was examined.

Microstructural evolution is a very important factor influencing the flow instability. The variation of microstructural evolution with temperature and strain rate, for Ti-622Si( $\beta$ ), was described in Chapter 4. Section 5.2 provides an explanation for the variation in the microstructural evolution with temperature and strain rate. Subsequently, Section 5.3 attempts to explain the variation in microstructural evolution with tem-

perature and strain rate in terms of power dissipation. Finally the influence of the microstructural evolution on the flow softening and flow instability has been examined in Section 5.4.

Another aspect of hot workability is the constitutive behaviour. Section 5.5 rationalizes the constitutive behaviour of Ti-622Si with equiaxed microstructure. The last section of this chapter, i.e. Section 5.6 discusses the best domain of workability for hot working of Ti-622Si.

## 5.1 Influence of Instability Parameters on the Flow Instability

In Chapter 1 two types of instability criteria have been discussed : (1) criteria based on flow localization parameters or the classical approach and (2) criteria based on DMM. In this section we aim to verify the prediction of flow instability by these criteria for Ti-622Si with  $\beta$  microstructure and determine the influence of the instability parameters on the extents of flow inhomogeneity and shear banding.

According to the classical approach discussed in section 1.3.2, unstable flow and shear banding occur when flow localization parameters for the two cases exceed zero. During compression at 1000°C and at strain rates varying between  $10^{-3} \text{ s}^{-1}$  and  $10^2 \text{ s}^{-1}$ ,  $\psi$  was found to be less than zero for all values of strain, indicating stable flow during the entire course of deformation, as per criterion proposed by Jonas et al. [35]. This confirms to the experimental observation of  $\lambda$  being approximately equal to 1.0 for the specimens deformed at 1000°C and at strain rates varying between  $10^{-3} \text{ s}^{-1}$  and  $10^2 \text{ s}^{-1}$ . At 950°C and at strain rates varying between  $10^{-3} \text{ s}^{-1}$  and  $10^0 \text{ s}^{-1}$ , the  $\psi$  shows variation of Type-II and the maximum value of  $\psi$  ( $\psi_{max}$ ) varied between 3 and 12. But the extent of flow inhomogeneity was low, as can be seen from the values of  $\lambda$

in Figure 4.60. At 950°C and higher strain rates the variation of  $\psi$  indicates stable flow through out the compression confirming to the experimental observation of  $\lambda > 0.95$ , i.e. insignificant flow inhomogeneity. At lower temperatures and in the strain rate interval  $10^{-3}\text{s}^{-1}$ - $10^0\text{s}^{-1}$ , the variation of  $\psi$  was of Type-II, similar to that observed for compression at 950°C and the same interval of strain rate. In this range of temperature and strain rate,  $\psi_{max}$  was mostly greater than 5.0. This, as per the criterion by Jonas et al., indicates flow inhomogeneity, confirming to observed values of  $\lambda$ , which mostly lied between 0.80 and 0.90.

However, at temperatures of 750°C and 800°C, and at a strain rate of  $10^2 \text{ s}^{-1}$ ,  $\lambda$  was found to be 1.0, which does not confirm to the very high values of  $\psi_{max}$  at these conditions of compression. Thus in the case of Ti-622Si( $\beta$ ), flow instability could be predicted with the help of the criteria:  $\psi > 0$ , except under conditions when shearbanding is intense.

In the present work shear banding has been quantified by the drift in the centre of the top and bottom faces of deformed specimen,  $\delta$ . The advantage of doing so is that by mere visual observation of etched cross section one may not be able to judge the extent of shear banding. The limitation of visual observation of etched cross section is evident from variation of  $\delta$  with strain rate at different temperatures in Ti-622Si alloy with  $\beta$  microstructure. At strain rate lower than  $1\text{s}^{-1}$  distinct shear bands were not visible on the etched cross section of deformed specimens. However values of  $\delta$  at lower strain rates indicate that shear banding had resulted into drift of the centres of top and bottom faces of the specimen during the compression. The variation of  $\psi_s$  parameter which is greater than  $\psi$  by  $\frac{1}{m}$  will be similar to that of  $\psi$ .  $\psi_{max}$  and consequently  $\psi_{smax}$  (maximum value of  $\psi_s$ ) was, in most of the cases, greater than 5.0 during compression in the ( $\alpha+\beta$ ) phase field. As expected from the criteria for shear banding;  $\psi > 0$ , noticeable values of  $\delta$  was observed at strain rates greater than  $10^{-2}\text{s}^{-1}$ .

Apart from indicating the occurrence of flow instabilities, the flow localization parameters has been also found to indicate the extent of flow instability. The work of Jonas as well as experimental observations on Ti-6242Si and Ti-10-2-3 alloy suggest that the extent of flow instability during uniaxial compression and side pressing depends on the value of  $\psi$  [12, 32]. Similarly it has been suggested that flow inhomogeneity and shear banding is significant only when the respective localization parameters exceeds 5.0. In the previous chapter the flow inhomogeneity and shear banding have been quantified by  $\lambda$  and  $\delta$ . In the present section we shall try to rationalize the variation in  $\lambda$  and  $\delta$  parameters, which are direct measure of flow instability, with temperature and strain rate in terms of variation of instability parameters  $\psi$  and  $\psi_s$ .

The maximum value of  $\psi$ , i.e.  $\psi_{max}$  was found to increase with strain rate at a given temperature which confirms to the experimental observation of decrease in  $\lambda$  (increase in the extent of inhomogeneous flow) with strain rate, at temperatures varying between 750°C and 900°C and strain rates lying in the interval  $10^{-3} \text{ s}^{-1}$ –  $1 \text{ s}^{-1}$ . However, at temperatures varying between 750°C and 900°C, the  $\lambda$  increased with strain rate beyond a strain rate of  $1 \text{ s}^{-1}$ , which does not confirm to the increase in  $\psi_{max}$  with strain rate in the same range of temperature and strain rate. This is possibly due to intense shear banding, which might have inhibited the inhomogeneous flow, as stated earlier. Also, similar correlation between the variation of  $\psi_{max}$  and  $\lambda$  with temperature, at a fixed strain rate was not possible.

Also a definite trend was observed in the variation of  $\delta$ , i.e. it increased with increase in strain rate and decreased with increase in temperature. The increase in  $\delta$  with strain rate can be explained in terms of increase in the  $\psi_{max}$  and consequently increase in the maximum value of  $\psi_s$ , i.e.  $\psi_{smax}$ , with strain rate. However variation of  $\delta$  with temperature cannot be explained using the  $\psi_{max}$  or  $\psi_{smax}$  values. Thus like in the case of flow inhomogeneity the increase in extent of shear banding with increase with  $\psi_s$  is for a given temperature only.

According to Kumar's [37] flow instability criteria, flow instability occurs when

$$\zeta = \frac{\delta \ln(\frac{m}{m+1})}{\delta \ln \dot{\epsilon}} + m < 0 \quad (5.1)$$

This criteria is based on irreversible thermodynamics and unlike the flow localization parameter is applicable for all manifestations of flow instability, i.e. applicable irrespective of state of stress. The specimens of Ti-622Si( $\beta$ ) deformed within the domain of instability predicted by Kumar's criteria, exhibit intense shear bands. However it does not predict unstable flow observed at strain rates varying between  $10^{-3} \text{ s}^{-1}$  and  $1 \text{ s}^{-1}$  and the less intense shear banding that occurs at low temperatures in the ( $\alpha+\beta$ ) phase field and at strain rates varying between  $10^{-1} \text{ s}^{-1}$  and  $1 \text{ s}^{-1}$ . So this criteria predicts only a limited domain of flow instability for Ti-622Si( $\beta$ ).

An alternative explanation can be given for the occurrence of intense shear bands within the temperature-strain rate domain predicted by Kumar's criteria. The term  $\frac{m}{m+1}$  is very close to  $m$  for  $m$  values less than 0.1. This is evident from the plot of  $\frac{m}{m+1}$  versus  $m$  shown in Figure 5.1. Also as the value of  $m$  or  $\frac{m}{m+1}$  approaches 0 the  $\ln \frac{m}{m+1}$  steeply decreases with  $\frac{m}{m+1}$  or with  $m$  (Figure 5.2). As a result when the  $m$  values become very low at high strain rates, significant drop in the  $\ln \frac{m}{m+1}$  value with small drop in the  $m$  value ensures the satisfaction of the criterion:  $\zeta < 0$ . Thus whenever  $m$  drops to very low values the criterion:  $\zeta < 0$  is automatically satisfied. On the other hand very low  $m$  will lead to very high values of  $\psi_s$  indicating intense shear band formation. In this way, the success of Kumar's criteria in predicting intense shear banding in Ti-622Si( $\beta$ ) can be explained from the criteria based on flow localization parameter, i.e. using the classical approach.

Another criteria for predicting unstable flow is by Gegel [40]. According to it flow instability occurs when

$$\frac{\delta s}{\delta \ln \dot{\epsilon}} \geq 0 \quad (5.2)$$



and

$$\frac{\delta\eta}{\delta\ln\dot{\epsilon}} \geq 0 \quad (5.3)$$

where  $s$  is  $\frac{1}{T}[\frac{\delta\ln\sigma}{\delta\frac{1}{T}}]$ . From Figure 4.18 it can be seen that  $[\frac{\delta\ln\sigma}{\delta\frac{1}{T}}]$  at a given temperature and thus  $s$  increases with strain rate. Hence the criterion  $\frac{\delta s}{\delta\ln\dot{\epsilon}} \leq 0$  is not satisfied at all temperatures and strain rates. Since the strain rate sensitivity decreases with strain rate at all temperatures the criterion  $\frac{\delta\eta}{\delta\ln\dot{\epsilon}} \geq 0$  is also not satisfied in the entire domain. Thus it can be concluded that the criteria based on flow localization parameters is better than the existing thermodynamic approaches in predicting flow instability in Ti-622Si with  $\beta$  microstructure.

## 5.2 Mechanism of Microstructural Evolution

As mentioned in the previous chapter, the morphology of  $\alpha$  plates in Ti-622Si with  $\beta$  microstructure was found to be unstable during the hot deformation and following changes were observed in the  $\alpha$  morphology as a result of hot deformation:

- (1)  $\alpha$  plates which were oriented unfavorably underwent kinking and differential straining.
- (2)  $\alpha$  plates oriented favorably were found to elongate and orient themselves towards the direction perpendicular to the compression axis.
- (3) The kinked and the elongated  $\alpha$  plates fragmented. The extent of fragmentation was more at higher temperatures and at lower strain rates.
- (4) Thickness of  $\alpha$ , in general changed during the deformation. Higher temperature and lower strain rate resulted in increase in the plate thickness.
- (5) The microstructural changes mentioned above were non uniform at low temperatures (750-850°C) especially at higher strain rates due to the shear banding. However at

higher temperatures, which correspond to higher volume fraction of  $\beta$  phase, the deformation was found to be uniform.

- (6) Complete transformation to equiaxed microstructure, similar to Ti-622Si in TMT condition, was not observed under any condition of temperature and strain rate.

Similar observations were made by other investigators on the microstructural changes in the  $(\alpha+\beta)$  titanium alloys during hot deformation. Semiatin et al. [85] have made a detailed study of the microstructural evolution during the heat treatment and hot iso-strain rate compression, which was also followed by heat treatment of Ti-6242Si in its  $\beta$  and  $(\alpha+\beta)$  microstructural states. They observed no significant morphological changes in the  $\beta$  microstructure during the heat treatment. However during the hot deformation, the microstructure was found to be unstable and underwent morphological changes. These changes were found to depend on the temperature, strain rate and strain of deformation.

At 899°C and 927°C Semiatin et al. [85] observed non uniform microstructural evolution in Ti-6242Si( $\beta$ ) at low temperature, i.e. between 899°C and 927°C, similar to what has been observed in Ti-622Si( $\beta$ ). The non uniform evolution of microstructure was of two types: (1) breakup and spheroidization of  $\alpha$  platelets in selected regions that surrounded the regions having Widmanstatten type of morphology and (2) formation of regions where the  $\alpha$  and  $\beta$  plates were having sharp curvature, i.e. kinked.

They deformed specimens of Ti-6242Si having  $\beta$  microstructural state at a temperature of 899°C and at a constant strain rate of  $2 \times 10^{-2}$  up to different strain levels. The kinked  $\alpha$  plates started forming at the minimum strain level of 0.2-0.3, whereas  $\alpha$  plate breakup into equiaxed particles started at a strain of approximately 0.4 in narrow regions near colony boundaries. The volume fraction of both kinked  $\alpha$  and equiaxed  $\alpha$  was found to increase with strain level. But complete transformation of Widmanstatten microstructure to equiaxed microstructure was not possible even at a strain level of 1.0.

In the present study also complete transformation to equiaxed microstructure was not possible.

Weiss et al. [83] carried out quantitative study on the breakup and spheroidization of  $\alpha$  plates in Ti-6Al-4V with two platelike microstructures having different average thickness of  $\alpha$  plates. They however carried out the study at fixed temperature of 955°C and a constant cross head speed of  $2 \times 10^{-4} \text{ s}^{-1}$ . They also observed increase in the mean plate thickness and decrease in the mean aspect ratio of the  $\alpha$  plates with the strain level similar to the observation of Semiatin et al. [85]. In the present study also the mean thickness of  $\alpha$  plates was found to increase as a result of hot deformation at lower strain rates at all temperatures. Thus Ti-622Si alloy in its  $\beta$  microstructural state is representative of other ( $\alpha+\beta$ ) titanium alloys in their  $\beta$  microstructural state.

The observed variation in the microstructural evolution can be rationalized in terms of combination of three mechanisms of microstructural changes which are as follows.

- (1) Elongation of  $\alpha$  plates: Deformation of  $\alpha$  plate favorably oriented to the compression axis, leading to elongation of the  $\alpha$  plate or increase in its aspect ratio ( $L/D$ ). During the deformation, formation of low and high angle  $\alpha/\alpha$  boundaries or shearing across the  $\alpha$  plates occur, as observed by Weiss et al. and others [83]. This mechanism of microstructural modification contributes to the overall plastic strain in the specimen.
- (2)  $\beta$  penetration: The  $\beta$  phase forms deep cusps at  $\alpha/\alpha$  boundaries with relatively high misorientation as shown schematically in Figure 5.3. The formation of cusp at the locations where  $\alpha/\alpha$  interfaces intersect  $\alpha/\beta$  interfaces is due to balance of interphase energies. From the criterion of balance of interphase energy the dihedral angle  $\theta$  is given by

$$2\cos\theta = \frac{\gamma_{\alpha/\alpha}}{\gamma_{\alpha/\beta}} \quad (5.4)$$

According to Weiss et al. the penetration of the  $\beta$  leads to break up of the  $\alpha$  plates. According to them the rate of cusp penetration depends on the diffusion of the alloying elements Al and V through or along the interfaces.

Kaibeshyev et al. [87] have proposed an alternative reason for the penetration of  $\beta$ . According to them the  $\beta$  cusp forms as a result of depletion of Al, which is the fastest diffusing solute element from the regions of compressive stresses and transformation of those regions into  $\beta$  phase which is having less concentration of Al as compared to the equilibrium.

It should be noted that unlike the plate elongation,  $\beta$  penetration mechanism does not contribute to the overall plastic strain of the specimen. This is evident from the fact that the  $\beta$  penetration also occur during post deformation annealing.

- (3) Coarsening and spheroidization of  $\alpha$  plates: Fragmented as well as unfragmented  $\alpha$  phase undergoes coarsening and spheroidization during deformation at high temperatures and low strain rates. The mechanism of coarsening is driven by the decrease in the  $\alpha$ - $\beta$  interphase area. At elevated temperatures its rate is controlled by the rate-limiting step for this process, i.e. diffusion rate of the substitutional solute element. Because of this, the rate of coarsening is expected to be low. However during concurrent deformation, the rates are generally several orders of magnitude higher [32]. Like the  $\beta$  penetration this mechanism also does not contribute to the plastic strain of the specimen.

Some of the important features that were observed can be explained in terms of combination of these mechanisms. We shall now consider them one by one.

- (1) The  $\alpha$  plates having thickness greater than the depth of  $\beta$  penetration will not undergo fragmentation. Thus the extent of plate breakup increases with the depth of  $\beta$  penetration. The penetration depth in turn depends on the rate of penetration and the period of deformation. According to the suggested mechanism [83, 87],

the  $\beta$  penetration occurs due to diffusion and thus its rate will increase with the temperature resulting into higher extent of  $\alpha$  fragmentation at higher temperatures. Also with the increase in deformation temperature, the initial thickness of  $\alpha$  plate decreases as was shown in Figure 4.5. So lesser penetration of  $\beta$  is required for the fragmentation. This will also enhance fragmentation of the  $\alpha$  platelets. On the other hand the with decrease in the strain rate the period of deformation increases (as total plastic strain was same for all the specimens) resulting into increase in the penetration depth and hence the extent of fragmentation.

- (2) The  $\alpha$  plates are subjected to two opposing changes, i.e. (1) they elongate due to plastic deformation resulting into decrease in their mean thickness and (2) coarsen leading to increase in the thickness of the plates, and the resultant thickness of  $\alpha$  plates at the end of compression will be decided by their relative contributions. The first one contributes to the overall plastic strain of the specimen and is same for specimens deformed at different temperatures and strain rates, as the total plastic strain was approximately same for all the specimens. Consequently the mean thickness of the  $\alpha$  plates after the deformation will be decided by the extent of coarsening. However coarsening occurs by diffusion and hence variation in the extent of coarsening varies with temperature and strain rate in a similar way as that of  $\beta$  penetration, i.e. increases with increase in temperature and decrease in strain rate. As a result mean thickness of Ti-622Si( $\beta$ ) was found to increase with temperature and decrease with strain rate.

### 5.3 DMM Interpretation of Microstructural Evolution

The efficiency maps corresponding to strain levels of 0.1, 0.3 and 0.5, for hot working of Ti-622Si with  $\beta$  microstructure are shown in Figures 5.4- 5.8. The maps show domain having peak efficiency value ( $\eta$ ) at  $800^\circ\text{C}/10^{-3}\text{s}^{-1}$  and  $1000^\circ\text{C}/10^{-3}\text{s}^{-1}$ , whereas the

temperature which shows the best transformation to equiaxed  $\alpha$  lie outside the two domains, with minima in the  $\eta$  values. Similarly recrystallization of  $\beta$  phase, which possibly also results into stress oscillation is not indicated by the efficiency map. In contrast to what has been reported for Cu-Zn alloys [51, 52, 53], Zr-alloys [49] and Ti<sub>3</sub>Al [47, 48] a separate domain for formation of equiaxed  $\alpha$  was not observed for Ti-622Si with  $\beta$  microstructure.

## 5.4 Influence of Microstructural Evolution on Stress-Strain Behaviour and Flow Instability

An important feature observed in the stress strain behaviour of Ti-622Si( $\beta$ ) is the flow softening. The flow softening per unit strain  $\gamma$  defined as

$$\gamma = \frac{d\sigma}{d\epsilon} \quad (5.5)$$

observed during the hot compression of Ti-622Si with  $\beta$  microstructure is shown in Figure 5.9.  $\gamma$  increased with increase in strain rate at all temperatures and at a given strain rate it was found to decrease with the increase in the temperature. The observed flow softening in the alloys is due to : (1) temperature rise during the deformation and (2) modification of microstructure. Since the effect of temperature rise has been eliminated in the temperature corrected stress-strain curves, the flow softening in the temperature corrected curves can be correlated with microstructural changes occurring during the deformation.

Flow softening per unit strain in the corrected stress-strain curves  $\gamma_c$  is shown in Figure 5.10. At 750°C and 800°C,  $\gamma_c$  was found to initially increase with strain rate. It subsequently decreased and finally increased rapidly with the strain rate at strain rate above 10s<sup>-1</sup>. However at higher temperatures in the ( $\alpha$ + $\beta$ ) phase field the rapid rise of  $\gamma_c$  above 10s<sup>-1</sup> was not observed. The rapid increase in the  $\gamma_c$  at strain rate above

$10\text{s}^{-1}$  is possibly due to the formation of intense shear band and the structural changes within the intense bands, as mentioned in the previous chapter. It can be noted that unlike  $\gamma$ ,  $\gamma_c$  showed very less change with the strain rate up to a strain rate of  $10\text{ s}^{-1}$  and thus its correlation with the microstructural evolution, which varied systematically with the strain rate of deformation was not observed.

The reason for this is that, the flow softening due to modification of microstructure will depend on. (a) resistance of the individual phases to deformation, which in turn depends on the temperature and strain rate of deformation and (b) morphological change. Thus, in order to correlate the softening with the coarsening, the effect of resistance of the individual phases to deformation has to be eliminated. This was done by normalizing the  $\gamma_c$  with respect to peak stress. The variation of normalized flow softening per unit strain,  $\gamma_{cn}$ , which is given by

$$\gamma_{cn} = \frac{1}{\sigma_p} \frac{d\sigma}{d\epsilon} \quad (5.6)$$

is shown in Figure 5.11. It can be observed that  $\gamma_{cn}$  decreased with strain rate at all temperatures except at  $750^\circ\text{C}$  and  $800^\circ\text{C}$  and at strain rate above  $10\text{s}^{-1}$ . This is due to decrease in the extent of coarsening, which is one of the reasons of flow softening with strain rate. Also the  $\gamma_{cn}$  at low strain rates was found to increase substantially with temperature up to  $900^\circ\text{C}$ . This can be similarly correlated with the increase in the extent of coarsening with the rise in deformation temperature. However, the  $\gamma_{cn}$  at  $950^\circ\text{C}$  was found to be minimum. This is possibly due to the simultaneous effect of changes in the  $\beta$  phase which hardens at higher temperatures, as can be seen from the corrected stress-strain curves at  $1000^\circ\text{C}$ .

Another feature that was characteristics of the stress strain curve for Ti-622Si( $\beta$ ) was stress oscillation at higher strain rates. Similar observations have been made on many alloys [49]. One of the possibilities of stress oscillation is dynamic recrystallization. This possibility is very likely as fine equiaxed grains of  $\alpha$  and  $\beta$  phases were observed in the specimens of Ti-622Si( $\beta$ ) deformed at the temperature and strain rates in which stress

oscillations were observed, i.e. in the  $(\alpha+\beta)$  phase field at 950°C and  $\beta$  phase field at high strain rates.

As mentioned in Chapter 1, the oscillatory behaviour during dynamic recrystallization has been rationalized in terms of cycles of dynamic recrystallization by Luton and Sellars [78] and Sandstrom and Lagneborg [80]. However, the observed stress oscillations, that have been explained by them occurred at strain rates, which are many orders of magnitude lower than that observed in the present study. Thus, the cause of the stress oscillation in Ti-622Si( $\beta$ ) is not yet clear.

Unstable flow has been correlated with microstructural evolution in Ti-25Al-11Nb using Gegel's criteria based on dynamic material modeling by Long and Rack [59, 58]. In their study, flow instability was predicted using Gegel's criteria and subsequently the microstructural evolution was correlated with the flow instability. Unstable flow was found to be associated with transformation of orthorhombic O to  $\alpha_2$ , kinking of the  $\alpha_2$  lamellae, shear band formation and coarsening of the dynamically recrystallized grain structure. Stable flow was found to be associated with dissolution of Widmanstätten  $\alpha_2$ , coarsening of primary  $\alpha_2$  and dynamic recovery of lamellar  $\alpha_2$ .

In case of Ti-622Si( $\beta$ ) coarsening of  $\alpha$  plate, kinking and formation of equiaxed  $\alpha$  was observed but as pointed out earlier, Gegel's criteria do not predict any domain of flow instability for Ti-622Si( $\beta$ ) in the temperature-strain rate domain of the present study. Within the domain of flow instability predicted by Kumar's criterion based on dynamic material modeling, kinking of  $\alpha$  plates and transformation of  $\alpha$  to  $\beta$  within the shear band were observed. However kinking is not unique of this domain as it is also observed at lower strain rates. Secondly, the transformation to  $\beta$  possibly occurred only in one specimen (deformed at 750°C/10<sup>2</sup> s<sup>-1</sup>) and not observed in other specimen deformed in the domain. So it has no relationship with the  $\zeta$  parameter being lower than 0.



It has been stated in Chapter 1 that microstructural changes like kinking, coarsening and spheroidization leads to flow softening which in turn results in flow instability. However in order to study the effect of microstructural changes on flow instability, the effect of temperature rise has to be eliminated and the the instability parameters obtained from the corrected stress-strain curves, namely  $\psi_c$  has to be considered. In contrast to  $\psi$ , which predicts the combined effect of temperature rise and microstructural changes, the flow instability parameter estimated from the corrected stress-strain curves ( $\psi_c$ ) is expected to predict the contribution of microstructural changes alone to the flow instability. As mentioned in Chapter 4, the variation of  $\psi_c$  with strain for different temperatures and strain rates of deformation of the  $\beta$  structure of Ti-622Si alloy were of Type-I and Type-II. Such a variation of  $\psi_c$  with strain indicates that either the flow remains completely stable throughout the deformation in spite of microstructural changes or turns into a stable flow from unstable one above a critical strain. Further, in case of Type-II behaviour it was observed that the critical strain at which the transition from unstable to stable flow occurred, increased with increasing strain rates at the deformation temperature of 750°C. In contrast, at deformation temperatures of 850°C, 900°C and 950°C, the critical strain decreased with increasing the strain rate. Such a variation of  $\psi_c$  with strain could be reasonably correlated with changes in the morphology of  $\alpha$  plates during the course of their deformation.

In order to do so, lets us first look at the nature of flow instability during the compression of Ti-622Si with  $\beta$  microstructure. During the deformation at temperatures of 750°C-800°C and at strain rate of  $10^{-1}\text{s}^{-1}$ , which did not result into formation of even a small fraction of equiaxed  $\alpha$  and coarsening, the variation in  $\psi_c$  was of Type-II. Now let us examine the effect of transformation of  $\beta$  structure into equiaxed structure and coarsening of  $\alpha$ , which occurs at relatively higher temperature and lower strain rates, on the variation of  $\psi_c$ . Transformation to equiaxed microstructure and microstructural coarsening will have two opposing effects, i.e. (a)formation of equiaxed microstructure will contribute to flow stability as the specimens with this type of microstructure relat-

ively undergo stable flow and (b) coarsening of  $\alpha$  that accompanies the deformation will contribute to flow softening and consequently to flow instability [32] if significant grain boundary sliding is not occurring.

At lower deformation temperatures, the coarsening is not significant. Thus the contribution to the stability of flow due to the transformation to equiaxed microstructure will predominate over the flow instability contributed by coarsening. As a result, transition to stable flow occurred earlier at low strain rates, due to higher extent of transformation to equiaxed microstructure. On the other hand, at higher temperatures due to greater diffusivity coarsening of  $\alpha$  will be significant. Under this condition the contribution of coarsening to the flow instability will be predominating. Since the extent of coarsening at a given deformation temperature increased with decreasing strain rate, the critical strain for transition to stable flow decreased with increasing strain rate at higher temperatures.

## 5.5 Constitutive Behaviour of Ti-622Si with Equiaxed Microstructure

The parameters of constitutive equation describing the flow behaviour of Ti-622Si with equiaxed microstructure, i.e. ( $\alpha+\beta$ ) microstructure), in the region II of superplasticity showed the following trend.

- (a) The value of strain rate sensitivity was found to lie within the range  $0.5 \pm 0.1$ , with few exceptions. On the whole the strain rate sensitivity was found to increase with temperature for a given strain rate.
- (b) The grain size exponent increased with temperature, from 1.0 at 800°C to 2.6 at 920°C. Above 920°C it decreased to 1.76 at 940°C and then again increased to 2.5

at 950°C.

- (c) The activation energy  $Q$  was found to be higher than that of self diffusion and grain boundary diffusion.

The strain rate sensitivity value of Ti-622Si alloy mostly lied within the interval 0.4-0.6. This observation confirms to predictions of the theoretical models proposed by Ball and Hutchinson [88], Mukherjee [89] and Gittus [90, 91]. In contrast, Nabarro Herring [92, 93] and Coble diffusional model [94] predict  $m=1$ , which does not confirm to the observation of  $m=0.5\pm0.1$  in the region II of superplasticity. The observed values of  $m$ , also apparently contradicts the models by Ashby-Verall [95], Gifkins [96] and Padmanabhan [97] which predict continuous variation of  $m$  with strain rate, from a maximum value of 1.0 to values corresponding to that observed for dislocation creep. In the present study, although a continuous variation of  $m$  was observed, the values of  $m$  rarely exceeded 0.6. However the observed values of  $m$  should not be taken as an indication of absence of mechanisms that give rise to  $m$  value of 1.0, as predicted by the models of Ashby-Verall, Gifkins and Padmanabhan, and presence of mechanisms that give rise to  $m=0.5$ . The reason for stating this is that  $m$  values, which are close to 1.0, have been observed for Ti-6Al-4V [26, 15, 18] as well as in Si containing VT-9 alloy [30] in the same range of temperature and strain rate as in the present study, confirming to the the models of Ashby-Verall, Gifkins and Padmanabhan. Thus, relatively lower value of strain rate sensitivity observed for Ti-622Si ( $\alpha+\beta$ ), which is very similar to Si containing VT-9 [30], is possibly due to the presence of Si and/or grain size distribution.

Grain size distribution is known to play a very crucial role in superplasticity [29, 98]. For Ti-6Al-4V with equiaxed morphology, it was observed that wider spread in the grain size distribution resulted in lower  $m$  values. In the present study considerable spread was observed in the grain distribution. This is indicated by the value of  $\sigma_{\alpha-\beta}$  given in Table 4.1. Also the presence of Si in Ti-622Si might be party responsible for  $m$

values of  $0.5 \pm 0.1$ , which is much lower than 1.0. Dutta [30] observed higher strain rate sensitivities in Si-free VT-9 alloy as compared to Si containing VT-9. He also observed silicide particle  $(\text{TiZr})_6\text{Si}_3$  at grain boundaries and suggested that silicide particles at the grain boundaries were responsible for providing resistance to grain boundary sliding and thus reducing the strain rate sensitivity.

A wide range of  $p$  values have been reported for  $(\alpha+\beta)$  titanium alloys in the literatures [26, 16, 27, 18]. In some cases the values reported has been as low as 0.74-0.86 [27], which is not expected in the region II of superplasticity. In the present study also the  $p$  values exhibit a wide range of values. But a systematic trend was observed, i.e.  $p$  increased with temperature. Most of the models of superplasticity assume grain boundary sliding and predict  $p=2.0$  and some greater than 2.0. The value of  $p$  for Ti-622Si alloy with equiaxed microstructure varied in the range 1.8-2.6 at temperatures above 850°C, which is close to the predictions of the models. However, at lower temperatures, the values of  $p$  were low and not predicted by any model of superplasticity. The variation of  $p$  with temperature in the range 800°C-920°C is possibly related to the change in the volume fraction of  $\alpha$  and  $\beta$  phases with the temperature which results into gradual increase in the fraction of the  $\alpha$ - $\beta$  and  $\beta$ - $\beta$  boundary with increase in temperature.

In Ti-622Si alloy in conditions TMT, TMT-A1, TMT-A2 and TMT-A3, the grain size and the volume fraction of primary  $\alpha$  underwent insignificant change with temperature up to 920°C. However, significant change had occurred in the volume fraction of Widmanstätten  $\alpha$  within the prior  $\beta$  grains, as the temperature was raised to 920°C. This results in change in relative proportion of  $\alpha$ - $\alpha$ ,  $\alpha$ - $\beta$  and  $\beta$ - $\beta$  interphases. At the prior  $\beta$  grain boundaries, the Widmanstätten  $\alpha$  can be either present as grain boundary  $\alpha$  or alternate lamellae of  $\alpha$  and  $\beta$  phase. The grain boundary  $\alpha$  will result in  $\alpha$ - $\alpha$  interfaces along the prior  $\beta$ - $\beta$  grain boundaries and the alternate lamellae of  $\alpha$  and  $\beta$  phases will result into  $\alpha$ - $\beta$ ,  $\alpha$ - $\alpha$  and  $\beta$ - $\beta$  interphases along the prior  $\beta$ - $\beta$  boundaries. Along the prior  $\beta$ -primary  $\alpha$  boundaries alternate  $\alpha$ - $\alpha$  and  $\alpha$ - $\beta$  interphases, as shown

in Figure 5.12. With the increase in the temperature the fraction of  $\alpha$ - $\alpha$  interface will decrease and that of  $\alpha$ - $\beta$  and  $\beta$ - $\beta$  will increase as shown schematically in Figure 5.12. Jain et al. [99] have suggested that the resistance to sliding of  $\alpha$ - $\alpha$ ,  $\alpha$ - $\beta$  and  $\beta$ - $\beta$  interface is different and that of  $\alpha$ - $\alpha$  interface to be maximum. Rosenblum et al. [100] have suggested that sliding rates is maximum or resistance to sliding minimum for  $\alpha$ - $\beta$  interfaces. Recent work of Inagaki [101] confirms to the suggestion of Rosenblum et al. Inagaki, employing a special technique of thermomechanical processing, obtained micrograins of  $\alpha$  surrounded by thin film of  $\beta$  and consequently very high fraction of  $\alpha$ - $\beta$  boundary. The alloy in this condition exhibited very high degree of superplasticity. Inagaki has thus concluded that, in order to maximize superplasticity, the total surface area of the  $\beta$  phase films surrounding  $\alpha$  grains should be maximized. This conclusion confirms to the hypothesis  $\alpha$ - $\beta$  boundaries have maximum sliding rate. On the other hand Partridge et al. [102] have reported maximum sliding rates for  $\beta$ - $\beta$  boundaries.

With the increase in the temperature the fraction of  $\alpha$ - $\alpha$  interface will decrease and that of  $\alpha$ - $\beta$  and  $\beta$ - $\beta$  will increase. Thus, assuming the sliding resistance of  $\alpha$ - $\alpha$  interface to be higher than that of  $\alpha$ - $\beta$  and  $\beta$ - $\beta$  interfaces, the contribution to the grain boundary sliding should increase with increase in temperature. With the decrease in the contribution of grain boundary sliding, the contribution of the dislocation creep mechanism to the total strain will increase. The increase in dislocation activity with increase in the area fraction of  $\alpha$ - $\alpha$  interface has been shown by Jain et al. [99] who have done detailed characterization of dislocation activities in  $\alpha$  phase during the superplastic deformation of Ti-6Al-4V.

The grain size exponent for mixed mechanism is expected to lie in between  $p=0$  (for dislocation creep) and  $p:2-3$  (for superplastic mechanism). As a result of decrease in contribution of grain boundary sliding at lower temperatures, there is significant contribution from non superplastic mechanism, i.e. dislocation creep and thus the grain size exponent decreases to 1-1.3, which lies midway between that of superplastic mechan-

isms and dislocation creep. This also explains the on the whole increase in strain rate sensitivity with temperature at a fixed strain rate in the region II.

An alternative explanation for the low value of  $p$  at temperatures varying between 750°C and 850°C is in terms of the higher accommodation ability of the  $\beta$  phase for the grain boundary sliding. Paton and Hamilton [18] considered that, since diffusion occurs two orders of magnitude more rapidly in the  $\beta$  phase than in  $\alpha$  phase, Nabarro-Herring-Coble creep would occur more rapidly in the  $\beta$  phase. Apart from this  $\beta$  being a BCC phase, is expected to have more number slip system than  $\alpha$  phase. Thus it is softer phase and will accommodate the grain boundary sliding more easily than  $\alpha$  phase. Yang et al. [103] have also considered that the grain boundary sliding in Ti-6Al-4V is mainly accommodated by the  $\beta$  phase as proposed by the core and mantle model of Gifkins [96]. As a result with the decrease in the volume fraction of  $\beta$  grain boundary sliding should decrease due to decrease in the volume fraction of  $\beta$  within the prior  $\beta$  grains. Hence with the decrease in temperature the extent of grain boundary sliding decreased, consequently decreasing the grain size exponent.

The activation energy in the region II is higher than that of self diffusion and consequently higher than that of grain boundary diffusion of titanium in  $\alpha$  and  $\beta$  phases. Similar behaviour has been reported for dislocation creep in  $\alpha$  titanium and superplastic deformation in other two phase titanium alloys [25]. According to the different models of superplasticity the activation energy for superplastic deformation should either be equal to grain boundary diffusion or lie in between grain boundary diffusion and self diffusion.

Apart from  $Q$ , the dimensionless constant  $A$  for region II was found to be order of magnitudes higher than that predicted by any of the models of superplasticity. Thus no model of superplasticity describes properly the flow behaviour of superplastic Ti-622Si alloy.

## 5.6 Best Domain of Workability

For the primary hot working of Ti-622Si( $\beta$ ), the best domain of working was in the temperatures close to  $\beta$  transus in the ( $\alpha+\beta$ ) phase field and in the  $\beta$  phase field, at all strain rates. This is indicated by the variation of flow localization parameters as well as the values of the parameters  $\lambda$  and  $\delta$ . However this domain is not predicted as high efficiency domain by the efficiency maps. In the  $\beta$  phase field and at strain rate of  $10^{-3}$  the strain rate sensitivity was close to 0.4. This is possibly due to the formation of subgrains of  $\beta$  phase and its boundaries, as suggested by Hammond [104]. At the temperatures varying between 750°C-850°C and at strain rates varying between  $10^{-3} \text{ s}^{-1}$  and  $5 \times 10^{-2} \text{ s}^{-1}$  the workability of equiaxed microstructure was better than that of  $\beta$  microstructure. This is evident from absence of inhomogeneous flow in this temperature-strain rate domain for Ti-622Si with equiaxed microstructure as stated in the previous chapter. This is because of the flow stability of the equiaxed microstructure.

Regions of high strain rate sensitivity(close to 0.6) was observed at strain rates of  $5 \times 10^{-4}$  for the alloy in TMT condition. Though higher strain rate sensitivity was observed for condition TMT as well as TMT-A1 at strain rates approaching  $10^{-5}$ , these conditions are expected to be comparatively less advantageous for superplastic forming as the time of the forming operation is about 50 times more as compared that at strain rate of  $5 \times 10^{-4}$ . Also the extent of grain growth leading to decrease in strain rate sensitivity is higher for lower strain rates.

Strain rate sensitivity of 0.4 was observed at temperatures higher than 900°C and low strain rates for grain sizes as high as  $15 \mu\text{m}$ . Thus superplasticity is retained and good workability is expected for Ti-622Si( $\beta$ ) even at grain sizes as high as  $15 \mu\text{m}$ . This is also possibly because of superplastic character of  $\beta$  phase, as explained by Hammond [25].

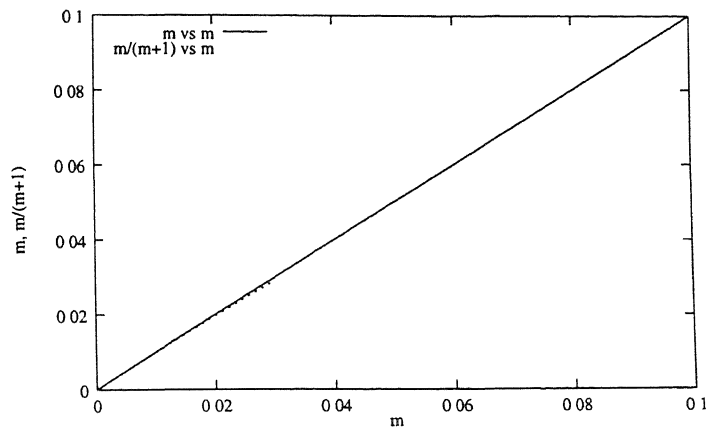


Figure 5.1: Variation of  $\frac{m}{m+1}$  with  $m$

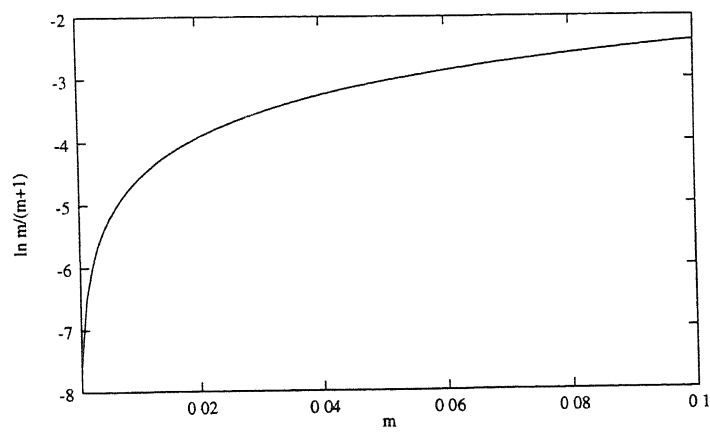


Figure 5.2: Variation of  $\ln \frac{m}{m+1}$  with  $m$



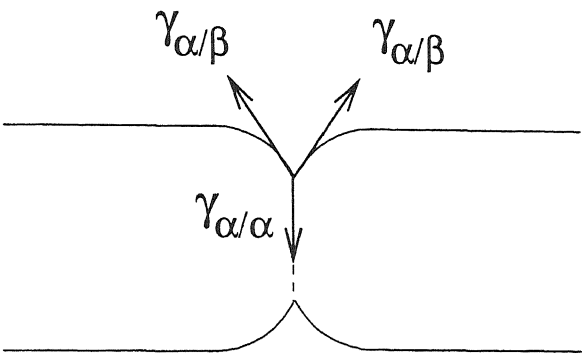


Figure 5.3: Schematic diagram of  $\beta$  penetration into  $\alpha$  plate

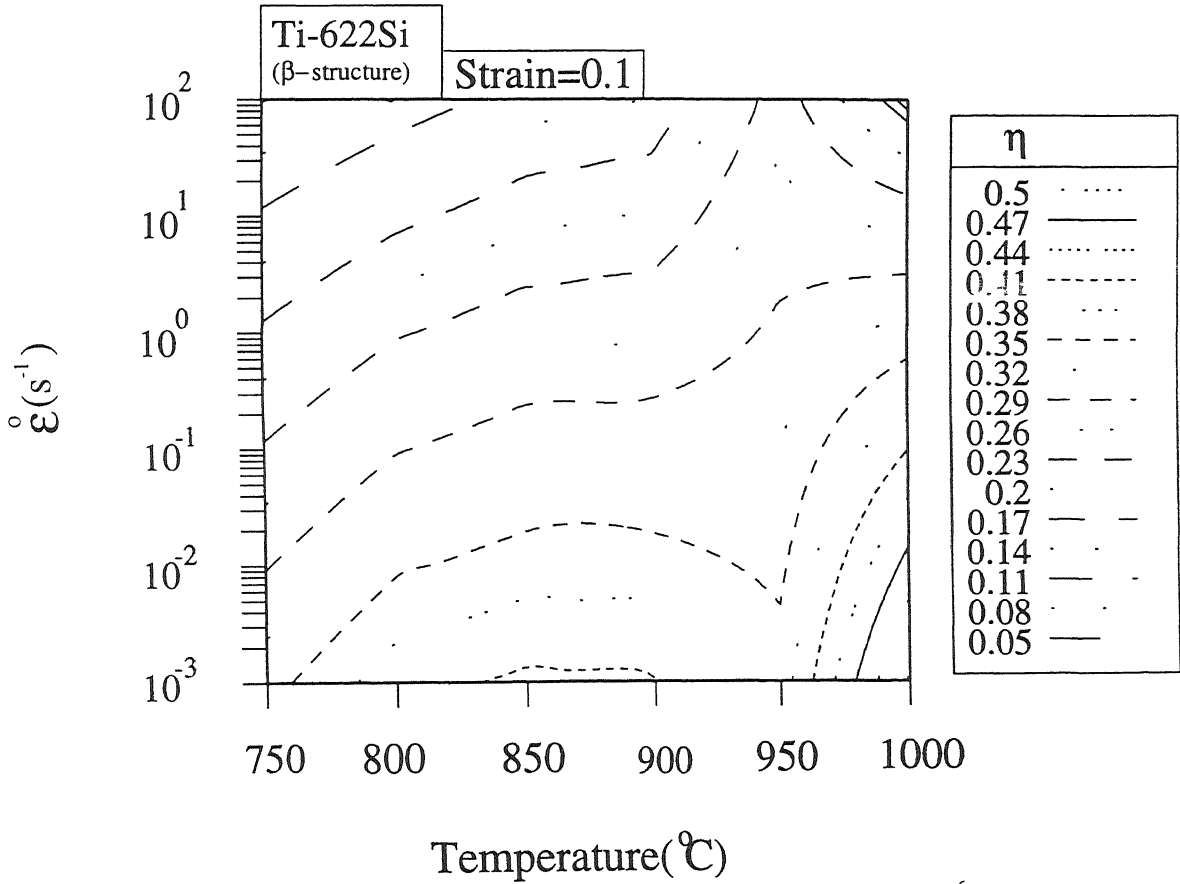


Figure 5.4: Efficiency map for Ti-622Si( $\beta$ ) corresponding to strain level of 0.1

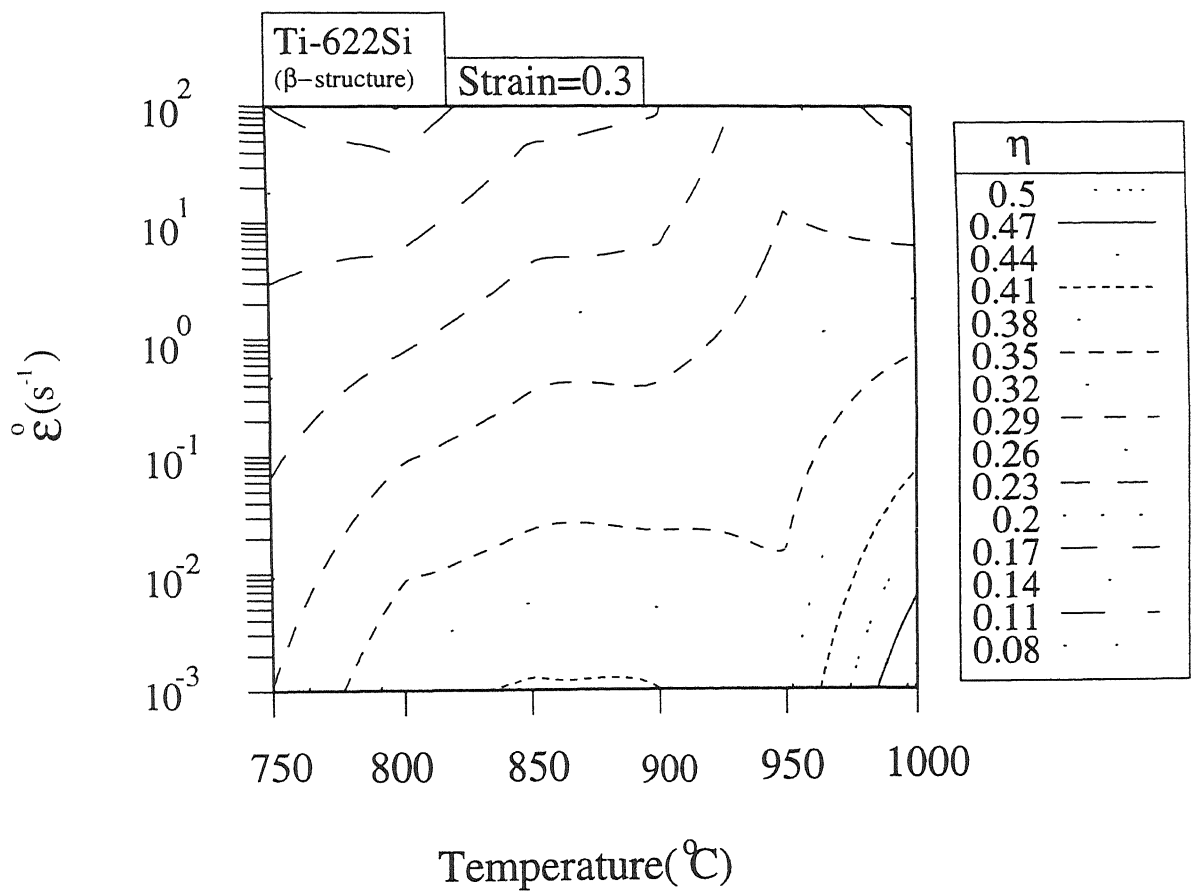


Figure 5.5: Efficiency map for Ti-622Si( $\beta$ ), corresponding to strain level of 0.3

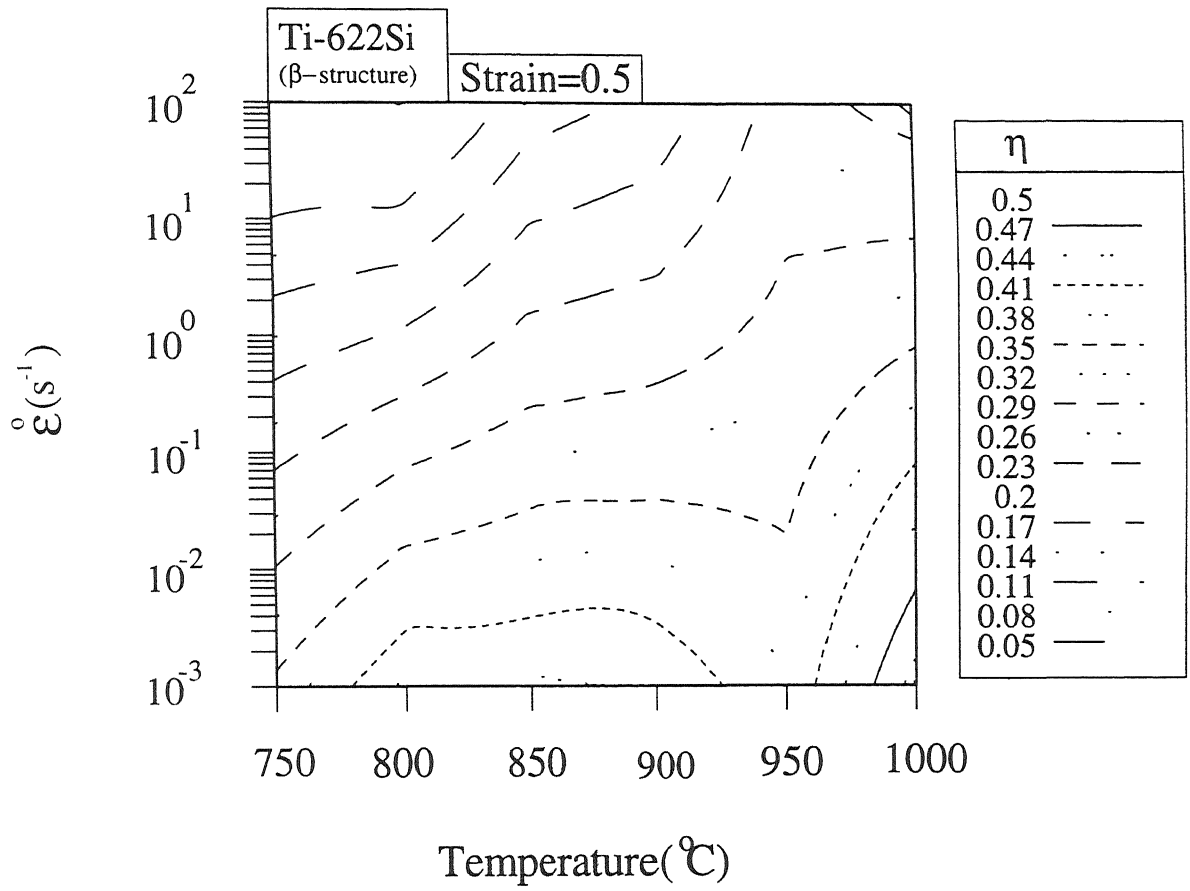


Figure 5.6: Efficiency map for Ti-622Si( $\beta$ ), corresponding to strain level of 0.5

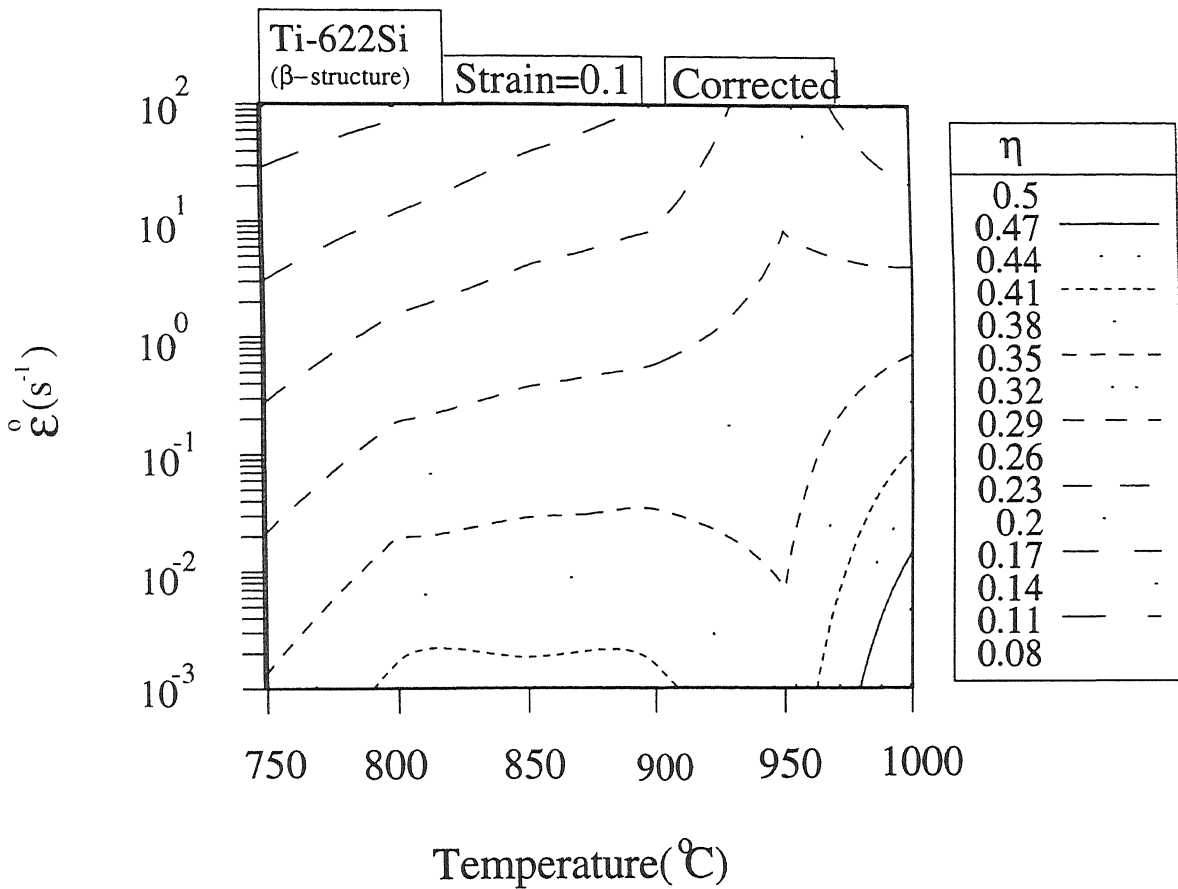


Figure 5.7: Efficiency map obtained after temperature correction, for Ti-622Si( $\beta$ ), corresponding to strain level of 0.1

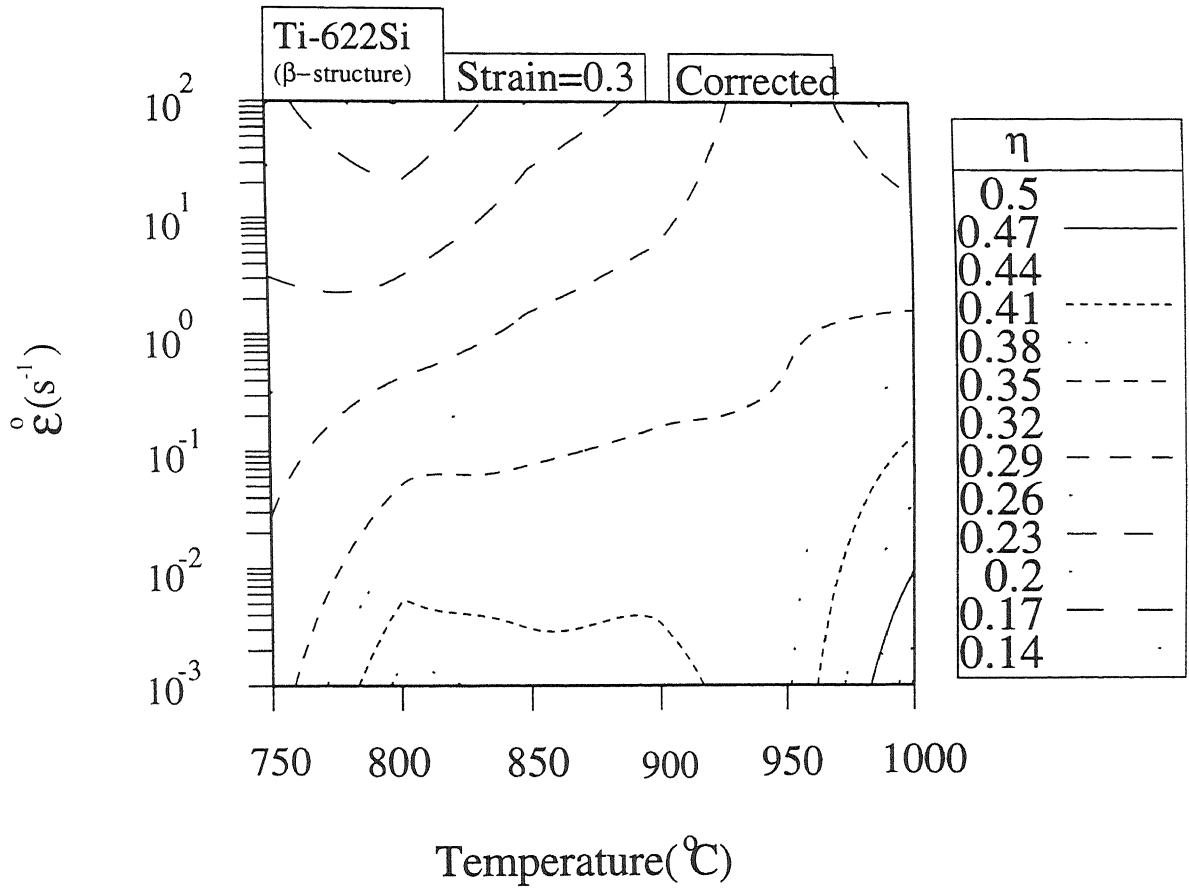


Figure 5 8: Efficiency map obtained after temperature correction, for Ti-622Si( $\beta$ ), corresponding to strain level of 0.3

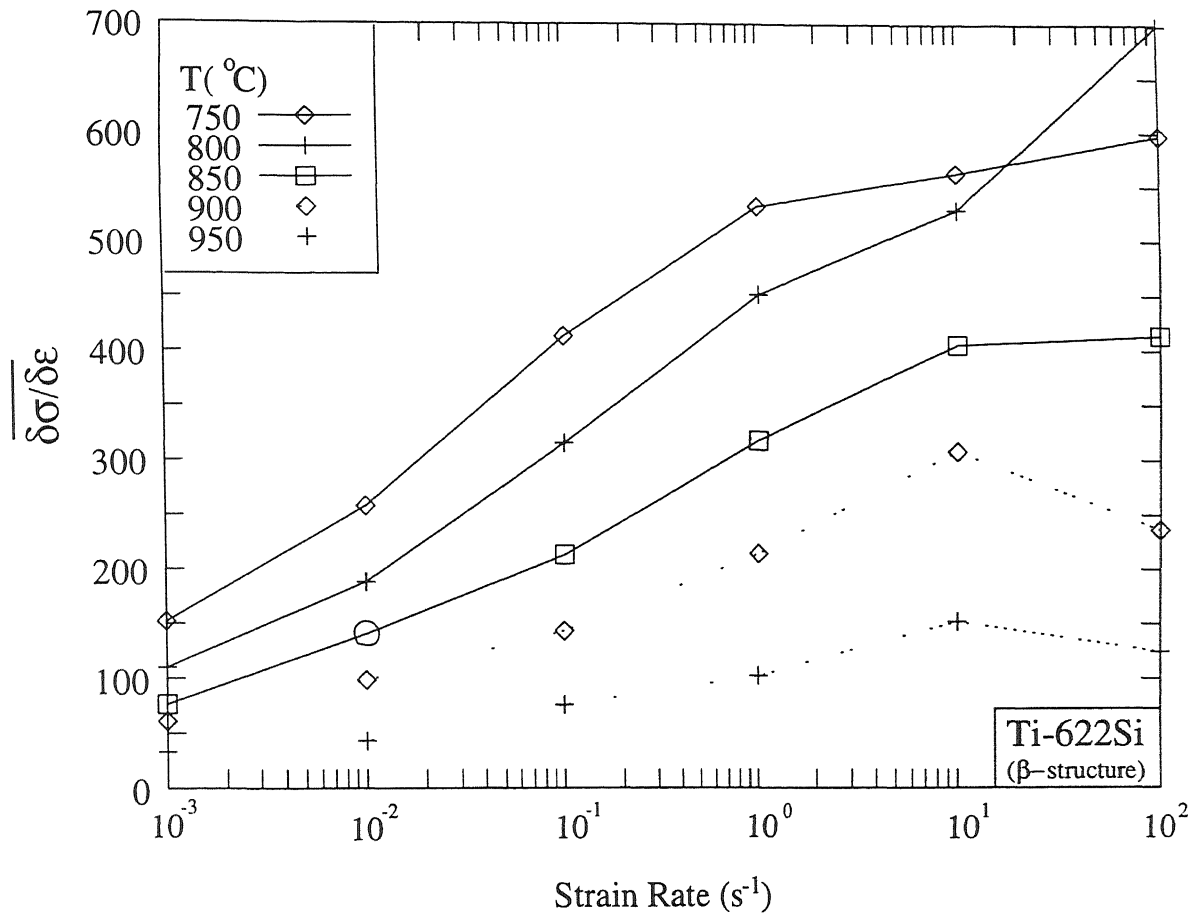


Figure 5.9: Plot of extent of flow softening in Ti-622Si ( $\beta$ ) versus strain rate

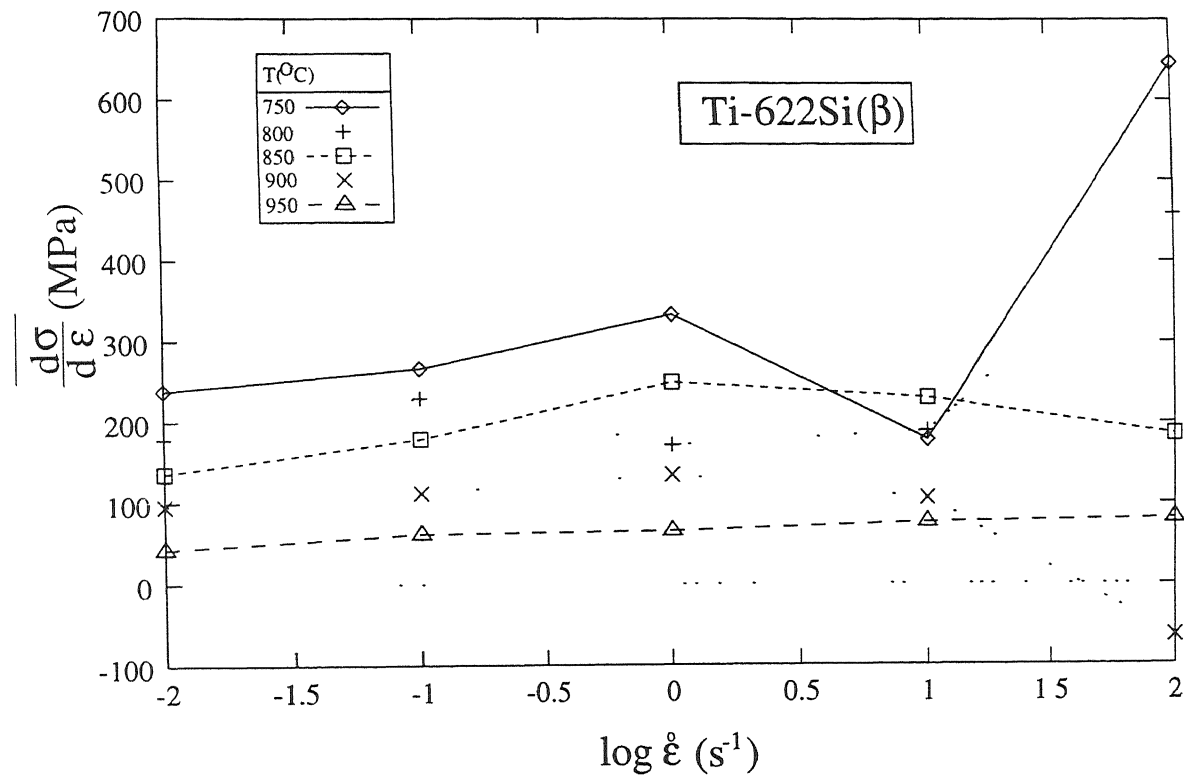


Figure 5.10: Plot of extent of flow softening in Ti-622Si ( $\beta$ ) exhibited by the temperature corrected stress-strain curves versus strain rate

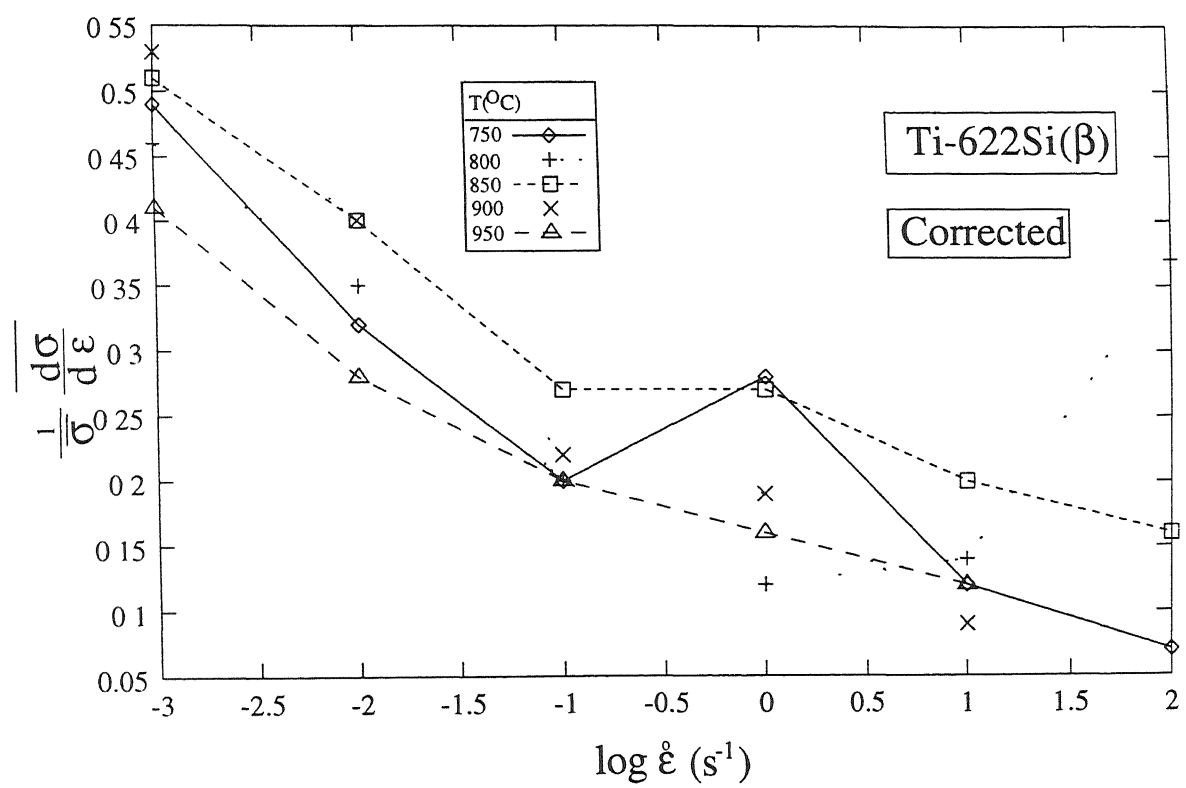


Figure 5.11: Plot of extent of flow softening in Ti-622Si ( $\beta$ ) exhibited by the temperature corrected stress-strain curves after normalization versus strain rate



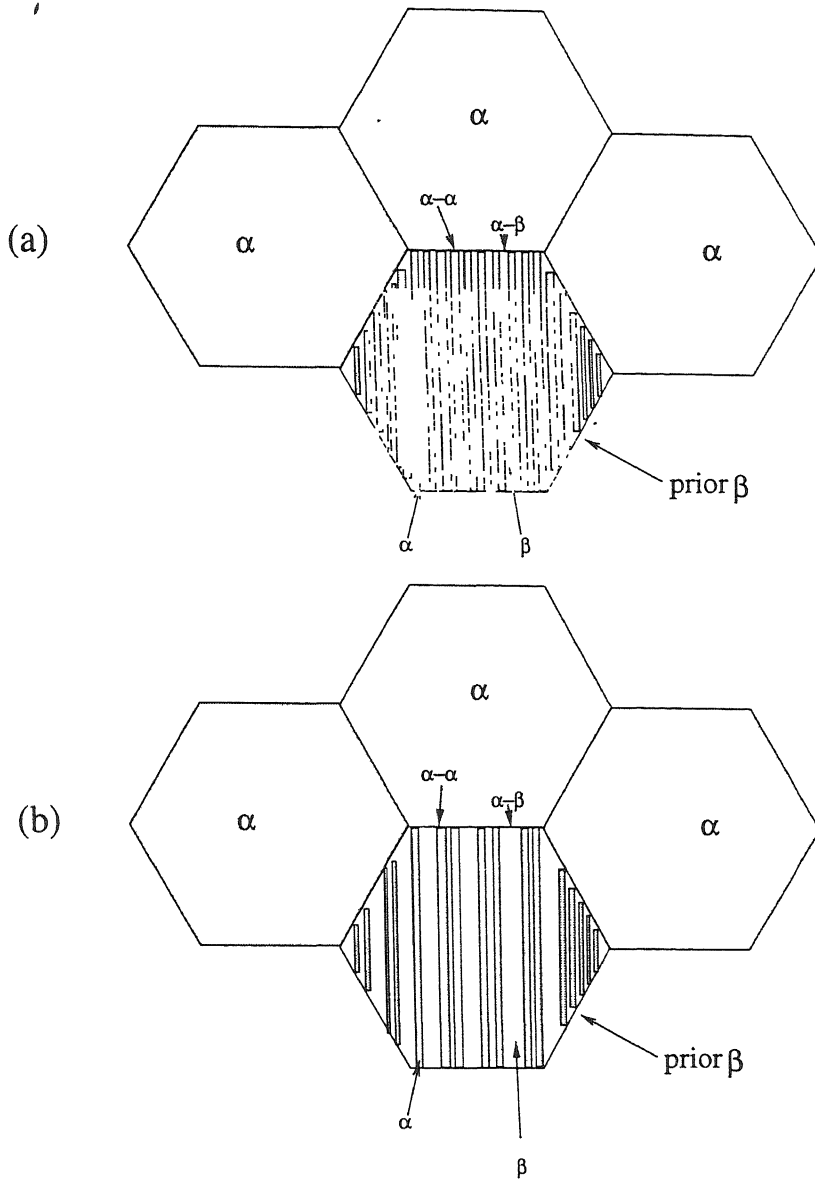


Figure 5.12: Schematic diagram of primary  $\alpha$  and prior  $\beta$  grains, showing  $\alpha-\alpha$  and  $\alpha-\beta$  boundaries (a) at lower temperatures and (b) at higher temperatures

# Chapter 6

## SUMMARY AND CONCLUSIONS

Hot isothermal compression of Ti-622Si alloy in its two microstructural states, i.e. Widmanstätten or  $\beta$  structure and equiaxed structure was carried out. Ti-622Si( $\beta$ ) was compressed under iso-strain rate condition at temperatures varying between 750°C and 1000°C, i.e. in both ( $\alpha + \beta$ ) phase field and  $\beta$  phase field, and at strain rates lying in the interval  $10^{-3} \text{ s}^{-1}$ - $10^2 \text{ s}^{-1}$ . Subsequently, deformed specimens of Ti-622Si( $\beta$ ) were examined for the macroscopic and microstructural changes in them during the compression. In order to quantify the manifestations of flow instability, the dimensions of top and bottom faces of the deformed specimens and misalignment in centers of grooves inscribed on them were measured. Further the deformed specimens were characterized for the shear band formation and microstructural evolution.

The results of the study on Ti-622Si( $\beta$ ) can be summarized as follows.

- (1) Ti-622Si( $\beta$ ) exhibited flow softening in the ( $\alpha + \beta$ ) phase field which was accompanied by stress oscillation at higher strain rates. In the  $\beta$  phase field the alloy exhibited steady state flow behaviour up to  $10 \text{ s}^{-1}$ . At  $10^2 \text{ s}^{-1}$  continuous strain hardening occurred. Stress oscillation in the  $\beta$  phase field was observed at  $10 \text{ s}^{-1}$

and  $10^2 \text{ s}^{-1}$ .

- (2)  $\log \sigma - \frac{1}{T}$  plots showed two regimes of temperature, i.e.  $750^\circ\text{C} < T < 900^\circ\text{C}$  and  $T > 900^\circ\text{C}$ , in which the variation of  $\log \sigma$  is linear with  $\frac{1}{T}$ .
- (3) Rigorous heat transfer analysis was carried out for specimens of Ti-622Si( $\beta$ ) in order to estimate the temperature rise during the deformation. The experimentally measured temperature rise was found to be significantly lower than that calculated, specially at higher strain rates. This is possibly due to very less time allowed for heat to transfer from specimen to the thermocouple embedded in the specimen. Using the  $\log \sigma - \frac{1}{T}$  plots the temperature correction was carried out. The temperature corrected stress strain curve showed flow softening at lower strain rates and strain hardening at higher strain rates, in the ( $\alpha + \beta$ ) phase field. On the other hand, in the  $\beta$  phase field they were found to exhibit strain hardening at all strain rates.
- (4) The strain rate sensitivity of Ti-622Si( $\beta$ ) was found to decrease with strain rate and had little dependence on temperature correction or strain level. Strain rate sensitivity of the alloy was different in  $\beta$  phase field and ( $\alpha + \beta$ ) phase field, at all strain rates. While it varied between 0.09 and 0.37 in the  $\beta$  phase field its value was lower in the two phase field and was found to lie between 0.03 and 0.27.
- (5) The activation energy,  $Q$ , was calculated from strain rate at constant stress versus  $\frac{1}{T}$  plot and found equal to  $540 \pm 20 \text{ KJ/mol}$ .
- (6) The constitutive behaviour over the entire range of temperature and strain rate was given by

$$\sigma = A(Z) \quad (6.1)$$

where  $A$  is a second order polynomial and  $Z$  is the Zenner-Holloman parameter given by

$$Z = e^{\frac{Q}{RT}} \quad (6.2)$$

(7)  $\psi$  showed four types of variation with plastic strain which are as follows.

**Type – I** : At all plastic strains  $\psi < 0$ , indicating that the stable flow occurs throughout the deformation;

**Type – II** :  $\psi > 0$  up to a critical strain and then  $\psi < 0$  indicating that the flow remains unstable up to a critical strain after which it tends to be stable;

**Type – III** :  $\psi < 0$  up to a critical strain and then  $\psi > 0$  indicating that the flow is stable to begin with but becomes unstable after reaching a critical strain,

**Type – IV** :  $\psi$  oscillates between positive and negative values indicating that the flow becomes stable and unstable several times during the deformation.

The maximum value of  $\psi$  in type-II variation increased with increase in strain rate. On the other hand  $\psi_c$  showed only two types of variation with plastic strain, i.e. Type-I and Type-II and the domain of flow instability is considerably reduced. This indicates that for a certain domain of temperature and strain rate the temperature rise plays a significant role in causing flow instability. In case of Type-II variation of  $\psi_c$  it was observed that the critical strain at which the transition from unstable to stable flow occurred increased with increase in the strain rate at deformation temperature of 750°C. In contrast, at deformation temperatures of 850°C, 900°C and 950°C, the critical strain decreased with increase in the strain rate.

(8) Shear banding was observed at low temperatures and high strain rates. At lower strain rates the bands were not distinct.  $\delta$ , which is a measure of shear banding increased with increase in strain rate and decrease in temperature.

(9)  $\lambda$  is the temperature range 750°C-900°C decreased with strain rate and again

increased at higher strain rates.

- (10) The  $\beta$  microstructure of Ti-622Si was found to be unstable during the deformation. The  $\alpha$  plates either kinked or got elongated depending upon their orientation with respect to the compression axis. Some of these  $\alpha$  plates underwent differential straining. The deformed plates subsequently fragmented due to  $\beta$  penetration. Apart from these coarsening of  $\alpha$  was also observed. The extent of fragmentation and coarsening was found to increase with increase in temperature and decrease in strain rate. During deformation in the  $\beta$  phase field bulges at the grain boundaries were observed at low strain rates and at strain rates of  $10 \text{ s}^{-1}$  and  $10^2 \text{ s}^{-1}$  recrystallization near prior grain boundary leading to the formation of smaller grains was observed
- (11) In the specimens deformed at temperatures of  $750^\circ\text{C}$  and  $800^\circ\text{C}$  and strain rate of  $10^2 \text{ s}^{-1}$ , separate and more intense bands were observed within the shear band. The separate band in the specimen deformed at  $800^\circ\text{C}$ - $10^2 \text{ s}^{-1}$  showed fine equiaxed  $\alpha$ . The separate band within the specimen deformed at  $750^\circ\text{C}$  consisted of: (a) low volume fraction of primary equiaxed  $\alpha$  which have been fragmented into very small size ( $1\text{-}2 \mu\text{m}$ ) and (b) equiaxed prior  $\beta$  grains having size of  $1\text{-}2 \mu\text{m}$  within which secondary  $\alpha$  had precipitated.
- (12) Step strain rate tests were carried out on Ti-622Si with equiaxed structure. i.e. in TMT, TMT-A1, TMT-A2, and TMT-A3 conditions. From the these tests,  $\log\sigma$  versus  $\log\dot{\epsilon}$  plots were obtained. From the slope of the  $\log\sigma$  versus  $\log\dot{\epsilon}$  plots variation of strain rate sensitivity with strain rate was obtained. From the variation of strain rate sensitivity regions I, II and III were identified. Ti-622Si in the TMT-A1, TMT-A2 and TMT-A3 conditions exhibited region II and region III of superplasticity. The alloy in TMT condition exhibited region I in the temperature range of  $900^\circ\text{C}$ - $940^\circ\text{C}$ . Constitutive equations of the form

$$\dot{\epsilon} = \frac{AD_oEb}{kT} \left(\frac{b}{d}\right)^p \left(\frac{\sigma}{E}\right)^n e^{-\frac{Q}{RT}} \quad (6.3)$$

were obtained for region II and III. The parameters of constitutive equation in the region II showed the following trend.

- (1) The value of strain rate sensitivity was found to lie within the range  $0.5 \pm 0.1$  with few exceptions.
- (2) The grain size exponent increased with temperature from 1.0 at 800°C to 2.6 at 920°C. Above 920°C it decreased to 1.76 at 940°C and then again increased to 2.5 at 950°C.
- (3) The activation energy,  $Q$ , was found to 230-260 KJ/mol and was higher than self-diffusion and grain boundary diffusion.

Activation energy in the region III was equal to  $290 \pm 12$  KJ/mol.

The following conclusions were drawn after analysis of the above results.

- (1) The flow localization parameters  $\psi$  and  $\psi_s$  could successfully predict inhomogeneous flow and shear banding in Ti-622Si( $\beta$ ) with exception at 950°C. At a given temperature the extent of flow instability was found to increase with increase in the maximum values of  $\psi$  and  $\psi_s$ . Thus the flow localization parameters can be successfully used for predicting flow instabilities in Ti-622Si( $\beta$ ) like in other two phase titanium alloys.
- (2) Kumar's criteria predicts a very limited domain of flow instability for Ti-622Si( $\beta$ ), i.e. at low temperature and high strain rates. In this domain, the shear bands were prominent. An alternative explanation of this is that in the domain in which Kumar's criteria is satisfied the value of strain rate sensitivity is low leading to very high values of  $\psi_s$ , the flow localization parameter for shear band formation. However, instabilities in the form of inhomogeneous flow were observed in a much wider domain which Kumar's criteria fails to predict. Gegel's criteria, on the other hand, does not predict flow instability in the entire domain of temperature and

strain rate in which the compression test was carried out for Ti-622Si( $\beta$ ). Thus the new approaches have no advantage in the predicting flow instability in the alloy with  $\beta$  structure.

- (3) Morphological changes in  $\alpha$  during hot deformation of Ti-622Si( $\beta$ ) can be explained in terms of two types of mechanisms, which are as follows.
  - (a) Mechanisms of morphological changes which contribute to the plastic deformation of the specimen. Example of this is dislocation movement leading to kinking and elongation of  $\alpha$  plates.
  - (b) Mechanisms of morphological changes which do not contribute to the plastic strain but their rates are enhanced during concurrent plastic deformation. Examples of this are  $\beta$ -penetration into  $\alpha$  plates, coarsening and spheroidization of  $\alpha$ . These mechanisms occur during heat treatment also but their rate get enhanced during plastic deformation.
- (4) Domains in the efficiency map of Ti-622Si( $\beta$ ) with peak efficiency at  $800^{\circ}\text{C}-10^{-3}\text{s}^{-1}$  and  $1000^{\circ}\text{C}-10^{-3}\text{s}^{-1}$  does not correspond to particular microstructural changes. The best temperature-strain rate condition for transformation to equiaxed  $\alpha$  and DRX of  $\beta$ -phase are not indicated by the efficiency map.
- (5) Instability parameters  $\eta$  and  $s$  which are based on concepts of irreversible thermodynamics do not indicate the microstructural changes occurring in Ti-622Si( $\beta$ ) during the deformation
- (6)  $\psi_c$  is obtained from the temperature corrected stress strain curves. Thus the criteria  $\psi_c > 0$  indicates the flow instability in specimen caused by factors apart from temperature rise, i.e. microstructural and textural changes.  $\psi_c$  as stated earlier exhibited only Type-I and Type-II variations. It was further observed, as stated earlier that the critical strain at which the transition from unstable to stable flow occurred, increased with increasing strain rates at deformation temperature

of 750°C and in contrast, at 850°C, 900°C and 950°C it decreased with increasing strain rate. Such variation could be reasonably correlated with morphological changes. The same extent of transformation of  $\beta$  structure which is unstable to stable equiaxed structure is achievable at lower strains when the strain rate is decreased. On the other hand, the extent of coarsening which contributes to flow instability is also higher at low strain rate resulting in delay in transition from unstable to stable flow. At 750°C the coarsening is not so significant as compared to higher temperatures. Thus at this temperature the effect of transformation to equiaxed microstructure, which is relatively more stable than  $\beta$  structure predominates resulting into increase in the critical strain with strain rate. At higher temperatures the effect of coarsening is predominant resulting into reverse trend.

- (7) The variation in grain-size exponent,  $p$ , for deformation of equiaxed Ti-622Si, with temperature has been correlated with the change in the microstructure of the alloy with the temperature. Ti-622Si, in TMT, TMT-A1, TMT-A2 and TMT-A3 conditions consist of  $\alpha$  phase with two morphologies viz primary equiaxed and Widmanstätten which has precipitated within the prior  $\beta$  grains. At lower temperatures (800°C-850°C) the fraction of  $\alpha$ - $\alpha$ , which is expected to have the maximum sliding resistance is high. Thus the contribution of grain boundary sliding to the deformation is lower and mechanism of dislocation creep will have significant contribution. The grain-size exponent in this case will lie in between that of purely superplastic mechanism ( $p:2-3$ ) and dislocation creep ( $p=0$ ). With the increase in temperature upto 920°C very less change occurs in the volume fraction of primary  $\alpha$  whereas the Widmanstätten  $\alpha$  transforms to  $\beta$  phase. This results in increase in the fraction of  $\alpha$ - $\beta$  and  $\beta$ - $\beta$  boundary and consequent increase in the contribution of grain boundary sliding and decrease in the contribution of dislocation creep to the overall strain in the region II. Thus, grain size exponent,  $p$ , increases to that of superplastic mechanism ( $p:2-3$ ). This explanation is supported by observed increase in strain rate sensitivity from 800°C to 920°C for Ti-622Si



with equiaxed microstructures.

c/ESTIMATION OF TEMPERATURE DISTRIBUTION AS A RESULT OF HEAT GENERATION

c/COMPRESSION SPECIMENS:

c/UNSTEADY ONE DIMENSIONAL HEAT CONDUCTION PROGRAM

c/\*\*\*\*\*

COMMON X(500),T(500),AE(500),AW(500),AP(500)

2 ,B(500),P(500),Q(500),DXEP(500),DXPW(500),XEW(500)

2 ,CON(500),SOR(500),HTCOF,N,TS,DELX,RO(500)

2 ,C(500),TO(500),APO(500),DELT,TIME,TMAX

2 ,ITER,SUMP,SUMNB,S,R,RES,TD,POW

2 ,TOLD(500)

open(unit=22,file='hfc.out')

open(unit=23,file='del\_T')

c write(22,15)

15 FORMAT(1X,///'DISTANCE(I)',5X,'TEMPERATURE(I)')

c WRITE(22,\*)'-----'

N=302

TD=750.0

POW=1.0e8

DELT=0.5

TMAX=10.0

TD=TD+273

DELX=3.0\*0.012/FLOAT(N-2)

X(1)=-DELX

X(2)=DELX

DO 20 I=3,N

X(I)=X(I-1)+DELX

20 continue

TIME=0.0

```
DO 32 I=1,N
T(I)=TD
c TO(I)=T(I)
TO(I)=TD
32      CONTINUE
CALL GRID
101     TIME=TIME+DELT
ITER=0
150     ITER=ITER+1
WRITE(*,*) TIME,RES,ITER,T(30)
CALL PROP
CALL CALT
CALL BOUND
CALL SOLVE
SUMP=0
SUMNB=0
        DO 58 I=1,N
S=AP(I)*T(I)
SUMP=S+SUMP
        R=AE(I)*T(I+1)+AW(I)*T(I-1)+B(I)
SUMNB=R+SUMNB
58      CONTINUE
        RES=ABS(S-R)
IF(ITER.LE.100) go to 150
CALL PRINT
DO 40 I=2,N-1
TO(I)=T(I)
40      CONTINUE
```







END

CC

SUBROUTINE SOLVE

CC

COMMON X(500),T(500), AE(500),AW(500),AP(500)

2 ,B(500),P(500),Q(500),DXEP(500),DXPW(500),XEW(500)

2 ,CON(500),SOR(500),HTCOF,N,TS,DELX,RO(500)

2 ,C(500),TO(500),APO(500),DELT,TIME,TMAX

2 ,ITER,SUMP,SUMNB,S,R,RES,TD,POW

2 ,TOLD(500)

P(2)=AE(2)/AP(2)

Q(2)=B(2)/AP(2)

DO 21 I=2,N-1

P(I)=AE(I)/(AP(I)-AW(I)\*P(I-1))

Q(I)=(B(I)+AW(I)\*Q(I-1))/(AP(I)-AW(I)\*P(I-1))

21 CONTINUE

T(N)=Q(N)

DO 75 I=N-1,2,-1

T(I-1)=P(I-1)\*T(I)+Q(I-1)

75 continue

RETURN

END

CC

subroutine print

CC

COMMON X(500),T(500), AE(500),AW(500),AP(500)

2 ,B(500),P(500),Q(500),DXEP(500),DXPW(500),XEW(500)

2 ,CON(500),SOR(500),HTCOF,N,TS,DELX,RO(500)

```
      2  ,C(500),TD(500),APO(500),DELT,TIME,TMAX
      2  ,ITER,SUMP,SUMNB,S,R,RES,TD,POW
      2  ,TOLD(500)
write(22, 88) TIME
      88      FORMAT(1X,F10.4)
           DO 90 I=2,N-1
write(22,120) X(I),T(I)
      120      FORMAT(1X,F14.8,4X,2F12.4)
      90      CONTINUE
avdt=0.0
           DO  I=102,201
DT=T(I)-TD
avdt=avdt+DT
write(23,*) X(I),DT
enddo
av=avdt/100.0
write(*,*) av
RETURN
END
```



# Bibliography

- [1] *Materials Properties Handbook: Titanium Alloys*. ASM International, 1996.
- [2] C.W.Collings. *The Physical Metallurgy of Titanium Alloys*. ASM International, Metals Park, OH 44073, 1984.
- [3] O.A.Kaibyshev, I.V.Kazachkov, and W.R.Galecv. *J. Mat. Sc.*, 16:2501, 1981.
- [4] G.E.Dieter. *Metals Hand Book*. volume 14 of *9th Edition*. ASM International, Metals Park Ohio, 1988.
- [5] P.Dadras and Jr. J.F.Thomas. *Metall. Trans. A*, 12A:1867, 1981.
- [6] J.J.Jonas, C.M.Sellars, and W.J.McG.Tegart. *Met. Rev.*, 14:1, 1969.
- [7] C.Zener and J.H.Hollomon. *J. Appl. Phys.*, 15:22, 1944. -
- [8] H.J.McQueen and J.J.Jonas. *Metal Forming Interrelation Between Theory and Practice*, Ed. A.L. Hoffmanner. page 393. Plenum Press, 1971.
- [9] H.J.McQueen. *J. Metals*, page 38. 1968.
- [10] H.J.McQueen and J.J.Jonas. Plastic deformation of materials. In *Treatise on Material Science and Technology*. Academic Press, New York, 1975.
- [11] W.Roberts. *Deformation, Processing and Structures*(Ed.G.Krauss), page 109. ASM, Ohio, 1984.

- [12] S.L.Semiatin and G.D.Lahoti. *Metall. Trans. A*, 12A:1705, 1981.
- [13] A.K.Mukherjee, J.E.Bird, and J.E.Dorn. *Trans. ASM*, 62:155, 1969.
- [14] J.A Wert and N.E.Paton. *Metall. Trans. A*, 14A:2535, 1983.
- [15] A.Arieli, B.J.Maclean, and A.K.Mukherjee. *Res. Mech.*, 6:131, 1983.
- [16] A.K.Ghosh and C.H.Hamilton. *Metall Trans. A*, 10A:699, 1979.
- [17] S.M.L Sastry, R.J.Lederich, T.L. Mackay, and W.R.Kerr. *Journal of Metals*, 35.48, 1983
- [18] N E.Paton and C.H.Hamilton. *Metall. Trans.*, 10A:241, 1979.
- [19] A K.Ghosh and C.H.Hamilton. *Defence Science Journal(INDIA)*, 36(2):153 – 177, 1986.
- [20] M.Y.Wu and O.D.Sherby. *Scripta Met.*, 8:773, 1984.
- [21] A.Arieli and A.K.Mukherjee. *Mat. Sci. Eng.*, 43:47, 1980.
- [22] F.H.Froes, C.F.Yolton, J.C.Chestnutt, and C.H.Hamilton. *Forging and Properties of Aerospace Materials*, page 371. The Metals Society of London, 1978.
- [23] R.R.Boyer and J.E.Magnuson. *Metall. Trans. A*, 10A:1191, 1979.
- [24] M.Kh.Shorshorov, A.S.Tikhonov, G.N.Kofanova, and I.I.Prokhorova. *Titanium and Titanium Alloys*, volume 2, page 837. Met. Soc. AIME, New York, 1982.
- [25] C.H.Hamilton. In *Superplasticity(Ed. B.Baudelet and M.Suery)*, page 14.1, 1985.
- [26] D.Lee and W.Backofen. *Trans. AIME*, 239:1034, 1967.
- [27] T.L.Mackay, S.M.L.Sastry, and C.F.Yolton. U.s. air force report no. afwal-tr-80-4038. Technical report, 1980.
- [28] H.J.McQueen, E.Evangelista, and M.E.Kassner. *Z. Metallkde.*, 82:336, 1991.

- [29] A.K.Ghosh and R.Raj. *Acta Met.*, 29:607, 1981.
- [30] A.Dutta. *Superplastic Behaviour in Titanium Alloys*. PhD thesis, Indian Institute of Technology, Bombay, 1988.
- [31] A.Arieli and A.Rosen. *Metall. Trans. A*, 8A:1591, 1977.
- [32] S.L.Semiatin and J.J.Jonas. *Formability and Workability of Metals: Plastic Instability and Flow Localization*. ASM International, Metals Park, Ohio, 1984.
- [33] S.L.Semiatin and G.D.Lahoti. *Metall. Trans. A*, 14A:105, 1983.
- [34] A.Considere. *Ann. des Ponts & Chaussees*, 9(6):574, 1885.
- [35] J.J.Jonas, R.A.Holt, and C.E.Coleman. *Acta Met.*, 24:911, 1976.
- [36] E.W.Hart *Acta Met.*, 15:351, 1967.
- [37] Y.V.R.K.Prasad, H.L.Gegel, S.M.Doraivelu, J.C.Malas, J.T.Morgan, K.A.Lark, and D.R.Barker. *Metall. Trans. A*, 15A:1883, 1984.
- [38] Y.V.R.K.Prasad. *Indian Journal of Technology*, 28:435, 1990.
- [39] H.L.Gegel, J.C.Malas, S.M.Doraivelu, and V.A.Shende. *Metals Handbook*, volume 14, page 417 ASM International, Metals Park Ohio, 1988.
- [40] H.L.Gegel. *Computer Simulation in Materials Science*, page 291. ASM International, Materials Park, Ohio, 1986.
- [41] J.M.Alexander *Modelling of Hot Deformation of Steels*, page 101. Springer-Verlag, Berlin, 1989.
- [42] H.Ziegler. *Progress in Solid Mechanics (Ed. I.N.Sneddon and R.Hill)*, page 93. North-Holland Publishing Company, Amsterdam, 1963.
- [43] F.Montheillet and J.J.Jonas. *Metall. Mater. Trans. A*, 27A:232, 1996.

- [44] Y.V.R.K.Prasad. *Metall. Mater. Trans. A*, 27A:235. 1996.
- [45] L.E.Malvern. *Introduction to the Mechanics of Continuous Medium*. Prentice-Hall, Eaglewood Cliffs, NJ, 1969.
- [46] S.V.S.Narayana Murthy. M.S.Sarma. and B.Nageswara Rao. *Metall. Mater. Trans. A*. 28A:1581, 1997.
- [47] P.K.Sagar. D.Banerjee, K.Muraleedharan, and Y.V.R.K.Prasad. *Metall. Mater. Trans. A*. 27A, 1996.
- [48] P K Sagar. D.Banerjee. and Y.V.R K.Prasad. *Mater. Sci. Tech.*, 13:755. 1997.
- [49] J K Chakravarty, Y.V.R.K.Prasad, and M.K.Asundi. *Metall. Trans. A*, 22A:829. 1991.
- [50] N.Ravichandran and Y.V.R.K.Prasad. *Metall. Trans. A*. 22A:2339. 1991.
- [51] D.Padmavardhini and Y.V.R.K.Prasad. *Metall. Trans. A*, 22A:2985. 1991.
- [52] D.Padmavardhini and Y.V.R.K.Prasad. *Metall. Trans. A*, 22A:2993. 1991.
- [53] D.Padmavardhini and Y.V.R.K.Prasad. *Mat. Sci. Tech.*, 7:947. 1991.
- [54] B.V.Radhakrishna Bhatt, Y.R.Mahajan, H.Md.Roshan. and Y.V.R.K.Prasad. *Metall. Trans. A*, 23A:2223, 1992.
- [55] M.C.Somani. E.S.B.Rao. N.C.Birla, M.L.Bhatia, V.Singh. and Y.V.R.K.Prasad. *Metall. Trans. A*, 23A:2249, 1992.
- [56] Satish V.Kailas, Y.V.R.K.Prasad, and S.K.Biswas. *Metall. Trans. A*, 24A:2513. 1993.
- [57] N.Srinivasan and Y.V.R.K.Prasad. *Mat. Sci. Tech.*, 8:206, 1992.
- [58] M.Long and H.J.Rack. *Mat. Sci. Engg. A*, 194A:99. 1995.

- [59] M.Long and H.J.Rack. *Mat. Sci. Eng. A*, 170A:215. 1993.
- [60] S.Venugopal, S.L.Mannan, and Y.V.R.K.Prasad. *Metall. Mater. Trans. A*, 27A:119, 1996.
- [61] S.Venugopal, S.L. Mannan, and Y.V.R.K.Prasad. *Mat. Sci. Eng.*, 160A:63, 1993.
- [62] S.Venugopal, S.L. Mannan, and Y.V.R.K.Prasad. *Mat. Sci. Eng.*, 177A:143. 1994.
- [63] S.Venugopal, S.L.Mannan, and Y.V.R.K.Prasad. *Mat. Lett.*, 15:79. 1992
- [64] S.Venugopal, S.L. Mannan, and Y.V.R.K.Prasad. *Mat. Sci. Tech.*, 9:1021. 1993.
- [65] S.Venugopal, S L.Mannan, and Y.V.R.K.Prasad. *J. Nucl. Mat.*, 206:77. 1993.
- [66] S.Venugopal, S.L.Mannan, and Y.V.R.K.Prasad. *Mat. Let.*, 17:388, 1993.
- [67] S.Venugopal, S.L. Mannan, and Y.V.R.K.Prasad. *Mat. Sci. Tech.*, 9:899. 1993.
- [68] S.Venugopal, S.L.Mannan, and Y.V.R.K.Prasad. *Scripta Met. Mat* , 28:715, 1993.
- [69] S.Venugopal, C.Ravishankar, S.L.Mannan, and Y.V.R.K.Prasad. *Scripta Met. Mat.*, 30:1611, 1994.
- [70] V.Gopala Krishna, Y.V.R.K.Prasad, N.C.Birla. and G.Sambasiva Rao. *J. Metals*, page 56, 1996.
- [71] M.Bocek and J.H.Choi. *Mat. Sci. Eng. A*, 137A:111. 1991.
- [72] G.Gottstein and S.Deshpande. *Mat. Sci. Eng.*, 94:147, 1987.
- [73] M.Ueki, S.Horie, and T.Nakamura. *Mat. Sci. Tech.*, 3:329. 1987.
- [74] C.M.Sellars. *Phil. Trans. Roy. Soc. Lond. A*. 288A:147, 1978.
- [75] T.Sakai and J.J.Jonas. *Acta Met.*, 32:189, 1984.

- [76] H J.McQueen, J.Sankar, and D.Fulop. *Mechanical Behaviour of Materials* (Eds. K.J.Miller and R.F.Smith), volume 2, page 675. Pergamon Press, Oxford, 1979.
- [77] G.Gottstein and S.Chen. *Proceedings of International Conference Recrystallization 90*(Ed. T.Chandra), page 69. Metals and Materials Society, Wollongong, Australia, 1990.
- [78] M.J.Luton and C.M.Sellars. *Acta Met.*, 17:1033, 1969.
- [79] A.D.Rollet, M.J.Luton, and D.J.Srolovitz. *Acta Met. Mat.*, 40:43, 1992.
- [80] R Sandstrom and R.Lagneborg. *Acta Met.*, 23:387, 1975.
- [81] B.Derby and M.F.Ashby. *Scripta Met.*, 21:879, 1987.
- [82] W.Roberts, H.Boden, and B.Ahlblom. *Met. Sci.*, 13:195, 1979.
- [83] I.Weiss, F.H.Froes, D.Elyon, and G.E.Welsch. *Metall. Trans. A*, 17A:1935, 1986.
- [84] M.Peters, G.Lutjering, and G.Ziegler. *Z. Metallkde*, 74:274, 1983.
- [85] S.L.Semiatin, Jr. J.F.Thomas, and P.Dadras. *Metall. Trans. A*, 14A:2363, 1983.
- [86] C Andres, A.Gysler, and G.Lutjering. *Z.Metallkd.*, 88:197, 1997.
- [87] O.A.Kaybyshev, R.YA.Lutfullin, and G.A.Salischev. *Phys. Met. Metall.* 66:109, 1988.
- [88] A.Ball and M.M.Hutchinson. *Met. Sci. J.*, 3:1, 1969.
- [89] A.K.Mukherjee. *High Temperature Creep*, volume 6 of *Treatise on Materials Science and Technology*, page 164. Academic Press, New York, 1978.
- [90] J.H.Gittus. *Trans. ASME*, 99:244, 1977.
- [91] J.H.Gittus. *Phil. Trans. Roy. Soc. Lond. A*, 288A:121. 1978.
- [92] F.R.N.Nabarro. page 75. *Strength of Solids*. The Physical Society, London, 1948.

- [93] C.Herring. *J. Appl. Phys.*, 21:437, 1950.
- [94] R.L.Coble. *J. Appl. Phys.*, 34:1679, 1963.
- [95] M.F.Ashby and T.G.Verall. *Acta Met.*, 21:149, 1973.
- [96] R.C.Gifkins. *Metall. Trans. A*, 7A:1225, 1976.
- [97] K.A.Padmanabhan. *Mat. Sci. Engg.*, 29:1, 1977.
- [98] M.G.Zeln, H.S.Yang, R.Z.Valiev, and A.K.Mukherjee. *Metall. Trans. A*, 23A:3135. 1992.
- [99] M.Jain, M.C.Chaturvedi, N.L.Richards, and N.C.Goel. *Mat. Sci. Engg. A*, 145A:205. 1991.
- [100] M.E.Rosenblum, P.R.Smith, and F.H.Froes. *Proceedings of Titanium Science and Technology (Ed. H.Kimura and O.Izumi)*, page 1015. Met. Soc. of AIME, Warrandale, PA, 1984.
- [101] H.Inagaki. *Z. Metallkde*, 87:179, 1986.
- [102] P.G.Partridge, D.S.McDarmaid, and A.W.Bowen. *Acta Met.*, 33:571, 1985.
- [103] H.S.Yang. G.Gurewitz, and A.K.Mukherjee. *Trans. JIM.*, 32:465, 1991.
- [104] G.C.Morgan and C.Hammond. *Mat. Sci. Eng.*, 86:159, 1987.

